FIELD PERFORMANCE MONITORING AND MODELING OF INSTRUMENTED PAVEMENT ON I-35 IN MCCLAIN COUNTY - PHASE 1

FINAL REPORT ~ FHWA-OK-13-05

ODOT SP&R ITEM NUMBER 2200

Submitted to:

John R. Bowman, P.E.
Planning & Research Division Engineer
Oklahoma Department of Transportation

Submitted by:

Pranshoo Solanki, Ph.D.
Nur Hossain
Marc Breidy
Dharamveer Singh, Ph.D.
Musharraf Zaman, Ph.D., P.E.
K.K. “Muralee” Muraleetharan, Ph.D., P.E., G.E.
University of Oklahoma
David Timm, Ph.D., P.E.
Auburn University

June 2013

TECHNICAL REPORT DOCUMENTATION PAGE

1. REPORT NO.	2. GOVERNMENT ACCESSION NO.	3. RECIPIENT'S CATALOG NO.
FHWA-OK- 13-05		

4. TITLE AND SUBTITLE	5. REPORT DATE
Field Performance Monitoring and Modeling of Instrumented Pavement on I-35 in McClain County – Phase 1	Jun 2013
	6. PERFORMING ORGANIZATION CODE

7. AUTHOR(S)	8. PERFORMING ORGANIZATION REPORT
Pranshoo Solanki, Nur Hossain, March Breidy, Dharamveer Singh, Musharraf Zaman, K. K. "Muralee" Muraleetharan, David Timm	Click here to enter text.

9. PERFORMING ORGANIZATION NAME AND ADDRESS	10. WORK UNIT NO.
College of Engineering, The University of Oklahoma 202 West Boyd St. #107, Norman, Oklahoma, 73019, and Department of Civil Engineering, Auburn University 238 Harbert Engineering Center, Auburn, Alabama, 36849	11. CONTRACT OR GRANT NO. ODOT SP&R Item Number 2200

12. SPONSORING AGENCY NAME AND ADDRESS	13. TYPE OF REPORT AND PERIOD COVERED
Oklahoma Department of Transportation Planning and Research Division 200 N.E. 21st Street, Room 3A7 Oklahoma City, OK 73105	Final Report Oct 2006 - Dec 2012
	14. SPONSORING AGENCY CODE

15. SUPPLEMENTARY NOTES
Click here to enter text.

16. ABSTRACT
Flexible pavements comprise about 93 percent of paved roads in the United States. Although flexible pavements are widely used for reasons such as cost, constructability and consistent performance, they are often subject to severe cracking and rutting. This combined laboratory and field study is conducted to better understand the mechanisms that cause pavement failure under actual traffic loading and environmental conditions. A 1,000-ft. long experimental pavement section was constructed on I-35 in McClain County and instrumented in collaboration with the National Center for Asphalt Technology (NCAT) and the Oklahoma Department of Transportation (ODOT) for field data collection. The test section was designed to fail in a relatively short amount of time under heavy interstate traffic. The field data collection focused on pavement response data (longitudinal and transverse strains at the bottom of the asphalt layer, Falling Weight Deflectometer testing), environmental data (temperature within the pavement), performance data (rut and cracks on the surface of the pavement) and actual traffic data (number of trucks, axles, and axle load). From the field data, fatigue and rut prediction models were developed. A separate statistical rut prediction model was also developed from the laboratory rut tests using the Asphalt Pavement Analyzer (APA). Additionally, from the laboratory four-point fatigue tests data, fatigue cracking susceptibility towards temperature was analyzed.

17. KEY WORDS	18. DISTRIBUTION STATEMENT
Mechanistic-Empirical, transfer functions, fatigue, rut, IRI, FWD, strain gage, WIM, APA	No restrictions. This publication is available from the Planning & Research Div., Oklahoma DOT.

19. SECURITY CLASSIF. (OF THIS REPORT)	20. SECURITY CLASSIF. (OF THIS PAGE)	21. NO. OF PAGES	22. PRICE
Unclassified	Unclassified	339	N/A

DISCLAIMER

The contents of this report reflect the views of the author(s) who is responsible for the facts and the accuracy of the data presented herein. The contents do not necessarily reflect the views of the Oklahoma Department of Transportation or the Federal Highway Administration. This report does not constitute a standard, specification, or regulation. While trade names may be used in this report, it is not intended as an endorsement of any machine, contractor, process, or product.

ACKNOWLEDGEMENT

The authors wish to express their appreciation to Ginger McGovern, David Streb, Jeff Dean, Bryan Hurst and Chris Westland from ODOT for their direct and indirect assistance with this research. Bryan Cooper from ODOT deserves special thanks for his considerable effort and contributions in the construction and instrumentation phase of this project. The FWD testing and data analysis assistance received from Scott Cosby and Christopher Clarke of ODOT is sincerely appreciated. We would also like to acknowledge the assistance of Angela Priest and Brian Waller of NCAT during the instrumentation and initial data analysis phase of this project.

SI* (MODERN METRIC) CONVERSION FACTORS

APPROXIMATE CONVERSIONS TO SI UNITS				
SYMBOL	**WHEN YOU KNOW**	**MULTIPLY BY**	**TO FIND**	**SYMBOL**
LENGTH				
in	inches	25.4	millimeters	mm
ft	feet	0.305	meters	m
yd	yards	0.914	meters	m
mi	miles	1.61	kilometers	km
AREA				
in^2	square inches	645.2	square millimeters	mm^2
ft^2	square feet	0.093	square meters	m^2
yd^2	square yard	0.836	square meters	m^2
ac	acres	0.405	hectares	ha
mi^2	square miles	2.59	square kilometers	km^2
VOLUME				
fl oz	fluid ounces	29.57	milliliters	mL
gal	gallons	3.785	liters	L
ft^3	cubic feet	0.028	cubic meters	m^3
yd^3	cubic yards	0.765	cubic meters	m^3
NOTE: volumes greater than 1000 L shall be shown in m^3				
MASS				
oz	ounces	28.35	grams	g
lb	pounds	0.454	kilograms	kg
T	short tons (2000 lb)	0.907	megagrams (or "metric ton")	Mg (or "t")
TEMPERATURE (exact degrees)				
^oF	Fahrenheit	5 (F-32)/9 or (F-32)/1.8	Celsius	^oC
ILLUMINATION				
fc	foot-candles	10.76	lux	lx
fl	foot-Lamberts	3.426	candela/m^2	cd/m^2
FORCE and PRESSURE or STRESS				
lbf	poundforce	4.45	newtons	N
lbf/in^2	poundforce per square inch	6.89	kilopascals	kPa

APPROXIMATE CONVERSIONS FROM SI UNITS				
SYMBOL	**WHEN YOU KNOW**	**MULTIPLY BY**	**TO FIND**	**SYMBOL**
LENGTH				
mm	millimeters	0.039	inches	in
m	meters	3.28	feet	ft
m	meters	1.09	yards	yd
km	kilometers	0.621	miles	mi
AREA				
mm^2	square millimeters	0.0016	square inches	in^2
m^2	square meters	10.764	square feet	ft^2
m^2	square meters	1.195	square yards	yd^2
ha	hectares	2.47	acres	ac
km^2	square kilometers	0.386	square miles	mi^2
VOLUME				
mL	milliliters	0.034	fluid ounces	fl oz
L	liters	0.264	gallons	gal
m^3	cubic meters	35.314	cubic feet	ft^3
m^3	cubic meters	1.307	cubic yards	yd^3
MASS				
g	grams	0.035	ounces	oz
kg	kilograms	2.202	pounds	lb
Mg (or "t")	megagrams (or "metric ton")	1.103	short tons (2000 lb)	T
TEMPERATURE (exact degrees)				
^oC	Celsius	1.8C+32	Fahrenheit	^oF
ILLUMINATION				
lx	lux	0.0929	foot-candles	fc
cd/m^2	$candela/m^2$	0.2919	foot-Lamberts	fl
FORCE and PRESSURE or STRESS				
N	newtons	0.225	poundforce	lbf
kPa	kilopascals	0.145	poundforce per square inch	lbf/in^2

*SI is the symbol for the International System of Units. Appropriate rounding should be made to comply with Section 4 of ASTM E380.
(Revised March 2003)

TABLE OF CONTENTS

LIST OF TABLES

LIST OF FIGURES

Chapter 1 INTRODUCTION

1.1 Background

The field performance evaluation of a pavement can provide useful data for future design and construction. The data becomes particularly useful if such data spans over the entire life of the pavement. Several test roads have been constructed for collecting such long-term pavement performance. For example, the foremost road test sponsored by AASHTO (American Association of State Highway and Transportation Officials), which ultimately resulted in the now famous AASHO Road Test (HRB, 1962). The data gathered during this test cycle formed the basis of the AASHTO Design Guide for Pavement Structures (AASHTO, 1993). Other notable test road projects are the WESTRACK experiment (Epps, et al., 1998), the Minnesota Road Research Project (MnDOT, 1990), the Virginia Smart Road (Loulizi, et al., 2001; Smart Road, 2003) and the NCAT (National Center for Asphalt Technology) Test Track (Brown, et al., 2002). Additionally, some studies used accelerated pavement testing data from Accelerated Load Facility (ALF) for simulating long-term pavement performance using a Heavy Vehicle Simulator (HVS) (e.g., Harvey et al., 1998; Elseifi et al., 2012).

A number of test road sections mentioned above were monitored and instrumented to evaluate and measure the effect of materials, load, and environment on pavement design. This helped the pavement engineering community to move beyond empirically-based design (e.g., AASHTO 1993 Design Guide) and analysis toward mechanistic-empirically (M-E) based procedures. From an engineering point of view, there is much to be desired about a mechanistic approach to pavement design (AASHTO, 2004). “Mechanistic” refers to the application of the principles of engineering mechanics, which leads to a rational design

process. According to Yoder and Witczak (1975), for any pavement design procedure to be completely rational, three elements must be considered fully: the theory used to predict the assumed failure or distress parameter, the evaluation of the materials properties applicable to the selected theory, and the determination of the relationship between the magnitude of the parameter in question to the performance level desired.

The above mentioned elements can be fully understood only by considering mechanistic pavement response (stress, strain and deflection) under moving vehicle loads and empirically relating these to observed field performance. This results in an M-E design approach which is applicable over a much wider range of material, traffic and environmental conditions (Timm et al., 2004). The Mechanistic-Empirical Pavement Design Guide (MEPDG), also known as AASHTOWare Pavement ME Design, is an outcome of continued movement towards mechanistic design of pavements through NCHRP Project 1-37A. The overall objective of NCHRP Project 1-37A was to develop and deliver the 2002 Guide for Design of New and Rehabilitated Pavement Structures, based on mechanistic-empirical principles, accompanied by the necessary computational software, for adoption and distribution by AASHTO (Hallin et al., 2011). One of the empirical parts of the MEPDG is relating field performance data used to correlate to accumulated damage. This "transfer" function (also called as prediction model in this report) relates to the theoretical computation of "damage" at some critical location with measured distress, completing the full mechanistic-empirical loop of the pavement design (AASHTO, 2004).

In the MEPDG procedures for flexible pavement, the primary transfer functions are those that relate (a) maximum tensile strain in the bottom of hot-mix asphalt (HMA) layer to fatigue cracking and (b) compressive strain at the top of the subgrade layer to rutting at the

surface. These functions, called fatigue and rutting equations, are usually derived from statistically-based correlations of calculated pavement response with observed field road test performance data (or accelerated pavement testing), laboratory specimen performance or by both methods. These transfer functions or prediction models that need local calibration since the equations generated for a particular climate and location may not be applicable for another region (Priest, 2005). Extensive field and laboratory calibrations are of paramount importance for the success of the M-E design approach (Ioannides, 1992).

The M-E design approach for designing flexible pavements is in the process of evaluation by many state agencies and researchers. There is a need to assess the accuracy of the load-response model and performance prediction models under actual vehicular loading and environmental conditions. These are the core components in the M-E design process. By measuring actual field response and monitoring performance, the relationship between response and life is more directly determined. To this end, an instrumented pavement section was constructed on I-35 in McClain County, for exploring two important aspects of M-E design; namely, the pavement performance models to predict fatigue and rutting, respectively. Details of the site evaluation, design, and construction of the I-35 instrumented pavement section are included in this report.

1.2 Scope and Objectives

As noted in the preceding section, the major objective of this research project was to develop prediction models for fatigue and rutting. A 1,000-ft long experimental pavement section on I-35 in McClain County located in Oklahoma was selected in coordination with the Oklahoma Department of Transportation (ODOT). The pavement design in the 1,000-ft section was selected thinner than a typical interstate pavement and equivalent to secondary

roadway pavement (NCAT, 2006) so that field performance data collected over a five-year period could be used by the agency to estimate the long-term (20 years) service life of a state highway. Thus, this project was similar in concept to accelerated pavement testing, but involved actual vehicular traffic and environmental conditions.

1.3 Organization of the Report

This report is organized into eight chapters including this "Introduction" chapter. Chapter 2 presents a brief review of AASHTO pavement design methods and existing rut and fatigue prediction models. Chapter 3 focuses on the construction and instrumentation of the test section including material properties of different pavement layers. Chapter 4 presents the procedure used for collecting and processing weekly field data. The performance data collected during quarterly field trips is also presented in this chapter. Chapter 5 presents the research approach used for developing a laboratory rut prediction model. Sample preparation and laboratory test procedures for developing the laboratory rut prediction model is also described in this chapter. In Chapter 6, the development of two rut prediction models, namely a vertical strain-based rut prediction model and a shear strain-based rut prediction model from field data is explained in detail. The four-point fatigue tests results and field fatigue prediction models are presented in Chapter 7. Lastly, the summary, conclusions and recommendations are given in Chapter 8.

Chapter 2 LITERATURE REVIEW

2.1 Introduction

In this chapter, literature related to the development of mechanistic-empirical (M-E) design concepts is discussed, followed by flexible pavement rutting progression and fatigue cracking. Also, an overview of some significant rut and fatigue prediction models is presented.

2.2 History of Pavement Design

2.2.1 Empirical Design

As noted in Chapter 1, test road results have been used over the years for efficient design of pavements and for better understanding of pavement performance over time under traffic loading. The foremost among these test roads was the AASHO Road Test conducted in Ottawa, Illinois from October 1958 to November 1960. The collected data formed the basis of AASHTO Guide for Design of Pavement Structures (AASHTO, 1993), which is the primary document used to design new and rehabilitated pavements in the United States (Li, 2009). During the AASHO road tests, performance measurements of pavement sections were taken at regular intervals. The performance data along with pavement material properties and traffic data were used to develop empirical models for pavement design.

2.2.1.1 Design Inputs

Following are the specific design inputs required for designing a flexible (asphalt) pavement using the AASHTO 1993 Design Guide (AASHTO, 1993):

1. Time Constraints: AASHTO categorized two types of time constraints, namely performance period and analysis period. Performance period is defined as the period of time that an initial pavement structure will last before it needs rehabilitation. Analysis period (or design life) refers to the period of time for which the analysis is conducted.
2. Traffic: The design procedure is based on the number of Equivalent Single Axle Load (ESAL) applications. ESAL is defined as total the number of applications of a standard axle (generally 80 kN, i.e., 18 kip single) required to produce the same damage or loss of serviceability as the number of applications of one or more different axle loads and/or configurations over the pavement life (Huang, 2004). It is a convenient way for converting mixed traffic data to a number of standard axles for design of a pavement.
3. Reliability: This design input is used for incorporating some degree of certainty into the design process to ensure that the various design alternatives will last the analysis period. Specifically, reliability accounts for variations in both traffic predictions and the performance prediction. For a given level of reliability, the reliability factor is defined by standard normal deviation (Z_R) and overall standard deviation (S_o). The recommended values of S_o for flexible and rigid pavements are 0.45 and 0.35, respectively (AASHTO, 1993).
4. Performance Criteria: Both functional and structural performance are considered in the AASHTO 1993 design guide by using the concept of serviceability. The serviceability of a pavement is defined as its ability to serve the type of traffic which uses the facility. The primary objective measure of serviceability is the Present Serviceability Index (PSI) which ranges from 0 (impassible road) to 5 (perfect road). The difference in Present

Serviceability Index (ΔPSI) between construction/initial and end-of-life/terminal is the serviceability life.

5. Material Properties: The subgrade layer properties are incorporated in terms of effective resilient modulus. Other layer properties are accounted for by using layer coefficients. The layer coefficients measure the relative ability of a unit thickness of a given material to function as a structural component of the pavement. The AASHTO 1993 design guide provides correlations between and charts of the resilient modulus of material and layer coefficients (AASHTO, 1993). For example, the following equation is recommended for a granular base material:

$$a = 0.277 \log(M_r) - 0.839 \quad (2.1)$$

where:

a = layer coefficient (in^{-1}) and M_r = resilient modulus (psi).

6. Drainage Characteristics: The level of drainage for a flexible pavement is accounted for by the use of a modified layer coefficient; a higher layer coefficient is used for improved drainage conditions. The factor for modifying the layer coefficient to account for drainage effect is referred to as an 'm' value. It depends on the drainage quality and the percent of time during the year the pavement structure is normally exposed to moisture levels approaching saturation. The m value ranges between 0.40 (very slowly draining layer) and 1.40 (quickly draining layer that never saturates).

2.2.1.2 Design Method

The AASHTO 1993 method utilizes the term Structural Number (SN) to quantify the structural strength of a pavement required for a given combination of pavement layer properties, total traffic, reliability, and serviceability level. The required SN is converted to

actual thickness of surface, base, and subbase, by means of appropriate layer coefficients representing the relative strength of the construction materials. The design equation used is as follows:

$$SN = a_1 D_1 + a_2 D_2 m_2 + a_3 D_3 m_3 \quad (2.2)$$

where:

a_i = ith layer coefficient, D_i = ith layer thickness, and m_i = ith layer drainage coefficient. For a flexible pavement, the subscripts 1, 2 and 3 refer to the asphalt concrete, stabilized subgrade, and subbase layer (if applicable), respectively. The basic design equation for flexible pavements in the AASHTO 1993 design guide is as follows:

$$\log_{10}(W_{18}) = Z_R \times S_o + 9.36 \times \log_{10}(SN+1) - 0.20 + \frac{\log_{10}\left[\frac{\Delta PSI}{4.2-1.5}\right]}{0.40 + 1094/(SN+1)^{5.19}} + 2.32 \times \log_{10} M_r - 8.07 \quad (2.3)$$

where:

W_{18} = predicted number of 80 kN (18 kip) ESAL applications. Equation. 2.3 can be solved iteratively or by using nomographs for the required SN value. The required design thickness of each layer is derived by using Eqn. 2.2 in combination with material properties of each layer.

2.2.1.3 Limitations and Assumptions

Since the AASHTO 1993 equations were developed from specific conditions at the AASHO Road Test, they have some significant limitations. The main limitations are listed below (WSDOT, 2003):

1. The design equations were developed for specific pavement materials and roadbed soil present at the AASHO Road Test section.

2. The equations were developed based on the specific environmental conditions prevailing at the AASHO Road Test site (Ottawa, Illinois).
3. The final design equations are based on an accelerated two-year testing period rather than for a longer, more realistic pavement life that normally ranges from 20 to 40 years. Therefore, environmental factors were difficult to extrapolate for longer periods.
4. The traffic loading applied during the testing cycle was only 1.1 million ESAL using the test vehicles. The loads used to develop the equations were operational test vehicles with identical axle loads and configurations, as opposed to mixed traffic on an actual highway.
5. The truck tire pressures used to apply accelerated loading was only 80 psi, which is low compared to the tire pressure of heavy vehicles which causes most of the damage to the pavement.

Further, in order to apply the equation developed from the AASHO Road Test, some unrealistic assumptions are needed (Selvaraj, 2007):

1. The characterization of subgrade soil support may be extended to other subgrade soils by an abstract soil support scale.
2. The mixed traffic loading may be characterized by the ESAL concept.
3. Material characterizations may be applied to other surfaces, bases, and subbases by assigning appropriate layer coefficients.
4. The two-year period accelerated testing done at the AASHO Road Test can be extended for longer design periods.

2.2.2 Mechanistic-Empirical Design

As discussed in Section 2.2.1.3, the limited nature of the AASHO Road Test in terms of loading patterns, environmental conditions and unrealistic assumptions forced pavement

engineers to look beyond existing empirical-based design and move towards the M-E design procedure. The research and development in the structural design of HMA pavements over the past fifty years have focused on a shift from empirical design equations to a more powerful and adaptive design scheme. M-E design has been developed to utilize the mechanical properties of the pavement structure, along with information on traffic, climate, and observed performance, to more accurately model the pavement structure and predict its life. Although M-E design still relies on observed performance and empirical relationships, it is a much more robust system that can easily incorporate new materials, different traffic distributions, and changing conditions (Priest and Timm, 2006).

Although there are several existing M-E pavement design approaches developed by various organizations, the AASHTO 2002 MEPDG developed under NCHRP 1-37A brought international attention to M-E design. The M-E design and analysis process, shown conceptually in Figure 2.1, integrates the environmental conditions and material properties of the HMA layer and underlying layers into the pavement structure. The responses of pavement structure to load (i.e., stresses and strains) are mechanistically calculated based on material properties, environmental conditions, and traffic characteristics. Thermal and moisture distributions are mechanistically determined using the Enhanced Integrated Climatic Model (EICM). These responses are then used as inputs in empirically-derived distress models (or transfer functions), translating them into damage and accumulating the damage into distresses (e.g., permanent deformation, fatigue cracking, thermal cracking, and roughness) that are responsible for reduced pavement performance over time (Priest and Timm, 2006; Papagiannakis and Masad, 2007). The damage for each condition is typically added together

using Miner's hypothesis, shown in Eqn. 2.4, where the failure criteria is reached when the ratio approaches unity (Miner, 1959):

$$D = \sum_{i=1} \frac{n_i}{N_i} \tag{2.4}$$

where:

D = total damage, n_i = number of load applications at condition i, and N_i = number of load application at failure for condition i. The distress models were calibrated by using data from the Long Term Pavement Performance (LTPP) database for conditions representative of the entire United States (Li, 2009). Because the design process is modular, varying degrees of accuracy and sophistication can be used at each step depending on the needs of the design (Priest and Timm, 2006). This section further describes the MEPDG design procedure and inputs.

2.2.2.1 Design Process

The MEPDG design process is not as straightforward as the 1993 AASHTO guide, in which the structure's thicknesses are obtained directly from the design equation (Li, 2009). In general, the design process consists of three major stages. Stage 1 of the MEPDG design procedure involves development of input values. In this stage, the potential strategies for analysis are identified. The input data for pavement materials (as discussed later), traffic characterization and EICM model are developed. In Stage 2, performance analysis is conducted using an iterative process that begins with the selection of an initial trial design. If the trial design does not meet the performance criteria, the design (thicknesses or material selection) must be modified and the calculations repeated until the design is acceptable. Stage

3 of the design process consists of the evaluation of structurally viable alternatives, such as an engineering analysis and life cycle cost analysis.

The MEPDG has adopted a hierarchical approach for the design inputs, which provides the designer with flexibility in obtaining the design inputs for a design project based on the availability of resources and the importance of the project (Von Quintus and Moulthrop, 2007). There are three levels of input, as outlined below:

Level 1 – This level provides the most accurate designs with the lowest level of uncertainty or error. Level 1 material inputs require laboratory measured material properties (e.g., dynamic modulus master curve for asphalt concrete, resilient modulus or modulus of elasticity for unbound and chemically stabilized materials) and project-specific traffic data (e.g., vehicle class, load distribution, axle configuration, monthly adjustments).

Level 2 – This level provides an intermediate design. Level 2 inputs are obtained through empirical correlations (e.g., resilient modulus estimated from soil and additive properties) or possibly from an agency database.

Level 3 – This level provides a design with the lowest level of accuracy. Inputs are selected from a database of national or regional default values according to the material type or highway class (e.g., soil classification to determine the range of resilient modulus, highway class to determine vehicle class distribution). Level 3 is recommended for minor projects, usually low traffic roads. In addition, Level 3 may be appropriate for pavement management programs implemented by highway state agencies (AASHTO, 2004; Schwartz and Carvalho, 2007). In this study, Level 3 inputs were used throughout because (a) at present there are rarely all the Level 1 input data to be used on a consistent basis, and (b) the final version of

the MEPDG software was calibrated using Level 3 data (Schwartz and Carvalho, 2006). Also, Level 1 and 2 inputs for a stabilized subgrade layer are disabled in the MEPDG software.

2.2.2.2 Design Inputs

The following are the specific design inputs required for designing a pavement using the MEPDG software (AASHTO, 2004):

1. General Information: This includes information regarding expected pavement design life, base/subgrade construction month, paving month, traffic opening month and pavement type. Information related to the construction is used for establishing a reference time for the EICM. On the other hand, selection of flexible or rigid pavement establishes the method of design and applicable performance models.
2. Site/Project Identification: The project site is identified using project ID, section ID and functional class of the pavement. The location of the project is provided in the form of latitude, longitude, and height above the sea level. This defines the climatic condition which is the extracted from the available databases of nearly 800 weather stations throughout the United States. This allows the user to select a given station or to generate virtual weather stations for a project site under consideration.
3. Analysis Parameters: Analysis parameters are defined by the initial International Roughness Index (IRI) and performance criteria. The typical initial IRI values range between 789 to 1,579 mm/km (50 to 100 in/mile). For semi-rigid pavements, an initial IRI value of 1,026 mm/km (65 in/mile) is recommended by the new M-EPDG. The current MEPDG software Version 1.1 supports six different performance criteria namely, AC surface down cracking (longitudinal cracking), AC bottom up cracking (fatigue or alligator cracking), AC thermal cracking, fatigue cracking in chemically stabilized layer,

permanent deformation, and terminal IRI. A designer may specify the desired level of reliability for each distress type and roughness.

4. Traffic Characterization: The MEPDG requires the full axle-load spectra inputs for estimating the magnitude, configuration and frequency of the loads to accurately determine the tire loads that will be applied on the pavement duringeach time increment of the damage accumulation (AASHTO, 2004; Li, 2009). The traffic characterization information is provided through four separate modules namely, basic information, traffic volume adjustment factors, axle load distribution factors, and general traffic inputs. The basic information includes Annual Average Daily Truck Traffic (AADTT) for base year, directional distribution factor, lane distribution factor, and operational speed of vehicles. The traffic volume adjustment is comprised of monthly adjustment factors, vehicle class distribution, hourly truck traffic distribution, and traffic growth factors. The general traffic inputs are used for calculating pavement response and include mean wheel location (default value = 457 mm (18 in)), traffic wander standard deviation (default value = 254 mm (10 in)), design lane width (default value = 3.66 m (12 ft)), number of axle types per truck class, axle configuration, and wheelbase.
5. Climate: The climatic inputs include hourly air temperature, precipitation, wind speed, percentage sunshine, and ambient relative humidity values over the design period. These data are used for considering the changes of temperature and moisture profiles in the pavement structure and subgrade over the design life of a pavement through the incorporation of the EICM model into the MEPDG design software. The EICM is a one-dimensional coupled heat and moisture flow program that simulates changes in the

behavior and characteristics of pavement and subgrade materials in conjunction with climatic conditions (AASHTO, 2004).

6. Pavement Structure: This input data includes drainage/surface characteristics and layer properties. Additionally/Furthermore, the material parameters for each layer needed for the design process are classified into three major categories, namely pavement response model material inputs, material related pavement distress criteria inputs, and other material properties. The pavement response model material inputs relate to the modulus and Poisson's ratio used to characterize layer behavior within the specific model (Li, 2009). Material parameters associated with pavement distress criteria are linked to some measure of material strength or to some manifestation of the actual distress effect (e.g., modulus of rupture, repeated load permanent deformation). The "other" category of material properties constitutes those associated with special properties such as the thermal expansion and contraction coefficient of asphalt mixtures.

2.2.3 Conceptual Difference: AASHTO 1993 and AASHTO 2002 M-EPDG

The main conceptual differences between AASHTO 1993 and the MEPDG can be summarized as follows (AASHTO, 2004; Schwartz and Carvalho, 2007; Li, 2009; Solanki, 2010):

1. The AASHTO 1993 guide designs pavements for a single performance criterion, the Present Serviceability Index (PSI), whereas the MEPDG approach simultaneously considers multiple performance criteria (e.g., rutting, cracking, and roughness).
2. The AASHTO 1993 guide directly computes the layer thicknesses. On the other hand, the MEPDG is an iterative procedure.

3. The MEPDG requires more input parameters such as environmental and material properties. It also employs a hierarchical concept in which a designer may choose different quality levels.
4. The AASHTO 1993 guide was developed on the basis of limited field data from the AASHO Road Test conducted at only one location. The seasonally-adjusted subgrade resilient modulus and the layer drainage coefficients are the only variables for environmental condition. The MEPDG utilizes a set of project-specific climate data (e.g., air temperature, precipitation, wind speed, and relative humidity) and the EICM to determine the material properties for different environmental conditions throughout the year.
5. The AASHTO 1993 guide uses the concept of ESALs to define traffic levels, while the MEPDG adopts a more detailed load spectra concept. Pavement materials respond differently to traffic pattern, frequency and loading. Traffic loading in different seasons of the year also has different effects on the response of the pavement structure. These factors can be most effectively considered using the load spectra concept.

2.3 Rut Prediction Models

Predicting rut performance of a pavement under the actual traffic loads and environmental conditions is a major part of the M-E design scheme. While M-E design relies heavily on mechanistic modeling, the results are meaningless without accurate prediction models that allow designers to predict pavement performance and design accordingly (Timm and Newcomb, 2003). Starting from early 1960's, many rut prediction models have been developed by researchers that ranged from simple linear regression equations to advanced M-

E rut prediction models. In this part of this chapter, a detailed literature review on available important rut prediction models along with the rut progression phenomenon is presented.

2.3.1 Rutting Progression Phenomenon

Typically, rutting in flexible pavements is categorized into three stages: primary, secondary, and tertiary (Zhou et al., 2004). The primary stage starts right after the introduction of loading to the pavement. In the primary stage, permanent deformation accumulates fairly rapidly along with the repetition of loading. So, the slope of the rutting curve (permanent deformation vs. load repetition) remains steep initially. With further increase in load application, the rate of rutting tends to decrease. That is, permanent strain per cycle tends to decrease, reaching a constant value defined as the onset of the secondary stage. Finally, the permanent strain per cycle starts to increase, and the permanent strain accumulates rapidly again. This increase marks the onset of the tertiary stage. The first two stages are very common in a pavement, while the third stage does not occur as often. In the tertiary stage of rutting, micro and macro level fractures are often seen in the pavement, which could be regarded as the onset of cracking rather than rutting. A typical field rut progression curve is shown in Figure 2.2.

2.3.2 Existing Rut Prediction Models

2.3.2.1 Finn et al. Model (1977)

Finn et al. (1977) proposed a rut prediction model based on the results obtained from the AASHO road test. Efforts were made to address the seasonal rate of rutting and also to determine whether a correlation could be found between the seasonal rates of rutting and the primary responses calculated from an 18-kip (80-kN) single axle load. Using this approach,

initially, a regression model relating the rate of rutting as a function of stress and strain in component layers, surface deflection, and the equivalent single axle load was attempted. Data from 32 test sections were selected to obtain the seasonal rate of rutting and the final rut prediction model. A stepwise regression analysis was used to correlate the rate of rutting with various combinations of primary response factors. The following independent variables were selected for this purpose:

1. Vertical surface deflection between dual tires;
2. Vertical subgrade strain under the centerline of one wheel;
3. Vertical compressive stress at the bottom of the asphalt concrete layer under one wheel;
4. Horizontal tensile stress at the bottom of asphalt concrete under one wheel;
5. Ratio of vertical and horizontal stresses from Items 3 and 4 above;
6. Cumulative traffic, expressed as equivalent 18-kip (80-kN) single axle loads.

The analysis indicated that the most significant correlations were obtained with vertical deflection at the surface of the pavement, followed by vertical compressive stress in the Hot Mix Asphalt (HMA) layer, cumulative traffic, and vertical strain in the subgrade. The stress ratio factor was not considered significant to be included in the final model. Vertical strain in the subgrade was found to be highly correlated with the surface deflection. Finally, two prediction models were obtained: one model for conventional sections up to 6-in. (150-mm) of HMA layer and the other for thick or full-depth HMA layer. The following models were reported:

For conventional construction:

$$\log(RR) = -6.866 + 4.325\log d - 0.131\log(N_{18}) \qquad (2.5)$$

For thick [> 6-in. (150-mm)] or full-depth asphalt concrete:

$$\log(RR) = -1.173 + 0.717\log d - 0.658\log(N_{18}) + 0.666\log(\sigma_c) \quad (2.6)$$

where:

RR = Rate of rutting (micro inches per repetition),

d = Surface deflection (10^{-3}-in.),

N_{18} = Total equivalent number of 18-kip single axle load, and

σ_c = Vertical compressive stress in asphalt concrete (psi).

The models given in the equations above are applicable to pavements similar to the AASHO Road Test, having similar climatic locations. In this particular model, the traffic coefficient had a negative sign which indicates a decrease in rutting rate with increased traffic applications. According to this model, at some point in time, the rutting rate decreased for increasing traffic applications.

2.3.2.2 Allen and Deen Model (1980)

In the Allen and Deen study (1980), an asphalt concrete base and a dense-graded aggregate were tested in the laboratory to determine the susceptibility to rutting. Twenty-seven repeated load tests were performed to determine the susceptibility of the mixture to deformation. The tests were conducted at three different temperatures: 7°C (45°F), 25°C (77°F) and 38°C (100°F). Three deviator stresses were used at each temperature: 80 psi (550 kPa), 50 psi (345 kPa) and 20 psi (140 kPa). In addition, three loading times (0.5, 1, and 2 sec) were used for each deviator stress. A linear regression analysis was performed on the test data. The following model was found to "best-fit" the data:

$$\log(\varepsilon_p) = C_0 + C_1(\log N) - C_2(\log N)^2 + C_3(\log N)^3 \quad (2.7)$$

where:

ε_p = Permanent strain (axial),

N = Number of deviator stress repetitions, and

C_0, C_1, C_2, C_3 = Regression constants.

An in-depth analysis and comparison of rut depths predicted by this model with actual ruts measured from in-service pavements have not been made yet. However, preliminary comparisons have been made and are briefly described below for two full depth HMA pavements. Both pavements were approximately 17 in. (430 mm) thick. A commercially available software, CHEVRON, was used to predict stresses for an 18 kip (80 kN) axle load. For the first pavement, the predicted rut depth was between 1.6 in. (40 mm) and 1.9 in. (50 mm), whereas the measured rut depth was 1.75 in. (45 mm). For the second pavement, the predicted rut depth was 1.25 in. (32 mm), whereas the measured rut depth was 1.15 in. (30 mm).

This model was developed entirely from laboratory tests so it does not represent the actual field condition very well. Because of equipment limitations, the HMA base layer was not tested at a high temperature. Also, tension tests were not conducted. Because of the latter limitation, the developed model considers only compressive stresses. Therefore, it is expected that this model would underpredict layer thinning because of neglecting tensile stresses present at the bottom of pavement layers.

2.3.2.3 Leahy's Model (1989)

Leahy's approach to develop a rut transfer function (also called rut prediction model in this study) involved extensive laboratory testing. The overall objective of the study was to determine the influence of test conditions (load level-temperature) and mix parameters on the permanent deformation characteristics of HMA using the repeated load triaxial test as well as

the static (creep) test. A total of 251 specimens were tested under the dynamic testing sequence. The test matrix included three asphalt contents, three air void contents, three stress levels, two binder types, three temperatures, and two aggregate types. The test results were based on the measurement of permanent deformation under repeated loading on unconfined specimens. About 2,860 permanent strain data were used in developing the model. The resilient strain was assumed to be constant and independent of the number of load repetitions. The final model was of the following form:

$$\log\left(\frac{\varepsilon_p}{\varepsilon_r}\right) = -6.631 + 0.435(\log N) + 2.767\log T + 0.11\log S + 0.118\log\eta + 0.930\log V_{beff} + 0.501\log V_a \quad (2.8)$$

where:

ε_p = Accumulated permanent strain,

ε_r = Resilient strain,

N = Number of load repetitions,

T = Mix temperature (°F),

S = Deviatoric stress (psi),

η = Viscosity at 70°F (10^6 poise),

V_{beff} = Effective asphalt content (percent by volume),

V_a = Air void content (%).

A sensitivity analysis was also performed by Leahy (1989). Based on this sensitivity analysis, it was concluded that temperature was by far the most important variable. Both the elastic and plastic strain values were found to be heavily dependent on the temperature, and to a much lesser degree, dependent on deviator stress, asphalt binder type, air void content, and asphalt content. It was generally observed that the elastic strain decreased slightly with

increasing number of load repetitions. Generally, the ratio of permanent strain to resilient strain decreased with decreasing temperature, but was essentially constant with deviator stress. Although the developed model had a R^2 value of 0.76, its usefulness was limited because of the complexity of the model with many parameters.

2.3.2.4 M-E based Rut models from LTPP Data (1998)

Subsequently, a mechanistic-empirical model was developed by Ali et al. (1998). The Asphalt Institute model and The Shell model were used to predict pavement rutting damage for 61 Long-Term Pavement Performance (LTPP) test sections. A number of analysis steps were performed before damage analysis. The pavement was modeled as an elastic multilayered system. Falling-weight deflectometer (FWD) data were used to backcalculate the layer moduli. Adjustments were applied to traffic loads and the structural properties of the pavement to account for the long-term, seasonal, and spatial variations in the system. Then, a forward structural analysis was performed to calculate the critical strain values specified in the selected "transfer functions" (also called rut prediction model in this study). Finally, a damage analysis was performed to calculate and accumulate the theoretical damage. Instead of taking only subgrade vertical strain, this model considers the effect of vertical strain on HMA layer and base layer.

Ali et al. (1998) developed a mathematical model and later calibrated it using data from 61 LTTP test sections. Vertical elastic compressive strains were calculated in the middle of each layer. The subgrade was divided into a number of layers until the strain value approached zero. An error minimization algorithm was implemented to find the calibration parameters for each pavement layer. The final model was of the following form:

$$\rho_p = 0.00011 * h_{AC}\left[\sum_{i=1}^{k} n_i \left(Ee_{i,AC}\right)^{1.111}\right]^{0.9} + 23.26 * h_{Base}\left[\sum_{i=1}^{k} n_i \left(Ee_{i,Base}\right)^{20}\right]^{0.05}$$

$$+ \ 0.022 * h_{Subgrade}\left[\sum_{i=1}^{k} n_i (Ee_{i,Subgrade})^{2.81}\right]^{0.356} \qquad (2.9)$$

where:

ρ_P = Total cumulative rut depth (in same units as h),

i = Subscript denoting load groups [e.g., single axle with 9-kip)],

k = Number of load groups,

h = Layer thickness,

$\varepsilon e_{i,AC}$, $\varepsilon e_{i,Base}$, $\varepsilon e_{i,Subgrade}$ = Vertical compressive elastic strain in the middle of asphalt concrete, base and subgrade layers, corresponding to load group i, respectively.

This model only considered vertical strain and did not consider shear strains in the asphalt concrete layer.

2.3.2.5 WesTrack Model (1999)

Comprehensive research has been conducted at the WesTrack facility to gain an insight of HMA behavior and environmental factors on pavement performance. The original WesTrack tests consisted of 26 different HMA test sections located on a 1.8-mile (2.9-km) oval test track 60 miles (96-km) east of Reno, Nevada. Loading was achieved using four driverless tractor trailers. Loads on each axle were 20 kip (80 kN), which is equivalent to a total ESAL value of 10.7 per truck pass. The trucks were fitted with 295/75R22.5 radial tires inflated to 100 psi (689 kPa). The test speed was 40 mph (64 kph). For the original 26 sections, a single Superpave performance-graded asphalt binder (PG 64-22) was used. A

single primary source of aggregate was selected for use in the test sections. Three different 0.75 in. (19 mm) aggregate gradations were used.

Based on the data collected, the researchers concluded that rutting was mainly controlled by shear deformation in the HMA layer. A regression model was developed to accurately predict the WesTrack rutting by considering elastic shear response and axle loadings. The model considered aging of mixes and hourly change in elastic shear strain in the HMA layer. The following model was proposed from that study (Hand et al., 1999):

$$\gamma^p = a\, e^{(b*\tau^e)} \gamma^e\, N^c \qquad (2.10)$$

where:

γ^P = Plastic shear strain at a depth of 2-in. from HMA top,

τ^e = Elastic shear stress at a depth of 2-in. from HMA top,

γ^e = Elastic shear strain at a depth of 2-in. from HMA top,

N = Number of 18-kip load applications, and

a, b, c = Regression coefficients.

The model in Equation (2.10) shows that shear stress and shear strain can be used to predict plastic deformation (shear deformation). However, the model has some limitations. A common limitation associated with this model is that it is applicable only to that particular environment where the tests were conducted. As this is a regression model, the model is only valid within the ranges of the variables from which it is developed. Another common constraint is that the ultimate end users of models may not have the resources necessary to perform sophisticated testing to generate model inputs such as plastic strains.

2.3.2.6 Mechanistic-Empirical Rut Prediction Model for In-Service Pavements (2000)

Kim et al. (2000) presented an M-E rut prediction model that utilized data from 39 in-service flexible pavements from Michigan. Their model accounts for the distribution of rutting in the subgrade, subbase, base, and HMA layers. The model addresses variables like pavement cross-section, ambient temperature, and asphalt binder consistency properties. Three cycles of field data were collected over a period of 7 years. The length of each section ranged from 328 ft (100 m) to 492 ft (150 m). The rut depth was measured by using a 6ft (1.8m) straight edge leveling rod with an accuracy of 0.05in. (1.27 mm). The rut depth was measured at intervals of 40ft (12.2 m) for both inner and outer wheelpaths. The backcalculation program MICHBACK was used to backcalculate pavement layer elastic moduli. With the backcalculated and temperature-adjusted elastic moduli of pavement layers, a structural analysis of the pavement using the mechanistic-based load-deformation model was conducted to calculate the critical pavement responses. The pavement responses were calculated by using a linear layered-elastic solution provided by CHEVRONX (Kim et al., 2000).

A non-linear regression analysis was conducted with data collected from 39 test sections in 1991 and 1997. More than 760 data points from these test sections were analyzed and then grouped into 51 statistical samples representing every test site. Based on numerical optimization using SYSTAT, a statistical computer program, the following model was reported:

$$RD=[-0.016\,H_{AC}+0.033\ln(SD)+0.011T_{annual}-0.01\ln(KV)]*[-2.703+0.657\,(\varepsilon_{v,\,base})^{0.097}+0.271\,(\varepsilon_{v,\,SG})^{0.883}+0.258\ln(N)-0.034\ln(\frac{E_{AC}}{E_{SG}})] \quad (2.11)$$

where:

RD = Rut depth (in.),

H_{AC} = Thickness of HMA layer (in.),

SD = Pavement surface deflection (in.),

T_{annual} = Annual ambient temperature (°F),

KV = Kinematic viscosity (centistokes),

$\varepsilon_{v,\ Base}$ = Vertical elastic compressive strain at the top of base layer (10^{-3}),

$\varepsilon_{v,\ Subgrade}$ = Vertical elastic compressive strain at the top of subgrade (10^{-3}),

N = Cumulative traffic volume (ESAL),

E_{AC} = Resilient modulus of asphalt concrete (psi), and

E_{SG} = Resilient modulus of subgrade (psi).

The model had a R^2 value of 0.91. The applicability of the model was validated by using data from 24 Long-Term Pavement Performance Global Positioning System (GPS) sites. For 19 of the 24 GPS sites, the predicted rut depth was within 0.2 in. (5 mm) of the measured rut depth.

Although the model predicted rut depth reasonably well, one of the disadvantages of the model is that it has too many variables. Too many variables make the model complex. Although temperature, layer stiffness and vertical strain are dependent on each other, Kim et al. (2000) did not explain the justification of including all these variables in the model.

2.3.2.7 Zhou et al. Model (2004)

This model is based on the tests that were conducted in the FHWAALF (Federal Highway Administration-Accelerated Load Facility) in McLean, VA from 1993 through 2001. Twelve pavements were constructed in 1993 at the Turner-Fairbank Highway Research Center in McLean, VA. Each pavement had a length of 144 ft (44 m), a width of 13 ft (4 m),

and was divided into four test sites. The FHWAALF was used to load these pavements. The pavements were tested under conditions that promoted either the rutting or the formation of fatigue cracks. For rutting validation tests, the pavement temperature ranged from 46°C (115°F) to 76°C (170°F) and was controlled during trafficking using infrared lamps. The 9.63 kip (43 kN) Accelerated Load Facility (ALF) load was applied using a super-single tire with a tire pressure of 100 psi (690 kPa). Three stages of permanent deformation were evident. Based on the test data, researchers from the Texas Transportation Institute (Zhou et al., 2004) developed three separate models to predict rut at primary, secondary, and tertiary stages. An algorithm was developed to determine the transition points between different rutting stages. The algorithm also included model parameters from accelerated load tests. Zhou et al.'s (2004) model was further validated through laboratory tests on seven different field HMA mixes from seven sections of a long-term pavement performance experimental site on U.S. 281 in south Texas. The developed model was reported in the following form:

Primary stage:

$$\varepsilon_P = aN^b \text{ , } N \leq N_{PS} \qquad (2.12)$$

where:

ε_p = Permanent strain,

N = Number of load repetitions,

N_{PS} = Number of load repetitions corresponding to the initiation of the secondary stage, and

a, b = Material constants.

Secondary stage:

$$\varepsilon_P = \varepsilon_{PS} + c\left(N - N_{PS}\right), \quad N_{PS} \leq N \leq N_{ST}, \quad \text{and } \varepsilon_{PS} = aN_{PS}^b \qquad (2.13)$$

where:

ε_{PS} = Permanent strain corresponding to the initiation of secondary stage,

c = Material constant, and

N_{st} = Number of load repetitions corresponding to the initiation of the tertiary stage.

Tertiary stage:

$$\varepsilon_P = \varepsilon_{ST} + d\left(e^{f(N-N_{ST})}-1\right),\ N \geq N_{ST} \quad and \quad \varepsilon_{ST}=\varepsilon_{PS} + c(N_{ST}-N_{PS}) \quad (2.14)$$

where:

ε_{ST} = Permanent strain corresponding to the initiation of tertiary stage, and

d, f = Material constants.

Although the model described by Equations (2.12), (2.13), and (2.14) defines the three stages of permanent deformation very well, one of the disadvantages of this model is that the material constants vary based on mix types. Moreover, as the model has three stages, it makes the process complicated.

2.3.2.8 Williams et al. Model (2005)

Williams et al. (2005) developed a rut prediction model based on the laboratory testing done at the WesTrack project. The WesTrack tests provided a unique opportunity to compare Asphalt Pavement Analyzer (APA) results with a full-size pavement testing facility where both the loading and temperature were known. APA test specimens were taken directly from the wheelpaths of the test track before truck loading and were tested at 60°C (140°F) which was nearly the same as the average high pavement temperature of 57.5°C (136°F). The highest rut observed on the WesTrack was 0.5 in. (12.7 mm). A 0.5 in. (12.7 mm) rut was

considered to be a failure, as noted by Barksdale et al. (1972), for pavements with 2% crown; rut depths of 0.5 in. (12.7 mm) are sufficiently deep to hold enough water to cause a car travelling at 50 mph (80 kph) to hydroplane. According to pavement rut measurements taken from the WesTrack, a 0.5 in. (12.7 mm) total rut depth (consolidation and shear deformation) was approximately equivalent to a downward rut depth (consolidation and shear deformation, less uplift due to shear flow) of 0.39 in. (10 mm). From the APA data, also taken from the WesTrack, it was determined that a 0.39 in. (10 mm) downward rut depth correlated well with a 0.28 in. (7 mm) APA rut depth. It was also observed that the WesTrack downward rut depth at 582,000 ESALs were in a reasonable agreement with the APA rut depth at 8,000 cycles.

Although the WesTrack and APA test temperatures were nearly the same, the number of ESALs per APA cycle could not be simply found by dividing 582,000 ESALs by 8,000 cycles. This was because the trucks that loaded the WesTrack travelled slower than the ordinary trucks on highways, and the wheel wander of the WesTrack was tighter than ordinary truck traffic. According to Haddock et al. (1998), for an HMA pavement of high density, a truck travelling at 40 mph (65 kph) does approximately 12% more damage to pavements than a truck travelling 62 mph (100 kph) does. Also, from in-service pavement data, it was shown that trucks tend to wander over a width of 18.1 in. (460 mm), when travelling on a 12 ft. (3.65 meter) wide lane. The WesTrack trucks wandered over a width of 5 in. (127 mm) because of their guidance system. A decrease in wheel wander caused the truck loads to be distributed over a smaller pavement area and consequently caused more pavement damage. So, Williams et al. (2005) had to come up with correction factors for wheel wander and speed as follows:

$$Increased\ Damage = \frac{Rut\ Damage\ at\ 127\ mm\ Wander - Rut\ Damage\ at\ 460\ mm\ Wander}{Rut\ Damage\ at\ 460\ mm\ Wander} = 0.594 \qquad (2.15)$$

Ordinary Truck ESALs

$$=(582{,}000\ ESALs)*(Wander\ Adjustment)*(Speed\ Adjustment) \quad (2.16)$$

$$=(582{,}000\ ESALs)*(1.594)*(1.12)=1{,}039{,}033\ ESALs \quad (2.17)$$

The amount of 80 kN (18 kip) ESALs per APA cycle is calculated as follows:

$$ESALs\ per\ APA\ Cycle=\frac{1{,}039{,}033\ ESALs}{8{,}000\ APA\ Cycles}=129.9\ ESALs\ per\ APA\ Cycle \quad (2.18)$$

But this correlation did not consider including the number of ESALs for all seasons. So, this correlation was further modified with an algorithm to include rutting seasons. Finally, Williams et al. (2005) came up with a rut prediction model based on the APA test data.

$$ESALs_{Failure}=\frac{(APA\ Cycles\ to\ 7\ mm\ Rut)*(129.9\ \frac{Rutting\ ESALs}{Cycles})}{(\frac{RS*RF}{365})} \quad (2.19)$$

where:

$ESALs_{Failure}$ = Amount of ESALs until rutting failure,

RS = Length of rutting season in days,

RF = The fraction of the total ESALs where rutting takes place.

2.3.2.9 Selvaraj Model (2007)

Selvaraj (2007) developed a rut prediction model based on the results obtained from accelerated pavement testing facility at the National Center for Asphalt Technology (NCAT) test track. Built in the year of 2000, the NCAT test track consists of 46 different test sections, out of which eight sections were assigned for structural study in 2003. The structural study sections were instrumented with earth pressure cells, strain gauges, temperature probes, moisture probes, and axle sensors. One box trailer and five triple trailers were used to apply traffic loading. The performance data (rutting data) from the test sections were collected once

a week using three different methods; dipstick profiler/precision level, laser profiler, and wire line measurement with a 6 ft (1.8 m) straight edge.

Two different models were developed by Selvaraj (2007): one was vertical strain-based model and the other was shear strain-based model. Multi-layered elastic analysis software, WESLEA, was used by the researcher to develop the models. Vertical strain at the top of base and subgrade was calculated by using WESLEA. WESLEA simulations were performed for different truck axles (steer, tandem, and single), and the average vertical strain (base, subgrade) value for a single truck pass (ε_{avg}) was calculated by the following equation:

$$\varepsilon_{avg} = \frac{\varepsilon_{st} n_{st} + \varepsilon_t n_t + \varepsilon_s n_s}{N_T} \quad (2.20)$$

where:

ε_{st} , ε_t , ε_s = Calculated strain (base, subgrade) for steer, tandem, and single axles, respectively,

n_{st} , n_t , n_s = Number of steer, tandem, and single axles in a truck, respectively, and

N_T = Total number of axles.

To predict vertical strain on the top of base and subgrade layers at any point of time for a given pavement temperature, WESLEA simulations were conducted for a wide range of temperatures [30^{o}F (-1.11^{o}C) to 120^{o}F (49^{o}C)], representative of pavement temperatures at the test track, and the strain responses were computed for the truck loading. Then a model was developed to predict vertical strain on the top of base and subgrade layers as a function of pavement temperature for both triple and box trailer. The basic form of the vertical strain prediction model was as follows:

$$\varepsilon = \alpha_1 e^{\alpha_2 * T} \quad (2.21)$$

where:

ε = Vertical strain (base, subgrade) (microstrain),

T = Temperature at 2 in. from top of HMA (^{o}F), and

α_1, α_2 = Regression coefficients.

By relating the measured hourly rutting to the vertical strain on the top of subgrade layers and the total number of axle passes, rut prediction models were developed by performing non-linear regression analyses. The following final rut prediction model, considering vertical strain, was proposed:

$$Rut_i = Rut_{i-1} + \beta_o N_i^{(\beta_1 * \varepsilon_i)} \quad (2.22)$$

where:

Rut_i = Rut at time "i" from field measurements,

Rut_{i-1} = Rut at time "i-1" from field measurements,

N_{si} = Total number of axle passes at time "i",

ε_i = Vertical base or subgrade strain calculated at time '*i*' from strain prediction models, and

β_0, β_1 = Regression constants for traffic and strain, respectively.

The vertical strain model coefficients did not explain the field rutting mechanism very well, so Selvaraj (2007) tried modeling the rutting by considering the shear strain response as a next step.

In developing the shear strain model, a similar methodology as in vertical strain-based model, was applied. But as WESLEA does not compute the shear strain, the shear strain was actually calculated from shear stress (computed through WESLEA) using the following equation:

$$\gamma = \frac{2\tau(1+\nu)}{E} \quad (2.23)$$

where:

γ = Shear strain (microstrain),

τ = Shear stress measured along the edge of a tire (psi),

v = Poisson ratio of HMA, taken as 0.35 for this study, and

E = HMA modulus (psi).

A similar approach adopted to compute vertical strain for a single truck pass was followed to compute shear strain. The shear strain for a truck pass was obtained from the following equation:

$$\gamma_{avg} = \frac{\gamma_{st} n_{st} + \gamma_t n_t + \gamma_s n_s}{N_T} \quad (2.24)$$

where:

γ_{st} , γ_t , γ_s = Calculated maximum shear strain in the HMA layer at 1-in. depth for steering, tandem and single axles, respectively.

Following the procedure outlined for vertical strain, the shear strain was expressed by the following equation, as a function of temperature:

$$\gamma = ae^{b*T} \quad (2.25)$$

where:

γ = Maximum shear strain at 1-in. from the top of HMA layer (microstrain), and

a, b = Regression coefficients.

The same approach followed for the vertical strain based model development was used to develop the shear strain based rut prediction model [Equation. (2.26)]:

$$Rut_i = Rut_{i-1} + \lambda_0 N_i^{(\lambda_1 * \gamma_i)} \quad (2.26)$$

where:

Rut_i = Rut at time "i" from field measurements,

Rut_{i-1} = Rut at time "i-1" from field measurements,

N_{si} = Total number of axle passes at time "i",

γ_i = Shear strain in HMA calculated at time '*i*' from the shear strain prediction model, and

λ_0, λ_1 = Regression constants for traffic and shear strain in HMA, respectively.

As the shear strain-based model satisfied the rut prediction on both modified and unmodified test sections fairly well, Selvaraj (2007) concluded that that this approach could be used to predict rutting in flexible pavements with a reasonable accuracy.

Although the model developed by Selvaraj (2007) predicts rutting fairly well in the NCAT Test Track region, the model may not be applied to low temperature regions where the pavement temperature goes below -6.7°C (20°F) and at very high temperature regions where the pavement temperature often goes above 43.3°C (110°F). Another inherent deficiency of this model is that it was developed solely from the accelerated pavement testing environment, meaning there was no variation in truck loading. A modified model based on the actual traffic data from an in-service pavement is desired, which is one of the primary objectives of the present study.

2.4 Fatigue Prediction Models

Similar to rut prediction models (Section 2.3), fatigue prediction models are helpful in predicting the failure of pavement due to fatigue cracking. A brief overview of fatigue failure mechanism and prediction models is provided in this section.

2.4.1 Fatigue Failure Mechanism

As mentioned earlier in Chapter 1, fatigue cracking is one of the three major modes of distresses that occurs in flexible pavement. Fatigue cracking initiates at the bottom of the flexible layer due to repeated and excessive loading and then propagates through the entire HMA layer, allowing water infiltration to the unbound layers (Figure 2.3). This causes accelerated surface and structural deterioration, pumping of the unbound materials, and rutting (Priest and Timm, 2006). Shook et al. (1982) explained that the M-E structural design process must limit the tensile strain in the HMA layer in order to control or design against fatigue cracking. Furthermore, the AI MS-1 development manual (Research and Development, 1982) refers to ten different M-E design procedures that use the tensile strain at the bottom of the HMA layer as the critical design criterion in regard to fatigue. Fatigue cracking is also referred to as alligator cracking because of its distinctive pattern that looks like the back of an alligator.

Fatigue distress is quantified in the field by measuring the affected pavement area, which is typically expressed as a percentage of the total lane area or the wheelpath area (Priest and Timm, 2006). According to the Strategic Highway Research Program (SHRP) Distress Identification Manual for the Long-Term Pavement Performance (LTPP) Program (Miller and Bellinger, 2003), there are different levels of severity to further define the cracking. Low severity fatigue cracking comprises of individual cracks in the wheelpath with no signs of pumping. Moderate severity is reached when the cracks become interconnected. High severity rating is given when pumping is evident. The SHRP distress guide gives a standard on how to measure and categorize fatigue cracking, however, it does not specify a specific failure criterion. For fatigue transfer function development, it is critical to determine what extent of

cracking is considered failure, or at what point should the damage ratio, *D*, becomes equal to one.

Presented here are some failure criteria examples considered for developing transfer functions. NCHRP 1-10B transfer functions were calibrated using two levels of cracking failure. The first calibrated function considered cracking of 10 percent of the wheelpath as failure, and the second considered greater than 45 percent of the wheelpath. The second failure criterion was reached using the previous function with a multiplier of 1.38. In another example, the AI transfer functions were also calibrated using the AASHO Road Test data while considering an area greater than 45 percent of the wheelpath or 20 percent of the total lane as failure (Monismith et al., 1985; Shook et al., 1982). The MEPDG used Long-Term Pavement Performance (LTPP) test sections to calibrate performance models, with 50 percent cracking of the total lane being considered failure (Priest and Timm, 2006).

2.4.2 Fatigue Performance

It is widely accepted and documented that HMA fatigue life performance is related to the horizontal tensile strain following the relationship of Equation (2.27). Additional developments included the HMA mixture stiffness in the fatigue life relationship to account for varying temperature and loading frequency, as shown in Equation (2.28) (Tangella et al., 1990). The HMA stiffness parameter is very important in the fatigue performance, and it must be considered in conjunction with the expected in situ HMA thickness and failure mode.

$$N_f = k_1\left(\frac{1}{\varepsilon_t}\right)^{k_2} \tag{2.27}$$

$$N_f = k_1\left(\frac{1}{\varepsilon_t}\right)^{k_2}\left(\frac{1}{E}\right)^{k_3} \tag{2.28}$$

where:

N_f = Number of load cycles until fatigue failure,

ε_t = Applied horizontal tensile strain at the bottom of the HMA layer,

E = HMA mixture stiffness (psi), and

k_1, k_2, k_3 = Regression constants.

Other fatigue relationships include asphalt material mixture parameters or mix volumetrics as an additional correction factor to the k_1 term. This parameter is also known as voids filled with bitumen (or asphalt), called VFB (or VFA). Previous studies have noted that minimizing the air voids and maximizing the amount of asphalt binder was beneficial to fatigue life. Pell and Cooper (1975) presented the effect of mix volumetrics in the form of

$$VFB = \frac{V_B}{(V_B + V_V)} \tag{2.29}$$

where:

VFB = Void filled with bitumen,

V_B = Percent asphalt volume, and

V_V = Percent air volume.

Based on Pell and Cooper (1975), the interaction of air and binder volume is an important parameter to produce a high density mix. They showed that the lower the voids in the mix, $V_B + V_V$, the denser the mix and the better use of the available binder. They also noted that at high VFB, the dynamic stiffness of the mixture increases, and thus the fatigue performance improves.

2.4.3 General Model Development Procedure

In general, fatigue life relationships or performance equations are developed in the laboratory using some form of a fatigue testing device, which is a simple flexure test with

third-point loading. Typically, HMA samples are cut into beams and subjected to repeated flexural loading either in a controlled strain or controlled stress mode (Priest and Timm, 2006).

Based on Harvey et al. (1995), laboratory-developed performance equations do not accurately predict the fatigue life of asphalt pavements in the field. There are many reasons for the difference in laboratory and field performance, and a few are listed below (Tangella et al., 1990):

- In the field, traffic loads are distributed laterally (wheel wander), so the same point of the pavement is not continually loaded.
- It is possible that in the field the HMA will sustain longer fatigue life after initial cracking due to support of underlying layers.
- Fatigue life relationships are greatly dependent on the type of fatigue test and mode of loading (i.e. flexural versus diametrical and controlled strain versus controlled stress) along with testing temperature.
- There are rest periods and the opportunity for healing in the field.
- Field performance is dependent on thickness of the in situ pavement.

As described by Priest and Timm (2006), fatigue life relationships must be calibrated or shifted to observed field performance due to discrepancies between laboratory and field behavior. The SHRP Project A-003A (Tangella et al., 1990) noted that "established correlations between laboratory data and field response are weak, [which] is a major area of concern when attempting to utilize the results of laboratory investigations to define performance criteria." This project further reported that the range of shift factors proposed by several researchers ranged from slightly over 1 to over 400. Therefore, field calibration is

essential in defining useful transfer functions, though the process can be very difficult and often imprecise. Many design manuals, including the AI MS-1 and AASHTO, rely on field performance data from the AASHO Road Test to calibrate laboratory-derived equations and come up with transfer functions. Unfortunately, these empirical relationships are considered outdated because they are reliant and restricted by the conditions of the AASHO Road Test, constructed in late 1950's. The conditions back then are more than likely irrelevant for today's conditions as the AASHO Road Test was limited to one subgrade soil, one environmental condition, 1950's vehicles and tires, 1950's materials and specifications and only a few million ESAL of traffic (Hallin, 2004). As noted earlier, one of the main benefits of M-E design is that performance predictions will no longer be based on outdated and restricted conditions but on more recent performance data and conditions which are merited to produce more accurate models.

2.4.4 Existing Fatigue Transfer Functions

2.4.4.1 Asphalt Institute MS-1

Finn et al. (1977) developed a calibrated fatigue transfer function for NCHRP 1-10B based on the laboratory equation developed by Monismith and Epps (1969).

$$logN_f = 14.82 - 3.291log\left(\frac{\varepsilon_t}{10^{-6}}\right) - 0.854log\left(\frac{E}{10^3}\right) \quad (2.30)$$

where:

N_f = Cycles until fatigue failure,

ε_t = Initial tensile strain, and

E = Complex modulus of the HMA (psi).

Equation (2.30) was calibrated using data from the AASHO Road Test to produce Equation (2.31), considering failure as 45 percent cracking of the wheelpath (20 percent of the total lane). This particular field calibration only shifted the intercept or multiplier (k_1).

$$log\ N_f = 16.086 - 3.291 log\left(\frac{\varepsilon_t}{10^{-6}}\right) - 0.854 log\left(\frac{E}{10^3}\right) \quad (2.31)$$

Or

$$N_f = 18.4 * (0.00432 * \varepsilon_t^{-3.29} * E^{-0.854})$$

According to Priest and Timm (2006), Equation (2.31) was adopted by the 9th edition of the AI Thickness Design Manual MS-1 (Research and Development, 1982) and further modified to include a correction factor to account for the volumetrics of the mixture as suggested by Pell and Cooper (1975). The final MS-1 design equation is following:

$$N_f = 18.4 * C * (0.00432 * \varepsilon_t^{-3.29} * E^{-0.854}) \quad (2.32a)$$

where:

$C = 10^M$

$$M = 4.84 * \left(\frac{V_B}{V_B + V_V} - 0.69\right) \quad (2.32b)$$

2.4.4.2 Shell Pavement Design Manual

Shell International Petroleum Company published an asphalt design manual in 1978 and included the fatigue transfer function below following a similar pattern of AI MS-1 (Ali and Tayabji, 1998):

$$N_f = 0.0685 * \varepsilon_t^{-5.6713} * E^{-2.363} \quad (2.33)$$

where:

ε_t = Initial tensile strain, and

E = Stiffness of the HMA (psi).

Equation (2.33) was developed from mainly laboratory fatigue test data. Further work was completed in 1980, and separate functions were developed for thin (less than 2 in.) and thick (6-8 in.) asphalt pavements, which are presented elsewhere (El-Basyouny and Witczak, 2005).

2.4.4.4 AASHTO 2002 MEPDG Model

The MEPDG fatigue cracking models considered first both the Shell Oil and AI fatigue transfer functions as starting points (Eres, 2004), but determined that the AI MS-1 equation was the most applicable (El-Basyouny and Witczak, 2005). Basically, Equation (2.31) was re-calibrated using the LTPP data and included a new correction factor, *K*, to account for thinner pavements (less than 4 in.). The final fatigue design equation, considering failure at 50 percent cracking of the total lane area, is as follows (El-Basyouny and Witczak, 2005):

$$N_f = 0.00432 * K * C * \left(\frac{1}{\varepsilon_t}\right)^{3.9492} \left(\frac{1}{E}\right)^{1.281} \quad (2.34)$$

where:

$K = \frac{1}{0.000398 + \frac{0.003602}{1+e^{11.02-3.49*h_{ac}}}}$, and

h_{ac} = Thickness of HMA layer (in).

2.4.4.5 Minnesota Department of Transportation

The Minnesota Department of Transportation (Mn/DOT) developed a fatigue transfer function following the Illinois Department of Transportation function developed for dense-graded asphalt mixtures (Alvarez and Thompson, 1998):

$$N_f = 5*10^{-6}*\left(\frac{1}{\varepsilon_t}\right)^{3.0} \quad (2.35)$$

The final Mn/DOT fatigue equation was calibrated using performance data from Mn/ROAD and is given as (Timm et al., 1999):

$$N_f = 2.83*10^{-6}*\left(\frac{1}{\varepsilon_t}\right)^{3.206} \quad (2.36)$$

2.4.4.6 NCAT Test Track

According to Priest and Timm (2006), the fatigue transfer functions developed from the NCAT Test Track were derived strictly from field data without laboratory testing or theoretical models. Since the track consisted of different sections, each with different layer thicknesses and materials, three fatigue models were considered: thin, thick, and rich bottom.

The following fatigue transfer function was developed for thin asphalt pavement sections (less than 5 in.):

$$N_f = 0.4875*\left(\frac{1}{\varepsilon_t}\right)^{3.031}*\left(\frac{1}{E}\right)^{0.6529} \quad (2.37)$$

Preliminary fatigue transfer function development for thicker asphalt pavement sections (5 in. or more) yielded the following equation:

$$N_f = 0.4831*\left(\frac{1}{\varepsilon_t}\right)^{3.063}*\left(\frac{1}{E}\right)^{0.5992} \quad (2.38)$$

Likewise, the following fatigue transfer function was developed from the rich bottom section:

$$N_f = 0.4814*\left(\frac{1}{\varepsilon_t}\right)^{3.007}*\left(\frac{1}{E}\right)^{0.6911} \quad (2.39)$$

2.5 Instrumentation and Dynamic Data

2.5.1 Mn/Road

The Minnesota Road Research Project (Mn/Road) is a full scale pavement testing facility located off of I-94 in Otsego, Minnesota (Figure 2.4). The facility is divided into two parts: the first part is a 3.5 mile mainline that runs parallel to I-94 and consists of real interstate traffic. As for the second part, it is a 2.5 mile road loop and consists of low-volume controlled traffic. The facility contains 40 test sections with a variety of both flexible and rigid pavement structures. The facility promotes cooperative research between Minnesota Department of Transportation (MnDOT), University of Minnesota, and Federal Highway Administration (FHWA), as well as other state DOTs (MnDOT website). As described by Alvarez and Thompson (1998), there are approximately 4,500 sensors embedded in the test sections to monitor both the pavement condition and the dynamic response under loading.

Three most important sensors are asphalt strain gauges, linear variable differential transducers (LVDT), and dynamic soil pressure gauges. The asphalt strain gauges are electrical resistance strain gauges on an H-shaped bar, and they were installed at the bottom of the asphalt layer in both the transverse and longitudinal directions. Furthermore, they were installed at the center of the wheelpath and at 1 ft transverse offsets. The LVDTs consist of an electromagnetic device and separate core. They were used to measure the vertical displacement at different depths within the pavement structure. Lastly, soil pressure cells were used to measure the dynamic vertical pressure due to truck loads. These gauges consisted of a liquid-filled steel cell with adjacent pressure transducer.

In addition to the response gauges, there are also pavement environmental condition sensors including thermocouples and time domain reflectometers (TDR). The TDRs were

installed in the soil layers, to measure the in situ moisture content. The thermocouples are used to measure the temperature profile in the pavement structure (Alvarez and Thompson, 1998; Beer et al., 1996).

The sensors are connected to 26 roadside boxes, and there are two main collection systems. Most of the gauges are sampled via an automated, continuous data acquisition system that is triggered by the passage of a vehicle which then records a burst of data. The condition gauges are also sampled automatically based on a routine time schedule. There are also sensors that are collected manually with an on-site system (Beer et al., 1996).

The automated data acquisition system at Mn/ROAD retrieves and processes the data and then sends the information to the Mn/DOT Materials Research Engineering Laboratory where it is checked and stored on an Oracle database (Alvarez and Thompson, 1998). In this way, the data collection and processing is completely automated. No further information could be found regarding how strain values were estimated from the actual dynamic traces (Priest and Timm, 2006).

2.5.2 Virginia's Smart Road

Virginia's Smart Road is a test track located in Montgomery County, Virginia, and was constructed by the Virginia Department of Transportation (VDOT) and Virginia Tech's Transportation Institute. The initial test section was 1.7 mile two-lane road and is part of a 5.7 mile highway that will connect Blacksburg, Virginia to I-81 (Figure 2.5) (Virginia Smart, 2011). The facility was designed to accommodate multiple interdisciplinary projects including bridge design, Intelligent Transportation Systems (ITS) development, safety and human factor research, vehicle dynamic research, and pavement design. The flexible pavement test track consists of a total of 12 diverse sections. Each section is approximately 350 ft. long,

constructed with different materials, and all include embedded response and conditions devices.

The instrumentation array is comprised of asphalt strain gauges, pressure cells, TDRs and, thermocouples (Priest and Timm, 2006). For the data acquisition system, the scheme used consisted of two units: one, to collect static or condition data, and two, to collect response or dynamic data. In terms of data collection and processing, three software programs were developed at Virginia Tech to collect, organize, and process the dynamic data (Al-Qadi et al., 2004). For collecting data, SmartAcq software was used to collect dynamic data in the presence of a vehicle and to collect condition data at specified time intervals. The dynamic gauges were sampled at 500 Hz per channel, the temperature probes are collected every 15 minutes, and the TDRs every hour. To organize the collected data, Smart Organizer software was used to separate them into distinct files by gauges, test section, and date. Finally, to process the dynamic strain and pressure data, SmartWave software was used. Al-Qadi et al. (2004) noted that the dynamic traces were originally viewed individually in a spreadsheet program, but the process was inefficient due to the large amount of traces and data points per trace. Therefore, researchers at Virginia Tech developed the SmartWave program which allowed for easier viewing and processing of the dynamic traces (Al-Qadi et al., 2004). The general process consisted of, first, cleaning the signal of electronic noise and, second, collecting the important values from the recorded trace. The software was developed to automatically collect the maximum value for each axle of the 6-axle test vehicle. The peak value per axle could be either compression or tension for the asphalt strain gauges and only compression for the pressure cells. The collected strain magnitude was the absolute value

from the baseline of the trace to the peak point determined from the SmartWave algorithm (Priest and Timm, 2006).

After processing, the dynamic response data were stored in an Access database along with the environmental (condition) data. The data were stored in such a way to allow for easy retrieval among the two databases. Furthermore, queries were developed to allow extraction of only maximum response values of replicate tests (Al-Qadi et al., 2004).

2.5.3 NCAT Test Track

NCAT's Test Track is a 1.7 mile full-scale asphalt testing facility located in Opelika, Alabama (Figure 2.6). The facility was created in 2000 as a part of a cooperative research program between state Department of Transportations (DOTs) and FHWA to investigate, at a full-scale level, the needs of the transportation system and asphalt industry (Priest and Timm, 2006).

The first test cycle, completed in 2002, investigated different materials in regard to rutting and surface distress. The second test cycle, which began in October 2003, consisted of eight test sections, each constructed with different materials. The sections were designed structurally using the 1993 AASHTO Design Guide (AASHTO, 1993), and mix designs were according to Alabama DOT (ALDOT) specifications. The traffic on the test track was controlled and consisted of five triple-trailer trucks and a standard FHWA class 9 18-wheeler truck, that applied over 1,000,000 passes (approximately 10 million ESALs) during the two-year testing cycle. In addition, the trucks were operated at 45 miles per hour and are driven by human drivers. The sections were designed to show a variety of distresses over the life of the experiment, and it was intended that at least the thinner sections would exhibit fairly extensive

structural distress in order to correlate performance (for both fatigue and rutting) to field-measured pavement responses.

The instrumentation at the NCAT Test Track consisted of dynamic pavement response sensors and in-situ conditions sensors. Similar to both Mn/ROAD and Virginia Smart Road, H-shaped strain gauges were installed at the bottom of the HMA layer, oriented in both longitudinal and transverse directions. Additionally, the gauges were installed at three different lateral offsets in the wheelpath to help ensure a direct hit of the truck tire over a gauge. To measure the critical vertical stresses involved in rutting analyses, earth pressure cells were installed at the top of the base layer and at the top of the fill layer, in each section.

As described by Priest and Timm (2006), a portable DATAQ high-speed dynamic data acquisition system was used to sample and collect dynamic data. A typical data collection day consists of three passes of each truck. Initially, dynamic response data were collected monthly, but once fatigue distresses were noticed, the efforts were increased to weekly. For measuring in-situ conditions of the pavement, thermistors and TDR probes were installed to measure the pavement temperature and the subgrade moisture content, respectively. According to Priest and Timm (2006), the temperature and TDR probes were sampled at every minute and recorded the hourly average, maximum, and minimum readings. Hourly readings were transmitted through the radio modem to the data storage computer throughout the two-year testing cycle to continuously monitor the pavement environmental conditions.

The instrumentation and the data acquisition scheme implemented at the I-35 test section were similar to the scheme at NCAT. As presented in the following chapter, exclusive programs and algorithms developed by NCAT were used to collect and process the data in a

Windows environment. Also, similar to NCAT, both processes involved some human interaction.

Table 2-1 Summary of the Rut Prediction Models

Model Author	Proposed Model	Parameters
Finn et al. (1977)	1) For conventional construction: $\log(RR) = -6.866 + 4.325 \log d - 0.131 \log(N_{18})$ 2) For thick (> 6-in.) or full-depth asphalt concrete: $\log(RR) = -1.173 + 0.717 \log d - 0.658 \log(N_{18}) + 0.666 \log \sigma_c$	Asphalt concrete thickness, no. of ESAL, Vertical compressive stress in asphalt concrete
Allen and Deen (1980)	$\log \varepsilon_p = C_0 + C_1(\log N) - C_2(\log N)^2 + C_3(\log N)^3$	Deviator stress
Leahy (1989)	$\log\left(\frac{\varepsilon_p}{\varepsilon_r}\right) = -6.631 + 0.435 \log N + 2.767 \log T + 0.11 \log S + 0.118 \log \eta + 0.930 \log V_{b\,eff} + 0.501 \log V_a$	Load repetitions, mix temperature, deviatoric stress, viscosity, asphalt content, air void content
Ali (1998)	$\rho_p = 0.00011 * h_{AC}[\sum_{i=1}^{k} n_i(\in e_{i,AC})^{1.111}]^{0.9} + 23.26 * h_{Base}[\sum_{i=1}^{k} n_i(\in e_{i,Base})^{20}]^{0.05} + 0.022 * h_{Subgrade}[\sum_{i=1}^{k} n_i(\in e_{i,Subgrade})^{2.81}]^{0.356}$	Layer thickness, vertical compressive elastic strain
Hand et al. (1999)	$\gamma^p = a\, e^{(b*\tau^e)} \gamma^e N^c$	Plastic shear strain, elastic shear stress and strain, no. of ESAL

Table 2-2 Summary of the Rut Prediction Models (Continued)

Model Author	Proposed Model	Parameters
Kim et al. (2000)	$RD = [-0.016\,H_{AC} + 0.033\ln(SD) + 0.011T_{annual} - 0.01\ln(KV)] * [-2.703 + 0.657\left(\varepsilon_{v,base}\right)^{0.097} + 0.271\left(\varepsilon_{v,SG}\right)^{0.883} + 0.258\ln(N) - 0.034\ln(\frac{E_{AC}}{E_{SG}})]$	AC layer thickness, surface deflection, ambient temperature, kinematic viscosity, vertical elastic compressive strain, cumulative ESAL, resilient modulus of AC and subgrade
Zhou et al. (2004)	Primary stage: $\varepsilon_P = aN^b,\ N \le N_{PS}$ Secondary stage: $\varepsilon_P = \varepsilon_{PS} + c\,(N - N_{PS}),\ N_{PS} \le N \le N_{ST},$ and $\varepsilon_{PS} = aN_{PS}^b$ Tertiary stage: $\varepsilon_P = \varepsilon_{ST} + d\left(e^{f\,(N - N_{ST})} - 1\right),\ N \ge N_{ST}$ and $\varepsilon_{ST} = \varepsilon_{PS} + c(N_{ST} - N_{PS})$	Material parameters, No. of load repetition corresponding to primary, secondary and tertiary stage
Williams et al. (2005)	$ESALs_{Failure} = \frac{(\text{APA Cycles to 7 mm Rut}) * (129.9\frac{\text{Rutting ESALs}}{\text{Cycles}})}{(\frac{RS*RF}{365})}$	Rutting ESAL, rutting factor, rutting season, wheel wander, speed
Immanuel Selvaraj (2007)	Vertical strain based model: $Rut_i = Rut_{i-1} + \beta_o N_i^{(\beta_1 * \varepsilon_i)}$ Shear strain based model: $Rut_i = Rut_{i-1} + \lambda_0 N_i^{(\lambda_1 * \gamma_i)}$	Vertical strain, no. of axles passes, shear strain

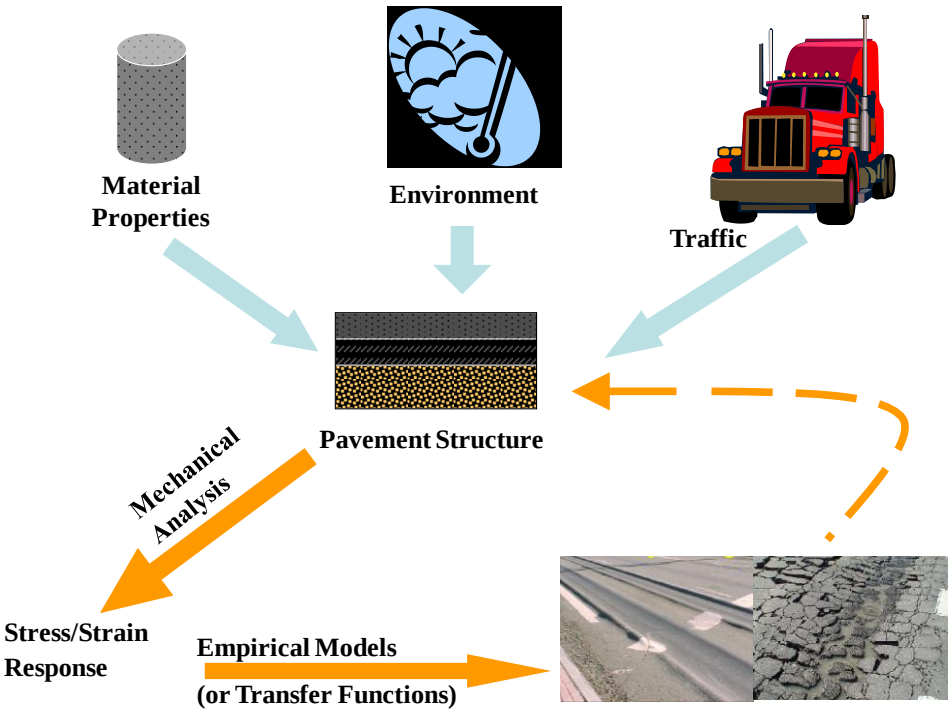

Figure 2-1 Schematic Summary of Mechanistic-Empirical Pavement Design

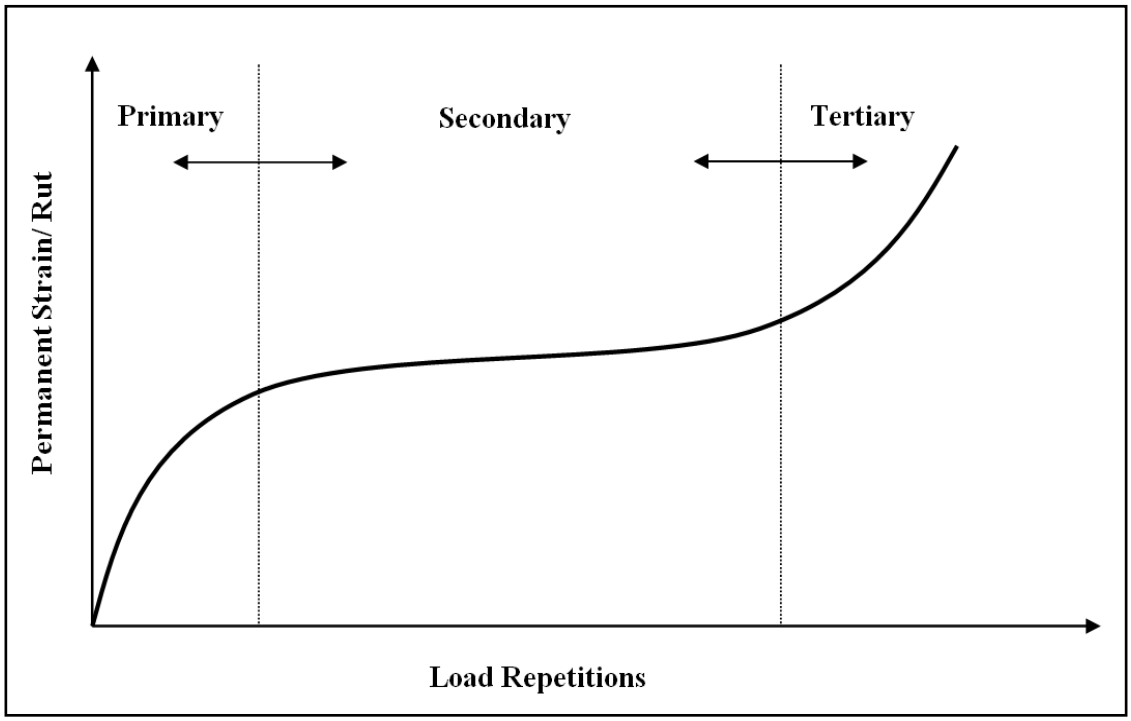

Figure 2-2 Rut Progression for Increasing Load Repetitions (after El-Basyouny et al., 2005)

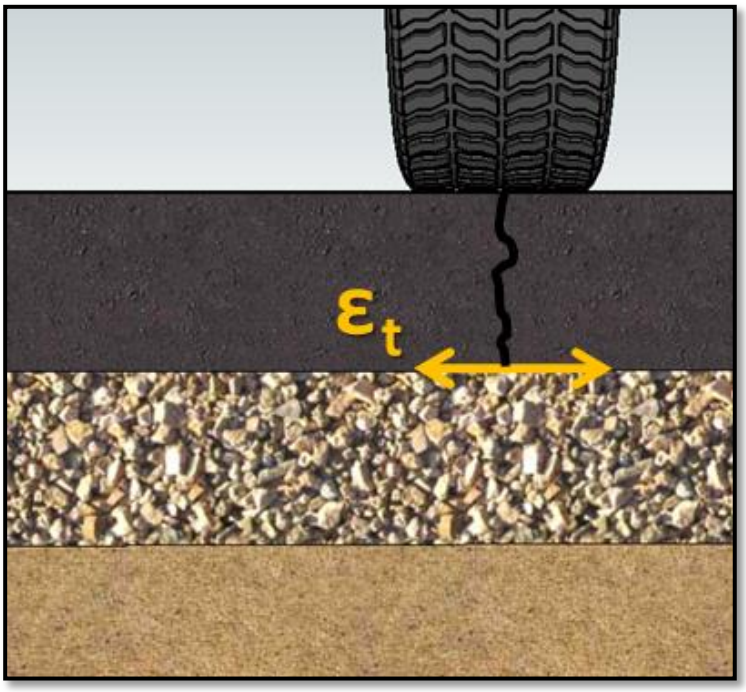

Figure 2-3 Sketch of Fatigue Cracking in Pavement Cross Section

Figure 2-4 Mn/ROAD facility (MnDOT website)

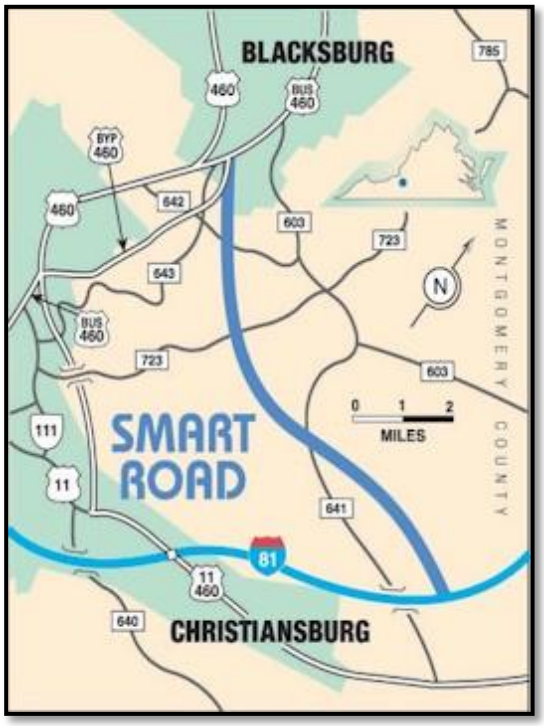

Figure 2-5 Map of Virginia's Smart Road (Virginia Smart, 2011)

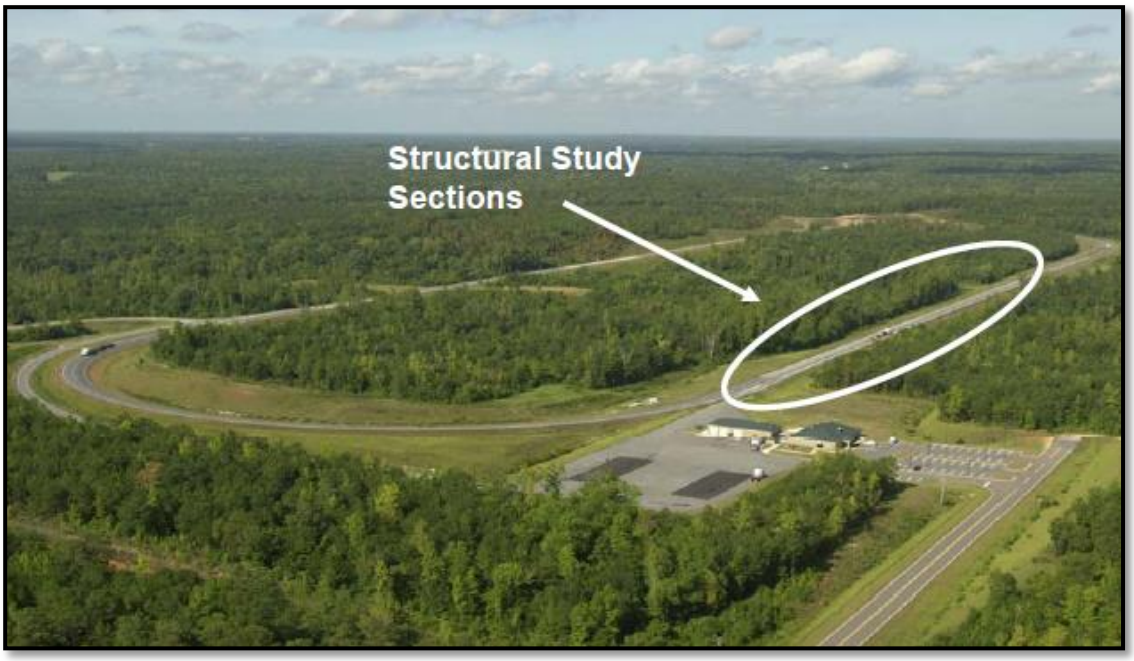

Figure 2-6 Aerial Photo of the NCAT Test Track (Priest and Timm, 2006)

Chapter 3 FIELD TEST SECTION

3.1 Introduction

An instrumented pavement section was used in this study to examine its in-service performance, particularly relative to rutting and fatigue cracking. An overview of the construction and instrumentation of the test section is given in this chapter.

3.2 Location of the Test Section

The 1000-ft instrumented pavement section is located in McClain County near Purcell, Oklahoma on the outer southbound lane of I-35 (Figure 3.1). A preliminary site visit was conducted by the OU research team along with personnel from the Oklahoma Department of Transportation (ODOT) to observe such factors as existing roadway elevation, width, slope, right of way, and proximity to electrical power supply. Based on this site visit and discussions with ODOT and NCAT personnel, this site was found to be suitable for the proposed site for instrumentation. In addition, a pre-existing WIM (Weigh-In-Motion) station approximately 0.75 miles south of the proposed instrumentation site was a factor in the site selection process. This WIM station was used to collect the traffic data. The test section and WIM station start approximately at milepost 95 and end at milepost 91. A photographic view of the site before construction is shown in Figure 3.2. The area surrounding the instrumented site is relatively flat, with large fields and pastures.

3.3 Pavement Structural Design

For typical interstate pavements, ODOT recommends the use of a minimum of 12 in. thick Hot Mix Asphalt (HMA) layers. However, for this particular test section, the thickness of the HMA layers was deliberately reduced and made similar to a state highway section so

that it would fail in a relatively short period of time due to heavy traffic on the interstate, allowing collection of field performance data over its entire service life. A thinner pavement section resembles the concept similar to accelerated pavement testing (APT), but under actual vehicular traffic and environmental conditions rather than controlled conditions used in APT.

A profile of the instrumented pavement section is shown in Figure 3.3. The section consists of five layers. (1) The top layer is a 2 in. thick HMA layer of type "S4" and containing PG 64-22 binder. (2) The second layer is a 5 in. thick HMA layer of type "S3." It is a recycled mix with PG 64-22 binder and 25% recycled asphalt pavement (RAP). (3) The third layer has a thickness of 8 in. It consists of "Type A" aggregate base. (4) The fourth layer is an 8 in thick cementitiously stabilized subgrade layer, stabilized with 12% fly ash. (5) The bottom layer is the subgrade soil. It is basically lean clay with a liquid limit of 33 and a plasticity index of 15. It is dark brown in color. The water table at the site varies from 10 to 13 ft from the surface, depending on the time of year. Based on the design parameters summarized in Table 3.1, the test section should withstand about 10 million ESALs. As noted before, the pavement in the test section is much thinner than typical interstate pavements. The idea behind using a thinner section was to let it fail in a relatively short period of time allowing collection of field performance data over its entire service life. It is estimated that the collected field data will reflect the long-term (about 20 years) service life of state highway pavements subjected to lower traffic level.

3.4 Subsurface Characterization

The purpose of this subsurface characterization was to obtain information that will aid in the preliminary assessment of geotechnical issues associated with the performance of the test section under actual traffic.

3.4.1 Natural Subgrade Soil

Limited geotechnical investigations were conducted on the existing subgrade layer at the test site. As part of this investigation, approximately 100 lb of soil was collected from a location close to the center of the proposed instrumentation array. The collected soil was air dried in the laboratory and processed by passing through a #4 sieve. The maximum dry density (MDD) and optimum moisture content (OMC) were determined by conducting standard Proctor tests in accordance with the ASTM D 698 test method. The moisture-density curve for the subgrade soil is shown in Figure 3.4. From this figure, the MDD and OMC were found to be approximately 110.4 pcf and 14.5%, respectively.

Since resilient modulus (M_r) is an important material parameter for pavement design (AASHTO, 2004), the subgrade soil was tested for M_r. A total of four specimens were compacted, two at OMC and the other two at 2% wetter than the OMC (OMC+2%). A desired amount of water was added to the soil, manually mixed for uniformity and pre-wetted for at least 16 hours in air sealed 2 gallon Ziploc® plastic bags. This mix was compacted in five layers in a mold with a diameter of 4.0-in. and a height of 8.0-in. to reach a dry density of between 95%-100% of the MDD. After compaction, samples were tested for M_r in accordance with the AASHTO T 307-99 test method. The M_r test consisted of applying a cyclic haversine-shaped load with a duration of 0.1 seconds and rest period of 0.9 seconds. For each sequence, the applied load and the vertical displacement for the last five cycles were measured and used to determine the M_r values. The load was measured by using an internally mounted load cell, having a capacity of 500 lbf. The resilient displacements were measured using two linear variable differential transformers (LVDTs) fixed to opposite sides of and equidistant from the piston rod outside the test chamber. The LVDTs had a maximum stroke

length of 1.0 in. An MTS Micro Controller system and Multi-Purpose Test Ware software were used in running these tests, as shown in Figure 3.5. The Multi-Purpose Test Ware software was used to write a program for controlling the applied cyclic deviatoric stress as well as to acquire the load and displacement data. Table 3.2 shows the average resilient modulus values at different deviatoric stress and confining pressures. One way to observe the resilient modulus is to evaluate the changes in M_r values at a specific deviatoric stress and confining pressure (Drumm et al., 1997). A simple model commonly used by ODOT was chosen in this study for this purpose.

$$M_r = k_1 \, x \, \sigma_d^{k2} \qquad (3.1)$$

In this model, the M_r is expressed as a function of deviatoric stress (σ_d). Table 3.2 presents the aforementioned model parameters (k_1 and k_2). The M_r values were calculated at a σ_d of 6 psi and a confining pressure (σ_3) of 4 psi, as suggested by ODOT (Dean, 2008). It is clear from Table 3.2 that subgrade soil samples compacted at OMC and OMC+2% provide a pavement design M_r values of approximately 17,008 and 12,327 psi, respectively.

Since M_r is a non-destructive test, a specimen compacted at OMC was further tested by the subjecting it to two unloading-reloading sequences and loading up to failure in the third sequence of reloading at an axial strain rate of 1% per minute. The detailed procedure has been discussed in Solanki et al. (2007). The stress-strain behavior is shown graphically in Figure 3.6. It is evident that the specimen failed at an axial stress and strain of 20.3 psi and 3.1%, respectively. Modulus of elasticity (M_E) determined from the first two cycles of unloading-reloading sequences is approximately 7,440 psi.

3.4.2 Stabilized Subgrade Layer

The subgrade layer was stabilized with 12% class C fly ash (CFA), provided by Lafarge Corporation, Red Rock, Oklahoma. The CFA used in this study had a combined silica, alumina, and ferric oxide (SAF) content of approximately 62.2%. The average calcium oxide (CaO) content was approximately 24.0%. The self-cementing characteristic (hydraulic reactivity) is expressed in terms of hydration modulus, which is defined as the ratio of CaO and SAF (Kamon and Nontananadh, 1991). The hydration modulus is determined with respect to Alite and Belite cement compounds. Their chemical compositions and the calculated hydraulic moduli are given in Table 3.3. For material quality control (acceptance/rejection) purposes, ODOT recommends that the requirements of AASHTO M 295 by met. As evident from Table 3.3, CFA used in this project meets all the ODOT requirements.

In the laboratory, subgrade soil was mixed manually with 12% CFA for determining the moisture-density relationship of soil-CFA mixture. The procedure consists of adding 12% CFA to the processed subgrade soil, based on the dry weight of the soil and conducting Proctor test in accordance with the ASTM D 698 test method. The moisture-density curve for the soil-CFA mix is shown in Figure 3.7. From Figure 3.7, the MDD and OMC of the soil-CFA mix are approximately 111.3 pcf and 14.0%, respectively.

A total of four specimens: (1) two at OMC and (2) two at 2% wetter then OMC (OMC+2%) were prepared for M_r test. The soil and CFA were mixed manually for uniformity. After the blending process, a desired amount of water was added based on the OMC and the mixture was compacted using a similar method, as described in Section 3.4.1. After compaction, specimens were cured at a temperature of $23.0^o \pm 1.7^o$ C and a relative humidity of approximately 96%. Both specimens were tested at a total of five different curing

periods: 2, 8, 16, 23, and 30 days. A summary of average M_r results is presented in Table 3.4 and 3.5 for specimens compacted at OMC and OMC+2%, respectively. To study the effect of curing period on M_r values of specimens, the same model as described in Section 3.4.1 was used and plotted in Figure 3.8. It is evident from Figure 3.8 that the addition of 12% CFA increases the M_r value by 470% and 886% after 2 and 30 days of curing, respectively. The CFA-stabilized specimen compacted at OMC+2% showed a lower (40%) M_r value as compared to a specimen compacted at OMC. After 23 days of curing, both specimens showed insignificant increase (< 1%) in M_r values.

After 30 days of curing, 12% CFA-stabilized specimens were further tested using the same test method as discussed in Section 3.4.1. Figures 3.9 and 3.10 show the stress-strain behavior of CFA-stabilized specimen at OMC and OMC+2%, respectively. The specimen stabilized at OMC failed at an axial stress of approximately 85.0 psi, a 319% increase as compared to raw subgrade soil specimen. On the other hand, a specimen stabilized at OMC+2% showed lower improvement and failed at 53.8 psi. The M_E values determined from the unloading-reloading curve also showed enhancements. For example, CFA-stabilized OMC and OMC+2% specimens showed average M_E values of 35,054 and 16,263 psi, respectively.

3.4.3 Aggregate Base Layer

The aggregate used in this study was supplied by the Dolese Co., located in Davis, Oklahoma. Bulk aggregate samples were collected from the test section site from five different locations during construction of the aggregate base layer. Bulk samples were shoveled into plastic buckets, sealed to avoid any contamination, and hauled to the laboratory for testing purposes. Before the start of any testing, moisture was removed from the bulk aggregates by oven-drying the aggregates for 24 hours in a pan.

The gradation curve of the aggregate samples was determined in accordance with the ASTM C 136 test method. Figure 3.11 shows the average gradation curve (based on six replicates) compared to the upper and lower limits of Type A aggregate base specified by the Oklahoma Department of Transportation (ODOT, 1999). From Figure 3.11, the maximum aggregate size (MAS) of the aggregate base layer is 1.5-in. The percent passing US Standard No. 200 sieve is approximately 4.3% (determined in accordance with ASTM C-117 test method), which is on the lower end of the gradation curves for a Type A aggregate base.

Before any further testing, the dry aggregates were sieved using a mechanical sieve shaker in accordance with the sieve sizes recommended for Type A gradation (ODOT, 1999). All particle sizes larger than No. 200 (0.075 mm) were washed individually to remove any fines attached to rock surfaces. This process eliminated the use of excess fines in the specimen gradations. The washed aggregate was once again oven-dried for 24 hours and then stored in sealed buckets in the laboratory for further testing. These dry aggregates were mixed in the laboratory according to the required weight for preparing specimens.

Moisture-density relationship for the aggregate base was established in accordance with the ASTM D 698 Method C test method. Specimens were compacted using an automatic mechanical compactor, which could be adjusted for the compaction pertaining to either standard Proctor or modified Proctor. The mechanical compactor can be set to count the number of blows applied. This compactor also allows the mold to rotate at a set number of revolutions per minute as to assure uniform compaction. The moisture-density curve for aggregate base determined using automatic mechanical compactor is shown in Figure 3.12. The OMC and MDD for the aggregate base was approximately 4.46% and 127.4 pcf, respectively.

The M_r test was performed on two specimens compacted at OMC in accordance with AASHTO T 307 test method. After aggregates were uniformly blended, the equivalent amount of water for OMC was added and mixed until uniform. Then, the mixture was compacted in a cylindrical split steel mold, having a diameter of 6.0-in. and a height of 12.0-in, according to the method described by Shah (2007). This method employs compaction of a specimen to a dry density approximately 98% of MDD in ten equal layers by applying 44 blows per layer. Figures 3.13 and 3.14 show the compacted specimen and setup used for M_r testing, respectively. The M_r values at different bulk stress ($\theta = \sigma_d + 3\sigma_3$) are presented in Figure 3.15. It is clear that the M_r value of specimen was in the range of 14,234 – 48,569 psi.

3.4.4 Asphalt Concrete Layer

The asphalt concrete mix was supplied by Haskell Lemon Construction Co. plant located in Norman, OK. As noted earlier, two types of mixes, namely S-3 (base mix) and S-4 (surface mix), were used for constructing the 7.0-in of asphalt concrete layer. About 1000 lbs of S-3 and S-4 bulk mixes were collected in paper bags from the plant located in Norman. These bulk mixes were used in the laboratory testing, as discussed later in this report.

A summary of mix properties for the collected loose asphalt concrete mixes is shown in Table 3.6. Additional information on the asphalt mixes is presented in the design sheets attached in the Appendix. It is evident from Table 3.6 that the S-3 mix was coarser with a nominal maximum size (NMS) of ¾ in. as compared to ½ in. NMS for S-4 mix. An asphalt cement (or binder) grade of PG 64-22 was used for both mixes. The percent of binder used in the design mix of S-3 and S-4 was 4.1 and 4.6, respectively.

3.4.5 Soil Profiling

The soil profiling included drilling one bore hole at the selected location (Figure 3.16), using a hand operated posthole auger in accordance with ASTM D 1452. A field log of the surface conditions encountered in boring was maintained and reported in accordance with ASTM D 5434. The drilling was performed to a maximum depth of 12 ft below the compacted subgrade elevation with an interval of one foot. Moisture content was recorded at 0.5 ft depth of each sample length. The recovered boring samples were removed from the sampler and visually classified in accordance with the ASTM D 2488 method, as shown in Table 3.7.

Representative portions of the on-site soil samples were sealed in plastic bags and returned to the laboratory to determine their natural moisture content (ASTM D 2216), Atterberg limits (ASTM D 4318), and gradation (ASTM D 6913) for classification according to the Unified Soil Classification System (USCS). A summary of results is presented in Table 3.8. It is seen that this site consisted of lean clay up to 7 – 8 ft below the existing grade, while soils below 8.0 ft were primarily sand. The water table was encountered at a depth of about 10.8 ft. The moisture content tests performed on the *in-situ* soils indicated moistures ranging from 13.6 to 24.1 percent. This *in-situ* moisture content decreased with depth for 2.0 ft of backfill material and then start increasing attaining a maximum moisture content of 19 percent at a depth of about 4.5-ft. Farther down, this moisture content decreased with depth and showed a minimum moisture content at a depth of about 7.5 ft. Due to capillary action, moisture content started increasing again from a depth of 8.5 ft.

3.4.6 Dynamic Cone Penetrometer Test

Dynamic Cone Penetrometer (DCP) tests were performed at three selected locations on the top of the aggregate base layer in accordance with the test procedure described in SHT (1992). These locations, called DCP-1, DCP-2, and DCP-3, are illustrated in Figure 3.16. The DCP tests were performed down to a depth of approximately 0.8 m (2.5 ft), as suggested by Miller (2000). The DCP results were assumed to be representative of the entire test section. The DCP results are summarized in terms of incremental cone index (ICI), which represents the depth of penetration per blow of the DCP hammer (SHT, 1992). A lower ICI value indicates a stronger or stiffer material, while a higher DCP value indicates a weaker subgrade. Complete DCP profiles for all locations are shown in Figure 3.17. From these plots, the following observations are made.

1. The ICI values for DCP-1 exhibited a lot of variation in the top 0.6-ft (8.0-in.) and then showed an increase, attaining a maximum value of approximately 24 mm/blow at a depth of 1.3-ft. As noted earlier, depth of aggregate base as well as stabilized subgrade layer was 8.0-in. each. Hence, no significant increase or decrease in the ICI values was observed for the top 8.0-in. After 0.6-ft, however, the DCP encountered the stabilized subgrade layer, causing a significant increase in the ICI values. This is consistent with the higher M_r results obtained for stabilized subgrade soil as compared to the aggregate base specimen.
2. For DCP-2, the ICI values revealed similar behavior as encountered for DCP-1 up to a depth of 1.3-ft. The ICI values, however, exhibited an increase with depth after 1.5-ft, attaining a maximum value of 27 mm/blow at a depth of 2.3-ft (1.8-ft below the

existing subgrade level). This can be attributed to lower moisture content at this particular depth, giving rise to stronger material.

3. The ICI values of DCP-3 weree relatively higher as compared to the other two locations. The maximum ICI value of 30 mm/blow was encountered at an approximate depth of 1.6-ft (1.0 ft below the existing subgrade level). A decrease in ICI values is observed beyond 1.6-ft, with the minimum ICI (12 mm/blow) occurring at approximately 1.9-ft.

3.5 Sensor Selection

In the mechanistic-empirical methods of flexible pavement design, the two most important failure criteria recognized are: (1) fatigue cracking based on the horizontal tensile strain at the bottom of the hot mix asphalt (HMA) layer; and (2) rutting or permanent deformation along the wheel paths (Huang, 2004). Therefore, when selecting instrumentation options, it was decided to have gauges that would measure responses at these locations. The research team from the National Center of Asphalt Technology (NCAT), experienced in instrumenting pavement sections (Timm et al., 2004; Priest and Timm, 2005), helped the OU research team in instrumenting the test section.

The two prime requirements in the instrument selection were sensitivity sufficient to produce the necessary information and reliability to ensure that dependable data could be obtained throughout the period for which the data is needed (Nassar, 2001). The NCAT research team selected pavement instrumentation equipment on the basis of a number of criteria (Timm et al., 2004). These include the following:

1. Ability to measure desired responses.
2. Cost.

3. Availability (i.e., delivery times).
4. Reliability.
5. Continuity with previous research efforts at the test track.

Overall, the instrumentation provided two main types of data:

Dynamic Data: This type of data includes data collected from the lateral positioning sensors (axle count, speed, and position of a vehicle), asphalt strain gauges (tensile strains), earth pressure cell (vertical stress), and WIM station (axle count, axle weight, axle spacing, vehicle class, vehicle length, speed, and ESAL).

Environmental Data: This type of data includes data collected from the weather station (ambient temperature, ambient humidity, wind speed, wind direction, incoming solar radiation, and rainfall), temperature probes (variation of temperature within the asphalt layer), and moisture sensors (variation of moisture under the pavement).

A brief description of the sensors and gauges is provided in the subsequent sections.

3.5.1 Asphalt Strain Gauges

A sensor that could withstand heavy construction operations and dynamic loads after construction was needed. On the basis of previous experiences, gauges manufactured by Construction Technologies Laboratories (CTL) were selected. Figure 3.18 shows the selected asphalt strain gauge. A total of 14 gauges along with 40-ft of lead wire were ordered, but only 12 gauges were selected for installation, as discussed later. Along with gauges, calibration sheets were also provided by CTL for each gauge.

The CTL asphalt strain gauge, coated with polysulfide liquid polymer and encapsulated in silicone with butyl rubber outer core, was built to withstand high temperatures and compaction loads associated with paving. More technical details of the CTL asphalt strain

gauge can be found in Appendix B. The maximum range on the gauges is ±1,500 micro-strain, which is within expected strain ranges for most flexible pavements (Timm et al., 2004).

3.5.2 Earth Pressure Cells

The main purpose of earth pressure cells (EPC) was to measure the dynamic vertical pressures generated under moving traffic loads. Geokon 3500 pressure cells were chosen for this project due to imprint size, accuracy, price, and survivability. In addition, these EPCs were used widely in previous test roads (e.g., MnDOT, 1990; Nassar, 2001; Timm et al., 2004) successfully.

As shown in Figure 3.19, this device consists of two circular stainless steel plates welded together around their periphery and spaced apart by a narrow cavity filled with de-aired oil (Timm et al., 2004). Application of pressure causes an increase in fluid pressure, resulting in a corresponding electrical signal from the semi-conductor type transducer in the form of voltage.

In this study, a total of three large diameter (9.0-in.) cells having a maximum stress bearing capacity of 36.3 psi (250 kPa) were used. One set of EPC was installed on the top of each layer, namely natural subgrade, stabilized subgrade, and aggregate base. In addition, these pressure cells had a special heat-resistant wire to withstand the high HMA lay-down temperature.

3.5.3 Lateral Positioning Sensors

It was decided to implement a system similar to that used at the NCAT Test Track (Timm and Priest, 2005). Three Dynax® axle sensors supplied by International Road Dynamics, Inc. were installed at the instrumentation site. The axle sensing strips on these

sensors were approximately 1.0-in. x 1.0-in. in cross-section. Two of these parallel sensors were 88.0-in. long (Model Number: AS400), while the diagonal sensor was 120.0-in. long (Model Number: AS405). Under no-load conditions, the resistance of each sensor exceeds 10 MΩ, while application of pressure reduces the resistance between 0.002 MΩ and 0.05 MΩ.

Dynax® axle sensors are specially designed to operate independent of speed in stop-and-go traffic and can be permanently installed with epoxy in a sawcut asphalt surface or held in place by locking bars in a treadle frame.

3.5.4 Temperature Probes

Five temperature probes (or thermistors) manufactured by Campbell Scientific, Inc. were used to measure pavement temperature at different depths. These probes consist of a thermistor encapsulated in an epoxy-filled aluminum housing. The housing protects the thermistor, allowing the probes to be buried or submerged. These probes (Model 108-L with a lead length of 100.0 ft) are capable of measuring temperature in the range of -35^{o}C to +50^{o}C. The five probes were bundled together and inserted vertically in a hole drilled in the pavement, with each probe's tip located at a different depth. Starting from the surface the probes were named as follows: T1 at 0.25 in., T2 at 2.0 in., T3 at 3.5 in., T4 at 7 in., and T5 at 10-in. (Figure 3.20).

3.5.5 Moisture Probes

The ECH2O soil moisture sensor (model number: EC-5) manufactured by Decagon Devices was chosen for moisture measurements (Figure 3.21). The EC-5 measures the dielectric constant of the soil in order to find its volumetric water content (VWC). Its two prong design and higher measurement frequency allow the EC-5 to measure VWC from 0 to

100%, allowing for accurate measurements of all soil types (with an accuracy of 0.003 m^3/m^3 and a measurement time of 10 milliseconds) and for a much wider range of salinities.

Three EC-5 moisture probes were used in this study. These were installed 3.0 in. below each layer, namely the natural subgrade, the stabilized subgrade, and the aggregate base layer. After opening the test road for traffic, all three moisture probes failed. Consequently, no moisture data readings could be collected in this study.

3.5.6 Weather Station

A weather station (Model MetData1) with a tower (Model UT10) manufactured by Campbell Scientific was installed on the side of the test section (Figure 3.22). The weather station site was representative of the general area of interest, away from the influence of any obstructions such as buildings, trees, and sprinklers. The station was capable of recording the ambient temperature, relative humidity, solar radiation, wind speed and direction, and precipitation. The tower, which is 10-ft high, provides a support structure for mounting the weather station components.

3.5.7 Weigh-In-Motion (WIM) Station

Traffic characterization and related inputs play a vital role in predicting fatigue failure of pavements. Since pavement design and analysis require a large and representative amount of traffic data, weigh-in-motion (WIM) technology is being used widely because of its ability to collect large amount of traffic data continuously. An existing WIM station, located approximately 3700-ft south of the instrumented section, was used in this study. Each traffic lane was instrumented with 2 inductive loops and 2 piezoelectric sensors, each having a length of 12-ft (Figures 3.23 and 3.24). The sensors detected the presence of a vehicle and

recorded the axle numbers, axle weight, axle spacing, vehicle class, vehicle length, speed, and ESAL. This specific location was chosen because the two piezoelectric sensors were needed to be embedded in the asphalt pavement on a straight section without any curvature. The WIM sensors were calibrated immediately after installation and then were calibrated on an annual basis. The weight calibration, performed by ODOT, was conducted with a vehicle of known weight passing 15 times over each lane and measuring the percent error of the gross vehicle weight. A piezoelectric WIM system is expected to provide gross weight that is within 15% of the actual vehicle weight for 95% of the vehicles in compliance with ASTM 1318-02.

3.6 Pre-Installation Efforts

All gauges were either factory calibrated or calibrated in the laboratory. In addition, before installing any gauge, a series of checks were conducted at NCAT and ODOT warehouse to ensure its functionality.

3.6.1 Asphalt Strain Gauges

There were no facilities either at the NCAT test track or OU laboratory able to calibrate asphalt strain gauges. Hence, the calibration factors provided by CTL were used in this study. A summary of multipliers, calculated from the calibration information provided by the manufacturer, is shown in Table 3.9. The following equation was used for calculating the conversion multiplier to get microstrain from output voltage:

$$Multiplier = \frac{V(Calib.\ Excitation\ Voltage)}{V(DATAQ\ Excitation\ Voltage)} \times Calibration\ Factor \times \frac{30mV}{5V} \qquad (3.2)$$

The 30 mV/5V term accounts for the signal output amplification that the DATAQ system (data acquisition) performs on the signal. In addition, each gauge was checked for

proper functionality by connecting each gauge to a laptop computer with a data acquisition system (Figure 3.25). Specifically, each gauge was pushed and pulled to check that the response had the proper sign (i.e., correct polarity). In addition, two cable ties were attached to the connection of asphalt strain gauge and the lead wire. This helped minimize any damage to the lead wire/gauge connection.

3.6.2 Earth Pressure Cells (EPCs)

The EPCs were calibrated in the NCAT test track calibration chamber (Figure 3.26; Timm, 2007a). All three EPCs were calibrated simultaneously, as shown in Figure 3.26(a). The cells were subjected to 0 to 30 psi in approximately 5 psi increments with two additional pressurization cycles for measuring the precision of the gauges (Timm, 2007a). Figure 3.27 shows the calibration data of all the three EPCs along with the best fit lines. It is evident from Figure 3.27 that the data is remarkably consistent with a high R^2 value. Hence, the following equations were used for calculating stresses:

On subgrade soil (EPC-1): $\text{Pr}essure = 7.2615 * Voltage - 0.2844$ (3.3)

On stabilized subgrade soil (EPC-2): $Pressure = 7.330 * Voltage - 0.3059$ (3.4)

On aggregate base layer (EPC-3): $Pressure = 7.2885 * Voltage - 0.2891$ (3.5)

3.6.3 Moisture Probes Calibration

Prior to sending moisture probes to OU, the NCAT research team conducted simple test to ensure that the Decagon EC-5 moisture probes could be interfaced with the CR10X datalogger. Some basic tests were conducted with soils readily available at the NCAT test track to ensure that the probe was reading properly (Timm, 2007a).

At OU all the moisture probes were calibrated using subgrade soil, stabilized subgrade soil, and aggregate base material sampled from the instrumentation site (see Figure 3.28). The soil collected from the instrumentation site was processed by passing through U.S. Standard Sieve No. 4. Then, the soil was mixed manually with various amounts of water to generate four different volumetric water contents (VWC), as shown in Table 3.10. The mix was compacted in cylindrical molds (diameter = 6.0 in., height = 12.0 in.) to achieve field density measured using a nuclear density gauge, as will be discussed later. Similarly, specimens were compacted at five and four different VWC for stabilized subgrade and aggregate base material, respectively.

For each moisture probe, VWC readings were obtained for each specimen, with the probe rotated 120^{o} between readings. As shown in Figures 3.29 to 3.31, the data were plotted and evaluated using best fit linear functions, consistent with Campbell-Scientific's recommendation. It is worth noting that all the moisture probes were calibrated for all three pavement materials. Moisture probes 2, 3, and 4 were installed in subgrade soil, stabilized subgrade soil, and aggregate base material, respectively. The resulting calibration coefficients for each gauge and corresponding pavement material were entered into the data acquisition system to obtain volumetric moisture contents from the EC-5 moisture probes.

3.6.4 Lateral Positioning Sensors

A sketch illustrating the location and dimensions of the embedded axle sensors is shown in Figure 3.32. Three lateral positioning sensors were installed at the instrumentation site in a Z-pattern. Each sensor provided a time stamp for the passage of a wheel going over it. These time stamps along with the geometry were used for calculating the velocity and

lateral offset of a vehicle from the end of the sensing strip of a sensor (Timm and Priest, 2005).

All axle sensors were checked for proper functionality by connecting each sensor to a laptop computer with a signal-processing card (Figure 3.33). Specifically, sensing strip of each sensor was pushed to check the response. In addition, after installation of the sensors at the instrumentation site, all sensors were again checked for functionality by driving a passenger van over the three sensors and recording the signals in a laptop using the computer data acquisition system.

3.6.5 Gauge Layout and Labeling

The instrumentation plan was developed by the NCAT research team by considering two important factors: (1) the placement of instruments where they would be traversed by vehicular traffic; and (2) a certain level of redundancy in each test cell in case gauges became dysfunctional during installation, construction, or operation of the facility (Timm et al., 2004).

The general layout of the instruments is shown in Figure 3.34. Since only the outside lane of I-35 southbound was to be removed and reconstructed, the instrumentation focused on the outside wheel path of the outside lane. As noted earlier, a total of twelve asphalt strain gauges were centered on the outside wheel path.

Six of these strain gauges (Strain Gauges # 1, 2, 3, 10, 11, and 12 in Figure 3.5) were installed in the longitudinal direction (parallel to traffic direction) and the other six (Strain Gauges # 4, 5, 6, 7, 8, and 9 in Figure 3.35) were installed in the transverse direction (perpendicular to traffic direction). The strain gauges were spaced 24 in. on center to capture the spatial distribution of strain and to provide sufficient space so that the presence of one

gauge would not greatly affect the other. The distance from the first column of gauges (numbered 1, 2, and 3) to the nearest parallel axle sensor was 84 in.

The geometric plan of the three EPCs used at the instrumentation site is shown in Figure 3.34. The first EPC placed on the top of the natural subgrade was at the center of the instrumentation array. The second EPC on the stabilized subgrade was positioned 7 ft after the center of the array, while the EPC at the top of the aggregate was positioned 5 ft before the center of the array.

The temperature probes were centered approximately 3-ft from the center of the gauge array. These sensors were installed on the top of compacted asphalt concrete to capture pavement temperature at depths 0.0 in., 2.0 in., 3.5 in., 7.0 in., and 10.0 in. The moisture probes were placed approximately 3.0-in. below the top of each layer and centered between the wheel paths.

To avoid any confusion in the later stages of the project and for maintaining continuity, all gauges were labeled to give relative positioning of each gauge prior to installation in the field. The labeling scheme was determined on the basis of gauge type (EPC = Earth Pressure Cell, ASG = Asphalt Strain Gauge, MP = Moisture Probe) and the connecting channel number on the data acquisition system. Figure 3.36 shows the corresponding channel numbers on data acquisition system for all the dynamic data sensors.

A summary of the gauge labels and channel assignments for the Dataq system is presented in Table 3.11. As shown in Figure 3.37, printed labels were pasted at different locations on the gauge and connecting wires using a heat gun and shrink tubing.

3.7 Data Acquisition

As noted earlier, two types of data, namely dynamic data and environmental data were captured using different gauges. This section details the types of data acquisition systems and wiring diagrams used at the instrumentation site.

3.7.1 Dynamic Data Acquisition

The short duration (20 to 100 millisecond) of loading under moving traffic loads necessitates the use of a data acquisition system with a very high sampling frequency (>1000 samples/second/channel). Hence, it was decided to collect dynamic data using DATAQ data acquisition system (Model Number: DI 785-32), having 14-bit resolution and maximum possible sampling rate of 180 kHz (Figure 3.38). The most important and user friendly feature of this system is that the acquisition software is entirely menu driven with point-and-click programming (Timm et al., 2004).

As shown in Figure 3.38, there are 32 available channels, indicated by the white rectangular cards, on the Dataq system. These cards serve as modules to control each of the sensors connected to the system and provides the required excitation voltage and amplification, as required by each sensor (Timm et al., 2004). Figures 3.39 and 3.40 show a complete wiring diagram used at the instrumentation site.

3.7.2 Environmental Data Acquisition

It was decided to collect environmental data (moisture probes, temperature sensor, and weather station) at a relatively slow sampling rate of once per minute and store hourly summaries (maximum, minimum, and mean). To collect and store these data, a data acquisition system from Campbell Scientific, Inc. (Model: CR 10-X), having a storage

capacity of 1 million values (2 MB SDRAM) was selected (Figure 3.41). A complete power supply and wiring diagrams of the CR 10-X system are shown in Figures 3.42 and 3.43, respectively.

3.8 Construction and Instrumentation

The chronological sequence of construction and sensor installation of the instrumented section is shown in Figure 3.44. The detail of the section along with instrument location is shown in Figure 3.45. Broadly, the construction and instrumentation of the site was divided into four phases. The first phase consisted of grading, leveling, and compaction of the subgrade, followed by the installation of sensors on the top of the subgrade. The second phase consisted of constructing the stabilized subgrade layer (SSG) followed by the installation of gauges on the SSG. In the third phase, the aggregate base layer (AGB) was constructed and pertinent sensors were installed on the top of the AGB. The last phase involved paving the road with asphalt concrete (AC). These phases are discussed next.

3.8.1 Natural Subgrade Soil

3.8.1.1 Removal of Existing Subgrade Soil

The milling operation at the proposed instrumentation site started on April 27, 2008. After removing the asphalt concrete and aggregate base layers, the machinery sank in the extremely soft subgrade. A site visit was conducted by the OU research team on April 28 for collecting bulk subgrade soil samples from the site in cooperation with the contractor. A photographic view of the weak (or soft) subgrade soil is shown in Figure 3.46. The laboratory test results showed that the soil is sandy, silty clay (CL-ML) with a liquid limit and plasticity

index of 25 and 7, respectively. The *in-situ* moisture content, however, was found to be very high (16%), contributing toward the weakness of the soil.

On April 28, 2008, a meeting was organized between the contractor (Haskell Lemon Construction Co.) and ODOT personnel. After discussions in the meeting, it was decided to remove 1- to 2-ft of existing soft subgrade layer and backfill it with imported soil from I-35 northbound. Figures 3.47 and 3.48 show the subgrade layer after excavation and backfilled with the imported soil, respectively.

3.8.1.2 Compaction of Exported Soil

The subgrade was graded uniformly using a dozer, as shown in Figure 3.49. The dozer, manufactured by Caterpillar (Model D6R having 170 HP), had a weight of about 41,800-lbs. Following the grading operation, the surface was compacted with the help of an Ingersoll Rand sheep-foot roller, as shown in Figure 3.50. On average, five to six passes in vibratory mode and three to four passes in static mode were needed to achieve the desired level of compaction. Further, subgrade was smoothed by using a smooth-drum roller manufactured by Ingersoll Rand. A nuclear density gauge, shown in Figure 3.51, was used to measure the *in-situ* moisture content and dry density of the compacted subgrade. The field density (determined by the nuclear density gauge) was compared with the laboratory moisture-density results. If the field density was not between 95% and 100% of the MDD, additional passes were made. Figure 3.52 shows the layout of the six selected sections, also called stations in this study, where moisture content and density measurements were conducted. A comparison between the field and laboratory densities is presented in Table 3.12. From Table 3.12, the densities in the field ranged between 102% and 108% of the MDD obtained from the Proctor tests. Since the moisture-density relationship was established from

soil from only one location due to time constraint, it may not be applicable for subgrade soils throughout the instrumentation site. Therefore, some variations in the maximum field compaction levels were observed. Also, the moisture contents in the subgrade soil (from the nuclear density gauge) at these locations were different than the OMC obtained from the laboratory (14.5%).

3.8.2 Stabilized Subgrade Layer

As noted earlier, class C fly ash (CFA) was used for stabilizing subgrade soil. The fly ash was hauled from Red Rock, located about 130 miles from the instrumentation site, on May 5, 2008. The CFA was spread using a motor grader (Figure 3.53). The motor grader, manufactured by John Deere (Model 672 D having 155-185 HP), had a weight of about 32,780-lbs. The mixing operation followed the grading of CFA. A 4,000 gallon water truck and a pulver mixer were used for *in-situ* mixing of soil with CFA (Figure 3.54). The water supply from the truck was adjusted to obtain uniform consistency of the soil-CFA mix, as per the OMC of the soil-CFA mix. A pulver mixer (Figure 3.55), Model RS500C, manufactured by CMI (Terex), was used for this purpose. The pulver mixer followed the water truck, mixing the soil with CFA. The teeth of the pulver mixer were lowered down to the required 8-in. depth of soil to ensure a thorough mixing.

3.8.2.1 Installation of Subgrade Earth Pressure Cell and Moisture Probe

According to the contractor, mixing of soil with CFA after installation of EPC and MP can cause breakage or rupture of instruments and cable by the teeth of the pulver mixer. Therefore, it was decided to install the earth pressure cell (EPC) and the moisture probe (MP) on the top of the natural subgrade after mixing with CFA.

As shown in Figure 3.56 (a), a Caterpillar dozer (Model D6R) was used to remove the soil-CFA mix and reach the top of the natural subgrade. Then, using string lines, the locations of EPC and MP were marked on the smooth leveled surface of subgrade. The dozer also helped in excavating the trenches required for placing the cables. The research team from NCAT suggested orienting the EPC along the direction of traffic so that traffic would hit the transducer first and then the pressure plate. Given that moving traffic would tend to push the pavement as it approaches a gauge, this arrangement should minimize damage to the cable/transducer/pressure plate connection by providing strain relief (Timm et al., 2004). This would ensure better contact between the transducer and the pressure plate. Further, the pressure cell cavity was excavated (approximately 11.0-in. diameter by 2.0-in. deep) using hand tools (small garden shovels), as shown in Figure 3.56 (b). Additional excavation was conducted for the pressure cell transducer (approximately 4.0-in. wide by 25.0-in. long). The depth was adjusted so that the pressure plate went completely inside the cavity with proper leveling. Additionally, trenches were excavated using pick axes and brushed clean to eliminate any sharp stone fragments that could damage the cables or instruments.

The bottom portion of pressure plate cavity was filled with subgrade soil passing U.S. Standard Sieve #8 and compacted using a standard Proctor rammer to ensure density (Figure 3.56 (c)). This was followed by filling of the cavity with finer subgrade material (minus #16), as pictured in Figure 3.56 (d). The finer material was used to ensure that no large particles would come into contact with the pressure plate (Timm et al., 2004). The stem connecting the pressure plate to the transducer was slightly bent before installation to give extra protection to the transducer. Then, the cell was leveled on the top of finer materials by examining and

filling the voids on the imprints made by the pressure plate, as shown in Figures 3.56 (e) and (f).

After leveling the pressure plate, additional finer (-#16) material was placed by hand around the transducer followed by coarser material (-#8) and carefully compacted (Figures 3.56 (g) and (h)). Then, the cable trenches were filled with the sieved material followed by the subgrade soil excavations. These trenches were then compacted by using metal tamping plate and brought to the grade level.

The moisture probe (MP) on the top of the natural subgrade layer was installed concurrently with the EPC. A complete step-by-step installation procedure is shown in Figure 3.57. The cable trench was excavated by hand shovel, as shown in Figure 3.57 (a). In addition, one circular cavity was dug by using a drill bit so that a MP could be placed at a depth of 3.0-in. below the existing grade (Figure 3.57 (b)). During the cavity backfilling process, the MP was placed so that the metallic probes ran parallel to the direction of traffic, as shown in Figure 3.57 (c) and (d). The gauges were oriented so that approaching traffic would tend to push the cable connection into the probe to keep the connection secure during construction and service life of the instrumented section (Timm et al., 2004). The cables were then placed along the length of trenches and filled with subgrade material passing #8 followed by compaction (Figure 3.57e). It is worth mentioning here that after the installation of gauges, locations were recorded using a Global Positioning System (GPS).

3.8.2.2 Compaction, Curing and Problems Encountered During the Curing Period

After the installation of the EPC, MP, and cables, all the trenches were filled using hand shovels, as shown in Figure 3.57 (f). Once the surface was graded, it was followed by compaction of soil-CFA mix by a 14-ton Ingersoll Rand smooth-drum roller. Figure 3.58

shows the roller compacting the soil-CFA mix. A pattern of six passes with heavy vibratory mode and three passes with static mode (no vibration) followed to reach the desired density. As noted by the contractor, heavy vibratory mode helps in deep compaction of the mix or near maximum dry density. Static mode helps in smoothening the surface of the compacted mix. The field density was measured at selected stations (as discussed in Section 3.8.1) using a nuclear density gauge, and the results are presented in Table 3.13. From Table 3.13, it can be observed that the compaction achieved was in the range of 102 to 105% of MDD with an average compaction level of approximately 103%.

After compaction (May 5, 2008), the compacted stabilized soil-CFA mix layer was allowed to cure for 3 days to allow the chemical reaction to take place. During the curing period, a heavy rainfall occurred in McClain County on May 7, 2008. This caused flooding of the instrumentation site, as shown in Figure 3.59 (a). Consequently, a meeting was organized among the contractor, NCAT, OU, and ODOT teams at ODOT Purcell Residency. It was decided to wait for few more days until the stabilized subgrade layer became dry. The dry and warm weather conditions in consecutive days helped dry the stabilized subgrade layer (Figure 3.59b). Finally, installation of EPC and MP on the top of the stabilized subgrade layer was started on May 12, 2008, seven days after the construction of the stabilized layer.

3.8.2.3 Installation of Stabilized Subgrade Earth Pressure Cell and Moisture Probe

Once the stabilized subgrade layer was dry, installation of the EPC and MP gauges on the top of the stabilized layer began. These gauges were also installed concurrently to utilize common cable trenches, thereby minimizing the disruption of the stabilized material.

The location of the gauges was marked using a highly precise GPS, as shown in Figure 3.60. As noted by the contractor, this GPS has an accuracy of 0.024-in. for vertical

measurements (depth/thickness) and 0.75-in. for horizontal measurements (distances/length). Once all the locations had been marked, excavation of the gauge cavities and cable trenches was undertaken. The procedure was similar to that used for installing the subgrade instrumentation. The subgrade material passing sieve #8 and #16 was again used for filling the voids and gaps in the cavities and trenches, as discussed in Section 3.7.2.1. A photographic view of installed gauges is shown in Figure 3.61.

The installation of gauges was followed by placement of a separator fabric (or geotextile), as shown in Figure 3.62 (a). Using GPS, the traces of gauges were marked on the separator fabric using a spray paint (Figure 3.62b). To protect the gauges from the trucks, dozers, and rollers during the construction process, a thick layer of aggregate base material passing sieve #4 was placed by hand on top of each sensor (Figure 3.62c). Then, it was compacted by applying very light compaction force using a metal plate, as evident from Figure 3.62d. Additionally, a thick layer of representative aggregate base material was applied and carefully compacted again using the metal plate (Figures 3.62e through f).

3.8.3 Aggregate Base Layer

3.8.3.1 Hauling and Compaction of Aggregate Base Layer

The construction of the aggregate base started on May 12, 2008, after installation of gauges on the stabilized subgrade layer. The NCAT team advised the contractor to take extreme care so that the dump trucks did not roll directly over any of the gauges. This was achieved by starting the construction from the south end of the section, as shown in Figure 3.63a.

The aggregates were hauled from the Dolese plant, Davis, Oklahoma, located about 42 miles north of the instrumentation site. The aggregates were spread using a Caterpillar D6R dozer (Figure 3.63 (b)) on the separator fabric. The un-compacted thickness of the aggregate base layer, called loose lift thickness, was kept larger than the desired thickness after compaction. A 4,000 gallon water truck was used for spreading water on top of the aggregate layer followed by compaction (Figure 3.63 (c)).

Figure 3.63d shows the compacted aggregate base layer facing south. A nuclear density gauge, shown in Figure 3.63 (e), was used to measure *in-situ* density at identified stations on the compacted aggregate base layer. The results were compared with the Proctor results and are presented in Table 3.14. It is clear that the field density ranged between 93% (135.2 pcf) and 99% (144 pcf) of MDD (144.8 pcf). Also, the moisture contents were lower than the OMC (5.6%) at all the stations, with an average moisture content of 3.6%. After compaction, the compacted aggregate base layer was coated with an emulsion layer, also known as prime coat, on May 13, 2008. The emulsion was spread on the aggregate layer with the help of a tanker equipped with a sprayer at the rear of the truck to achieve a uniform spraying (Figure 3.63f).

3.8.3.2 Installation of Asphalt Strain Gauges

After applying the prime coat, it was allowed to cure for one day, and installation of gauges on the top of the aggregate base layer started on May 14, 2008. The first step was to locate the center of the gauge array and EPCs using the precision GPS, as described in Section 3.7.2.3. As shown in Figure 3.64 (a), stringlines were run from the center of the gauge array and EPC location using tape measurements.

Once all the locations had been marked, asphalt strain gauge (ASG) boxes (prepared during pre-installation efforts) were placed at the corresponding locations, as shown in Figure 3.64 (b). Further, ASGs were positioned with proper orientation so that the cables extended in upstream in the direction of traffic, as evident from Figure 3.64 (c). This also helped in identifying the location of trenches, which were dug for the cables. Then, cables were laid in the trenches and filled with the aggregate materials passing sieve #4 (Figures 3.64 (d) and (e)).

After the ASGs had been placed in their locations, a prime coat was applied again in the surrounding area of the gauges to simulate the actual construction conditions (Figure 3.64f). A sand-binder (PG 64-22) mix was also prepared and applied on the top of the strain gauges after positioning the sensor in the required orientation (Figure 3.64g). This mixture acted like glue between the strain gauge and the aggregate base layer. Finally, a layer of sieved HMA material was placed on the top of each ASG. This cover material was spread using a metal trowel and compacted using a metal compacting plate, as shown in Figure 3.64 (h).

3.8.3.3 Aggregate Base Earth Pressure Cell and Moisture Probes

The EPC and MP in the aggregate base followed more or less similar procedure of installation, as described previously in Section 3.7.2.3. The only significant difference, however, was the use of aggregate material passing #4 sieve as a fill material for the EPC and MP (Figure 3.65). Both EPC and MP were also covered by using the sieved HMA material before construction.

3.8.4 Asphalt Concrete Layer

3.8.4.1 Paving

The paving-related work started on May 14, 2008, after lining the paver up to straddle the gauge array (Figure 3.66a). The hot mix asphalt (S3-type mix for the base layer) was laid first on the north end of the instrumentation site. Paving was performed with a paver manufactured by Caterpillar. During paving the gauges were monitored from time to time for survivability and response. After laying the mix, a vibratory roller (Figure 3.66 (b)), manufactured by Ingersoll Rand, was used for compaction. A pattern of two passes with heavy vibratory mode and one pass with static mode (no vibration) followed to achieve the desired density. Two passes of a pneumatic roller manufactured by Ingersoll Rand were also used for deep compaction (Figure 3.66c). The asphalt surface was further smoothed with a single pass of static roller to an approximate thickness of 2.5-in.

The next day, a tack coat was applied followed by the second lift of the S3-type mix. The paving and compaction procedure was similar to that outlined for the first lift (Figure 3.66d). A surface course (S4-type mix) was also laid on the same day and compacted to an approximate thickness of 2.0-in. A photograph of the paved instrumented site, section, and plan is shown in Figures 3.66 (e) and (f), respectively.

3.8.4.2 Installation of Temperature Probes

A complete installation procedure for the temperature probes is pictured in Figures 3.67 (a through f). After paving, these probes were installed on May 16, 2008. As noted by Timm et al. (2004), the installation process followed the following steps:

1. A hole of approximately 1.5-in. diameter was drilled using a hammer drill vertically into the pavement. The hole was approximately 10in. deep.
2. A U-notch approximately ¾-in. deep was cut from the hole to the edge of the pavement as a cable trench.
3. The gauge was covered with a rubberized asphalt joint and crack filler (or roof cement) commonly available at home improvement stores.
4. The hole was filled with the same rubberized asphalt material.
5. The temperature gauge array was then inserted into the hole so that the top gauge was just below the surface and worked around to ensure no air pockets would be present.
6. The cable was laid in the U-notch trench and covered with an epoxy-sand mix, supplied by IRD, Inc.

3.8.4.3 Installation of Lateral Positioning Sensors

An overview of the installation procedure for Dynax® axle sensors is provided in this section. Further details regarding sensor installation can be found in the NCAT report (Timm and Priest, 2005) and the International Road Dynamics (IRD) installation manual (IRD, 2003).

After paving, string lines were drawn and locations of sensors were marked, as shown in Figures 3.68 (a) and (b). A hammer drill was used to drill three holes near the edge of pavement for sending cables into the pull boxes located along the side of the instrumentation section (Figure 3.68 (c)). As depicted in Figure 3.68 (d), a concrete saw was used to cut slots in the pavement approximately 1.5 in. wide by 1.5 in. deep in this section. Then, a leaf blower was used to dry out the slots and remove debris.

After the slots were dry, metal brackets supplied by IRD were attached to the sensors and each sensor was suspended in the slot with duct tape along the edges (Figure 3.68e). A mix was prepared using epoxy and sand supplied by IRD, Inc. All the sensors were taken out and the slot was filled with the epoxy-sand mix, as shown in Figure 3.68f. The sensors were then placed in each slot and gently moved back and forth to eliminate any air bubbles between the sensor and epoxy-sand mix. Any excess epoxy-sand was removed using hand tools. After 45 minutes of solidification time for the epoxy, metal brackets and duct tape were removed to give a clean final installation (Figures 3.68 (g) and (h)).

3.8.4.4 Extraction of Field Samples

The field compacted cylindrical and block samples were extracted on May 16, 2008 from the shoulder along the instrumented section. The cylindrical samples (or cores) were extracted using a coring machine, as shown in Figures 3.69 (a through d). At first, the locations were marked on the pavement using a yellow paint (Figure 3.69 (a)). Then, samples were cored using a coring rig with a diameter of 6 ¼-in. and extracted by using the grip of two sharp chisels, as shown in Figures 3.69b through c. A total of six full-depth cores were extracted from the pavement (Figure 3.69d). Similar to cores, the locations of block samples were marked on the pavement and cuts were made using a masonry saw (Figure 3.70a). However, the extraction of block samples was tricky, as each block sample was approximately 20 in. long x 5 in. wide x 7 in. thick and weighed approximately 60 lbs. A brick tong was used to extract the blocks without any damage (Figure 3.70 (b) and (c)). A total of four full-depth blocks were extracted from the pavement (Figure 3.70d). The extracted cores and blocks were further saw-cut and tested for density (Figure 3.71). Also bulk asphalt concrete mix used for construction was collected from the Haskell Lemon plant located in

Norman, OK. The mix was tested for maximum specific gravity (Rice test) in accordance with the AASHTO T 209 test method. Additional samples were prepared in the laboratory using these mixes for APA rut test, as will be discussed later in Chapter 5. The maximum specific gravity (G_{mm}) values for S-3 and S-4 mixes are presented in Tables 3.15 and 3.16, respectively. The bulk specific gravity (G_{mb}) values of core and block samples were also determined in accordance with the OHD L-45 test method. The air void contents of cores and block samples are presented in Figures 3.72 and 3.73, respectively. It is evident from Figures 3.72 and 3.73 that the air voids of compacted mix in the field varies between 6.7 – 10.6% for the S3 layers and 8.2 – 10.6% for the S4 layer.

3.8.4.5 Preparation of Pavement for Traffic

The contractor and ODOT team decided to open the instrumented section to traffic on May 30, 2008. One of the major issues was to keep track of the identified stations for future field performance data collection. The OU research team decided to triangulate the locations of the identified stations before opening the lanes to traffic. This was achieved by driving approximately 2.5 in. long nails on the shoulder. The location of the identified stations and the triangulation point (or mark point) measurements is shown in Figure 3.74. The procedure of driving nails is shown in Figure 3.75.

On May 28, 2008, all the concrete barriers were removed, as shown in Figure 3.76. These were replaced with orange plastic cones and the pavement was cleaned with the help of a mechanical broom, as shown in Figure 3.77. Further, white paint stripes were drawn on the pavement with the help of a paint truck equipped with a sprayer at the rear of the truck (Figure 3.78). Finally, the instrumented lane was opened to traffic on May 30, 2008 around 11:00 a.m. with help from the ODOT traffic management team (Figure 3.79).

Table 3-1 Pavement Design Parameters

Design Parameters	
AADT	42,500
Initial Serviceability	4.5
Terminal Serviceability	2.5
Reliability	90%
Standard Deviation	0.46
Overloaded Trucks	16%
Truck Growth Rate	2%
Design Direction	56%
Avg Initial Truck Factor	2%
Design Life	5 years

Table 3-2 Resilient Modulus Values of Subgrade Soil Specimens

σ_3 (psi)	σ_d (psi)	M_r (psi) OMC	M_r (psi) OMC+2%
6	1.8	20,447	15,907
6	3.6	19,741	15,172
6	5.4	18,488	13,786
6	7.2	17,690	12,695
6	9.0	16,957	11,755
4	1.8	18,687	14,688
4	3.6	18,259	13,821
4	5.4	17,499	12,860
4	7.2	16,851	12,107
4	9.0	16,312	11,480
2	1.8	17,354	13,406
2	3.6	16,750	12,662
2	5.4	16,154	11,858
2	7.2	15,609	11,170
2	9.0	15,189	10,646
k_1		20,185	16,498
k_2		-0.10	-0.16
R^2		0.70	0.66
Design[a] M_r		17,008	12,327

[a] $M_r = k_1 \times \sigma_d \wedge k_2$ (σ_d = 6 psi, σ_3 = 4 psi)

σ_d : Deviator Stress; σ_3 : Confining Pressure

Table 3-3 Properties of class C fly ash (CFA) used in this study

Chemical Compound	Percentage by weight, (%)			ODOT requirements[d]	
	CFA[a]	Alite[b] (C_3S)	Belite[b] (C_2S)	Minimum	Maximum
Silica (SiO_2)	38.16	24.83	32.50	-	-
Alumina (Al_2O_3)	18.17	1.24	2.13	-	-
Ferric Oxide (Fe_2O_3)	5.91	0.94	1.03	-	-
SiO_2+Al_2O_3+Fe_2O_3 (SAF)	62.24	27.01	35.66	50.0	-
Calcium oxide (CaO)	24.03	72.23	62.83	-	-
Magnesium oxide (MgO)	5.55	0.98	0.52	-	
Sulfur trioxde (SO_3)	1.20	-	-	-	5.0
Sodium Oxide (Na_2O)	1.67	0.09	0.20	-	-
Potassium Oxide (K_2O)	0.57	0.14	0.30	-	-
Na_2O eq.	-	-	-	-	1.5
Loss on Ignition (LOI)	0.32	-	-	-	5.0
Free Lime	-	-	-	-	-
Hydration Modulus[c]	0.39	2.67	1.76	-	-
Fineness (retained No. 325)	3.40	-		-	34.0

[a]Provided by manufacturer; [b]Kamon and Nontananandh (1991);

[c]Hydration Modulus = $CaO/(Al_2O_3+SiO_2+Fe_2O_3)$; [d]AASHTO M 295

Table 3-4 Resilient Modulus Values of the 12% CFA-Stabilized Subgrade Soil Specimen at OMC

σ_3 (psi)	σ_d (psi)	M_r (psi) @ OMC				
		2-day	8-day	16-day	23-day	30-day
6	1.8	120,955	150,609	175,146	184,386	189,430
6	3.6	101,200	145,032	161,564	176,745	177,369
6	5.4	103,218	140,698	155,854	170,115	172,560
6	7.2	98,384	138,275	155,374	168,630	169,780
6	9.0	92,000	138,166	148,290	165,991	165,891
4	1.8	113,664	144,116	171,959	179,970	181,801
4	3.6	97,960	139,566	158,112	167,580	175,600
4	5.4	96,565	138,446	153,659	166,209	168,243
4	7.2	96,327	138,199	151,789	165,210	165,434
4	9.0	93,035	136,614	148,215	160,313	161,269
2	1.8	112,369	139,178	161,377	176,760	177,321
2	3.6	96,885	136,846	155,247	165,773	168,231
2	5.4	96,960	133,180	152,711	165,212	167,232
2	7.2	95,633	132,843	148,089	163,014	163,329
2	9.0	92,053	132,222	145,334	160,815	160,712
k_1		121,609	147,881	177,284	185,967	190,532
k_2		-0.13	-0.04	-0.08	-0.06	-0.07
R^2		0.82	0.48	0.84	0.77	0.81
Design[a] M_r		96,900	137,372	152,603	166,240	167,617

σ_d : Deviator Stress; σ_3 : Confining Pressure; [a]$M_r = k_1 \times \sigma_d \wedge k_2$ (σ_d = 6 psi, σ_3 = 4 psi)

Table 3-5 Resilient Modulus Values of the 12% CFA-Stabilized Subgrade Soil Specimen at OMC + 2%

σ_3 (psi)	σ_d (psi)	M_r (psi) @ OMC + 2%				
		2-day	8-day	16-day	23-day	30-day
6	1.8	69,738	104,221	113,625	117,186	117,667
6	3.6	69,041	98,103	109,152	109,606	109,651
6	5.4	63,802	98,523	106,478	106,728	106,205
6	7.2	58,558	94,283	100,573	103,629	103,778
6	9.0	54,464	90,165	97,254	100,294	100,286
4	1.8	62,055	99,682	106,812	112,890	112,817
4	3.6	61,061	97,720	104,417	104,527	104,656
4	5.4	57,672	94,433	99,131	100,147	102,019
4	7.2	55,398	91,058	97,740	98,611	98,792
4	9.0	52,755	89,156	94,568	98,707	99,182
2	1.8	59,477	97,170	100,293	101,767	101,648
2	3.6	60,381	97,093	98,013	98,167	99,253
2	5.4	56,381	93,008	96,500	96,861	97,280
2	7.2	55,871	91,435	94,764	96,023	96,208
2	9.0	51,837	89,379	94,004	95,128	96,171
k_1		69,986	105,469	112,268	114,894	114,960
k_2		-0.11	-0.07	-0.07	-0.07	-0.07
R^2		0.54	0.77	0.52	0.50	0.51
Design[a] M_r		57,326	93,248	98,887	100,527	100,939

σ_d : Deviator Stress; σ_3 : Confining Pressure; ; [a]$M_r = k_1 \times \sigma_d \wedge k_2$ (σ_d = 6 psi, σ_3 = 4 psi)

Table 3-6 Summary of Mix Properties for the Collected Loose HMA Mixes

Properties	**S-3 Mix Type**	**S-4 Mix Type**
Blended Materials		
1.0 in. Rock	20	00
5/8 in. Chips	00	25
Manufactured Sand	44	38
Asphalt Sand	11	00
Sand	00	15
Screenings	00	22
Recycled Asphalt Pavement (R.A.P)	25	00
Binder Information		
Binder Type	PG 64-22	PG 64-22
Binder Content	4.1	4.6
Binder Source	Valero, Ardmore, OK	Valero, Ardmore, OK
Binder Specific Gravity	1.01	1.0173
Aggregate Property		
Maximum Aggregate Size (MAS)	1.0 in.	¾ in.
Nominal Maximum Size (NMS)	¾ in.	½ in.
Sand Equivalent	94	70
L.A. Abrasion % Wear	28.0	11.0
Durability	71	63
Ignition Oven Correction Factor (IOC)	0.14	0.26
Fractured Faces	100/100	100/100
Effective Specific Gravity (G_{se})	2.671	2.678
Mixture Property		
Voids in the Mineral Aggregate (VMA) (%)	13.6	14.1
Indirect Tensile Strength (psi)	158.8	110.5

Table 3-7 Boring Log and Visual Classification of the Soil Obtained from Pre-Construction Testing

Depth (ft.)	**Moisture Sample depth (ft.)**	**Strata Change**	**Visual Classification and Remarks**
0 – 1	0.5	No	Dark brown backfill silty clay (CL), low plasticity, damp
1 – 2	1.5	No	Dark brown silty clay (CL), low plasticity, dry
2 – 3	2.5	Yes	Reddish brown silty clay (CL), low plasticity, moist
3 – 4	3.5	No	Reddish brown silty clay (CL), low plasticity, moist
4 – 5	4.5	No	Reddish brown silty clay (CL), low plasticity, moist
5 – 6	5.5	No	Reddish brown silty clay (CL), low plasticity, moist
6 – 7	6.5	Yes	Reddish brown silt (CL), low plasticity, moist
7 – 8	7.5	Yes	Reddish silt (CL), low plasticity, moist
8 – 9	8.5	Yes	Reddish silty sand (CL-ML), low plasticity, moist
9 – 10	9.5	Yes	Reddish well graded sand (SW), moist
10 – 11	10.5	No	Reddish well graded sand (SW), wet
11 – 12	11.5	No	Wet well graded sand (SW), Water table at 10.8-ft.

Table 3-8 Consistency Index, Gradation and Classification of Soils

Depth (ft.)	**Natural Water Content (%)**	**PL**	**LL**	**PI**	**% Finer No. 200 (75 µ)**	**USCS Classification**
0 – 1	17.2	18	33	15	87.1	CL (Lean Clay)
1 – 2	14.5	18	33	15	86.2	CL (Lean Clay)
2 – 3	17.8	14	35	21	86.0	CL (Lean Clay)
3 – 4	18.9	15	35	20	84.6	CL (Lean Clay with Sand)
4 – 5	19.0	15	38	23	84.0	CL (Lean Clay with Sand)
5 – 6	17.5	14	37	23	85.9	CL (Lean Clay)
6 – 7	17.1	15	32	17	84.5	CL (Lean Clay with Sand)
7 – 8	13.6	20	25	5	90.8	CL (Silty Clay)
8 – 9	17.5	NP	NP	NP	83.2	--
9 – 10	27.9	NP	NP	NP	59.3	--
10 – 11	29.0	NP	NP	NP	47.5	--
11 – 12	24.1	--	--	--	1.5	--

Note: Ground water table encountered at 10.8-ft.
PL: Plastic Limit; LL: Liquid Limit; PI: Plasticity Index; USCS: Unified Soil Classification System

Table 3-9 Summary of Multipliers and Calibration Factors of Asphalt Strain Gauges

Channel	Strain Gauge ID	Calibration Factor	Calibration Excitation Voltage	Multiplier
1	0-72	117.86	4.98	352.17
2	0-77	114.40	4.98	341.83
3	0-75	128.27	4.98	383.27
4	0-73	189.91	4.98	567.45
5	0-74	125.86	4.98	376.07
6	0-78	132.59	4.98	396.18
7	0-80	124.21	4.98	371.14
8	0-81	135.08	4.98	403.62
9	0-82	129.16	4.98	385.93
10	0-83	118.47	4.98	353.99
11	0-84	124.86	4.98	373.08
12	0-85	115.99	4.98	346.58

Table 3-10 Summary of Specimens prepared for Moisture Probe Calibration

Sample Number	Weight of Pan (gm)	Wet Weight + Pan (gm)	Dry Weight + Pan (gm)	Wet Weight (gm)	Dry Weight (gm)	Volumetric Water Content* (%)
Subgrade Soil						
R-1	2136	12882	10956	10746	8820	34.6
R-3	2148	12149	9458	10001	7310	48.4
R-4	2152	11372	10934	9220	8782	7.9
R-5	2154	12224	11160	10070	9006	19.1
Stabilized Subgrade Soil @ 12% Fly Ash						
T-1	2194	13082	11088	10888	8894	35.9
T-2	1556	11744	9552	10188	7996	39.4
T-3	2230	11962	10994	9732	8764	17.4
T-4	2184	12214	11506	10030	9322	12.7
T-5	2150	12146	9790	9996	7640	42.4
Aggregate Base						
A-1	2148	14206	13668	12058	11520	9.7
A-2	2154	14762	13754	12608	11600	18.1
A-3	2158	13938	13592	11780	11434	6.2
A-4	2138	14870	13770	12732	11632	19.8

*Volumetric Water Content = (Wet weight-Dry weight) / (Density of water x Volume of the sample before drying)

Table 3-11 Summary of Gauge Labels

Label	Type of Gauge	ID number	Channel	Base voltage	Remarks
EPC-1	Earth Pressure Cell	0-7-2433	DATAQ 13	0.14	On natural soil
EPC-2		0-7-2432	DATAQ 14	0.10	On stabilized soil
EPC-3		0-7-2434	DATAQ 15	0.10	On aggregate base
ASG-1	Asphalt Strain Gauge	0-72	DATAQ 1	0.9	Longitudinal
ASG-2		0-77	DATAQ 2	1.1	Longitudinal
ASG-3		0-75	DATAQ 3	0.2	Longitudinal
ASG-4		0-73	DATAQ 4	2.3	Transverse
ASG-5		0-74	DATAQ 5	-1.7	Transverse
ASG-6		0-78	DATAQ 6	1.2	Transverse
ASG-7		0-80	DATAQ 7	-0.7	Transverse
ASG-8		0-81	DATAQ 8	1.2	Transverse
ASG-9		0-82	DATAQ 9	-0.7	Transverse
ASG-10		0-83	DATAQ 10	0.0	Longitudinal
ASG-11		0-84	DATAQ 11	-2.8	Longitudinal
ASG-12		0-85	DATAQ 12	-1.5	Longitudinal
ASG-13		0-76	NA	---	Not installed
ASG-14		0-79	NA	---	Not installed
LPS-1	Lateral Positioning Sensor	NA	DATAQ 16	---	Traffic will hit this 1st
LPS-2		NA	DATAQ 17	---	Traffic will hit this 2nd
LPS-3		NA	DATAQ 18	---	Traffic will hit this 3rd
MP- 2	Moisture Probe	NA	CR 10-X	---	On natural soil
MP- 3		NA	CR 10-X	---	On stabilized soil
MP- 4		NA	CR 10-X	---	On aggregate base

Table 3-12 Summary of Moisture Content and Dry Density Measurements on Subgrade

Point	**Typical Section**	**Dry Density from Field** (pcf)	**Moisture from Field** (%)	**MDD from Lab.** (pcf)	**OMC from Lab** (%)	**Relative Compaction** (%)
1	144	117.2	11.8	110.4	14.5	106
2	235	117.7	11.4	110.4	14.5	107
3	319	112.7	15.7	110.4	14.5	102
4	540	119.4	12.1	110.4	14.5	108
5	738	118.6	12.1	110.4	14.5	107
6	900	117.5	12.1	110.4	14.5	106
Average		117.2	14.6	110.4	14.5	106

Table 3-13 Summary of Moisture Content and Dry Density Measurements on Stabilized Subgrade

Point	**Typical Section**	**Dry Density from Field** (pcf)	**Moisture from Field** (%)	**MDD from Lab.** (pcf)	**OMC from Lab** (%)	**Relative Compaction** (%)
1	144	114.5	14.7	111.3	14.0	103
2	235	115.7	14.2	111.3	14.0	104
3	319	116.6	13.1	111.3	14.0	105
4	540	114.9	14.7	111.3	14.0	103
5	738	113.5	15.3	111.3	14.0	102
6	900	115.3	13.9	111.3	14.0	104
Average		115.1	14.3	111.3	14.0	103

Table 3-14 Summary of Moisture Content and Dry Density Measurements on Aggregate Base Layer

Point	**Typical Section**	**Dry Density from Field** (pcf)	**Moisture from Field** (%)	**MDD from Lab.** (pcf)	**OMC from Lab** (%)	**Relative Compaction** (%)
1	144	140.5	3.6	144.8	5.6	97
2	235	140.0	3.6	144.8	5.6	97
3	319	135.2	3.5	144.8	5.6	93
4	540	144.0	4.0	144.8	5.6	99
5	738	141.6	3.3	144.8	5.6	98
6	900	141.0	3.8	144.8	5.6	97
Average		140.4	3.6	144.8	5.6	97

Table 3-15 Determination of the theoretical maximum specific gravity of type S-3 asphalt concrete mix

Sample#	**S3-1**	**S3-2**	**S3-3**
Flask # :	1	2	3
Test Temperature (T^oC)	27.0	30.0	31.0
Mass of dry sample (A), gms	1960.0	2013.9	2631.3
Flask + Water @ T^oC (F), gms	5990.3	5987.1	5986.7
Sample + Flask + Water @ T^oC (G), gms:	7166.4	7200.8	7569.3
% Bitumen	3.40	3.40	3.40
Mass of Butimen Sample (gms)	66.64	68.47	89.46
Correction for thermal correction of bitumen (H)	-0.05	-0.10	-0.10
Density of water @ T^oC (dw), Mg/m^3	0.9965	0.9956	0.9953
Density of water @ 25^oC, Mg/m^3	0.9970	0.9970	0.9970
G_{mm}:	**2.499**	**2.513**	**2.505**
Average			**2.505**

Table 3-16 Determination of theoretical Maximum Specific Gravity of S-4 mix

Sample#	**S4-1**	**S4-2**	**S4-3**
Flask # :	1	2	3
Test Temperature (T^oC)	29.0	29.0	28.0
Mass of dry sample (A), gms	1593.8	1562.1	1874.6
Flask + Water @ T^oC (F), gms	5987.5	5987.5	5988.8
Sample + Flask + Water @ T^oC (G), gms:	6935.6	6918.0	7104.5
% Bitumen	4.60	4.60	4.60
Mass of Butimen Sample (gms)	73.31	71.86	86.23
Correction for thermal correction of bitumen (H)	-0.05	-0.10	-0.10
Density of water @ T^oC (dw), Mg/m^3	0.9959	0.9959	0.9962
Density of water @ 25^oC, Mg/m^3	0.9970	0.9970	0.9970
G_{mm}:	**2.465**	**2.470**	**2.468**
Average		**2.468**	

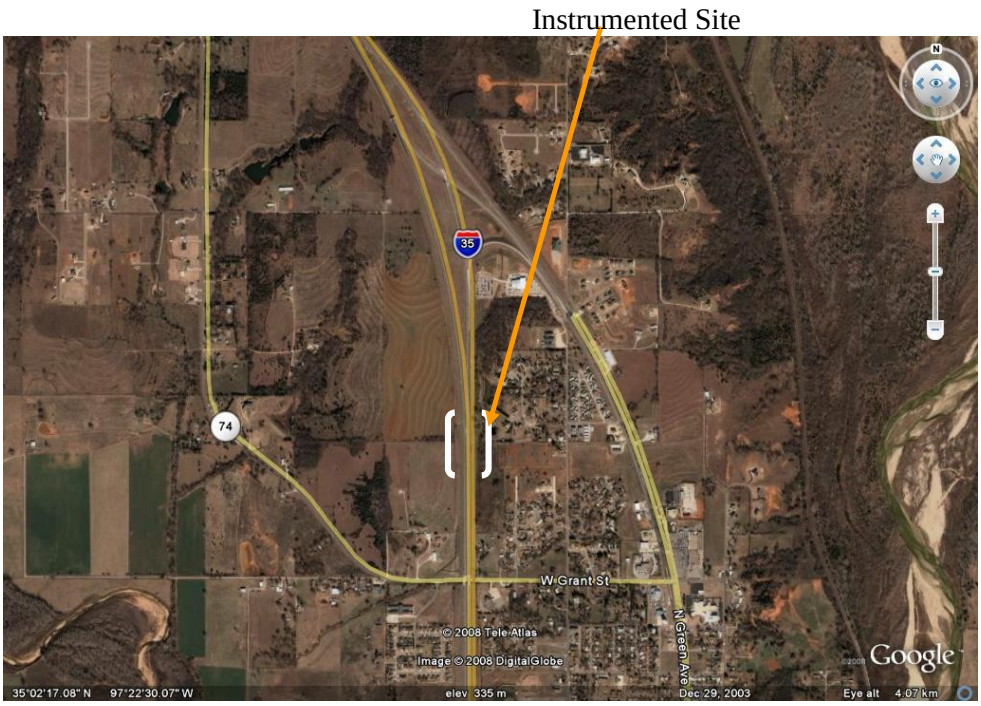

Figure 3-1 Location of Instrumented Pavement Site, McClain County, Oklahoma

Figure 3-2 Instrumentation Site Before Construction, Looking South

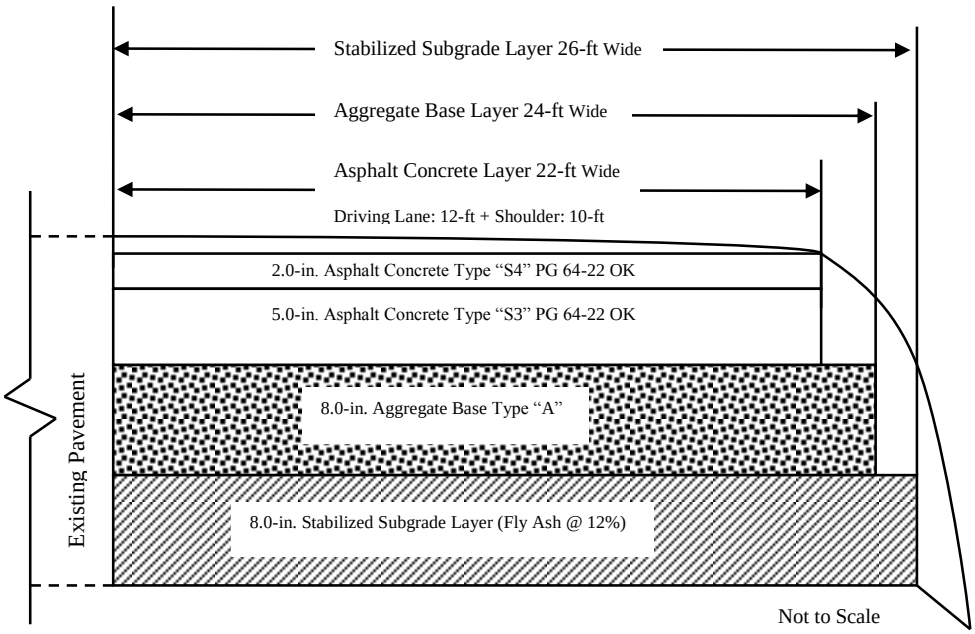

Figure 3-3 Sketch of Typical Section, Looking South

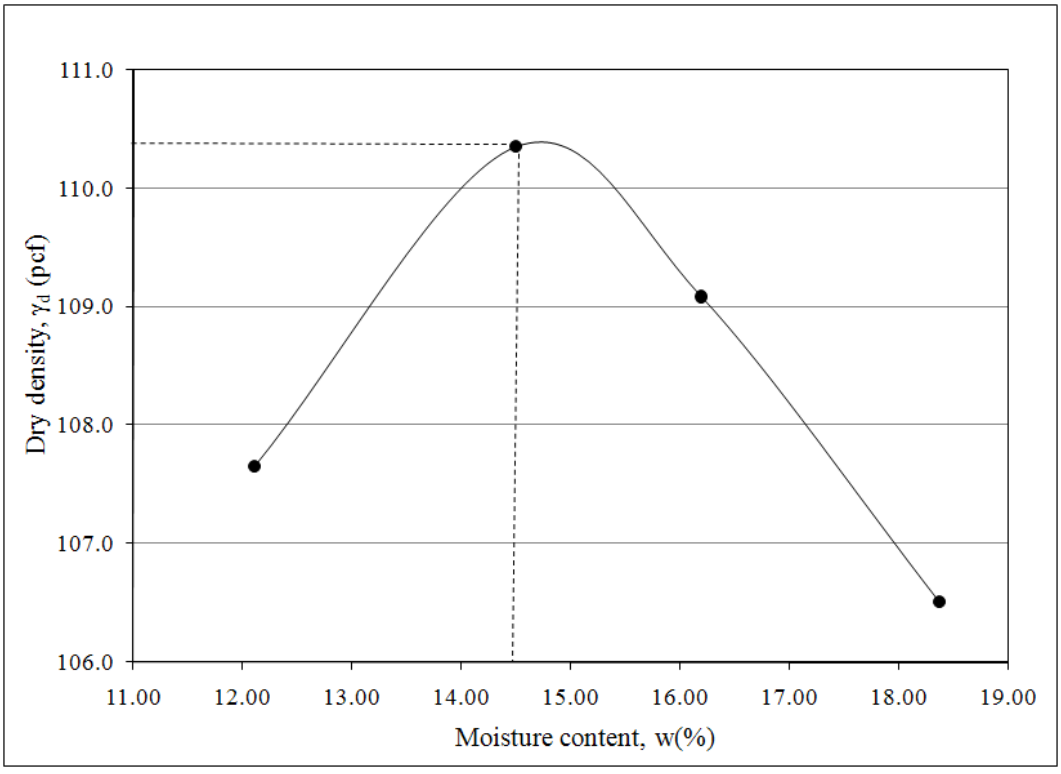

Figure 3-4 Moisture-Density Relationship of Subgrade Soil

Figure 3-5 Setup for Resilient Modulus Testing on Subgrade Soil Specimen

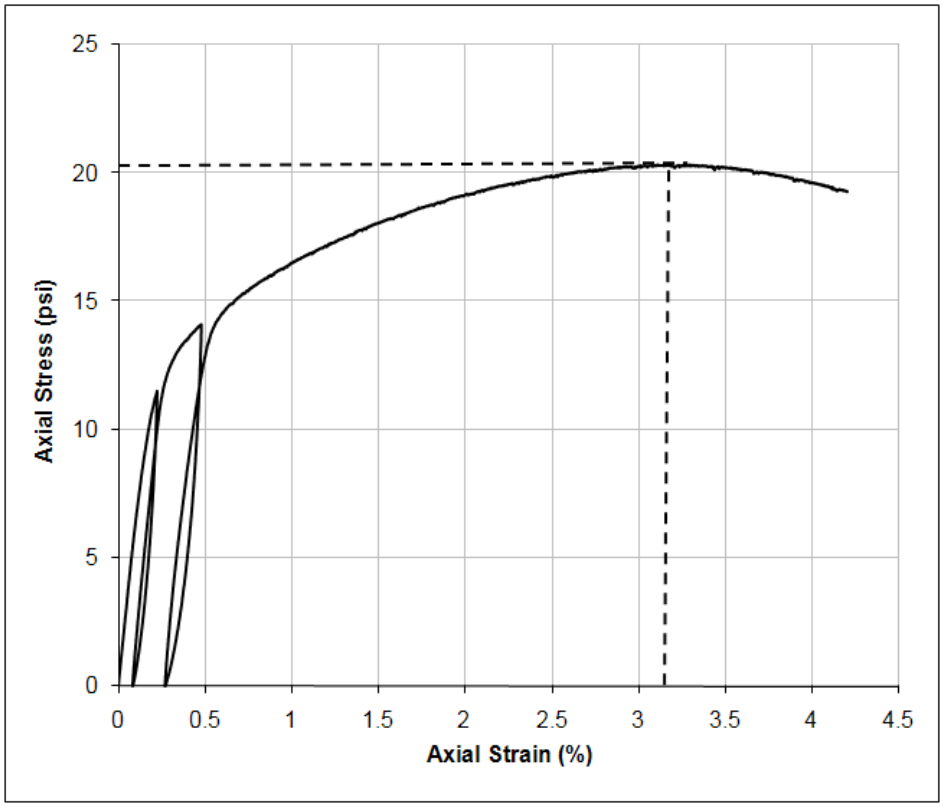

Figure 3-6 Stress-strain Behavior of Subgrade Soil Specimen

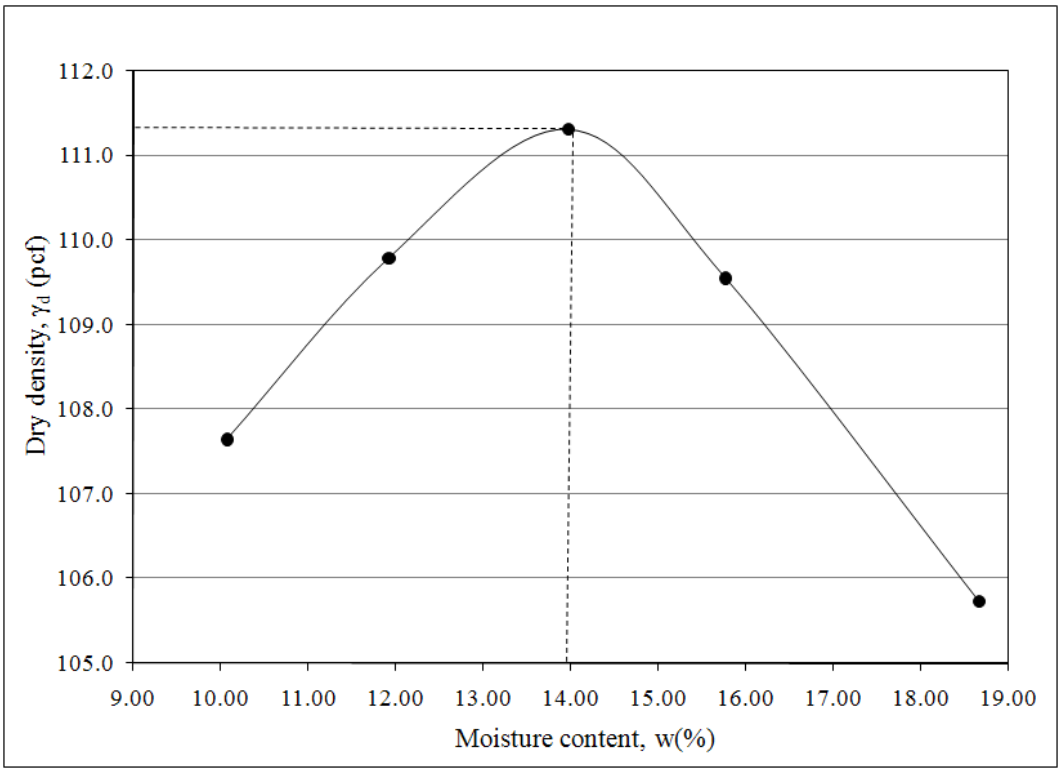

Figure 3-7 Moisture-Density Relationship of Subgrade Soil-CFA Mix

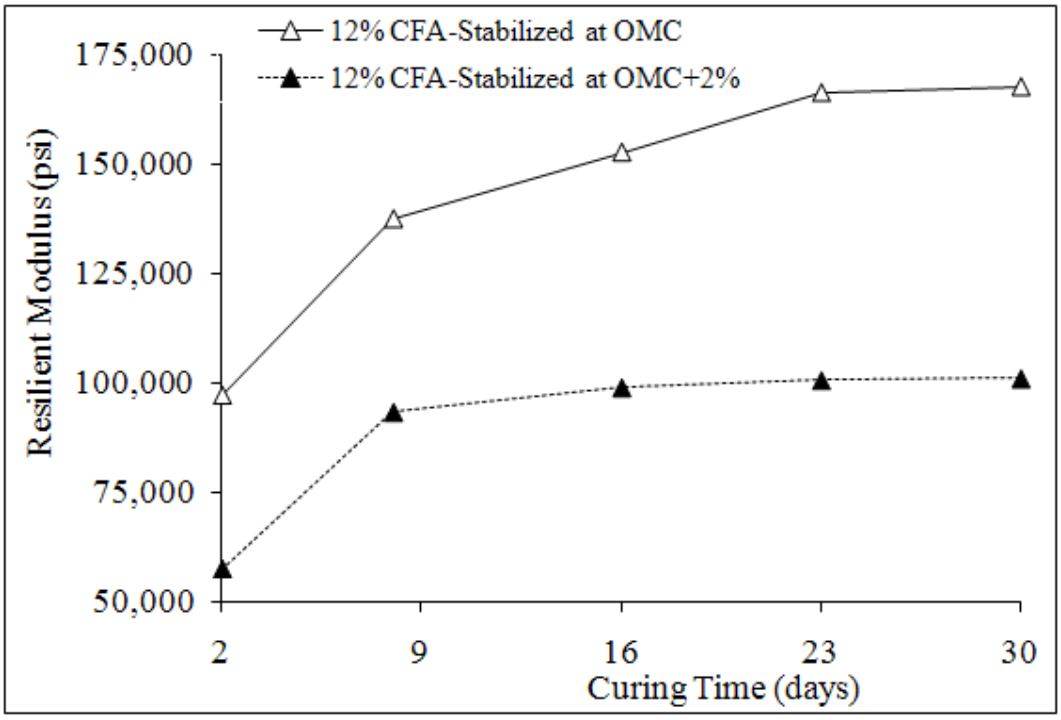

Figure 3-8 Variation of Design Resilient Modulus Values with Curing Time

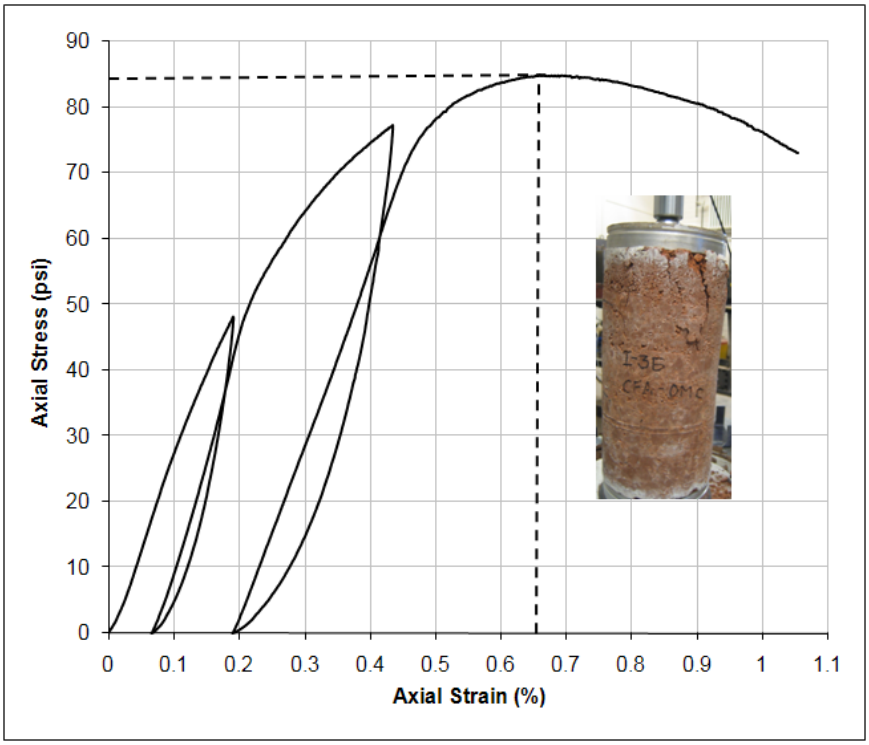

Figure 3-9 Stress-strain Behavior of CFA-Stabilized Subgrade Soil Specimen at OMC

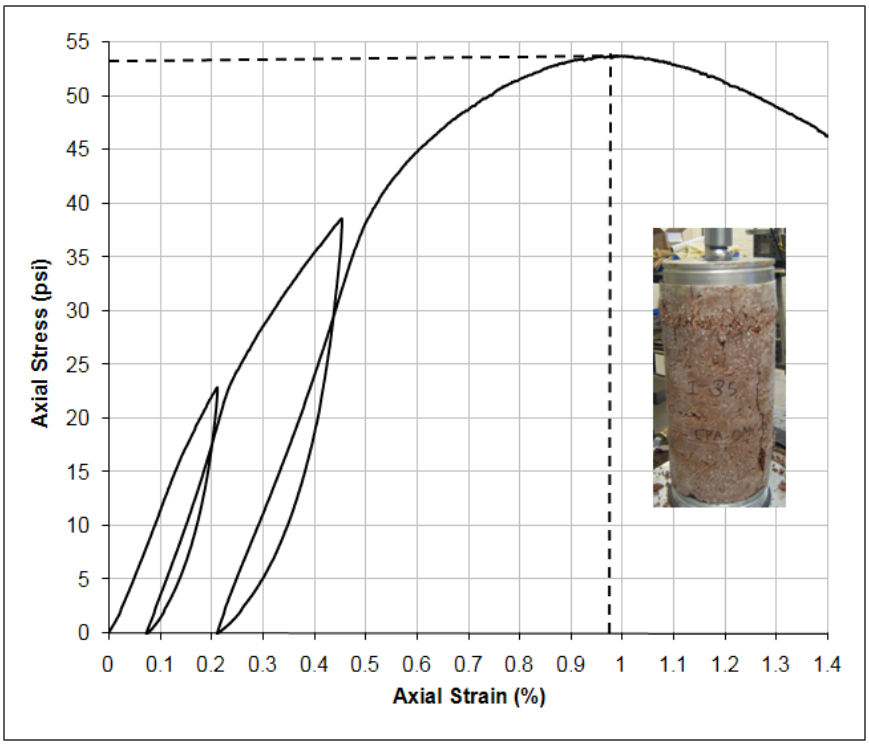

Figure 3-10 Stress-Strain Behavior of CFA-Stabilized Subgrade Soil Specimen at OMC+2%

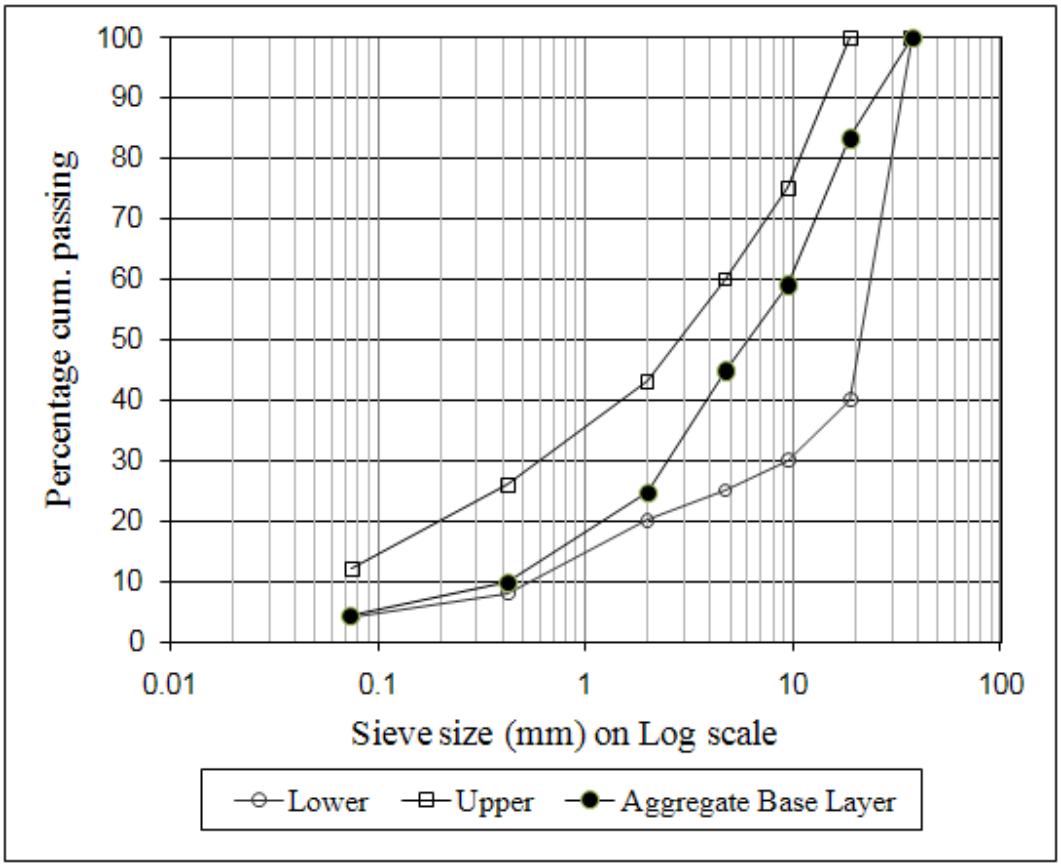

Figure 3-11 Gradation of Aggregate Base Layer

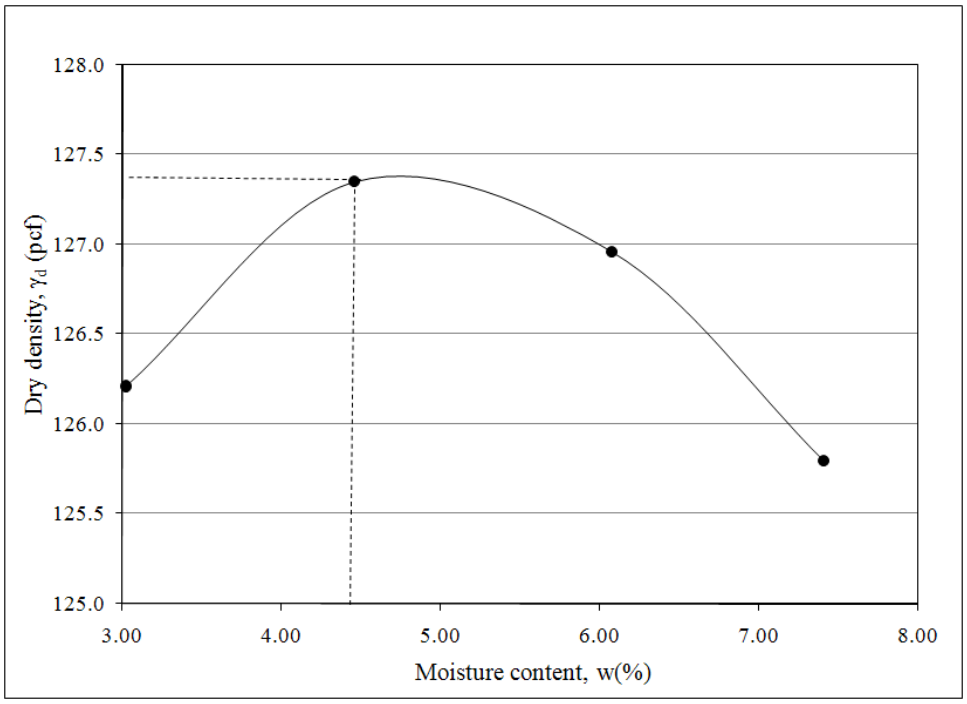

Figure 3-12 Moisture-Density Relationship of Aggregate Base

Figure 3-13 Compacted Resilient Modulus Specimen of Aggregate Base

Figure 3-14 Setup for Resilient Modulus Testing on Aggregate Base Specimen

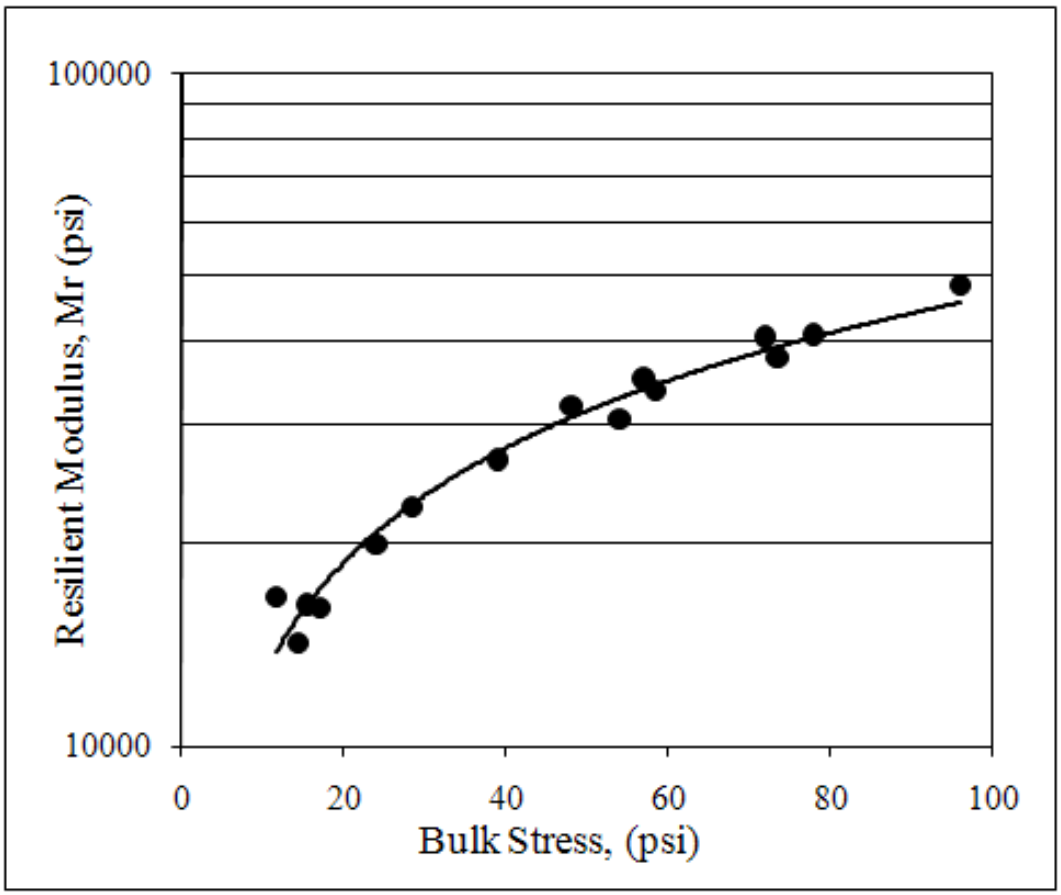

Figure 3-15 M_r Variation with Bulk Stress

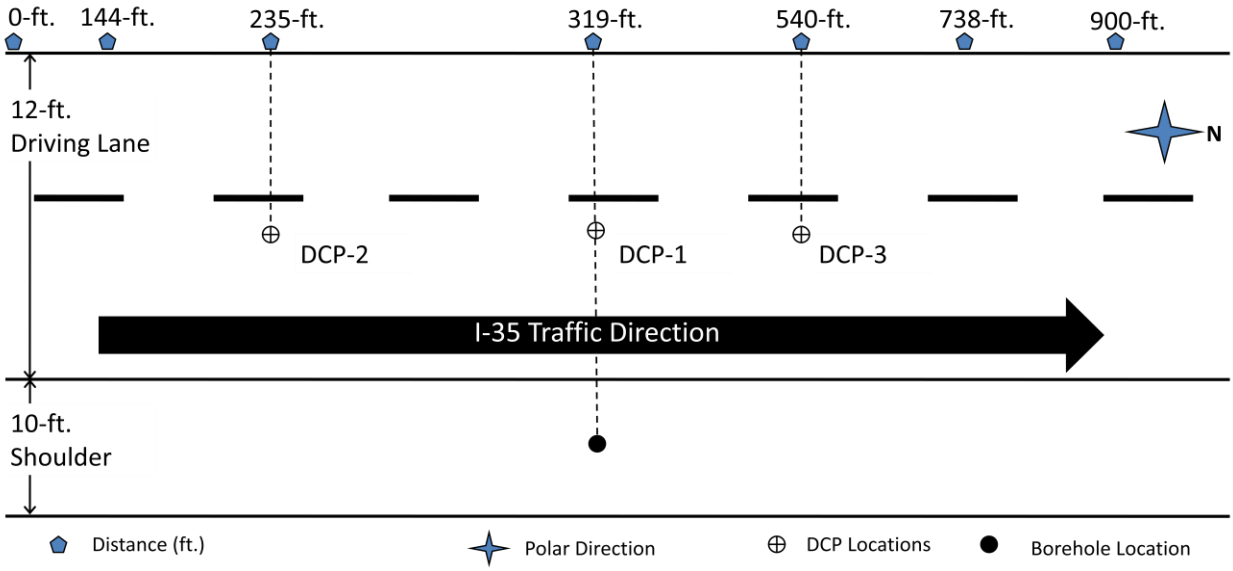

Figure 3-16 Location of Borehole and DCP Tests at Instrumentation Site

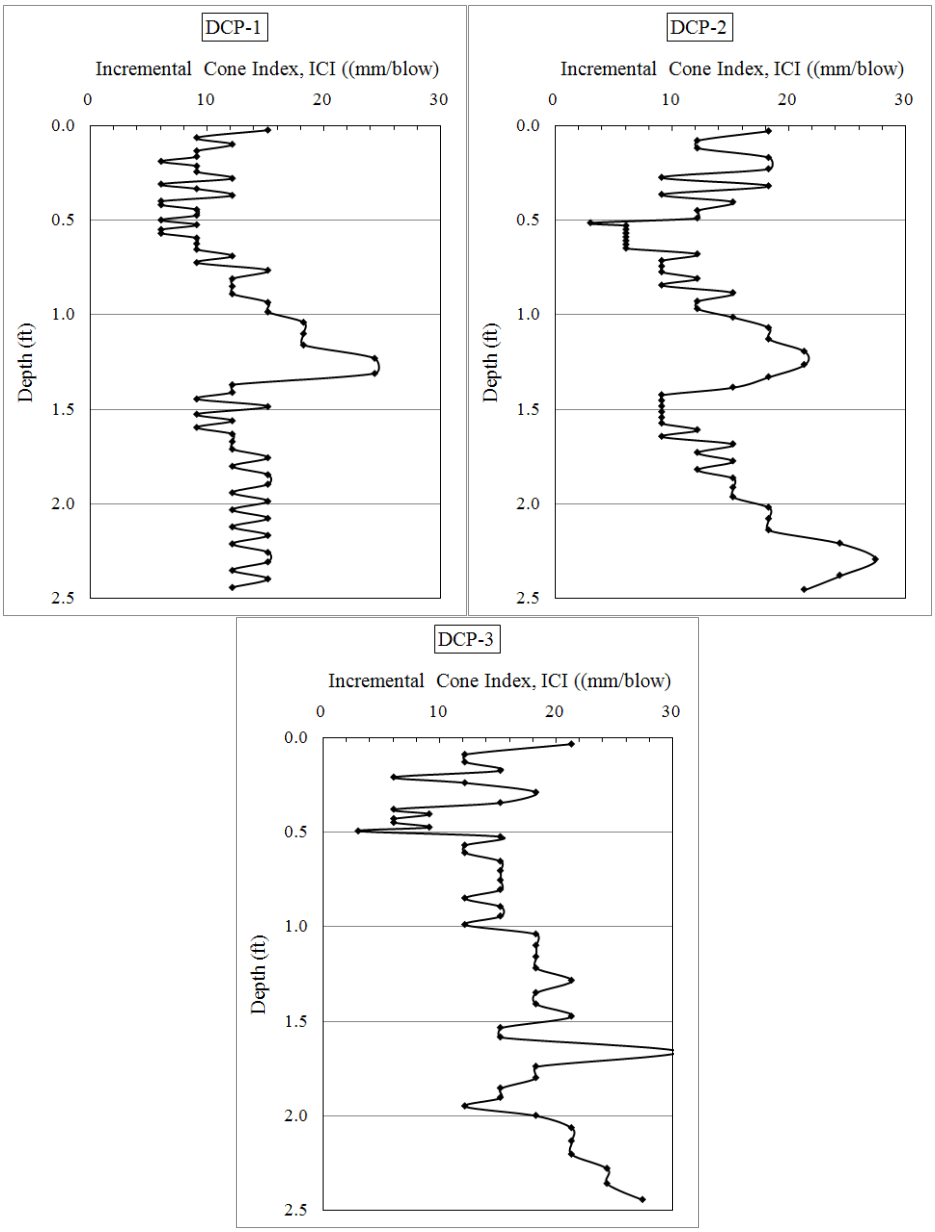

Figure 3-17 Summary of Dynamic Cone Penetrometer (DCP) Test Results

Figure 3-18 CTL Asphalt Strain Gauge

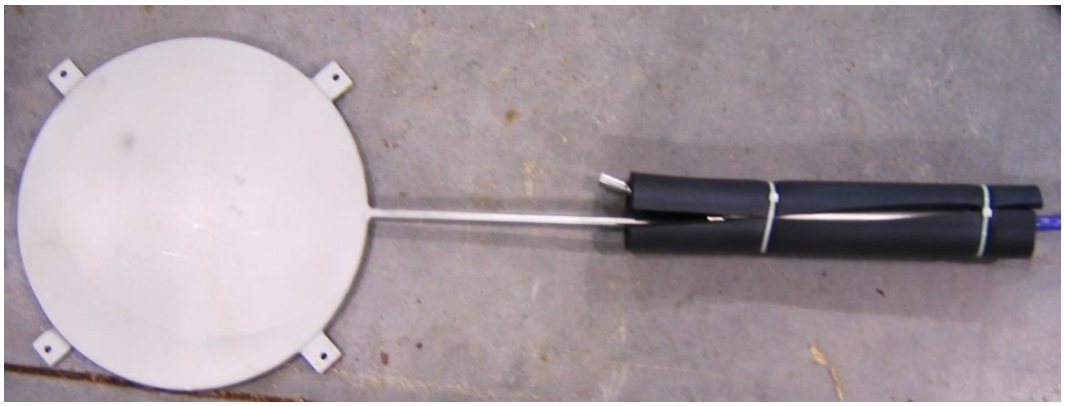

Figure 3-19 Geokon Earth Pressure Cell

Figure 3-20 Thermistor Bundle for Measuring Pavement Temperature

Figure 3-21 ECH2O EC-5 Moisture Probe

Figure 3-22 Photograph of the Weather Station

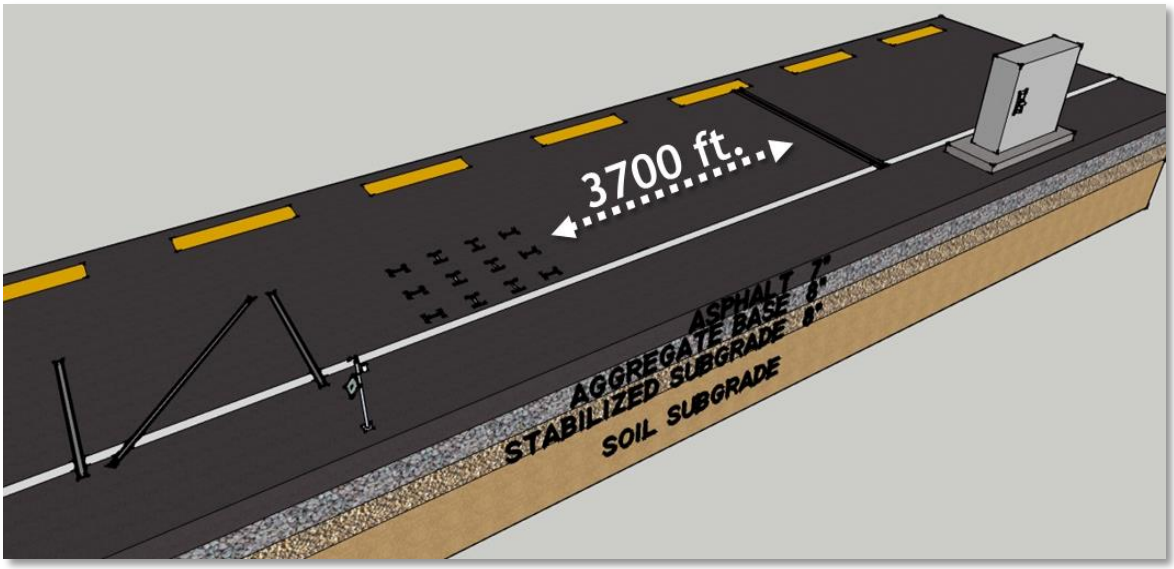

Figure 3-23 WIM Station Location Relative to the Test Section

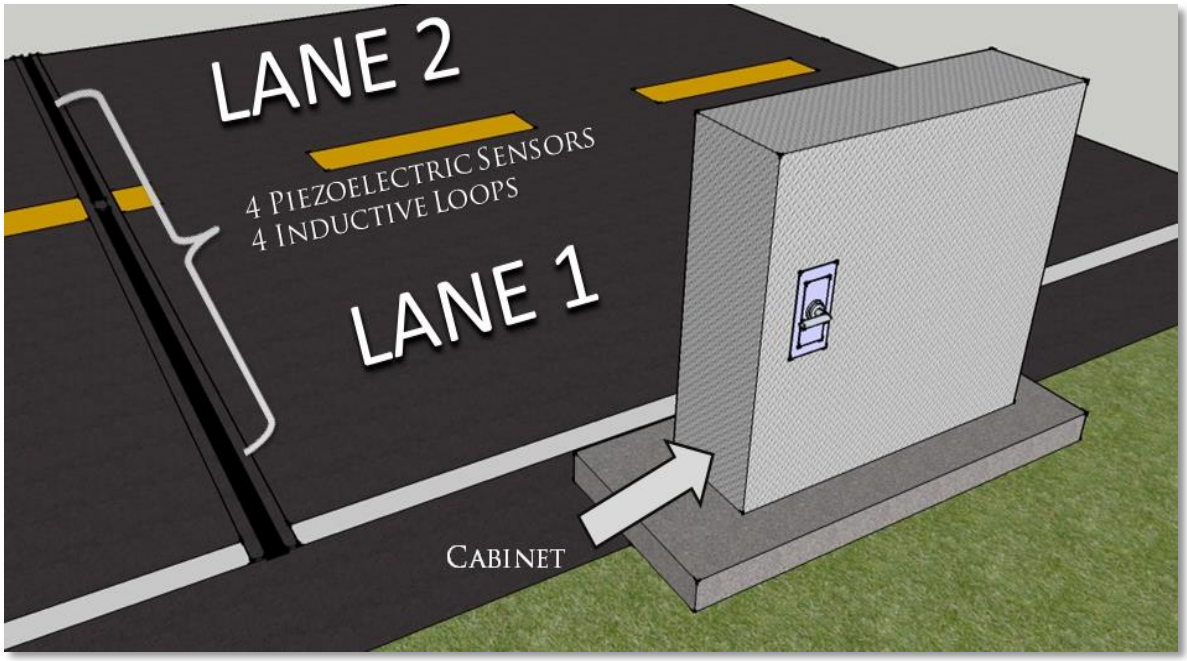

Figure 3-24 WIM Station Sensors

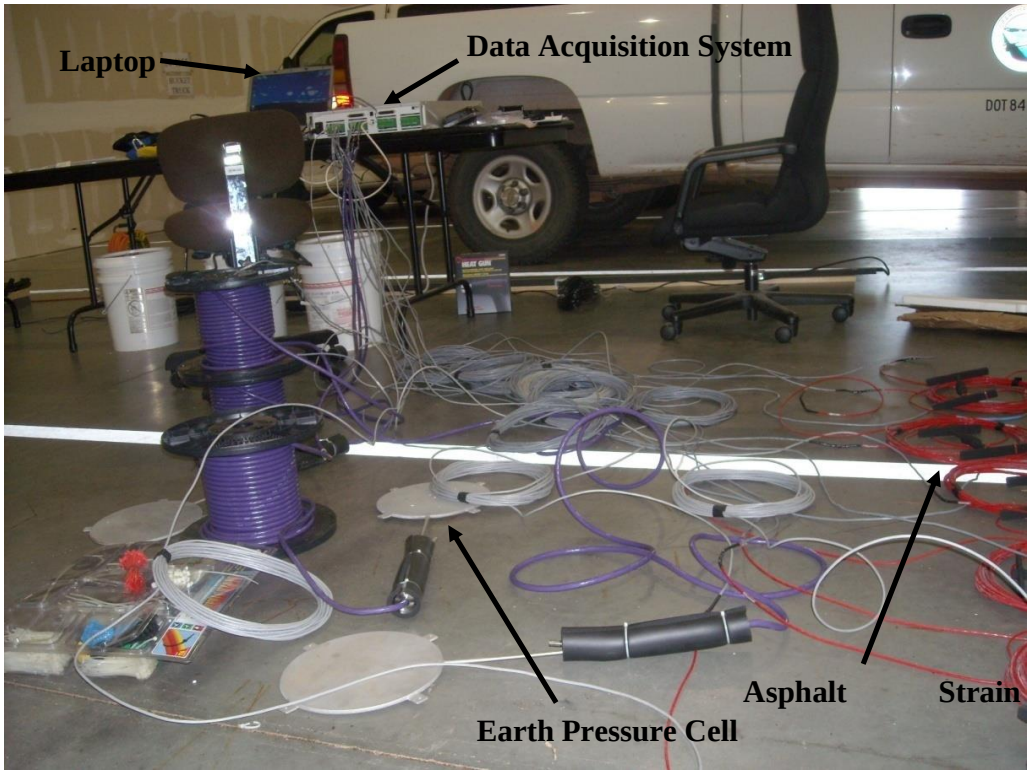

Figure 3-25 Functionality Check of Asphalt Strain Gauges and Earth Pressure Cells

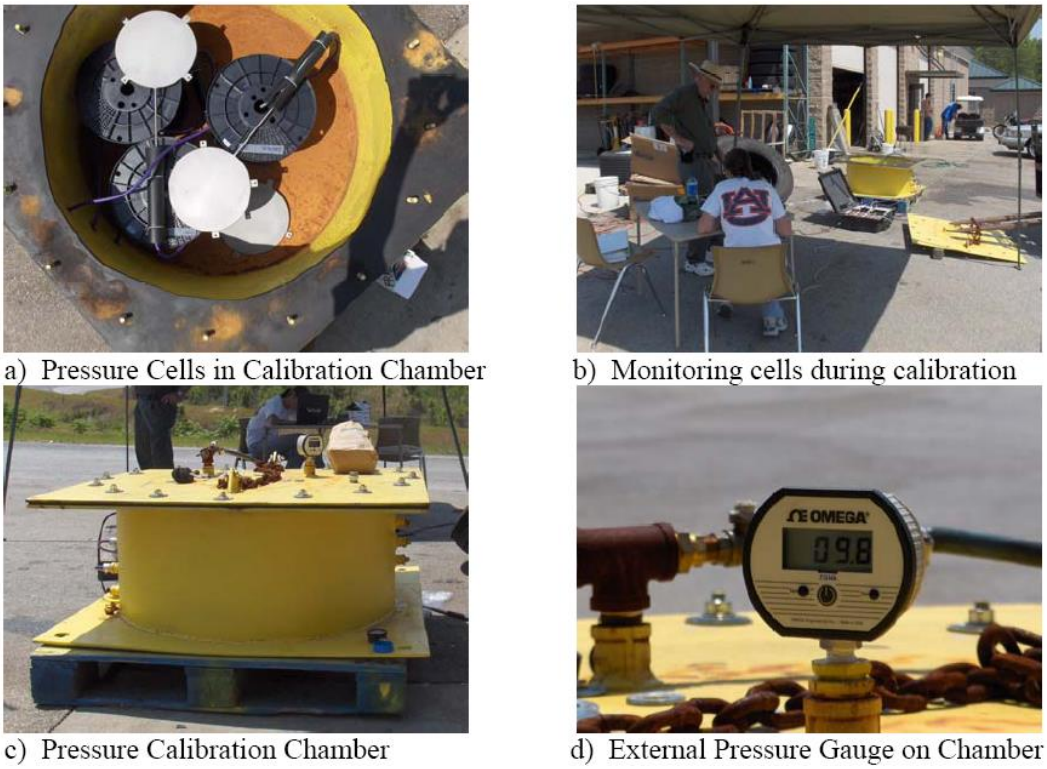

Figure 3-26 Earth Pressure Cell Calibration at NCAT (*Timm, 2007a*)

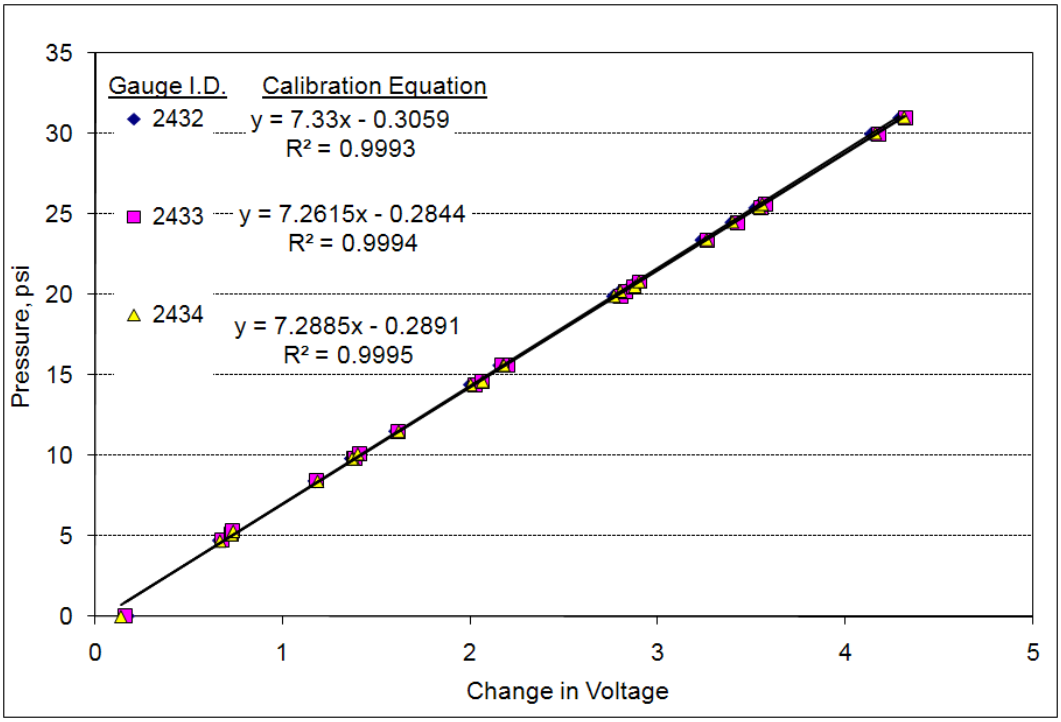

Figure 3-27 Earth Pressure Cell Calibration Data (*Timm, 2007a*)

(a) Soil Sampling and Processing

(b) Prepared Specimens after Compaction

(c) ECH2O EC-5 While Taking Readings

Figure 3-28 Calibration of Moisture Probes

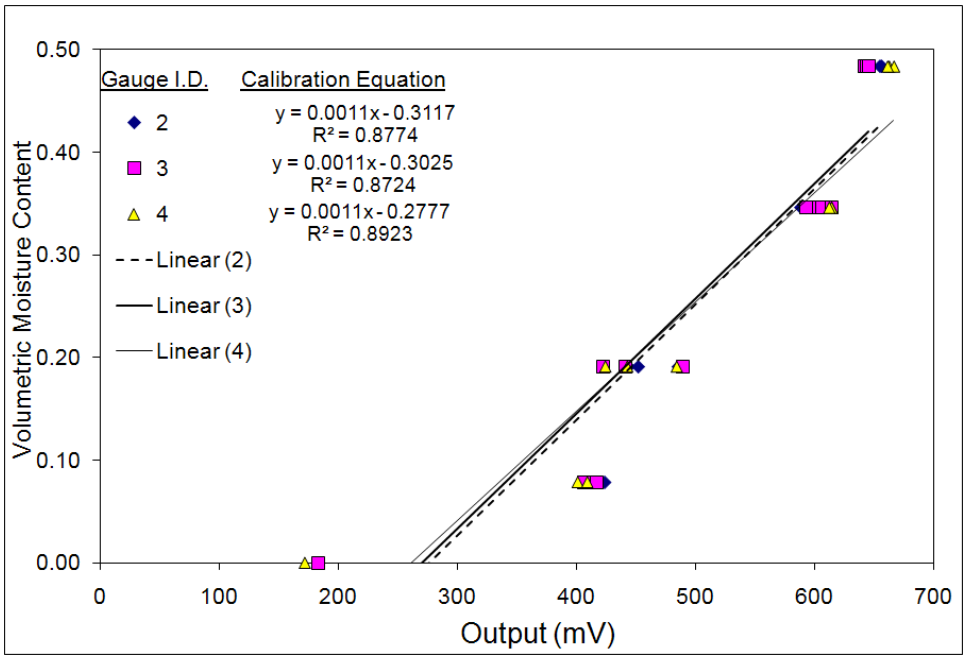

Figure 3-29 Moisture Probe Calibration Data for Subgrade Soil

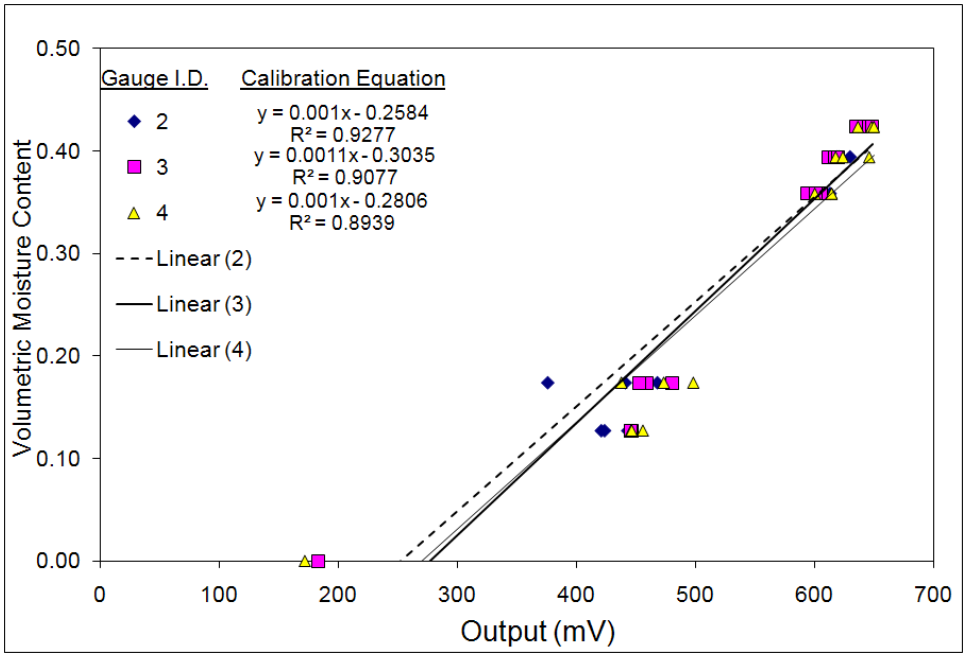

Figure 3-30 Moisture Probe Calibration Data for Stabilized Subgrade Soil

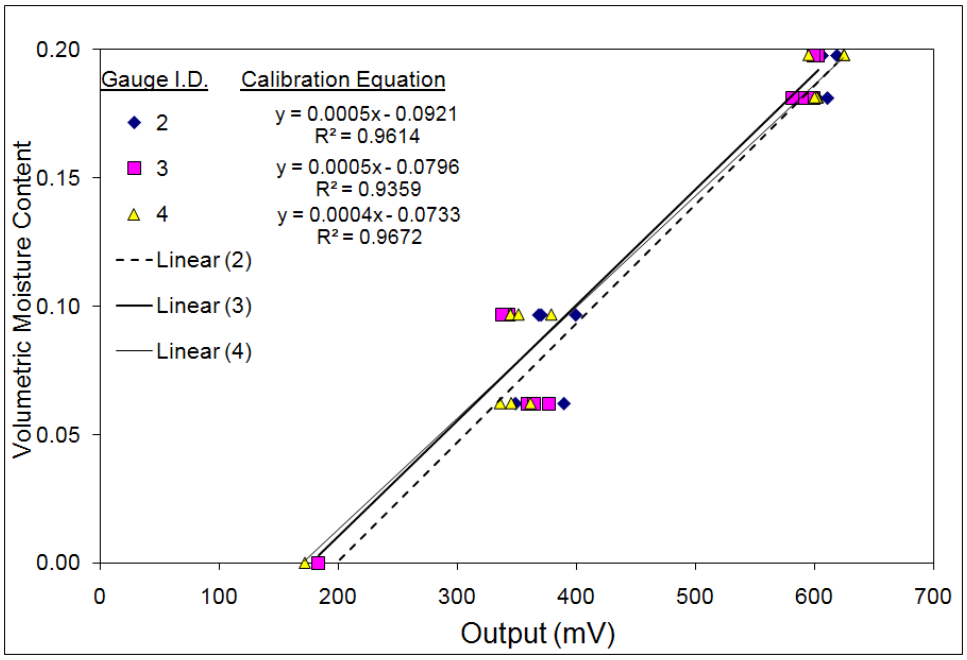

Figure 3-31 Moisture Probe Calibration Data for Aggregate Base

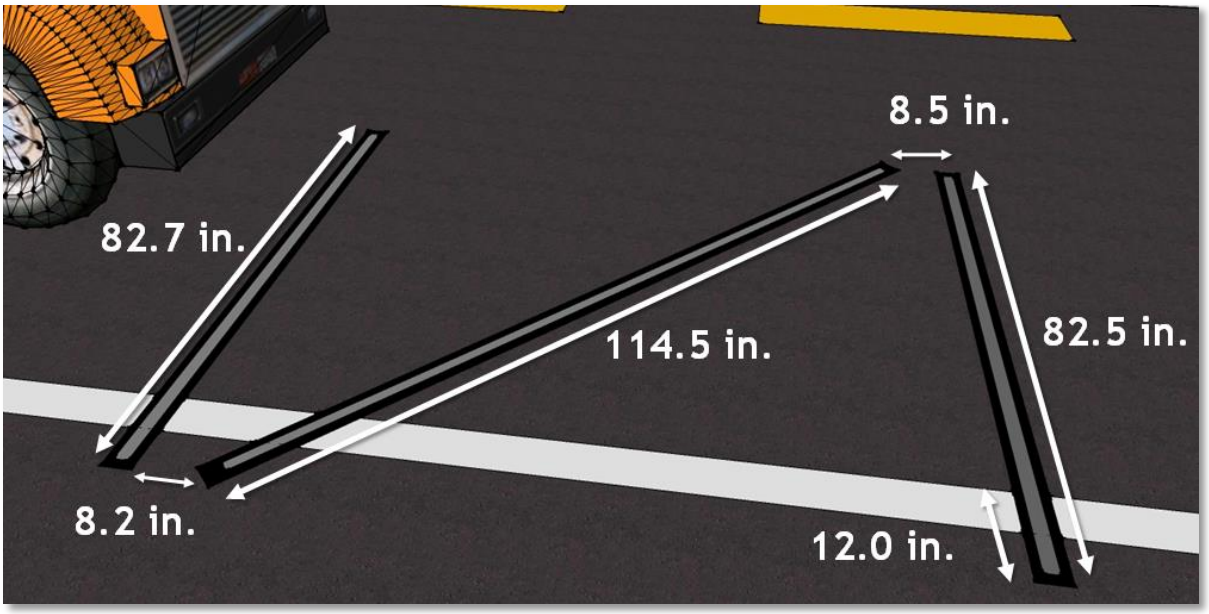

Figure 3-32 Dimensions of the Lateral Positioning System

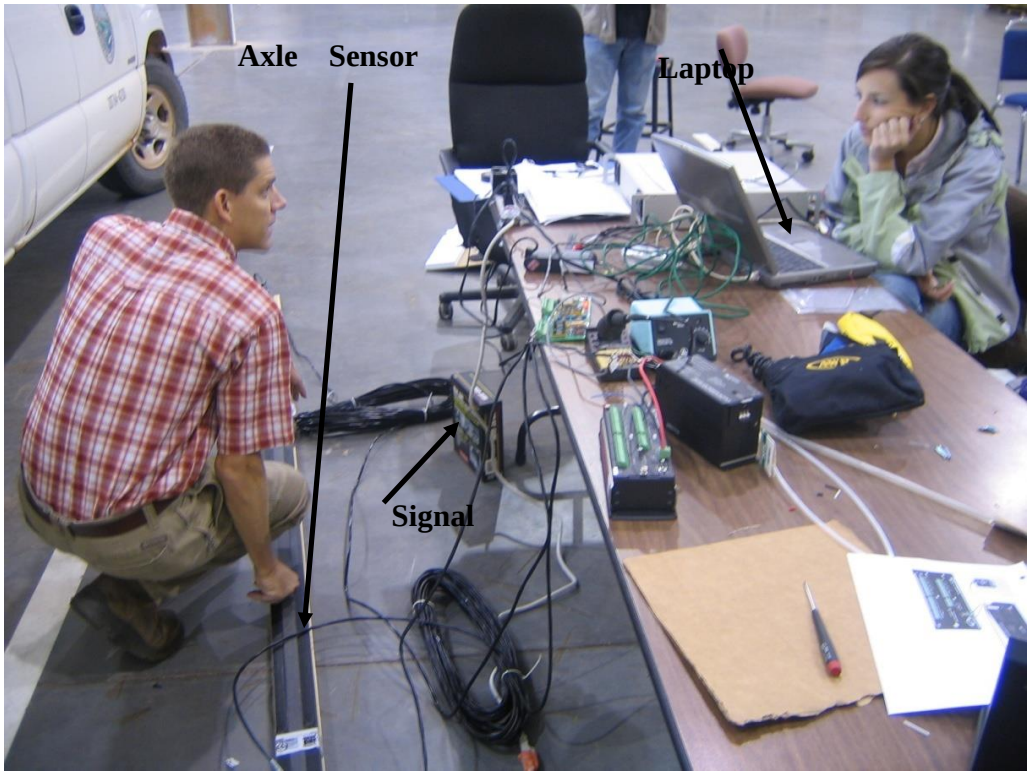

Figure 3-33 Functionality Check of Lateral Positioning Sensors

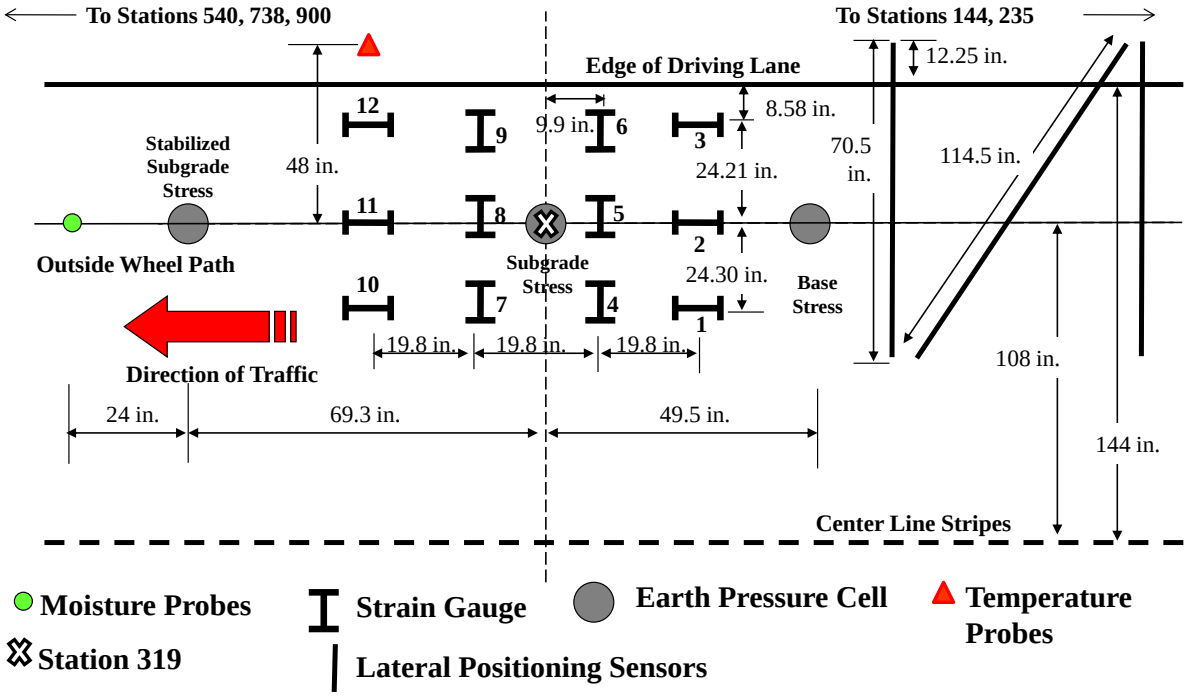

Figure 3-34 Instrumentation layout

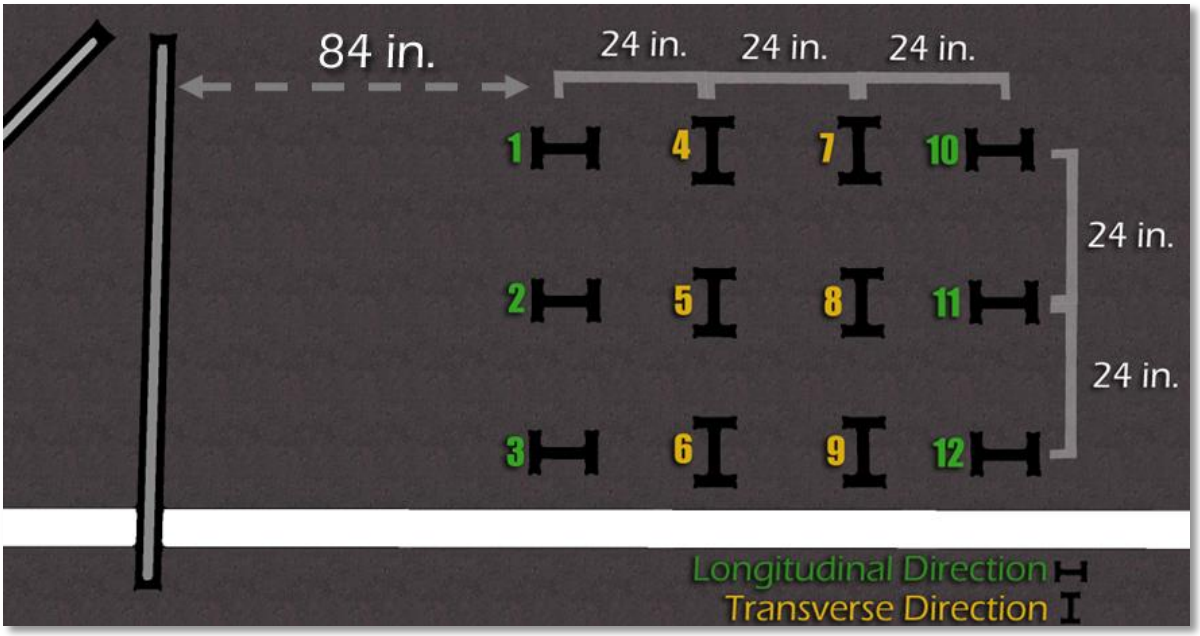

Figure 3-35 Layout of Strain Gauges

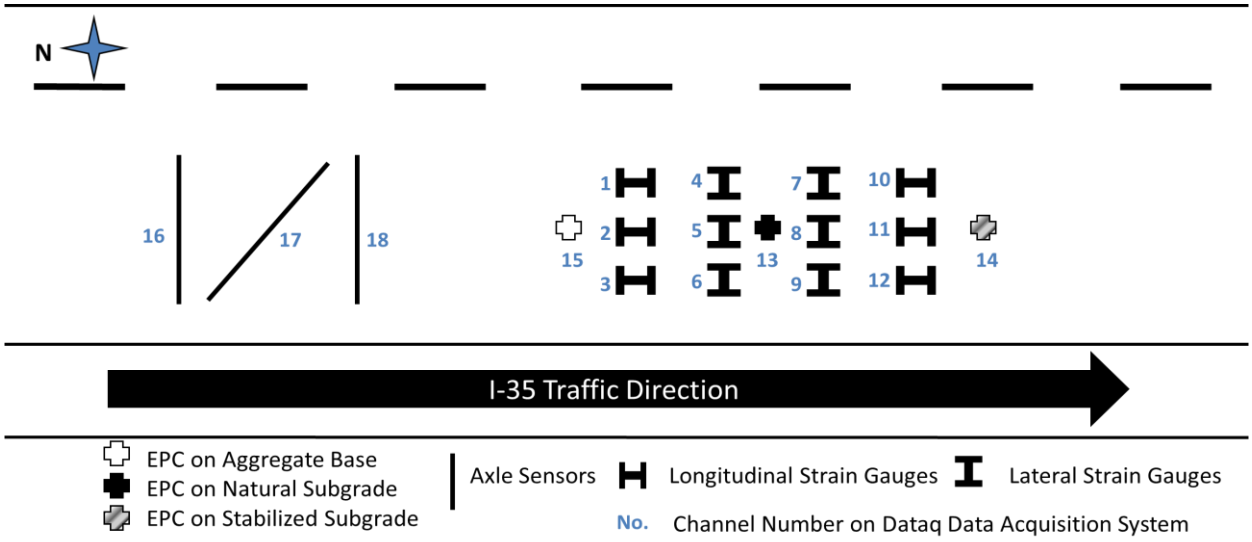

Figure 3-36 Dynamic Data Sensors Layout (Channel Information)

Figure 3-37 Labeling of Gauges

Figure 3-38 Dataq DI 785-32 Dynamic Data Acquisition System

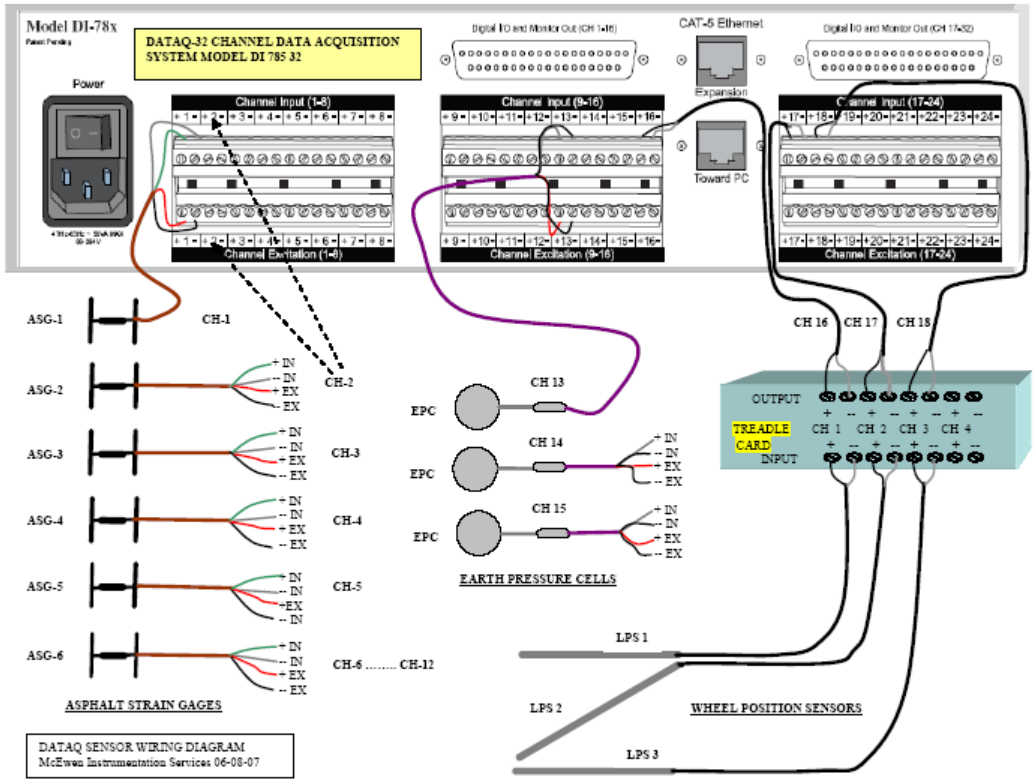

Figure 3-39 Dataq Wiring (*Timm, 2007b*)

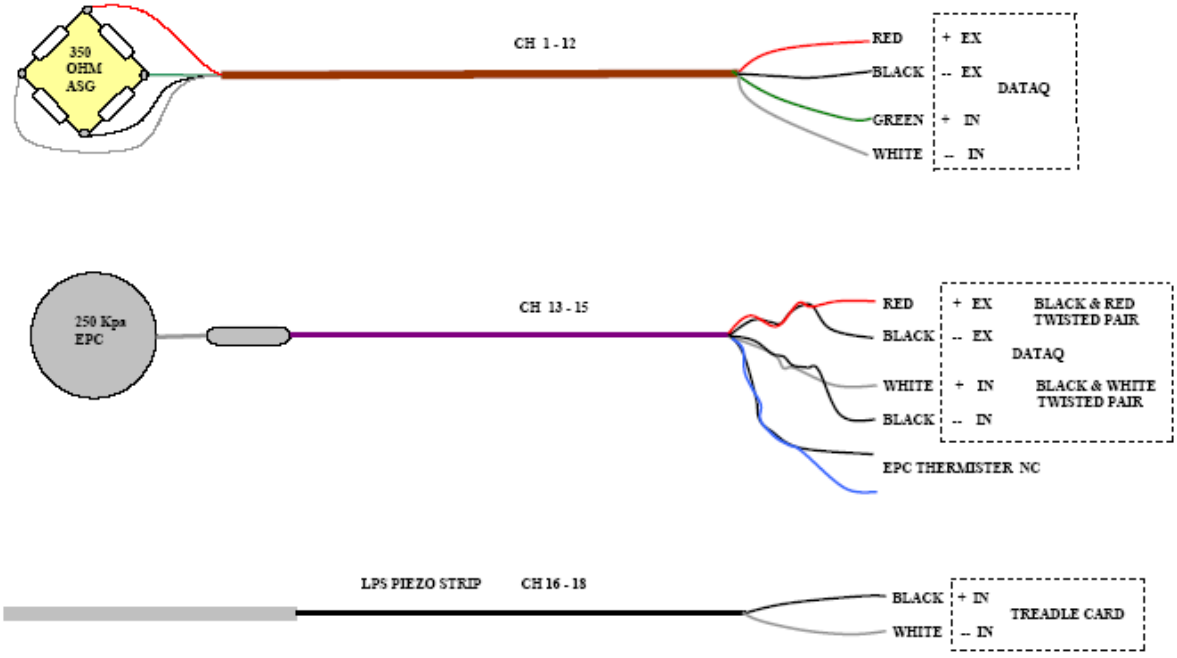

Figure 3-40 Dynamic Sensor Wiring (*Timm, 2007b*)

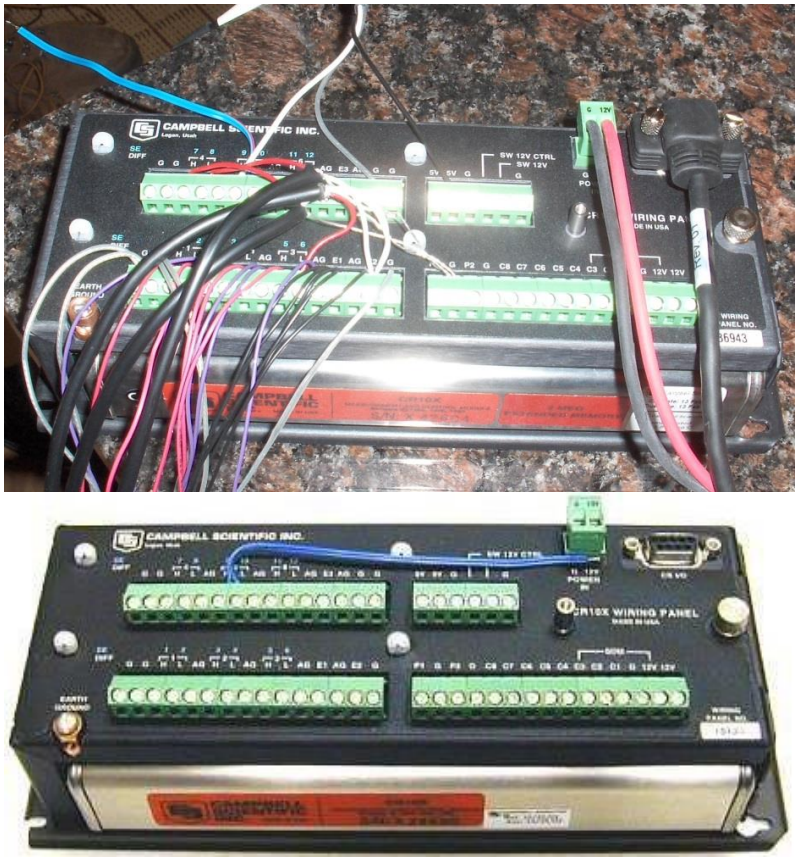

Figure 3-41 Campbell Scientific CR 10-X Environmental Data Acquisition System

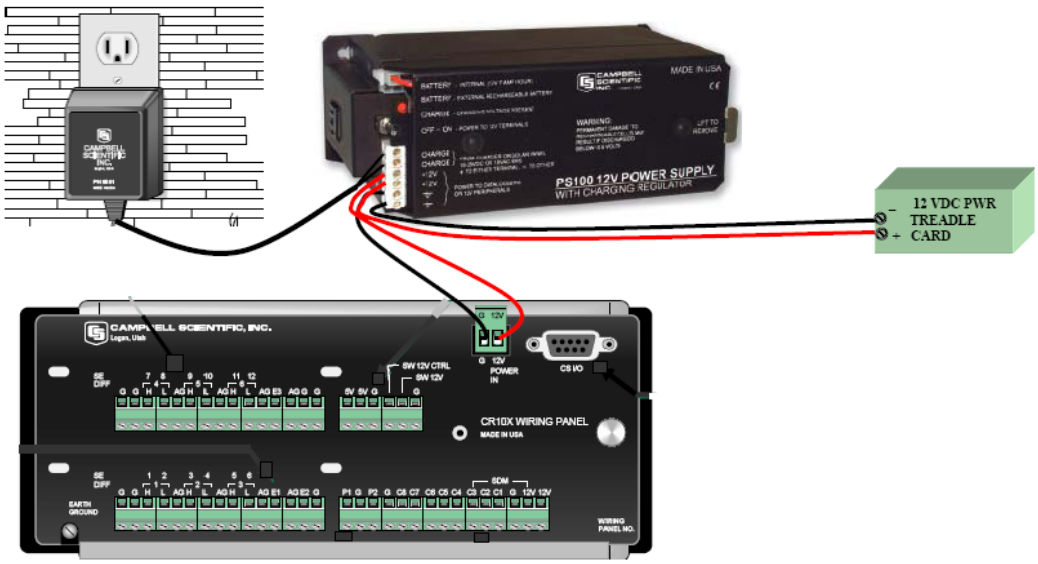

Figure 3-42 CR 10-X Power Supply Diagram (*Timm, 2007b*)

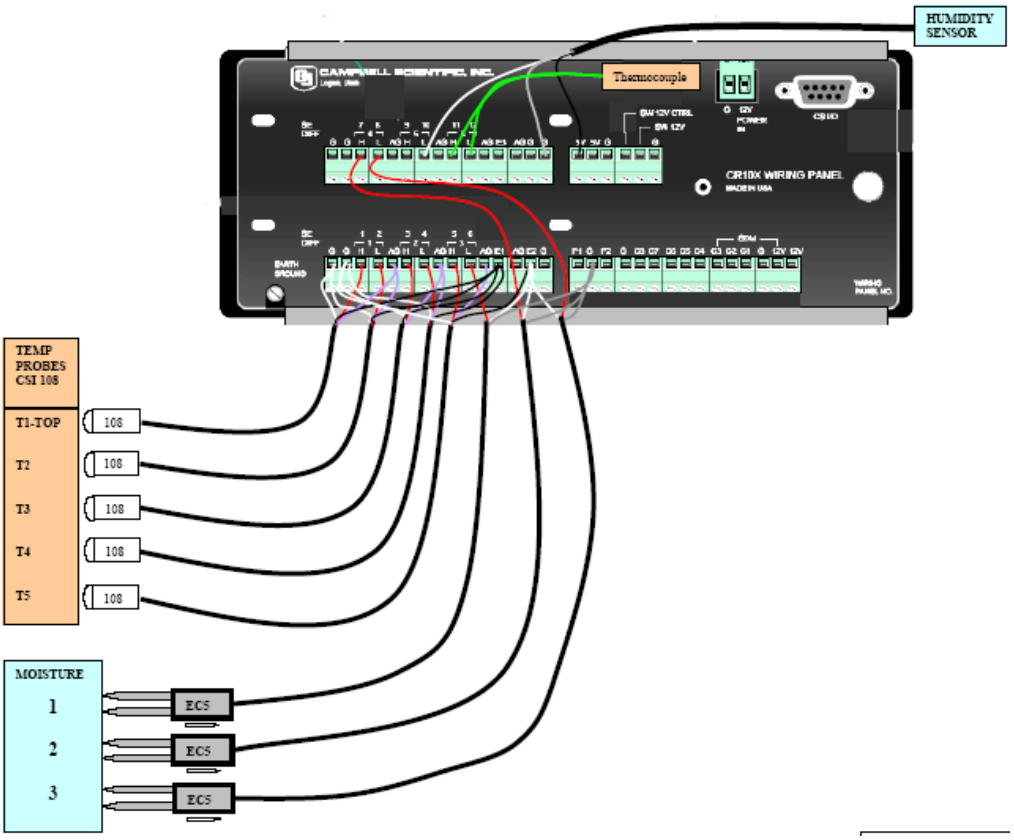

Figure 3-43 CR 10-X Wiring Diagram (*Timm, 2007b*)

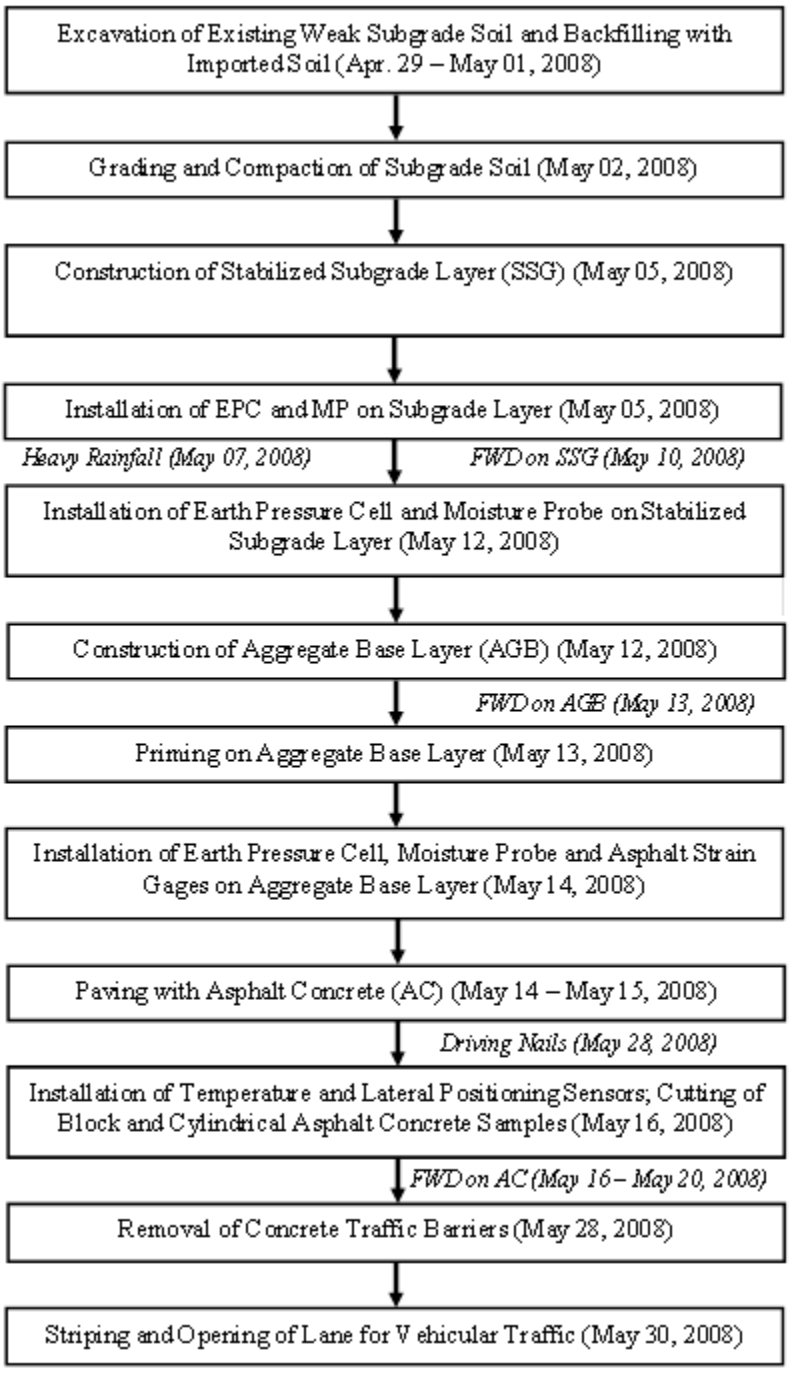

Figure 3-44 Flow Chart of Construction and Instrumentation Process

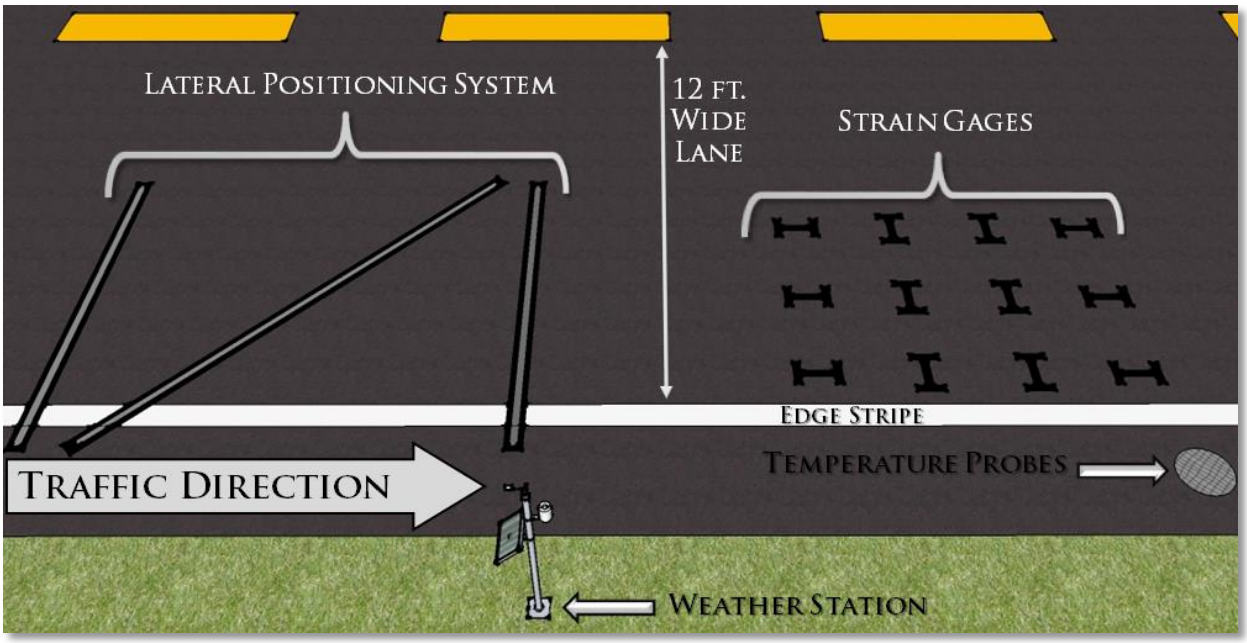

Figure 3-45 Details of Instrumented Section

Figure 3-46 Weak Subgrade Soil Encountered during Milling Process

Figure 3-47 After Excavation of Weak Subgrade Soil

Figure 3-48 Backfilling with Imported Soil

Figure 3-49 Grading of Subgrade Soil

Figure 3-50 Compaction of Subgrade Soil

Figure 3-51 Measuring Moisture Content and Dry Density using a Nuclear Density Gauge

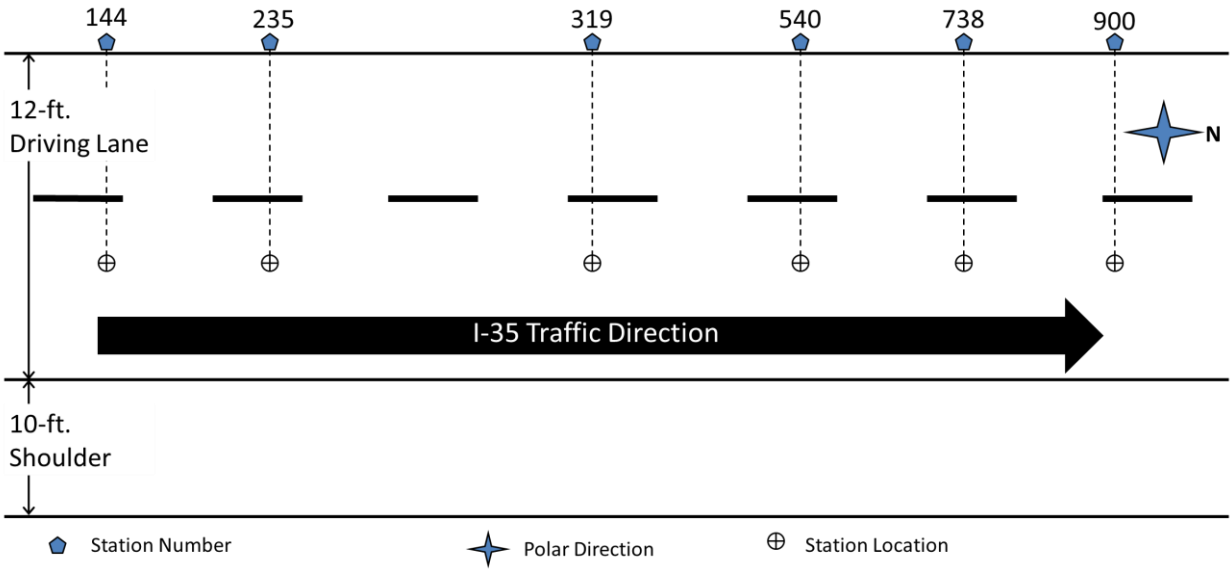

Figure 3-52 Layout of Selected Stations for Moisture Content and Density Measurement During Subgrade Compaction

Figure 3-53 A Motor Grader Spreading CFA

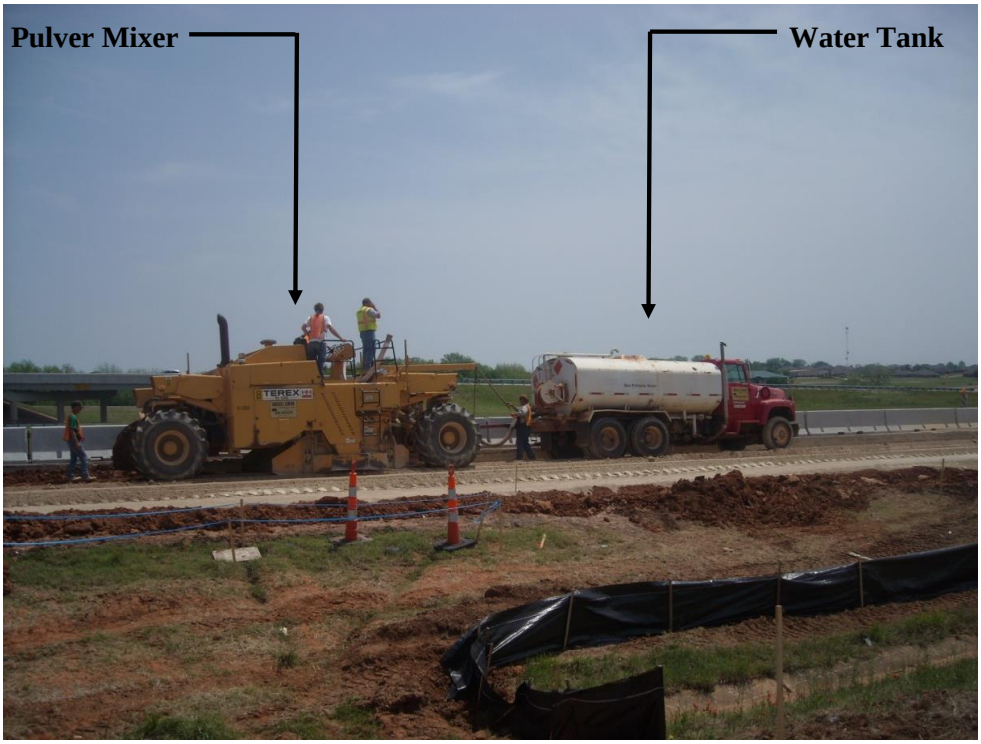

Figure 3-54 Water Tanker and Pulver Mixer Working at the Site

Figure 3-55 Pulver Mixer

(a) (b)

(c) (d)

Figure 3-56 Installation of Earth Pressure Cell on Subgrade

(e) (f)

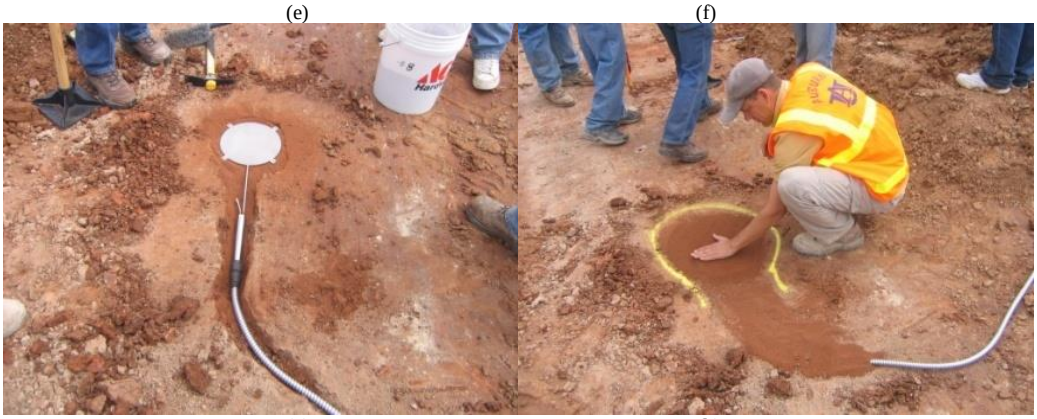

(g) (h)

Figure 3-57 Installation of Earth Pressure Cell on Subgrade (Cont'd)

Figure 3-58 Installation of Moisture Probe on Subgrade

Figure 3-59 Compaction of Stabilized Subgrade Layer

(a) (b)

Figure 3-60 Stabilized Subgrade Layer, Facing South (a), After Heavy Raining (b), After Drying

Figure 3-61 Marking Location of Earth Pressure Cell using GPS

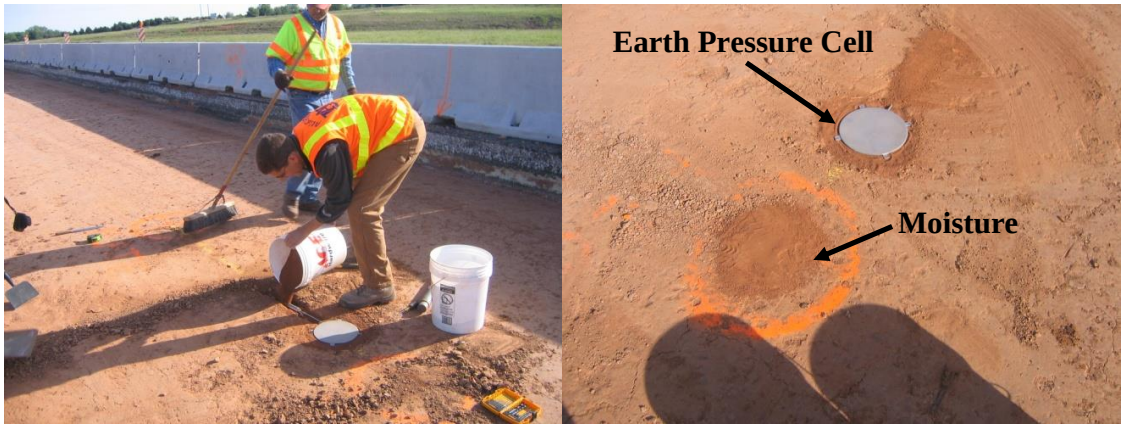

Figure 3-62 Gauges on the Top of Stabilized Subgrade Layer

(a) (b)

(c) (d)

(e) (f)

Figure 3-63 Hand Placement of Aggregate Base Material

(a) (b)

(c) (d)

(e) (f)

Figure 3-64 Construction of Aggregate Base Layer

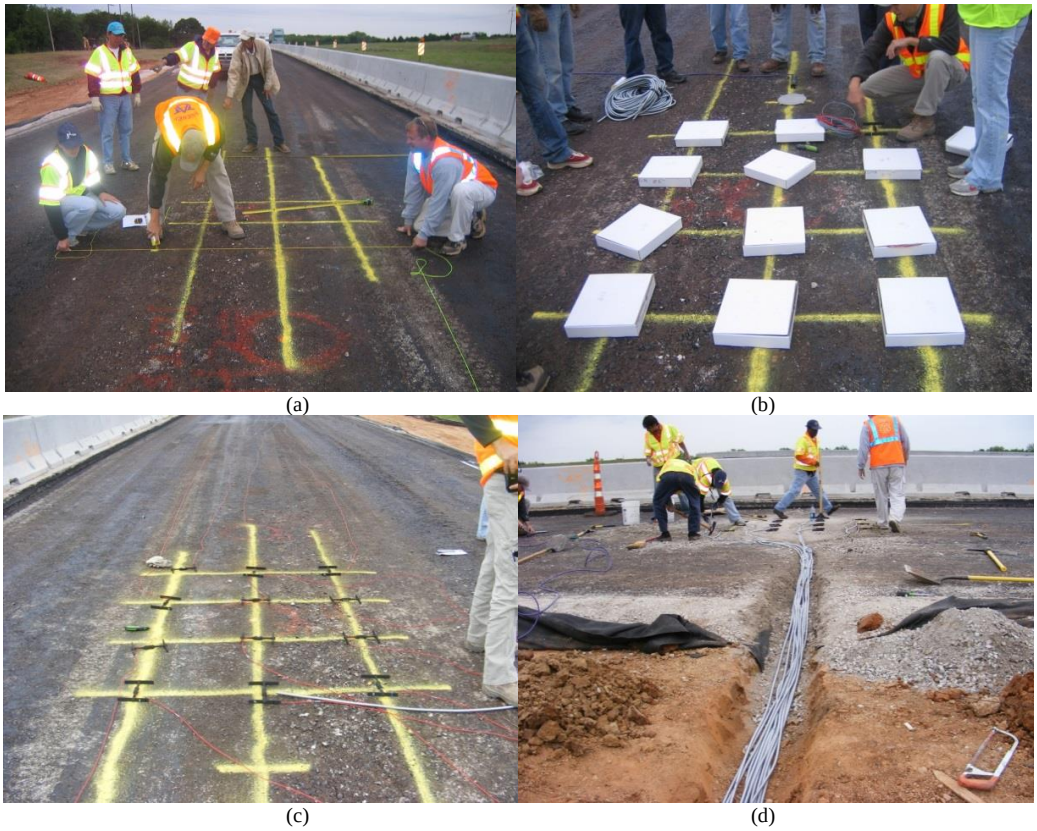

(a) (b)

(c) (d)

Figure 3-65 Installation of Asphalt Strain Gauges

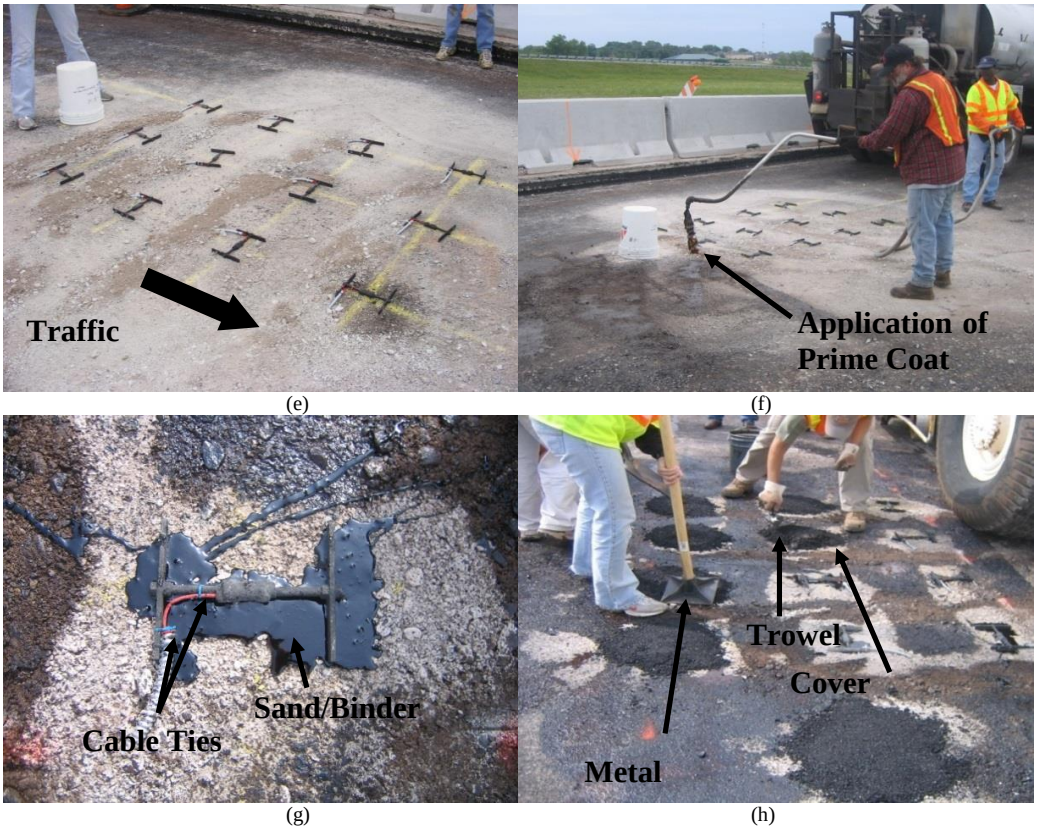

Figure 3-66 Installation of Asphalt Strain Gauges (Cont'd)

Figure 3-67 Installation of Earth Pressure Cell and Moisture Probe

(a) (b)

(c) (d)

(e) (f)

Figure 3-68 Paving

(a) (b)

(c) (d)

(e) (f)

Figure 3-69 Installation of Temperature Sensors

(a) (b)

(c) (d)

Figure 3-70 Installation of Dynax® Axle Sensors

(e) (f)

(g) (h)

Figure 3-71 Installation of Dynax® Axle Sensors (Cont'd)

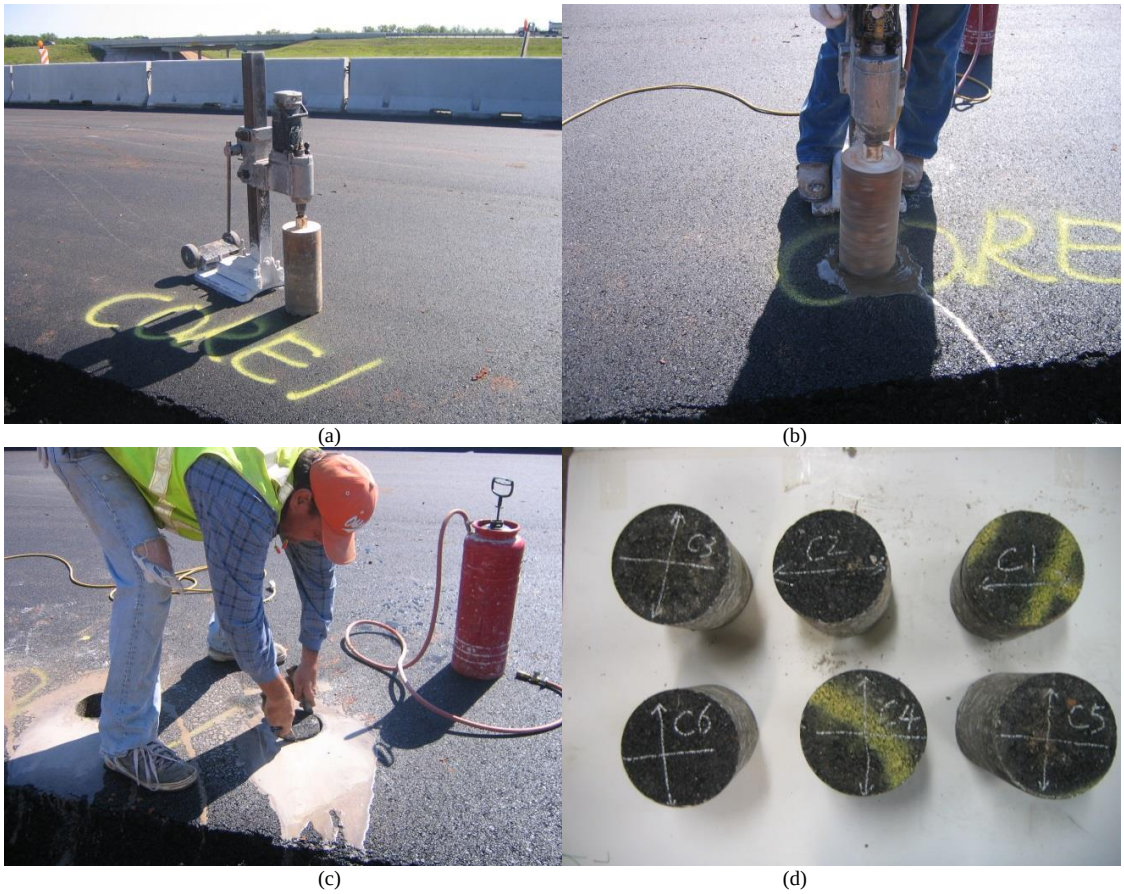

(a) (b)

(c) (d)

Figure 3-72 Extraction of Cores

(a) (b)

(c) (d)

Figure 3-73 Extraction of Block Samples

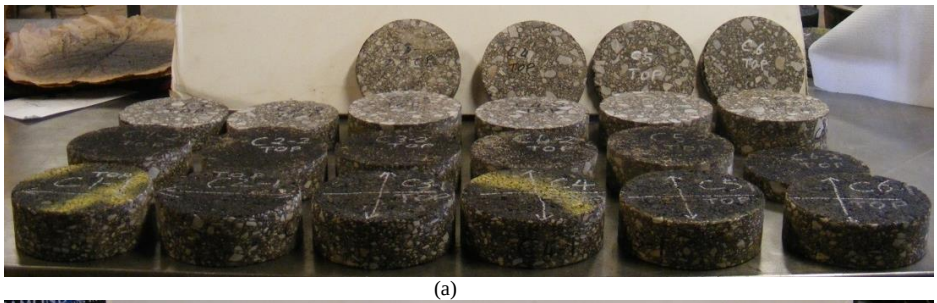

(a)

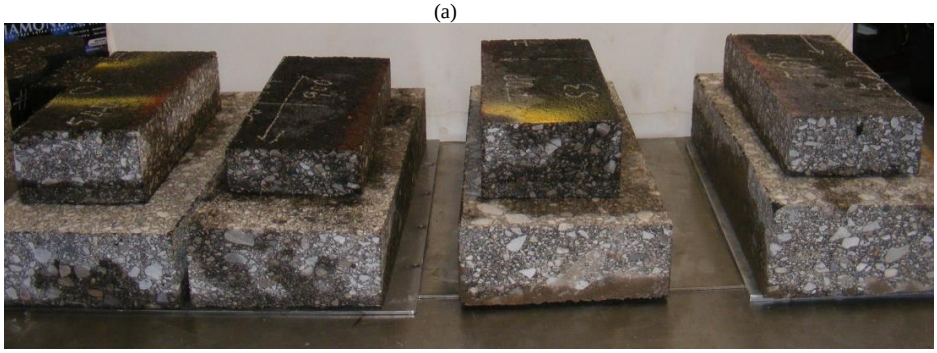

(b)

Figure 3-74 Field Compacted (a) Cores and (b) Blocks After Saw Cutting

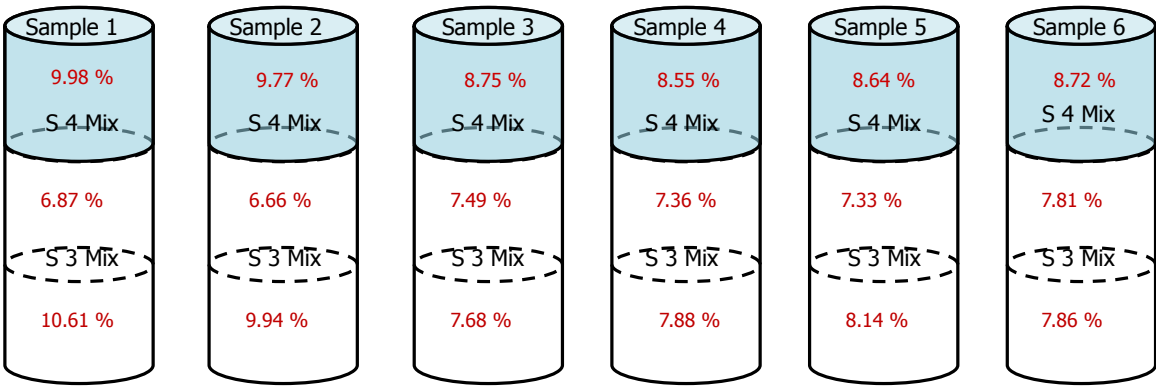

Figure 3-75 Air Void Content of Cores

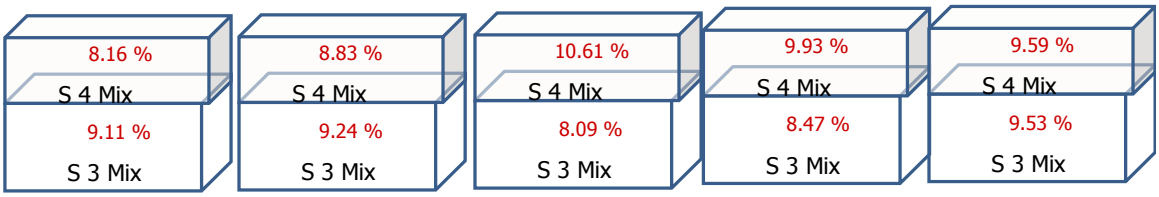

Figure 3-76 Air Void Content of Blocks

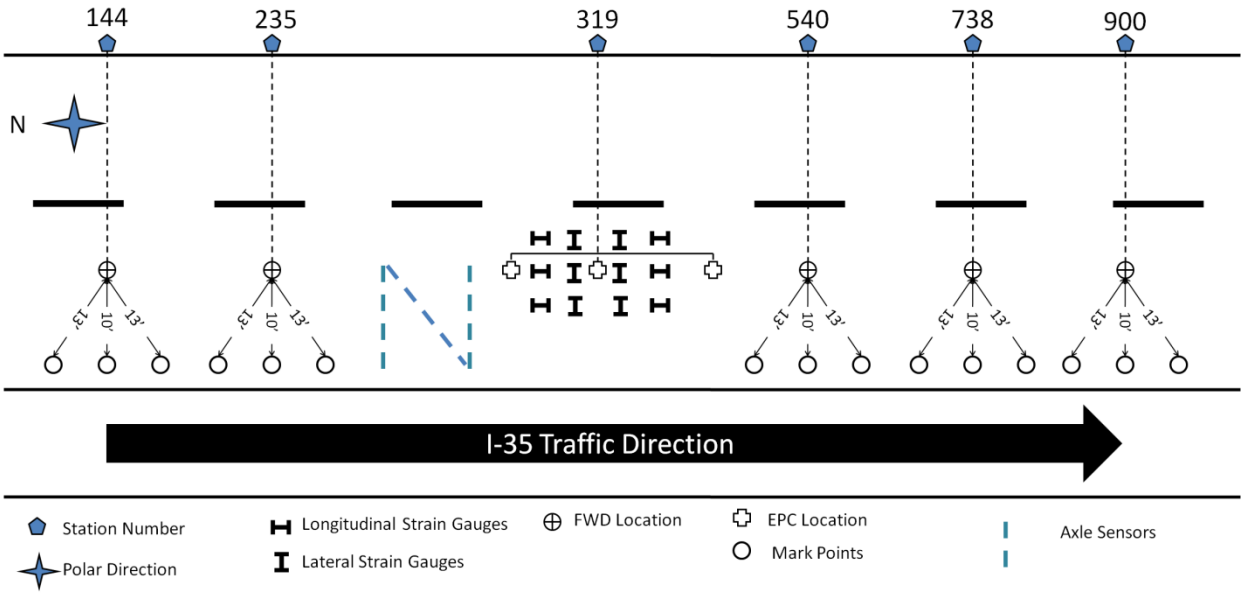

Figure 3-77 Triangulation of Identified Stations

Figure 3-78 Driving Nails on the Identified Stations

Figure 3-79 Removal of Concrete Barriers

Figure 3-80 Mechanical Broom

Figure 3-81 Paint Truck

Figure 3-82 Opening of Lane for Traffic

Chapter 4 FIELD DATA COLLECTION AND PROCESSING

4.1 Introduction

The amount of data that can be retrieved from the instrumented section is large, complex, and diverse. Therefore, a data collection protocol was established on March 19, 2008, in coordination with ODOT, NCAT, and OU. It was decided that four types of data would be collected. Dynamic data are typically collected on a weekly basis, and field performance data are collected every three months. As for environmental and traffic data, they are programmed to record data on a daily basis and thus can be collected at any time. A description of the various data collection efforts made in this project is given in this chapter.

4.2 Dynamic Data

Dynamic pavement response, especially tensile strain at the bottom of the HMA layer, is a significant parameter in developing a fatigue model. Dynamic data includes data collected from the lateral positioning sensors (axle spacing, vehicle speed, and lateral offset), asphalt strain gauges (strains), and earth pressure cells (vertical stress). A data acquisition system DATAQ (Model: DI-785), located in the cabinet near Station 319, was used to collect the dynamic data. Based on the data collection protocol, it was decided to collect dynamic data every day for a week after opening the lane to traffic. Data was then collected weekly for the remainder of this project (i.e., until the pavement shows failure in form of excessive rut (>10 mm) or cracking (>20% of total lane area) or carried 20% of the design ESALs). Consequently, dynamic data was collected bi-weekly for the reporting period. Moreover, data was collected at different times during the day, generally between 9:00 a.m. and 3:00 p.m., to capture a wide spectrum of pavement response at different temperatures. Each data collection

trip typically included data from at least 20 Class-9 trucks passing through the test section. AASHTO classifies trucks with five axles as Class-9 vehicles, where one is a steering axle and four are tandem axles (Figure 4.1a).

4.2.1 Data Collection

The dynamic data collection procedure involved the following. First, the data acquisition system (DATAQ) was turned on and then connected to the laptop computer through an ethernet cable. The data were streamed live on the laptop computer using a data acquisition software, WinDaq (Version: 2.49). Before recording, the reading on strain gauges was checked and tuned, if needed. When a truck was about to drive over the LPS (20-30 feet north of Station 319), the record button was clicked and the pavement response was recorded. After the truck passes, the pause button was clicked until another truck approached. The process of collecting dynamic data of 20 Class-9 passing vehicles took about 5 to 15 minutes, depending on the traffic, volume, and composition. During the data collection process, two video cameras (Model: Sony DHC-HC52), one on top of the road cabinet by Station 319 and the other on top of the WIM station cabinet, were used to record the passing trucks (Figure 4.2). The clocks on both video cameras were synchronized to the second to match the time on the WIM data acquisition system and accurately identify the passing trucks. This method was essential to check if the truck captured on the WIM station had actually passed through the Test Section. Recall that the WIM station was located 3700 ft south of the Test Section. Due to the live traffic at the test section, it was neither practical nor necessary to continuously collect dynamic data.

4.2.2 Data Processing

The method and algorithm used in processing and handling dynamic data were established by the NCAT team. This method, which was automated yet required some engineering judgment and interaction, was based on a graphical engineering software package called DADiSP 2000. The software was developed by DSP Development Corporation and was provided to the OU team by NCAT.

Once the data were collected, the signals were first cleaned to minimize electrical noise by taking a moving average of 20 points. The moving average smoothed the curve (Figure 4.3) without losing the important peaks and valleys (Timm and Priest, 2006). The data were then automatically processed by first establishing and marking the peak and base points in the signal trace of a particular Class-9 truck, marked in black dots and squares presented in Figure 4.4. This step involved human judgment and interaction, because some traces had erroneous peaks or base points which did not need to be marked. Next, the base line was established by linking the two base points using a straight line. Following this, the strain amplitude of each passing axle was determined by calculating the difference between the base line and the peak points. This process took into account both compressive and tensile responses into an overall amplitude. Figure 4.5 represents the strain trace for a typical Class-9 vehicle (one steering axle and four tandem axles) from longitudinal and transverse gauges.

In addition to strain amplitudes, the processing method also generated wheel wander values and velocity of each passing axle using the lateral positioning system (LPS). Finally, for each data collection trip, the generated data were stored in an efficient and streamlined manner using Microsoft Excel.

4.2.3 Strain Orientation

As mentioned previously, a total of twelve strain gauges were installed in the pavement in order to capture the strain at the bottom of the asphalt layer. Six of these gauges were located in the longitudinal direction and the remaining six in the transverse direction (Figure 3.35). When a truck passed over the LPS, the twelve strain gauges captured the pavement response and recorded the strain amplitude of each passing axle.

It is important to examine any relationship between the strain values and the direction (longitudinal or transverse) of the strain gauges. In order to see the relationship between strain values and gauge orientations, the maximum transverse amplitudes values were compared to the maximum longitudinal strain amplitudes for 2387 axle hits. The results of the comparison are presented in Figure 4.6, where the x-axis represents the longitudinal strain values and the y-axis represents the transverse values. An equality line is plotted and presented as a red dashed line. According to the results in Figure 4.6, it can be concluded that the longitudinal strain gauges at this site appear to record about 20 percent higher strain values than the transverse gauges. Similar analysis on other test sections, such as the NCAT Test Track, also found that longitudinal strain values were higher than the ones in the transverse direction (Timm and Priest, 2006). Al-Qadi et al. (2004) also observed that the longitudinal strain was higher than the complementary transverse strain. If the two orientations were considered together, an average would have falsely reduced the strain value. As a result, only the longitudinal strain was considered in the development of the strain-prediction model.

4.2.4 Strain Prediction Model

The I-35 test section was an open-access facility with live traffic. Therefore, truck axle loads are not identical and the strain response values were different for every truck. Another

major factor that affects strain values is temperature. The higher the temperature, the greater the strains for the same axle load. Consequently, development of a strain prediction model was necessary in this study to estimate the strain response of passing axles, while taking into account load and temperature. To account for different loads, dividing the axle strain by its corresponding weight recorded at the WIM station normalized the axle strain values. For temperature effects, the mid-depth pavement temperature values recorded by probe T3 on an hourly basis were used. The strain-temperature correlations were used in the fatigue transfer function and other pavement distress studies.

As noted by Timm and Priest (2006), strain-temperature correlations are usually of the following form:

$$\varepsilon_t = \beta_1 T^{\beta}_2 \qquad (4.1)$$

where

ε_t = Horizontal tensile strain at the bottom of the asphalt layer,

T = Temperature at the middle of the HMA asphalt layer, and

β_1, β_2 = Regression constants.

For a given axle weight, the strain distribution beneath one tire will be different than that beneath two tires. Therefore, two strain-temperature relationships were developed, one for steering axles (one tire) and one for tandem axles (two tires). Both of these correlations use longitudinal strain under the wheels, specifically strain gauges 3 and 12, which represent the maximum strain orientation. The procedure for obtaining longitudinal strain under the wheels from recorded readings is discussed in Appendix A. The strain-temperature correlations for steering and tandem axles are shown in Figures 4.7 and 4.8, respectively. In Figure 4.6, a total of 72 data points (field trips) showing the normalized strain of numerous

single axles, over a wide range of HMA mid-depth temperatures (34 to 110 °F) are presented. It is easily observed that the strain increases with increasing temperature. Similarly, data for tandem axles from the same field trips are presented in Figure 4.8. The data show more scatter for higher temperatures, though the correlations obtained were considered reasonable. The two correlations cover field data collected from May 30, 2008 through May 27, 2011.

For steering axles the strain-temperature correlation is given by:

$$\varepsilon_t = 0.042T^{1.4226} \qquad (R^2 = 0.7985) \qquad (4.2)$$

For tandem axles the corresponding correlation is given by:

$$\varepsilon_t = 0.0379T^{1.42} \qquad (R^2 = 0.5675) \qquad (4.3)$$

4.3 Environmental Data

Another important factor in developing a fatigue model is temperature, namely asphalt temperature. Environmental data include data collected from temperature probes (asphalt temperature), moisture probes (moisture data), and weather station (ambient temperature, ambient humidity, wind speed, wind direction, incoming solar radiation, and rainfall).

4.3.1 Data Acquisition

Unlike dynamic pavement response data, environmental data were sampled continuously throughout the entire project and saved on its own data acquisition systems (Model: CR10X). The data were recorded at one-minute intervals, but only hourly averages (namely maximum, minimum, and mean) were stored. The data were transferred to the project's laptop computer using a USB cable connection during field visits to the test section.

4.3.2 Data Processing

The processing part of environmental data was fairly straightforward. For the temperature probes, software called PC200W (Build 3.3.0.11) was used to access the temperature data. As for the weather station, VisualWeather (Build 2.1.0.31) was used to view and create weather reports. The aforementioned software was developed by Campbell Scientific, Inc.

4.3.3 Temperature Trends

To examine the temperature trends, 27,695 data points representing the hourly average temperature values from May 16th, 2008 through July 10th, 2011, were selected from which the daily average was calculated. This was done for air temperature data obtained from the weather station and for the pavement mid-depth temperature data from the embedded probes.

Figure 4.9 shows the recorded seasonal variation of both the air and the mid-depth temperature. As expected, November, December, January, and February recorded the lowest temperatures (below 40°F), and June, July, and August recorded the highest (above 90°F). This trend is repeatable throughout the entire time period (2008 - 2011). Also, it is evident from Figure 4.9 that the recorded mid-depth temperature values (represented in blue) are always higher than the air temperature values (represented in black), as expected. Figure 4.10 shows a strong correlation between air and mid-depth daily average temperature. This relationship (linear trend line) can be expressed in the following form:

$$y = 1.0103x + 10 \qquad (R^2 = 0.9359) \tag{4.4}$$

where

y = mid-depth daily average temperature, ^{o}F

x = air daily average temperature, ^{o}F.

4.4 Traffic Data

Vehicles traversing a pavement, especially heavy trucks, cause strains within the structure. These strains accumulate over time, resulting in pavement deterioration, such as rutting and fatigue cracking. Therefore, truck traffic data is an essential input to the analysis of pavement (Pagagiannakis and Masad, 2009). In this study, traffic data were comprised of weight/axle, axle count, ESAL, speed, length, gross weight, and classification of each passing vehicle according to the FHWA 13-category scheme. This dataset was used to analyze the traffic spectrum for the test site (see Breidy et al., 2011 for details).

4.4.1 Data Acquisition

As noted earlier, the WIM station located at 3,700-ft. south of the Test Section was used to collect traffic data. The station was installed on June 22, 2007. As mentioned in Section 3.5.7, each traffic lane was instrumented with two inductive loops and two piezoelectric sensors, both having a length of 12-ft. The sensors detect the presence of a vehicle and record the axle count, axle weight, axle spacing, vehicle class, vehicle length, speed, and ESAL. The data were recorded using a 2 MB onboard-automated electronic counter, called ADR 3000 (Figure 4.11), installed in a cabinet on the side of the WIM sensors. Traffic files were generated on a daily basis, and were downloaded weekly on the laptop computer using a dial-up modem connection

This specific location was chosen because the two piezoelectric sensors needed to be embedded in the asphalt pavement on a straight section where no curvatures were present. WIM sensors were calibrated immediately after installation and then were calibrated on an annual basis. The weight calibration, performed by ODOT, was conducted with a vehicle of known weight passing 15 times over each lane and measuring the percent error of the gross

vehicle weight. A piezoelectric WIM system is expected to provide gross weight that is within 15% of the actual vehicle weight for 95% of the vehicles in compliance with ASTM 1318-02.

4.4.2 Data Processing

When a vehicle passes through the WIM site, the inductive loops detect its presence and the piezoelectric sensors record the number of axles and distances between each consecutive pair. Additionally, the piezoelectric sensor records the weight of each axle and computes the gross vehicular weight. The piezoelectric sensor is triggered when a pressure is applied to it and produces an electric charge. By measuring and analyzing the electric charge produced, the sensor can calculate the weight of a passing tire or a group of axles. The daily traffic data are then downloaded on the laptop computer using a dial up Internet connection. For each day, two files are created, each ending with a different extension (.bin and .pvr). However, both files are needed to generate the traffic data.

A user-friendly Windows™ software is available to read the traffic data files recorded by the WIM station. This software used is called Traffic Operations Processing Software (TOPS version 3.7.1), which was provided by PEEK Traffic, through ODOT. The TOPS program opens the appropriate raw WIM files, and allows multi-file processing, previewing, and editing of reports. It is also capable of generating a suite of daily, weekly, and monthly reports (PEEK ADR-3000, 2010).

4.4.3 Wheel Wander

Wheel wander or the lateral distribution of wheel loads is a natural phenomenon observed on public-access roadways (Timm and Priest, 2005). It is defined as the calculated distance between the center of the right wheel of a vehicle's axle and the inside of the edge

stripe of the road. Figure 4.12 is an example illustration of two calculated distances for a steering and a tandem axle of a Class-9 vehicle. A wheel wander histogram is generated by selecting distances for hundreds of passing axles calculated from the LPS. Assuming a constant speed, the axle sensors calculate the distance by first recording the time stamp when the axle hits each of the three (z-shaped) axle sensors, and then by using the geometry (Figure 3.32) to compute the lateral offset from the edge stripe. Wheel wander data were used for the interpretation of strain gauge measurements. Since a wheel positioned directly over a strain gauge will give a higher strain value compared to a wheel positioned to the right or left of the strain gauge, knowing the location of the wheel is important when selecting a representative strain reading.

The wheel wander histogram shown in Figure 4.13 was generated using 3,872 data points corresponding to 3,872 truck axles (steering and tandem) collected from 37 field trips, between May 30th, 2008 and April 14th, 2009. By examining the histogram, it is clear that most axles traveled between the right and the center array of strain gauges, with a mean, μ, distance of 15.5-in. (represented by dashed black line) and a standard deviation, σ, of 10.2-in. The data followed an approximately normal distribution, which is consistent with other wheel wander studies such as the NCAT Test Track study; however, the average value is not consistent. The NCAT Test Track had an average value of 31.8-in. (Timm and Priest, 2006). The difference in the average distance value is primarily due to the characteristic of traffic; the NCAT Test Track is a closed-access facility with controlled traffic, whereas the I-35 Test Section is an open-access facility with actual live traffic. When compared with the default inputs used in the MEPDG software (MEPDG, 2004), the values were fairly close. For the mean wheel distance, the MEPDG software uses a default value of 18.0-in., and for the

standard deviation, a default value of 10.0-in is used. Based on the results shown in Figure 4.13, the strain gauges 3, 6, 9, and 12 are expected to give the maximum strain values since they are closer to the mean wheel distance. These findings justify the use of strain gauges 3 and 12 for constructing the longitudinal strain prediction model.

4.4.4 Traffic Volume, Load and ESAL

In order to develop the fatigue transfer function, the number of cycles to failure and the applied traffic load were needed. The volume of vehicles that passed over the Test Section represents the number of cycles, and the measured axle load of each passing vehicle represents the applied load. Both parameters, volume and load, were captured from the WIM station. Because of the gap (3700 ft.) between the instrumented section and WIM station, some vehicles could have switched lanes over that distance.

The analyses presented here summarize traffic data collected between June 1, 2008 and May 31, 2011 (Year-1: June/08 – May/09; Year-2: June/09 – May/10; Year-3: June/10 – May/11). The data during this three-year period are not entirely continuous; data from some days were lost due to technical problems with the WIM station. Furthermore, data included are only for vehicles with two or more axles (Class 4 through 13). Motorcycles, cars and SUVs (Class 1 through 3) are excluded from the analysis because, first, these types of vehicles are not detectable by the WIM station, and second, their load impacts on the pavement are insignificant when compared to trucks.

Table 4.1 shows the yearly traffic volume that passed on the instrumented section and the difference in volume between the current and the past year. Year-2 had the lowest traffic volume, with a difference of -0.6% from its previous year. It is presumed that this drop in vehicle volume can be linked to the economic recession. Year-3 showed an increase in traffic

volume of about +1.3%. In total, more than 3.5 million vehicles passed through the section during the first three years. This translates into Annual Average Daily Truck Traffic (AADTT) of 3,217 trucks per day.

Table 4.2 represents the yearly traffic load, in kips, that passed through the Test Section. The difference in loads between the current and the past year is also shown. Here, Year-3 recorded the lowest traffic load, with a drop of -4.2% from Year-1, and -1.3% from Year-2. Again, this drop can be linked to the economic recession that started in December 2007. In total, more than 142 million kips have passed over the Test Section.

ESAL is the acronym for equivalent single axle load. It is a concept developed to establish a relationship for comparing the damage effects of axles carrying different loads, with a reference to an 18,000 lb. single axle with dual tires. Table 4.3 shows the yearly traffic in ESAL passing through the Test Section, in addition to the difference between the years. Concerning total ESALs per year, Year 3 recorded the lowest, with a difference of -6.2% from Year-1, and a difference of -3.9% from Year-2. In total, more than 2.2 million ESALs have passed through the section.

It is important to note that stress values recorded from embedded pressure cells were not used because of discrepancy in the results. It is believed that the cells were damaged right after the construction of the Test Section. Consequently, vehicular stress response values used in the study were generated from the WIM station. Furthermore, when producing the fatigue model and calibrating the transfer functions, the two traffic parameters used in the procedure (volume and load) were sorted and arranged on the basis of axles and not vehicles.

4.4.5 Traffic Class Distribution

The class distribution analysis consists of sorting the passing vehicles based on the Federal Highway Administration (FHWA) grouping system, which divides vehicles into 13 classes (Appendix B). The WIM station classifies each passing vehicle based on the time difference between axles. According to the three-year data presented in Table 4.4, Class-9 is the most common commercial truck, typically consisting of five total axles (one steering and four tandem axles) and comprises 59% of the traffic. The second most common truck is Class-5, which consists of 15% of overall traffic. Based on these findings, collecting pavement strain response data for 20 Class-9 vehicles is reasonable and justified.

4.4.6 Traffic Violation

Traffic violations considered in this chapter are related to vehicle speed and load. The allowed speed in the Test Section is 70 MPH and the maximum gross vehicular weight allowed is 80 kips. Trucks that exceed the speed and weight limits are considered as violations. Based on Table 4.5, it was found that vehicles driving on Lane 2 have a higher percentage of violations, 62.2% for speed and 4.3% for weight compared to 30.5% and 2.5%, respectively, for vehicles using Lane 1.

4.5 Pavement Performance Data Collection

A total of four types of pavement performance data, namely rutting, visual crack mapping, International Roughness Index (IRI), and FWD measurements were collected at regular intervals. Based on discussions between ODOT, NCAT, and OU teams, it was decided to collect performance data every three months. Furthermore, DCP and moisture content data along the pavement cross-section were collected as an additional performance

indicator of the Test Section. The process of collecting data requires a high level of collaboration between the OU research team and ODOT, since the instrumented paved section had to be temporarily closed to traffic with the help of ODOT traffic control. Additional details are provided in the subsequent section.

4.5.1 Rut Depths

In the 1000-ft. (305-meter) long Test Section, rut measurements were conducted along the transverse direction of traffic flow at six selected locations, namely Stations 144, 235, 319, 540, 738, and 900. These stations were located at approximately 100-ft. (30.5-meter) intervals (see Figure 3.52). Road straps were laid down on the pavement surface at these stations during the first distress survey on August 21, 2008. The rut measurements were taken along these straps to ensure that the measurement locations did not change with time.

Two significantly different methods were used for measuring ruts. One method used a straight edge/rut gauge combination, while a Face Dipstick® was used in the second method. During the first three distress surveys (on August 21, 2008; December 3, 2008; and January 8, 2009), the straight edge/rut gauge combination method was used. The rut data obtained from the straight edge/rut gauge combination exhibited some inconsistencies for two reasons: (i) because the straight edge was not long enough, it had to be shifted during measurements to cover the entire width of the Test Section, which changed the reference points; and (ii) the rut gauge, having an increment of 0.05-in. (1.27-mm), was not precise enough to measure small changes in rut values. Consequently, a more sophisticated equipment, called Face Dipstick®, was purchased for measuring changes in rut values more accurately. Rut data measured using the Face Dipstick® during the distress survey on May 19 and October 28 of 2009 and February 16 and March 10 of 2010 were more accurate and consistent. On May 19, 2009, the

rut values were measured using both the straight edge/rut gauge combination and the Face Dipstick® so that the measurements could be compared. An overview of the rut data collected using the two aforementioned approaches are given in the following sections.

4.5.1.1 Measurements with Straight Edge/Rut Gauge Combination

According to the ASTM E 1703/E 1703M test method, the preferred lengths of a straight edge are 6-ft (1.8-m), 6.56-ft (2-m), 9.84-ft (3-m), 10-ft (3.05-m), or 12-ft (3.66-m). A 6-ft (1.8-m) long straight edge was used in the first distress survey on August 21, 2008. Because this 6-ft (1.8-m) straight edge needed frequent shifting to cover the entire width of the Test Section, in the following two distress surveys (on December 3, 2008 and January 8, 2009), a longer [10-ft (3.05-m)] straight edge was used. The same rut gauge was used in these surveys. The procedure followed for data collection with the straight edge and the rut gauge is described below:

1. At first, a starting point was selected to measure rut along the transverse direction at each station (Figure 4.14). The inner edge of the edge stripe was taken as the starting point.
2. The straight edge was then placed on the road strap (as shown in Figure 4.15), and the rut values were measured by inserting the rut gauge between the straight edge and the pavement surface at 1-ft (0.3048-m) intervals.
3. The rut values were collected for the entire 12-ft (3.66-m) width of the Test Section at each station.

Data collected with the straight edge/rut gauge combination are presented in Table 4.6. From Table 4.6, it can be observed that there are some inconsistencies in the rut data collected with straight edge/rut gauge combination in some stations. For example, at Station 319, the highest measured rut depth (measured with straight edge/rut gauge) was 0.4-in. (10-mm) on

August 21, 2008. With increased time and cumulative axles passing through the Test Section, the rut values should increase. The highest rut depth measured on December 3, 2008 at the same station was 0.35-in. (8.9-mm) and on January 08, 2009 it was only 0.25-in. (6.35-mm). Both of these values were smaller than the maximum rut depth measured on August 21, 2008. Similarly, at Station 540 and Station 738, the highest rut depth from the straight edge/rut gauge combination was 0.3-in. (7.62-mm) on August 21, 2008. However, on December 3, 2008 and January 8, 2009, the highest measured rut depths at both of these stations were only 0.2-in. (5.08-mm). With increased cumulative traffic traversing the pavement, the rut depth is expected to increase, not decrease. After repeatedly noticing this problem, it was decided to use a more sophisticated equipment to measure subsequent ruts. Hence, the Face Dipstick® was purchased with assistance by ODOT.

4.5.1.2 Rut Measurements with Face Dipstick®

Face Dipstick® is a manually operated device capable of precision profile measurements at rates greater than the traditional straight edge and rut gauge technique (www.dipstick.com). The body of the Dipstick® includes an inclinometer (pendulum), liquid crystal display panels, and a battery for power supply (Figure 4.16). The Dipstick® sensor is mounted in such a way that its axis and line passing through footpad contact points are coplanar (www.dipstick.com). The sensor becomes unbalanced as the Dipstick is pivoted from one leg to the other as it is moved along the line of measurement. Spacing between the two footpads, called "moonfoot spacing," can be varied depending upon needs. Three different moonfoot spacings [3-in. (75-mm), 6-in. (150-mm), and 12-in. (300-mm)] are available in the Face Dipstick®. In this study, 12-in. (300-mm) and 6-in. (150-mm) moonfoot spacings were used for collecting rut data. Before using the Face Dipstick® for actual rut

measurements, exploratory tests were conducted using each of the three moonfoot spacings, and repeatability of results was examined. It was seen that the data collected with 6-in. (150-mm) and 3-in. (75-mm) moonfoot spacings were very close, with a minimum standard deviation of 0.004 and a maximum standard deviation of 0.017. Thus, it was decided to use the 6-in. (150-mm) and 12-in. (300-mm) moonfoot spacings for rut measurements at the Test Section.

At first, data was collected with 6 in. (150 mm) moonfoot spacing at each of the six stations starting from Station 144 and ending at Station 900. Then, the moonfoot spacing was changed to 12 in. (300-mm) and the measurements were repeated, starting from Station 900 and ending at Station 144. The data collection steps with the Face Dipstick® are described below:

1. First, a reference point was marked on the shoulder (Figure 4.17), approximately 12-in. (300-mm) away from the outer edge of edge stripe. The reference point was marked at each of the six stations.
2. The Face Dipstick® was calibrated (i.e., zeroed) with respect to this reference point, following the procedure described in the User's Manual (Face Dipstick® Model 2272 user's manual).
3. After that, the Dipstick® was operated in a pivotal manner along the road strap of each station to collect 13 ft (3.9 m) long transverse profile/rut data (Figure 4.18).

Data collected with Face Dipstick® were analyzed with the RoadFace 6.0 software in the following manner:

1. The elevation of each point where the footpad was in contact with the pavement section, along the transverse direction of traffic flow, was obtained.

2. From the RoadFace 6.0 software, a graphical view of the pavement section was obtained (Figure 4.19).
3. The slope of the pavement section measured by Face Dipstick® was also calculated using the program.
4. Then, maximum pavement rut depths at inner and outer wheel path were obtained from the program for both moonfoot spacings [6-in. (150-mm) and 12-in. (300-mm)].

The analyzed data obtained from the distress surveys, conducted on May 19 and October 28, 2009 and February 16, 2010 were compared with each other. Comparisons of rut depths with moonfoot spacings of 12-in. (300-mm) and 6-in. (150-mm) are presented in Tables 4.7 and 4.8, respectively.

From Table 4.7, it can be seen that the maximum rut depths [with 12-in. (300-mm) moonfoot spacing] on May 19, 2009, October 28, 2009, and February 16, 2010 were 0.451-in. (11.5-mm), 0.471-in. (11.9-mm), and 0.471-in. (11.9-mm), respectively. All of these maximum values were recorded at Station 235. The location of maximum rut was found under the wheel path at 9-ft (3-m) away from the reference point. From Table 4.8, it can be seen that the maximum rut depths [with 6-in. (150-mm) moonfoot spacing] from the data collected on May 19, 2009, October 28, 2009, and February 16, 2010 were 0.395-in. (10-mm), 0.483-in. (12.3-mm) and 0.476-in. (12-mm), respectively. These rut values were measured at Station 738. From Table 4.8, it can also be observed that rut values measured with 6-in. (150-mm) moonfoot spacing at Station 738 are very close to the rut values measured at Station 235. Location of the maximum rut was noted at 2-ft (0.6-m) away from the reference point on May 19, 2009 and 2.5-ft (0.75-m) away from the reference point on October 28, 2009 and February 16, 2010. A close review of Tables 4.7 and 4.8 shows that rut depths increased at all the

stations [both for 12-in. (300-mm) and 6-in. (150-mm) moonfoot spacing] from May 19 to October 28 of 2009. However, if the rut depths are compared from October 28, 2009 to February 16, 2010, it can be observed that rut depths did not increase significantly at all stations. In some stations, the rut depths decreased by a small amount [from 0.001-in. (0.0254-mm) to 0.019-in. (0.5-mm)], whereas in other stations the rut depths increased by a small amount [from 0.001-in. (0.0254-mm) to 0.006-in. (0.152-mm)]. From these observations one could conclude that the rut depths did not change significantly between October 28, 2009 and February 16, 2010. Similar type of rut behavior was observed in the AASHO road test (Finn. et al., 1977) and NCAT test track (Selvaraj, 2007). In those field studies, it was observed that the rut depth exhibits a visible increase during summer and fall months, but not in winter months. Thus, the observations from the present study are in agreement with those from the AASHO road test and the NCAT studies.

4.5.1.3 Comparison of Rut Depths from Face Dipstick and Straight Edge/Rut Gauge Combination

On May 19, 2009, rut depths were measured with both Face Dipstick® and straight edge/rut gauge combination. To be consistent with previous measurements, when using the straight edge/rut gauge combination, the measurement started from the edge stripe (as shown in previously mentioned Figure 4.17). In case of Face Dipstick®, the measurement started from the shoulder, about 16.5-in. (429-mm) away from the edge stripe (as shown in previously mentioned Figure 4.17). To address this difference in starting points, an additional set of data was collected with the Face Dipstick® at Station 540, taking the same starting and ending points for both measurements (Figure 4.20)

A comparison of the rut values is shown in Figures 4.21 through 4.25. Also, a comparison of the maximum rut depths is presented in Table 4.9. Face Dipstick® can measure rut depths with an accuracy of 0.001-in. (0.0254-mm), whereas a rut gauge can measure with an accuracy of 0.05-in. (1.27-mm). From Table 4.9, it is seen that the rut depths measured with the straight edge/rut gauge combination are always lower than the rut depths measured with the Face Dipstick®. Only at Station 738, the inner wheelpath's rut depth measured with the straight edge/rut gauge combination was slightly (0.40%) higher than the rut depth measured with the Face Dipstick®. When taking the same start and end points for both methods, the rut depths measured with the straight edge/rut gauge combination were lower than those obtained from the Face Dipstick® by about 45%.

Once again, from Figures 4.20 through 4.25., it is evident that rut depths measured with the Face Dipstick® are constantly larger than rut depths measured with the straight edge/rut gauge combination. The maximum rut depth measured with Face Dipstick® [moonfoot spacing = 12-in. (300-mm)] and analyzed with the straight edge length of 10-ft (3-m) (an input in the software) in the RoadFace 6.0 software was 0.471-in. (11.9-mm), whereas the maximum rut depth measured with the straight edge/rut gauge combination was only 0.3-in. (7.6-mm). Therefore, one can conclude that Face Dipstick® can capture rut more precisely than straight edge/rut gauge combination.

4.5.1.4 Repeatability of Face Dipstick

To address the repeatability of results from the Face Dipstick®, it was decided to collect data twice at a selected station (Station 144) on May 19, 2009. Specifically, rut data were collected using two different moonfoot spacings [6-in. (150-mm) and 12-in. (300-mm)]. It was observed that the data obtained from the Face Dipstick® were very repeatable. For

example, in the first trial with 12-in. (300-mm) moonfoot spacing, the maximum rut depth was 0.375-in. (9.5-mm) at 10-ft (3-m) away from the starting point (Table 4.10). In the second trial, the maximum rut depth changed only slightly to 0.382-in. (9.7-mm), and the location remained unchanged (Table 4.10). The two profiles obtained from these two trials are presented in Figure 4.26. When using 6-in. (150-mm) moonfoot spacing at the same station, the maximum rut depths obtained from two trials were 0.382-in. (9.7-mm) and 0.390-in. (9.9-mm). As in the previous case, the location [9.5-ft (2.89-m) away from the starting point] remained unchanged (Table 4.11). The two profiles obtained from these trials are presented in Figure 4.27. From Figure 4.27, it is observed that rut depth values measured either with 6-in. (150-mm) spacing or 12-in. (300-mm) spacing were very close.

A comparison of rut depths measured with moonfoot spacing 6-in. (150-mm) and 12-in. (300-mm) of Face Dipstick® is presented in Table 4.12. From Table 4.12, it can be observed that percentage differences between 6-in. (150-mm) and 12-in. (300-mm) moonfoot spacings were in the range of 0% to 9.51%. For all the stations, pavement profiles (without slope) obtained with 6-in. (150-mm) and 12-in. (300-mm) moonfoot spacings were also superimposed in the same graph for comparison. In this narrative, only one superimposed graph is presented for reference (Figure 4.28). After observing rut values from Table 4.12 and Figure 4.28, one can conclude that rut measurements with Face Dipstick® are very repeatable.

4.5.1.5 Rut Progression in the Test Section

According to Zhou et al. (2004) and El-Basyouny et al. (2005), flexible pavement rutting can be categorized into three distinct stages: primary, secondary, and tertiary. As of May 02, 2012, approximately four years after the Test Section was opened to traffic, both the primary and secondary stages were observed in the Test Section at all the stations (Figures

4.29 through 4.34). Tertiary stage has not yet been observed in the Test Section. During the primary stage [(from May 30, 2008 through August 21, 2008) (Figures 4.29 through 4.34)], the rutting rate was relatively high. After the primary stage [(after September 2008) (Figures 4.29 through 4.34)], the rutting progression rate decreased and a slight increase in rut values was observed only during summer months.

As noted earlier, there are six stations in the Test Section. Rut measurements were taken in each of these stations during each field testing. A summary of the rutting progressions in all the Test Sections is presented in graphical and tabular form in Figure 4.35 and Table 4.13, respectively. In Figure 4.35, there are six rutting progression curves, each curve representing the rutting progression at a specific station. The first three points of each curve (pertaining to August 21, 2008, December 3, 2008, and January 8, 2009) present the highest rut depth of two wheelpaths, measured with the straight edge/rut gauge combination method. The last 12 points of each curve (from May 19, 2009 to August 21, 2012) present the highest rut values of the two wheelpaths measured with the Face Dipstick® using 6-in. moonfoot spacing. A similar rut progression trend was also observed in the AASHO road test (HRB, 1962; Finn et al., 1977) and the NCAT test track (Selvaraj, 2007); as number of axle increased, the rutting rate decreased.

After roughly four years of service, the maximum rut of 0.77 in. and the minimum rut of 0.44 in. were observed at Station 738 and Station 900, respectively. The corresponding cumulative axles traversing the Test Section were about 18.7-million. Although the rut values increased with time, most of the rut was accumulated during the summer months. For example, out of 0.77 in. rut measured at Station 738, approximately 0.48 in. was accumulated during the summer months. Also, the rate of rutting during the first summer month was much

higher than in the second, third, and fourth summer months, although the cumulative axles during each summer were similar (approximately 1.2-million). Similar behavior of accumulation of rut in summer has been reported in previous studies (e.g., AASHO road test, NCAT Test Track).

4.5.1.6 Contribution of Different Layers to Test Section's Rutting

A comprehensive research study was undertaken by the National Cooperative Highway Research Program (NCHRP) to investigate the contribution of pavement structural layers to rutting of HMA pavements. Findings of that study were reported in NCHRP Report 468 (2002). The shape of the pavement profile observed after rutting in the I-35 Test Section was very similar to the shape of rutted pavement profile in the NCHRP study, where HMA layer or aggregate base layer was the only contributor of rutting. Also, the I-35 Test Section has a stabilized subgrade layer above the natural subgrade layer to minimize the effect of subgrade layer contribution to rutting. Based on NCHRP study as well as the results presented, one could conclude that the HMA layer or aggregate base layer primarily contributes to the rut of the Test Section. In order to identify the actual contributions of different layers to the total rut, forensic trenching is planned at selected locations to measure the actual ruts as part of phase II of this study.

4.5.2 Crack Mapping

As noted earlier, crack mapping was performed during the quarterly field-testing of the Test Section. Crack mapping was performed at each station over a 100-ft segment in the north station and 50-ft in the south direction (see Figure 3.52). To eliminate overlapping of mapping areas, crack mapping was performed at 41-ft north and 34-ft south of Station 235. So

far, no visible fatigue cracking has been observed on the Test Section. However, visible longitudinal cracking originating from the construction joint was observed along the pavement edge stripe. Figures 4.36 (a) shows a photographic view of the visible construction joint on February 14, 2011 at a distance of 38-ft from the north end of the Test Section. For comparative purpose, additional photographs were taken on February 22nd, 2012, May 2nd, 2012, and August 21st, 2012 as shown in Figures 4.36 (b) and (c), respectively. The photographic views of the construction joint at a distance of 795-ft from the north end of the Test Section are presented in Figures 4.37 (a) through (c). It is evident from Figures 4.36 and 4.37 that the longitudinal crack opening is increasing with time. It is believed that repeated freeze-thaw cycles and precipitation played a key role in the significant growth in these longitudinal cracks.

The pavement surface also showed loss of aggregates (or raveling), as shown in Figures 4.38 and 4.39 for a distance of 318- and 741-ft from the north end, respectively. Furthermore, Figures 4.40 (a), (b), and (c) show a comparison of pavement surface condition at Station 144 in the form of photographs taken on June 5, 2009, February 14th, 2011, May 2nd, 2012, and August 21st, 2012, respectively. It is clear from Figures 4.40 (a) through (c) that the pavement has undergone noticeable deterioration along the edges (between the driving lane and the shoulder). Additional freeze-thaw cycles and precipitation are likely to cause formation of potholes, if cracks are not sealed.

4.5.3 Evaluation of Smoothness

In this study, the pavement smoothness was measured by a worldwide standard called the International Roughness Index or IRI. The index measures the pavement smoothness in terms of the number of inches per mile that a laser, mounted in a specialized van, travels

vertically up and down as it is driven across the road (http://www.penndot8.com/iri.htm). Specifically, IRI is a longitudinal slice of the road showing elevation as it varies with longitudinal distance along a travelled track on the road. The correlation between IRI values and pavement smoothness condition is presented in Table 4.14. It is evident from Table 4.14 that the lower the IRI number, the smoother the ride.

To evaluate the changes in IRI with time, smoothness was measured 50-ft north and 50-ft south of Station 319 along the outer wheel path, mid lane, and the inner wheel path (Figure 4.41). A summary of all IRI values for all locations is presented in Table 4.15. Furthermore, a summary of the average IRI values for outer wheel path, mid lane and inner wheel path is presented in Table 4.16. Furthermore, results are graphically presented in Figures 4.42 and 4.43. It is evident from Figure 4.42 that the inner wheel path showed the highest IRI values followed by the outer wheel path. For example, the inner wheel path showed 16% and 7% higher IRI values as compared to the corresponding IRI values measured for the outer wheel path on May 19, 2009 and June 07, 2011, respectively. One of the explanations could be that the inner wheel path experienced higher traffic as compared to outer wheel path due to lane changes while driving. This is also evident from the higher rut values of the inner wheel path as compared to the corresponding outer wheel path values on Station 319 (see Table 4.17). No such trend was observed for IRI values collected from the mid lane. The average rut of the entire section has increased with time. In approximately three years (May 19th, 2009 to May 2nd, 2012), the average IRI value increased from 72 to 97.

4.5.4 Falling Weight Deflectometer (FWD) Measurements

A Dynatest (Model: 8002-057) type FWD was used in this study. The testing pattern was designed for a series of six stations located at approximately 100 ft intervals along the

outer wheel path (as discussed in Section 3.7.1.2, Figure 3.52). For conducting FWD tests on the top of asphalt concrete layer, an 11.8 in. diameter plate was used with seven deflection sensors spaced at 8, 12, 24, 36, 48, and 72 in. from the center, as recommended by the ASTM D 4694 test method. The deflection sensors had an accuracy of 0.04 mils. The loading pattern included three seating drops plus one load drop from different heights in sequential order. The loading pattern included four different loads (6, 9, 12 and 15 kips) for testing on the top of the asphalt concrete layer. For this investigation, the FWD data was collected periodically covering a wide range of temperatures. Specifically, FWD data was collected from May 16, 2008, through May 20, 2008, at different times of the day before opening the Test Section to actual traffic. Also, after morning lane closures, FWD data was collected on August 21 and December 3, 2008; May 19 and October 28, 2009; February 16, May 18, August 11, and November 22, 2009; February 14, June 07, and October 18, 2011; February 22, and May 02, 2012. For rut models, the correlation developed using data collected from May 16, 2008 through October 28, 2009 was used. For fatigue model, however, the data collected from May 16, 2008 through February 14, 2011 was used.

The modulus values from the FWD data were back-calculated using MODULUS 6.0 software. Several techniques, as mentioned in Von Quintus et al. (1994), were used for analyzing and interpreting the FWD data. The first approach involves the validation of the deflection data obtained from sensors. This procedure involved investigating the deflection basins and verifying that they were sensible. The depth of each layer was specified on the basis of measured thicknesses from the extracted cores. In addition, several trial sections with different depths to bedrock were analyzed. The modulus values of each layer and absolute error were examined carefully for all six stations. The backcalculated modulus values for

aggregate base, stabilized subgrade, and natural subgrade layer were compared with the range of resilient modulus (M_r) values obtained from laboratory testing on the corresponding field collected material in accordance with the AASHTO T 307 test method (Solanki et al., 2009; Solanki et al., 2011). The deflection basins providing backcalculated modulus values outside the range of adjusted laboratory M_r values were discarded. An adjustment factor of 1.43, 0.62, and 0.75 was used for aggregate base, stabilized subgrade and natural subgrade layers, respectively (AASHTO, 2004). The depth of bedrock giving sensible M_r values and the lowest absolute error was selected.

4.5.4.1 Backcalculation of Modulus Values from FWD Data

As noted earlier, modulus values were backcalculated from the FWD data using MODULUS 6.0 software. Also, mid-depth (approximately 3.5 in.) pavement temperature values were calculated from the data generated by the temperature sensors installed on the shoulder of the instrumented site. The variation of backcalculated asphalt concrete modulus values were then plotted with temperature to establish modulus-temperature relationships, as shown in Figure 4.44 for data collected from May 16, 2008 through October 28, 2009. The relationships were used for the development of the field rut prediction models. The regression analysis on back-calculated data from FWD yielded an exponential best-fit line of the following form:

$$E_{FWD} = \alpha_1 e^{\alpha_2 T} \quad (4.5)$$

where E_{FWD} = modulus of asphalt concrete back-calculated from the FWD data, α_1 = regression constant (18,840.961 ksi), α_2 = regression constant (–0.045), and T = mid-depth temperature of asphalt concrete from temperature sensors. In general, Equation (4.5) is a good predictor (R^2 = 0.863) of asphalt concrete modulus at different temperatures. At a low

temperature (50^{o}F), the average back-calculated modulus value is approximately 1,792 ksi with a 40% coefficient of variation. At higher temperature of approximately 105^{o}F, the average back-calculated modulus value and the coefficient of variation are approximately 131 ksi and 4%, respectively.

The variation of back-calculated asphalt concrete modulus with temperature is shown in figure 4.45. Data collected from May 16, 2008 through February 14, 2011 were used in developing the modulus-temperature correlations (*used for development of fatigue prediction models*). The best-fit line for this case can be expressed by the following equation:

$$E_{FWD} = 9{,}456.636e^{-0.036T} \quad (4.6)$$

The regression constants α_1 and α_2 for this case are found as 9,456.636 ksi and –0.036, respectively. Additional data collected from the Test Section was also analyzed and plotted in Figure 4.46 for comparison purposes.

4.5.4.2 Backcalculation of Modulus Values from Asphalt Strain Gauge (ASG) Data

Based on request from ODOT, modulus values were also backcalculated from the asphalt strain gauge measurements. For this investigation, the data collected once per week for the period of May 30, 2008, through October 28, 2009 was used. As discussed earlier in Section 4.3.2, commercial software, DADiSP, was used to process the high sampling frequency data. Although each steering and tandem axle data were processed for all the Class 9 vehicles, only steering axle data with the "best hit" are used in this study. The "best hit" was defined as the response of the wheel of a Class 9 vehicle traveling at a speed between 60 to 70 MPH that yielded a maximum offset of 4 in. (one-half of the length of ASG) from the center of the nearest gauge. As evident from Figure 3.35, each ASG had a duplicate in the gauge array (1& 10, 2 & 11, 3 & 12, 4 & 7, 5 & 8, 6 & 9). The average strain value from

duplicate ASG's nearest to the steering axle wheel was used for backcalculating the modulus values, as discussed later.

For backcalculation of modulus values from ASGs, strain and traffic data collected over a wide range of mid-depth pavement temperature ($40^oF - 110^oF$) were selected. A multi-layer elastic theory-based computer program, WinJULEA (AASHTO, 2004), was employed to backcalculate the modulus values of the asphalt concrete layer. In general, the procedure consisted of predicting tensile strains (longitudinal or transverse) for a given offset (distance of strain gauge from wheel) by using the given loading configuration (axle load, contact area, and tire pressure) and material properties (layer thickness, modulus values, and Poisson's ratio of each layer). As noted earlier, the offset value was obtained from the lateral positioning sensors. The axle load value for a particular vehicle was retrieved from the traffic data captured at the WIM site. A tire pressure of 120 psi (the default value recommended by MEPDG) was assumed as the contact pressure applied to a circular area on the pavement surface. The average backcalculated modulus value of 28.2 ksi, 69.7 ksi and 20.1 ksi from the FWD data were used as inputs for aggregate base layer, stabilized subgrade layer, and natural subgrade layer, respectively. In WinJULEA the values of Poisson's ratios for asphalt concrete, aggregate base, stabilized subgrade, and natural subgrade layer respectively were assumed as 0.35, 0.35, 0.20, and 0.40, consistent with the range of values reported by the new MEPDG (AASHTO, 2004). The modulus value of the asphalt concrete layer was changed until predicted tensile strain was within ±0.5 μstrain of the measured values from ASG.

A summary of the longitudinal modulus values ($E_{SG,L}$) obtained by the matching predicted and measured longitudinal strain measurements is presented graphically in Figures 4.47 and 4.48 on linear and semi-logarithmic scale, respectively. It is evident that $E_{SG,L}$

decreases with an increase in temperature, as expected. The following exponential regression equation was fitted to the data (Figure 4.47):

$$E_{ASG,L} = \alpha_1 e^{\alpha_2 T} \quad (4.7)$$

where regression constant α_1 and α_2 are found as 7,867 ksi and –0.034, respectively (R^2 = 0.812). Further, for comparison purpose the FWD modulus values predicted at different temperatures using Equations (4.5) and (4.6) are also plotted in Figure 4.47 and 4.48. From Figures 4.47 and 4.48 it is seen that backcalculated modulus from longitudinal strain gauge (Equation 4.7) and the back-calculated modulus from the FWD data show close agreement at temperatures above 50^{o}F. However, at temperatures below 50^{o}F, the FWD modulus predicted from Equation (4.5) is higher as compared to the modulus $E_{SG,L}$ predicted by equation 4.7. One of the reasons for this difference could be low confidence in FWD back-calculated modulus values at low temperature. Also, Equation (4.5) was developed by using the FWD data collected over a temperature ranging between 50 to 105^{o}F, and extrapolation at lower temperatures (< 50^{o}F) may not be feasible. Additional analysis and results are presented elsewhere (Solanki et al., 2011).

4.5.5 DCP and In-Situ Moisture Content Data

DCP tests were conducted on June 07, 2011 on the shoulder near six stations. Approximately 15 in. deep holes were drilled using a HILTI TE 55 driller before conducting the DCP test (Figure 4.49 (a)). This hole was drilled on the asphalt concrete layer to reach the top of the stabilized subgrade layer. Then, the sample was collected for moisture content and sealed in a Ziploc bag (Figure 4.49 (b)). These samples were later oven dried and used for determining *in-situ* moisture content. The *in-situ* moisture content values are presented in Table 4.18. It is important to note that these values represent only to 1 – 2 in. of stabilized

subgrade and not the entire stabilized layer. It is evident from Table 4.18 that the *in-situ* moisture content ranges between 12.2 – 16.1%. The lowest and highest moisture content of 12.2% and 16.1% was observed at Station 540 and 319, respectively.

The DCP tests were performed down to a depth of approximately 15 in., as suggested by Miller (2000). The DCP results are summarized in terms of incremental cone index (ICI), which represents the depth of penetration per blow of the DCP hammer (SHT, 1992). A lower ICI value indicates a stronger or stiffer material, while a higher DCP value indicates a weaker subgrade. Complete DCP profiles for all stations are shown in Figure 4.50. From Figure 4.50, the ICI values are less than 15 mm/blow for the top 8 in. This could be attributed to comparatively stiffer stabilized subgrade on soft natural subgrade. Station 738 revealed significant increase (> 40 mm/blow) in the ICI value for a depth greater than 10 in. It is also interesting to note that the rut values at Station 738 were found to be higher as compared to rut depth at other stations (see Figure 4.35). It is believed that the highest ICI value and rut depth at Station 738 is due to the high moisture content of the natural subgrade. Forensic investigations to be conducted in phase II of this study are expected to provide specifics on the moisture variation issues.

Table 4-1 Traffic Volume Statistics

Traffic Volume	Lane 1	Lane 2	Total	Difference
Year 1	1,170,870	263,609	1,434,479	--
Year 2	1,156,246	248,544	1,404,791	-1.0%
Year 3	1,187,837	282,139	1,469,976	2.3%
Total Years	3,514,954	794,292	4,309,245	
Percentage	81.6%	18.4%	100%	

Table 4-2 Traffic Load Statistics

Traffic Load, kips	Lane 1	Lane 2	Total	Difference
Year 1	49,865,633	8,753,064	58,618,697	--
Year 2	47,073,984	8,018,928	55,092,911	-3.1%
Year 3	45,845,346	9,529,003	55,374,349	0.3%
Total Years	142,784,963	26,300,995	169,085,958	
Percentage	84.4%	15.6%	100%	

Table 4-3 Traffic ESAL Statistics

Traffic ESAL	Lane 1	Lane 2	Total	Difference
Year 1	773,922	121,719	895,641	--
Year 2	738,831	118,837	857,668	-2.2%
Year 3	683,916	148,642	832,558	-1.5%
Total Years	2,196,670	389,198	2,585,867	
Percentage	84.9%	15.1%	100%	

Table 4-4 Traffic Class Statistics

Vehicle Class	**4**	**5**	**6**	**7**	**8**	**9**	**10**	**11**	**12**	**13**
Lane 1	5.7%	14.8%	7.2%	0.1%	9.8%	58.5%	0.6%	2.2%	1.1%	0.1%
Lane 2	5.9%	25.7%	9.8%	0.1%	11.4%	44.8%	0.7%	0.9%	0.7%	0.0%
Total	**5.8%**	**16.8%**	**7.7%**	**0.1%**	**10.0%**	**56.0%**	**0.6%**	**1.9%**	**1.0%**	**0.1%**

Table 4-5 Traffic Violations Statistics

Violations	**Lane 1**	**Lane 2**
Speed	30.5%	62.2%
Weight	2.5%	4.3%

Table 4-6 Rut Data measured with Straight Edge/Rut Gauge Combination

I - 35 INSTRUMENTATION PROJECT RUT MEASUREMENTS AUG. 21,2008

Location in Lane (ft.)	0	1	2	3	4	5	6	7	8	9	10	11	12
						Rut Depth (in.)							
Station No.													
144	0	-0.1	-0.1	0	0	0	0	-0.2	-0.2	-0.1	0	0	0
235	0	-0.15	-0.1	0	0	0	-0.3	-0.3	-0.3	-0.1	-0.1	-0.1	0
319	0	-0.4	-0.3	-0.1	0	0	0	-0.2	-0.3	-0.05	0	0	0
540	0	-0.3	-0.3	-0.1	0	0	0	-0.2	-0.2	-0.1	0	-0.05	0
738	0	-0.3	-0.2	-0.1	0	0	0	-0.1	-0.2	-0.1	0	0	0
900	0	-0.2	-0.1	-0.05	0	0	0	-0.15	-0.2	-0.1	-0.05	0	0

I - 35 INSTRUMENTATION PROJECT RUT MEASUREMENTS DEC 03,2008

Location in Lane (ft.)	0	1	2	3	4	5	6	7	8	9	10	11	12
						Rut Depth (in.)							
Station No.													
144	0	-0.1	-0.1	-0.1	0	0	0	-0.1	-0.25	-0.3	-0.1	0	0
235	0	0	-0.05	0	0	0	-0.1	-0.3	-0.25	-0.15	-0.1	-0.1	0
319	0	-0.2	-0.2	-0.1	0	0	-0.05	-0.3	-0.35	-0.1	0	0	0
540	0	-0.2	-0.2	-0.1	0	0	0	-0.2	-0.2	-0.1	0	0	0
738	0	-0.2	-0.2	-0.1	0	0	0	-0.15	-0.2	-0.1	0	0	0
900	0	-0.1	-0.05	0	0	0	0	-0.15	-0.2	-0.1	0	0	0

I - 35 INSTRUMENTATION PROJECT RUT MEASUREMENTS JAN 08,2009

Location in Lane (ft.)	0	1	2	3	4	5	6	7	8	9	10	11	12
						Rut Depth (in.)							
Station No.													
144	0	-0.1	-0.2	-0.2	0	0	0	-0.1	-0.3	-0.3	-0.1	0	0
235	0	-0.2	-0.1	0	0	0	-0.15	-0.3	-0.35	-0.1	-0.05	-0.1	0
319	0	-0.2	-0.2	-0.05	0	0	-0.05	-0.25	-0.2	-0.05	0	0	0
540	0	-0.2	-0.2	-0.1	0	0	0	0	-0.2	-0.2	-0.1	0	0
738	0	-0.2	-0.2	-0.1	0	0	0	-0.1	-0.2	-0.1	0	0	0
900	0	-0.1	-0.1	0	0	0	0	-0.15	-0.2	-0.1	0	0	0

I - 35 INSTRUMENTATION PROJECT RUT MEASUREMENTS MAY 19,2009

Location in Lane (ft.)	0	1	2	3	4	5	6	7	8	9	10	11	12
						Rut Depth (in.)							
Station No.													
144	0	-0.1	-0.1	-0.05	0	0	0	-0.2	-0.25	-0.2	0	0	0
235	0	-0.05	0	0	0	0	-0.2	-0.3	-0.3	-0.1	0	-0.1	0
319	0	-0.2	-0.2	0	0	0	0	-0.2	-0.3	-0.15	0	0	0
540	0	-0.2	-0.2	-0.1	0	0	0	-0.1	-0.2	-0.1	0	0	0
738	0	-0.2	-0.2	-0.1	0	0	0	-0.2	-0.25	-0.1	0	0	0
900	0	0	-0.05	0	0	0	0	-0.1	-0.2	-0.1	0	0	0

* Red circles represent highest rut measurements at Station 319
* Green circles represent highest rut measurements at Station 540
*Violet circles represent highest rut measurements at Station 738

Table 4-7 Comparison of Rut Depth among May 19, October 28, 2009 and February 16, 2010 (Moonfoot Spacing = 12-in.)

Station No.	Distance from Reference Point (ft) (May 19, 2009)	Rut Depth (in.) (May 19, 2009)	Distance from Reference Point (ft) (October 28, 2009)	Rut Depth (in.) (October 28, 2009)	Distance from Reference Point (ft) (February 16, 2010)	Rut Depth (in.) (February 16, 2010)
144	2.00	**-0.262**	3.00	**-0.299**	3.00	**-0.293**
	10.00	**-0.382**	10.00	**-0.404**	10.00	**-0.403**
235	2.00	**-0.295**	2.00	**-0.315**	2.00	**-0.321**
	9.00	**-0.451***	9.00	**-0.471***	9.00	**-0.471***
319	2.00	**-0.425**	2.00	**-0.444**	2.00	**-0.425**
	9.00	**-0.345**	9.00	**-0.419**	9.00	**-0.411**
540	2.00	**-0.368**	2.00	**-0.391**	2.00	**-0.378**
	9.00	**-0.250**	9.00	**-0.283**	9.00	**-0.274**
738	2.00	**-0.396**	2.00	**-0.465**	2.00	**-0.463**
	9.00	**-0.249**	9.00	**-0.321**	9.00	**-0.322**
900	2.00	**-0.279**	2.00	**-0.275**	2.00	**-0.281**
	9.00	**-0.256**	9.00	**-0.298**	9.00	**-0.300**

* Maximum field rut values

Table 4-8 Comparison of Rut Depth among May 19, October 28, 2009 and February 16, 2010 (Moonfoot Spacing = 6-in.)

Station No.	Distance from Reference Point (ft) (May 19, 2009)	Rut Depth (in.) (May 19, 2009)	Distance from Reference Point (ft) (October 28, 2009)	Rut Depth (in.) (October 28, 2009)	Distance from Reference Point (ft) (February 16, 2010)	Rut Depth (in.) (February 16, 2010)
144	2.50	**-0.269**	3.00	**-0.298**	3.00	**-0.301**
	9.50	**-0.390**	9.50	**-0.418**	9.50	**-0.419**
235	1.50	**-0.326**	1.50	**-0.341**	1.50	**-0.338**
	9.00	**-0.444**	9.00	**-0.468**	8.50	**-0.465**
319	2.00	**-0.425**	2.00	**-0.444**	2.00	**-0.431**
	9.00	**-0.348**	9.00	**-0.411**	9.00	**-0.413**
540	2.50	**-0.363**	2.00	**-0.393**	2.00	**-0.381**
	9.00	**-0.265**	9.00	**-0.277**	9.00	**-0.277**
738	2.00	**-0.395***	2.50	**-0.483***	2.50	**-0.476***
	9.50	**-0.245**	9.00	**-0.323**	9.00	**-0.326**
900	2.00	**-0.280**	2.00	**-0.283**	2.00	**-0.279**
	9.50	**-0.275**	9.50	**-0.310**	9.50	**-0.307**

* Maximum field rut values

Table 4-9 Comparison of Rut Depth using Dipstick® and Rut Gauge

Station No.	Wheelpath	Rut depth from FD (spacing = 12-in.) with RoadFace 6.0 Software (with 10-ft SE) (in.)	Rut depth from Rut Gauge and Conventional SE (in.) (% difference)*
144	Outer	-0.260	-0.10 (- 61.54%)
	Inner	-0.375	-0.25 (-33.33%)
235	Outer	-0.295	-0.05 (-83.05%)
	Inner	-0.471	-0.30 (-36.31%)
319	Outer	-0.425	-0.20 (-52.94%)
	Inner	-0.334	-0.30 (-10.18%)
540	Outer	-0.368	-0.20 (-45.65%)
	Inner	-0.248	-0.20 (-19.35%)
540 (Special)	Outer	-0.435	-0.20 (-54.02%)
	Inner	-0.358	-0.20 (-44.13%)
738	Outer	-0.396	-0.20 (-49.49%)
	Inner	-0.249	-0.25 (0.40%)
900	Outer	-0.279	-0.05 (-82.08%)
	Inner	-0.256	-0.20 (-21.88%)

* Rut depth obtained from Face Dipstick® (spacing = 12-in.) with RoadFace 6.0 software (with 10-ft straight edge) was taken as reference

* FD = Face Dipstick® and SE = Straight Edge

Table 4-10 Repeatability of Face Dipstick® (for Moonfoot Spacing = 12-in.)

Station No.	Trial No.	Distance from Reference Point (ft)	Depth of Rut (in.)
144	1	2.00	-0.262
		10.00	-0.375
144	2	2.00	-0.262
		10.00	-0.382

Table 4-11 Repeatability of Face Dipstick® (for Moonfoot Spacing = 6-in.)

Station No.	Trial No.	Distance from Reference point (ft)	Depth of Rut (in.)
144	1	2.50	-0.268
		9.50	-0.382
144	2	2.50	-0.269
		9.50	-0.390

Table 4-12 Comparison of Rut Depths between Moonfoot Spacing 6-in. and 12-in. of Face Dipstick®

Station no.	Wheelpath	Rut depth from FD (Spacing = 12-in.) with RoadFace 6.0 Software (in.)	Rut depth from FD (Spacing = 6-in.) with RoadFace 6.0 Software (in.)	(% Difference)*
144 (Trial # 1)	Outer	-0.260	-0.268	2.99
	Inner	-0.375	-0.382	1.83
144 (Trial # 2)	Outer	-0.262	-0.269	2.60
	Inner	-0.382	-0.390	2.05
235	Outer	-0.295	-0.326	9.51
	Inner	-0.451	-0.444	-1.58
319	Outer	-0.425	-0.425	0.00
	Inner	-0.345	-0.348	0.86
540	Outer	-0.368	-0.363	-1.38
	Inner	-0.250	-0.265	5.66
738	Outer	-0.396	-0.395	-0.25
	Inner	-0.249	-0.245	-1.63
900	Outer	-0.279	-0.280	0.36
	Inner	-0.256	-0.275	6.91

Rut depth obtained from Face Dipstick® (spacing = 6-in.) with RoadFace 6.0 software was taken as reference

Table 4-13 A Summary of Rut Progression on the Test Section

Date	Highest Rut (in.)					
	Station 144	Station 235	Station 319	Station 540	Station 738	Station 900
31-May-08	0	0	0	0	0	0
21-Aug-08	0.2	0.3	0.4	0.3	0.3	0.2
3-Dec-08	0.3	0.3	0.35	0.2	0.2	0.2
8-Jan-09	0.3	0.35	0.25	0.2	0.2	0.2
19-May-09	0.39	0.444	0.425	0.363	0.395	0.28
28-Oct-09	0.418	0.468	0.444	0.393	0.483	0.31
16-Feb-10	0.419	0.465	0.431	0.381	0.476	0.307
10-Mar-10	0.409	0.465	0.429	0.384	0.483	0.304
18-May-10	0.427	0.469	0.437	0.388	0.501	0.303
10-Aug-10	0.409	0.424	0.509	0.409	0.612	0.317
22-Nov-10	0.441	0.439	0.545	0.457	0.678	0.359
14-Feb-11	0.44	0.4	0.532	0.435	0.653	0.361
7-Jun-11	0.421	0.405	0.538	0.441	0.663	0.377
18-Oct-11	0.441	0.485	0.606	0.48	0.714	0.435
22-Feb-12	0.476	0.461	0.598	0.47	0.712	0.421
2-May-12	0.479	0.491	0.6	0.456	0.712	0.41
21-Aug-12	0.65	0.499	0.58	0.456	0.769	0.437
Most recent recorded rut at the test section = 0.769 inch or 19.53 millimeter						
Maximum recorded rut at the test section = 0.769 inch or 19.53 millimeter						

Table 4-14 Roughness category based on the Federal Highway Administration

Smoothness Category	IRI Rating, in./mile	
	Interstate	Other
Very Good	< 60	< 60
Good	60 - 94	60 - 94
Fair	95 - 119	95 - 170
Mediocre	120 - 170	171 - 220
Poor	> 170	> 220

Table 4-15 A Summary of IRI Values on the Test Section

Date	Outer Wheel Path		Mid-Lane		Inner Wheel Path	
	North	South	North	South	North	South
May 19, 2009	63.5	67.66	102.9	48.53	73.01	78.91
Oct 28, 2009	60.49	67.51	83.24	47.77	71.92	93.6
Feb 16, 2010	62.79	75.73	81.67	66	74.17	103.79
May 18, 2010	70.78	62.28	89.51	48.33	79.01	96.26
Aug 10, 2010	69.33	70.14	124.2	57.68	75.71	78.61
Nov 22, 2010	76.3	79.58	117.97	67.98	99.63	75.27
Feb 14, 2011	78.1	77.99	124.49	137.2	86.02	109.12
Jun 07, 2011	74.9	78.93	130.69	60.57	80.68	84.04
Oct 18, 2011	78.2	77.38	101.86	66.32	94.68	91.93
Feb 22, 2012	110.5	88.69	126.74	54.22	93.73	142.34
May 2, 2012	95.77	115.13	133.32	66.67	82.03	87.02
August 21, 2012	101.62	107.7	108.71	74.53	93.18	159.27

Table 4-16 A Summary of Average IRI Results on the Test Section

Date	Outer Wheel Path	Mid-Lane	Inner Wheel Path
	Average	Average	Average
May 19, 2009	65.58	75.72	75.96
Oct 28, 2009	64.00	65.51	82.76
Feb 16, 2010	69.26	73.84	88.98
May 18, 2010	66.53	68.92	87.64
Aug 10, 2010	69.74	90.94	77.16
Nov 22, 2010	77.94	92.98	87.45
Feb 14, 2011	78.05	130.85	97.57
Jun 07, 2011	76.92	95.63	82.36
Oct 18, 2011	77.79	84.09	93.31
Feb 22, 2012	99.60	90.48	118.04
May 2, 2012	105.45	100.00	84.53
August 21, 2012	104.66	91.62	126.23

Table 4-17 Rut Measurements of Station 319

	RUT Depth (in.) - Station # 319												
Date	May 19, 2009	Oct 28, 2009	Feb 16, 2010	Mar 10, 2010	May 18, 2010	Nov 22, 2010	Feb 14, 2011	Jun 7, 2011	Oct 18, 2011	Feb 22, 2012	May 2, 2012	Aug 21, 2012	AVG
OWP 15.5" (1.3')	0.425	0.444	0.431	0.429	0.437	0.462	0.449	0.454	0.520	0.515	0.535	0.542	0.470
IWP 15.5" + 102" (9.8')	0.345	0.419	0.413	0.414	0.405	0.545	0.532	0.537	0.606	0.598	0.600	0.580	0.499

Table 4-18 In-situ Moisture Content Values at Different Stations Collected on June 07, 2011

Station No.	Tin Weight gm	Tin+Wet Soil gm	Tin+Dry Soil gm	Moisture Content %	Average %
	31.3	75.6	69.9	14.8	
144	31.3	69.6	64.6	15.0	14.9
	31.0	68.9	64.4	13.5	
235	30.9	69.5	64.8	13.9	13.7
	30.5	64.3	59.7	15.8	
319	31.3	68.2	63.0	16.4	16.1
	30.5	55.6	53.0	11.6	
540	30.6	54.4	51.7	12.8	12.2
	30.4	77.7	71.7	14.5	
738	31.1	80.5	74.3	14.4	14.4
	30.7	70.1	64.8	15.5	
900	30.8	77.1	71.0	15.2	15.4

Figure 4-1 Typical Class 9 Truck

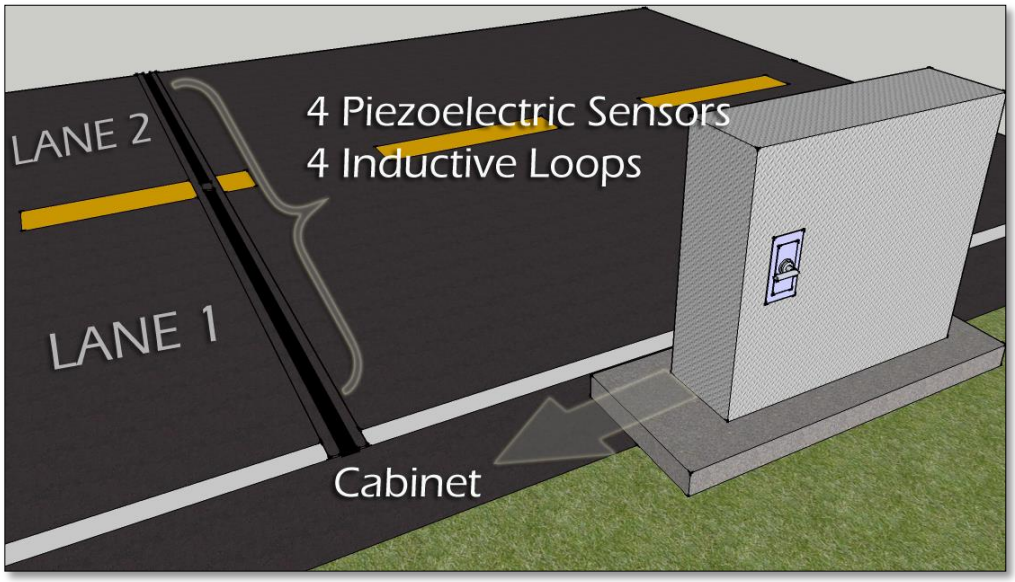

Figure 4-2 WIM Station Layout

Figure 4-3 Video Camera Facing Station 319 of the I-35 Test Section

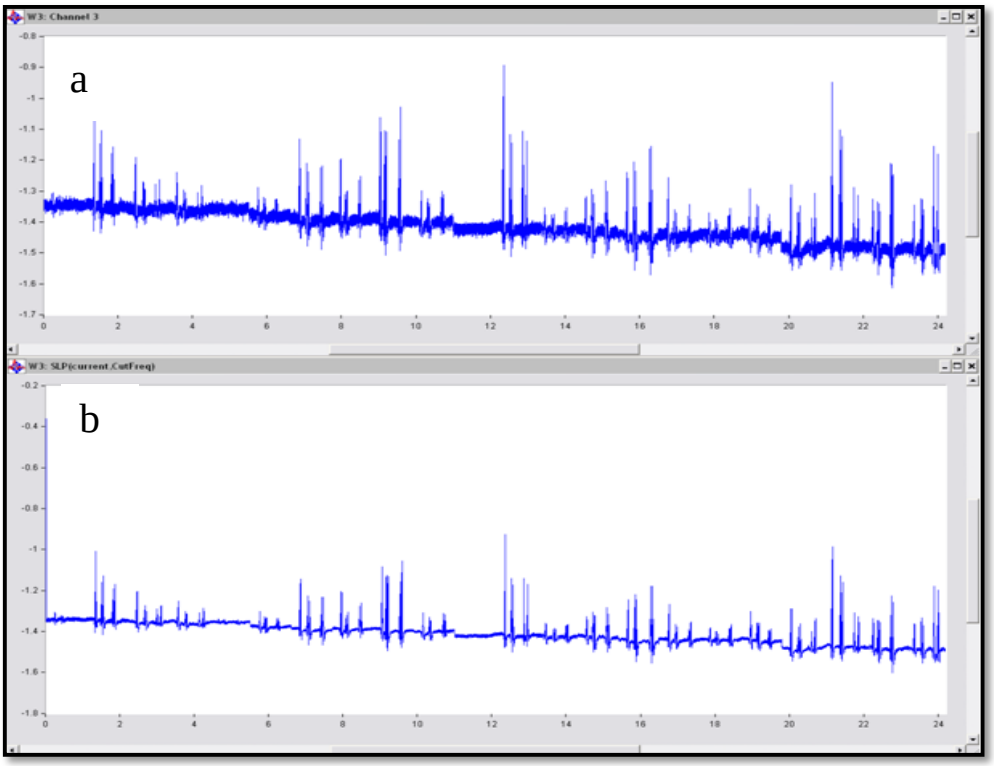

Figure 4-4 Strain Trace of One Trip a) Raw, b) Cleaned (June 01, 2010)

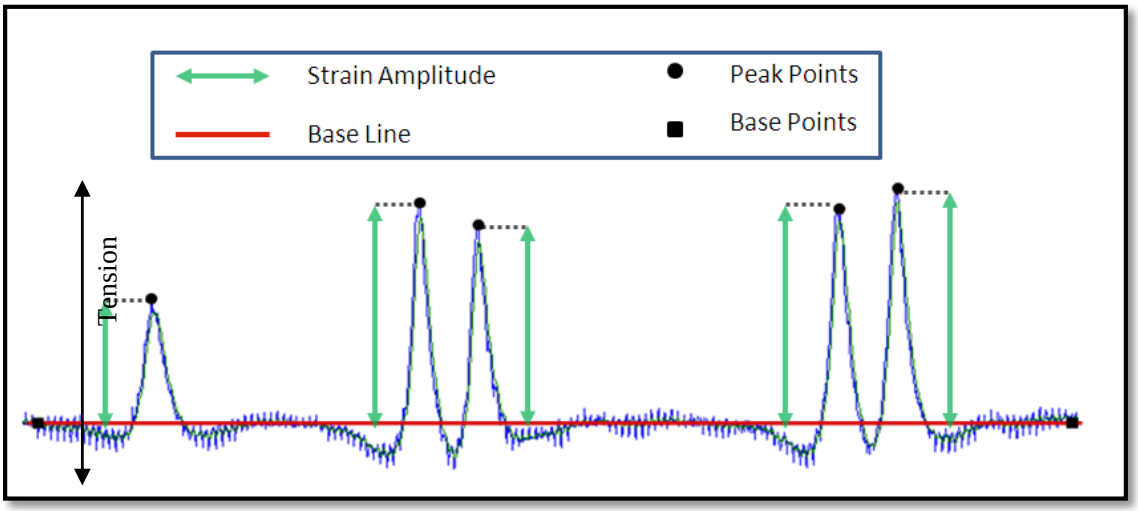

Figure 4-5 Strain Amplitude Illustration Example

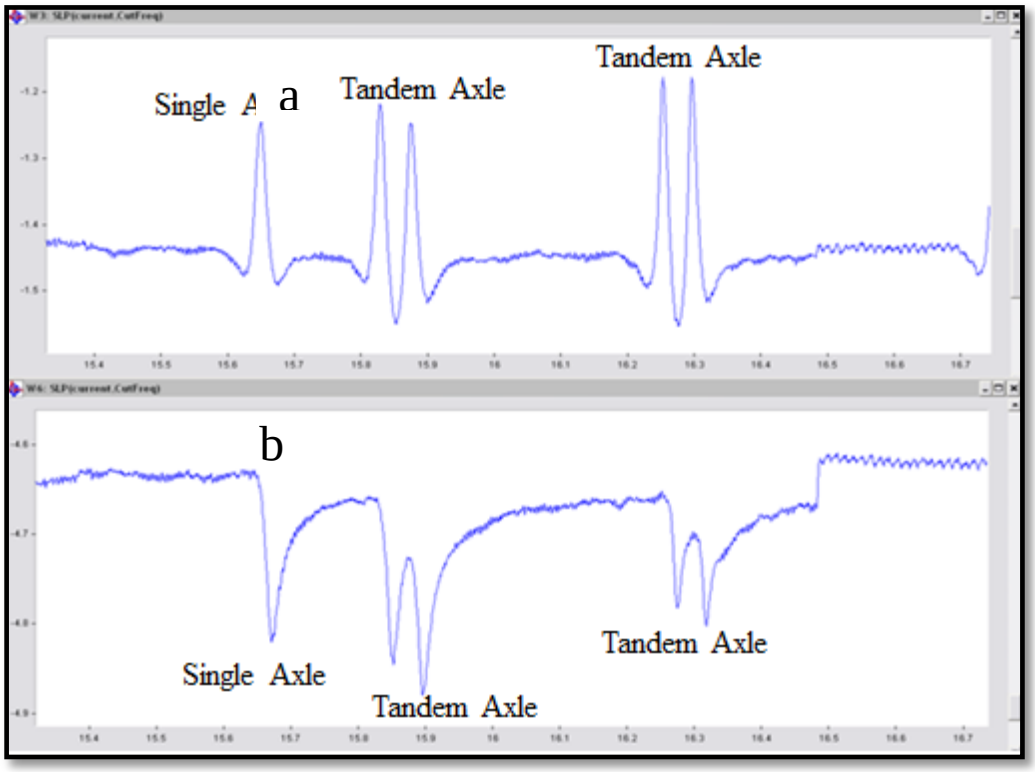

Figure 4-6 Typical Strain Trace of a Class-9 Vehicle from a) Longitudinal Gauge b) Transverse Gauge

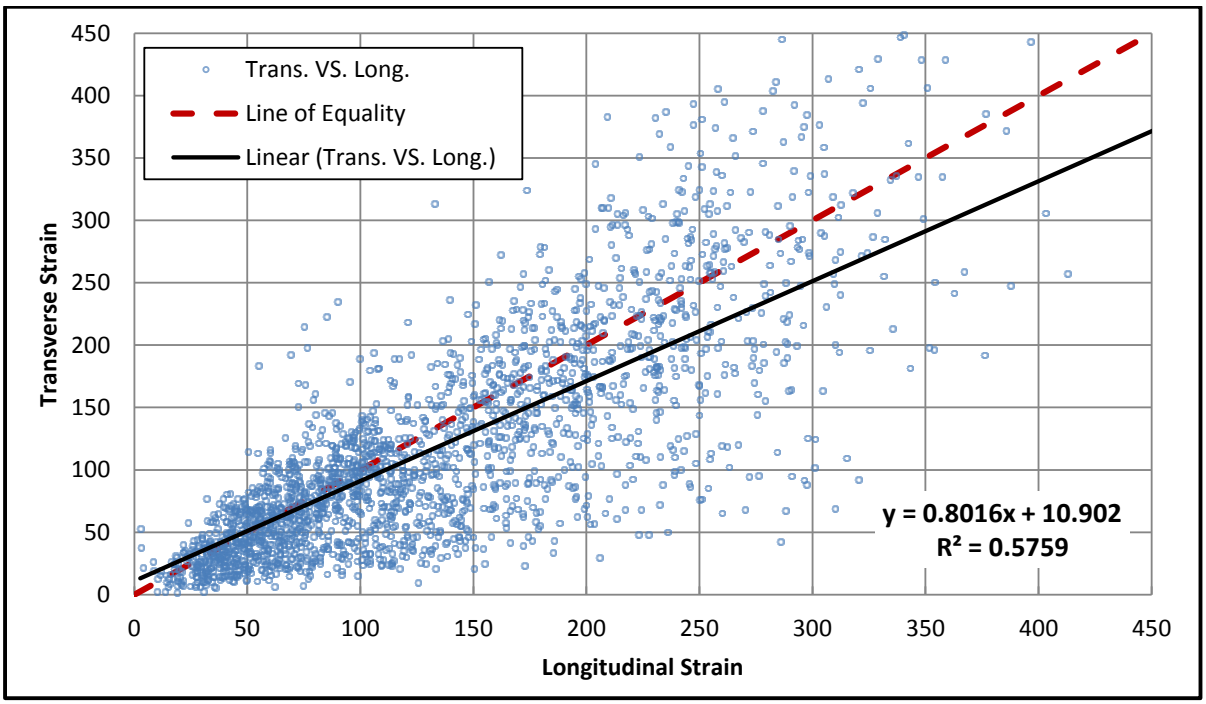

Figure 4-7 Longitudinal vs. Transverse Strains

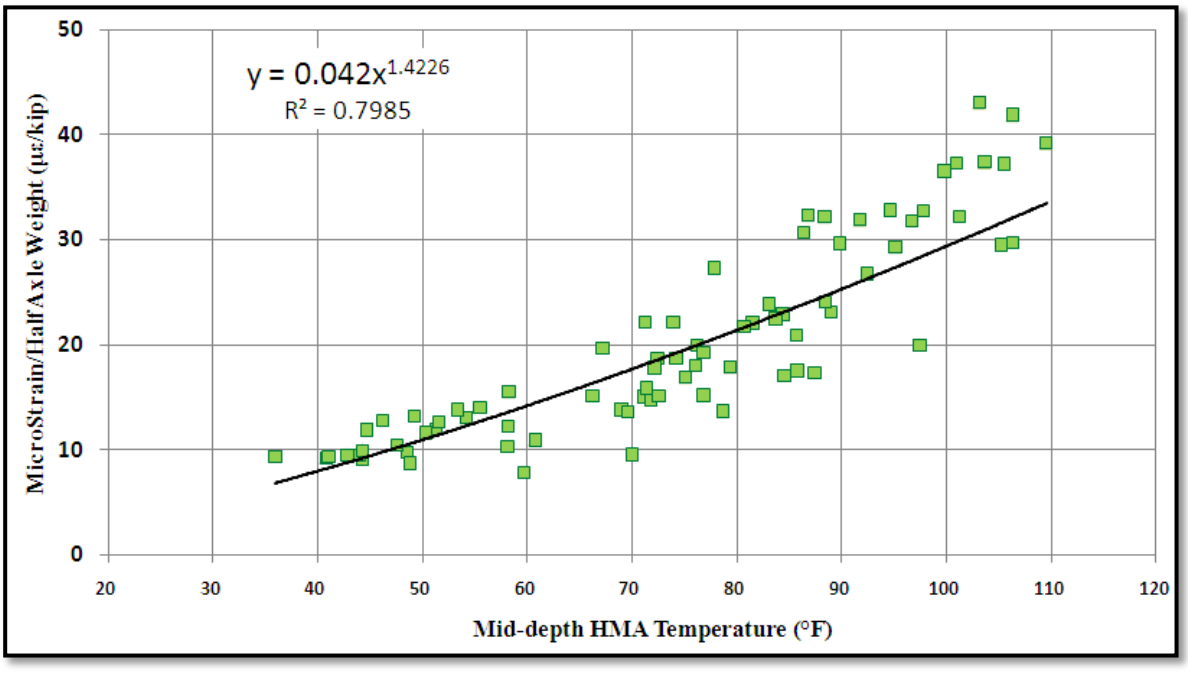

Figure 4-8 Strain-Temperature Relationship for Steering Axles

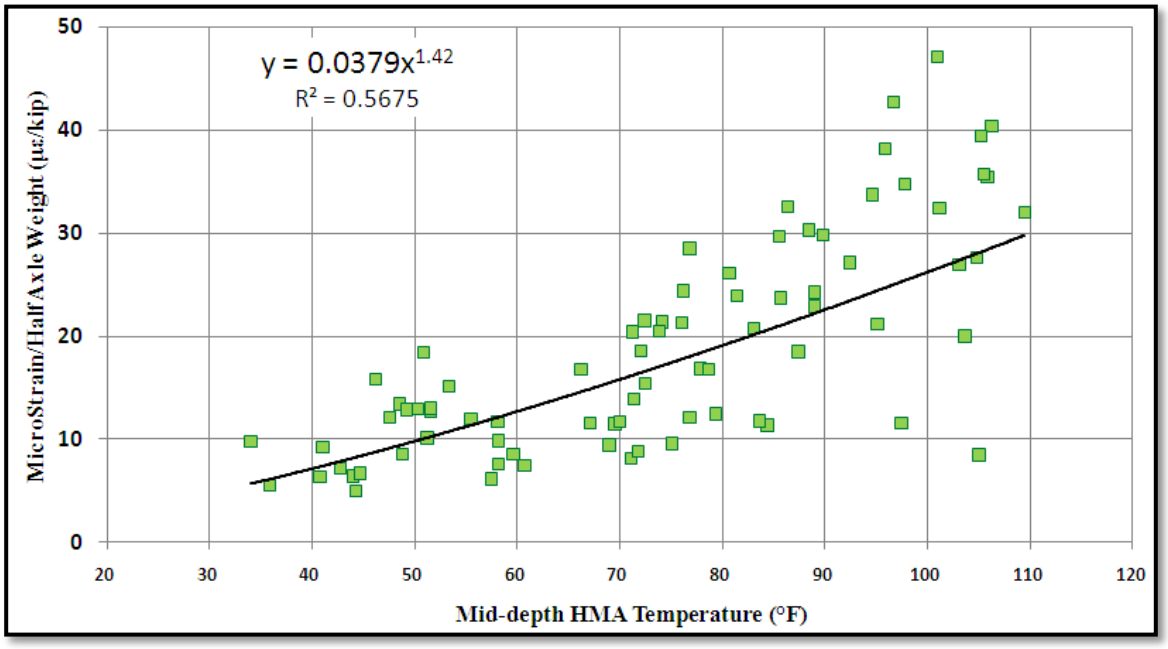

Figure 4-9 Strain-Temperature Relationship for Tandem Axles

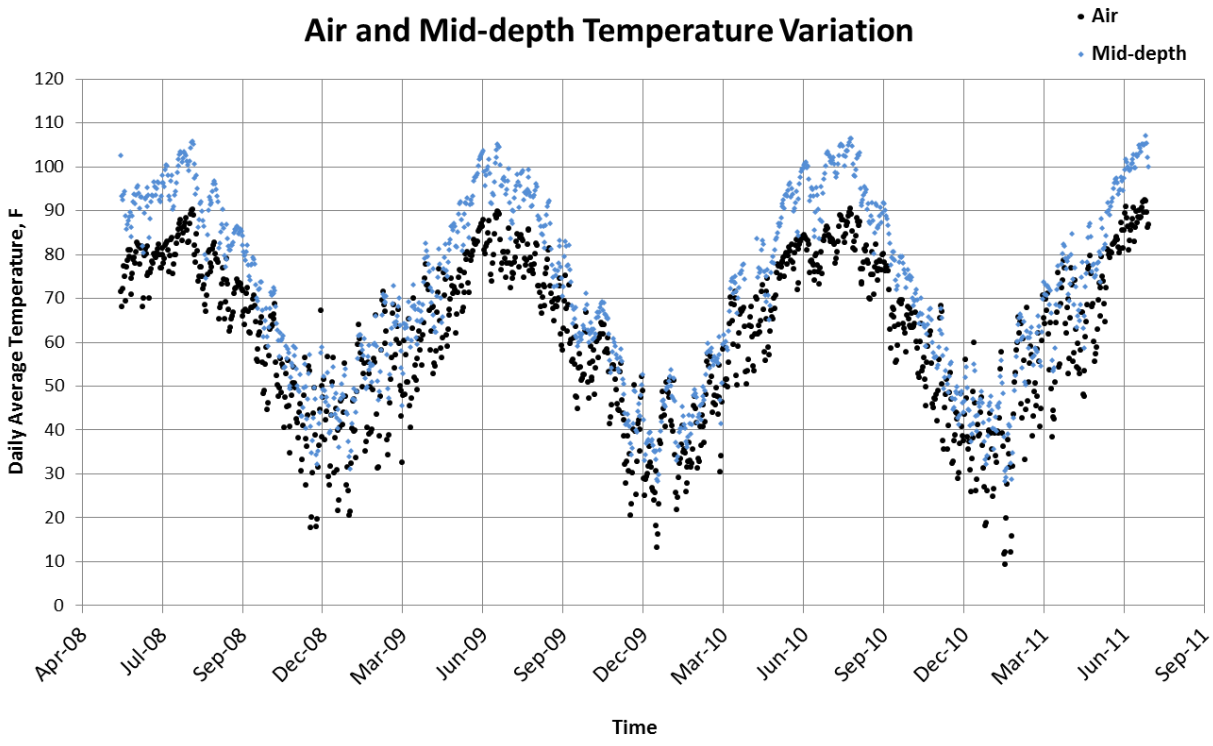

Figure 4-10 The Daily Average Air and Mid-depth Temperature at the Test Section

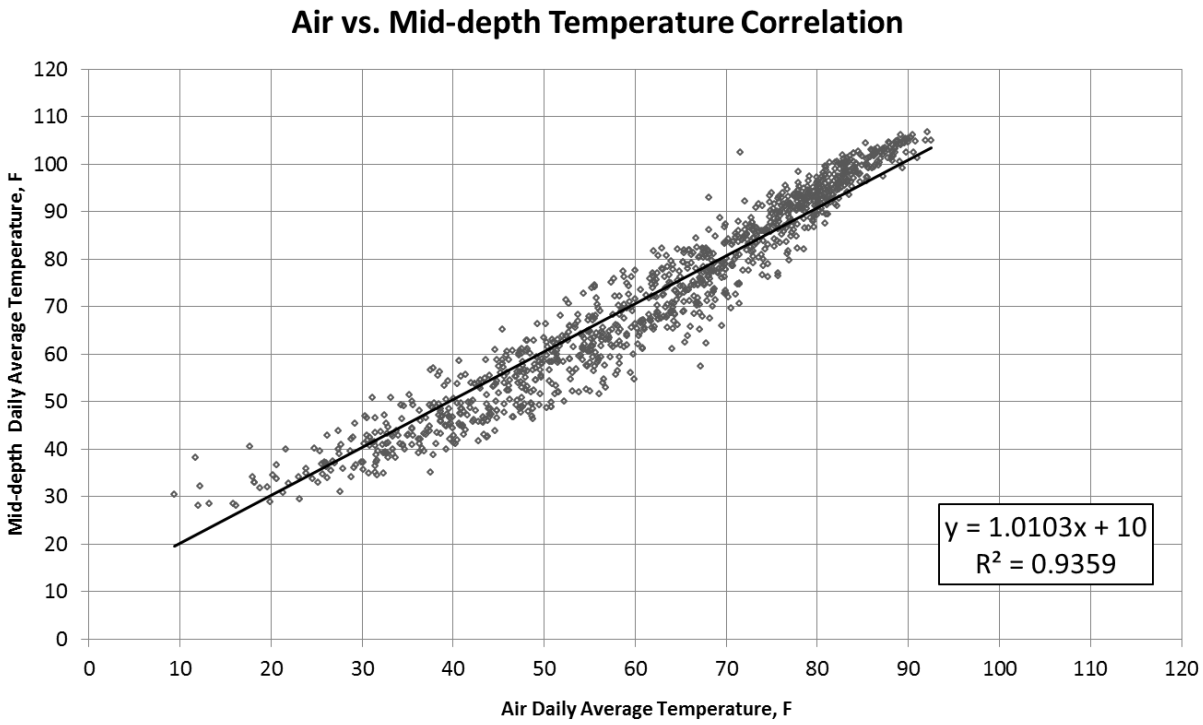

Figure 4-11 Air and Mid-depth Temperature Correlation

Figure 4-12 Automated Traffic Counter, ADR 3000

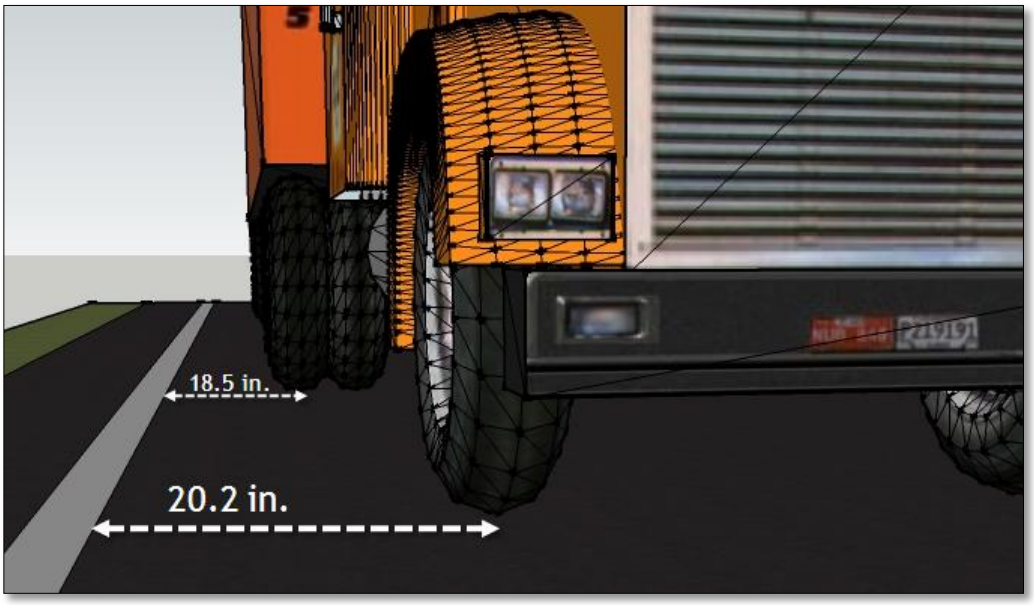

Figure 4-13 Distances Used in Calculating Wheel Wander

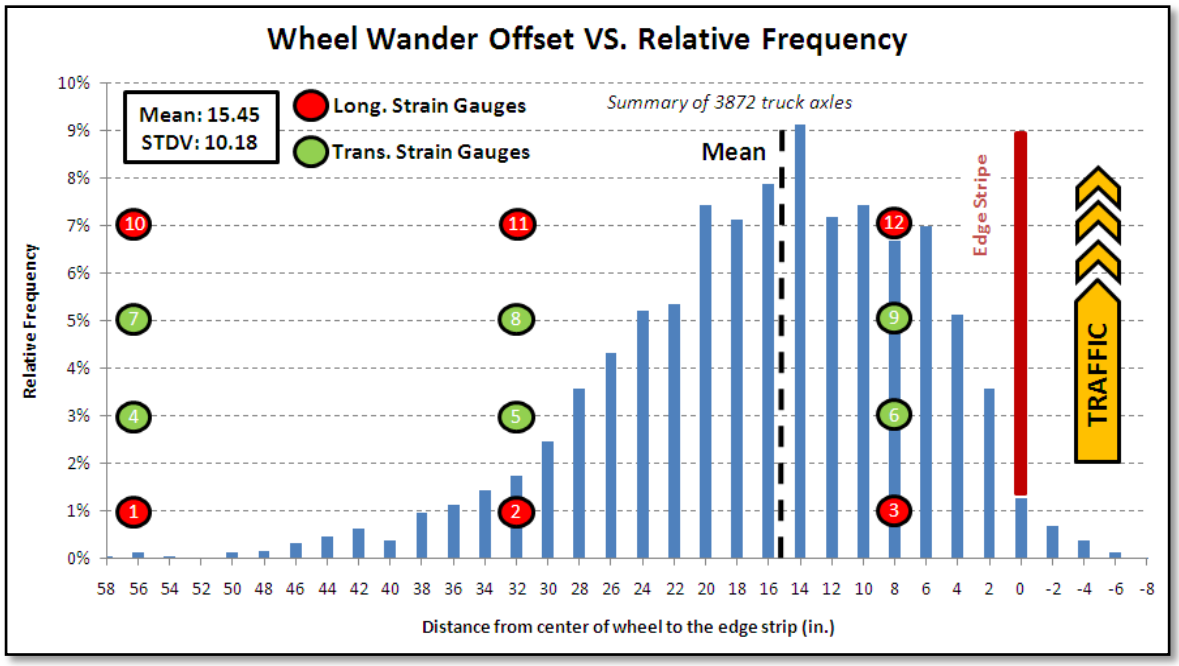

Figure 4-14 Statistical Distribution of Wheel Wander Data

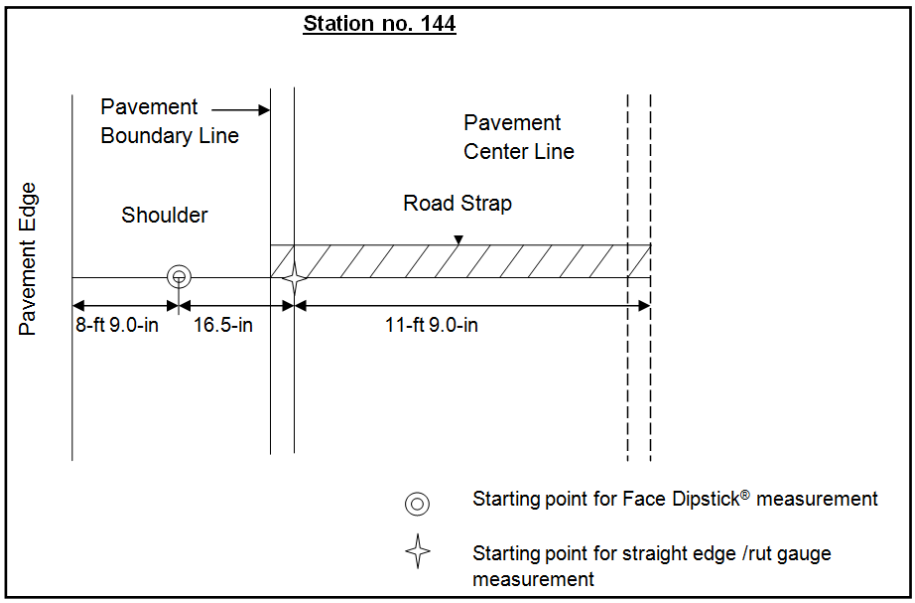

Figure 4-15 Rough Sketch of Pavement Section at Station 144

Figure 4-16 Rut Measurements with Straight Edge/Rut Gauge Combination

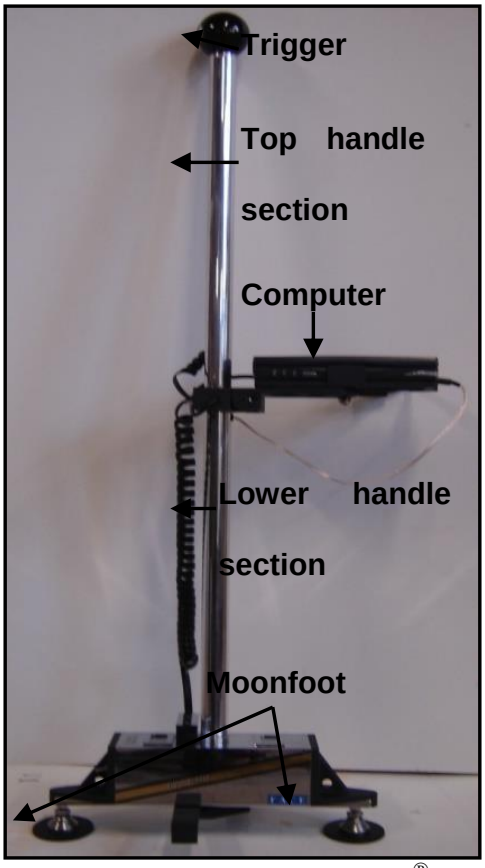

Figure 4-17 Face Dipstick®


Figure 4-18 Marking the Starting Point for Face Dipstick® Data Collection

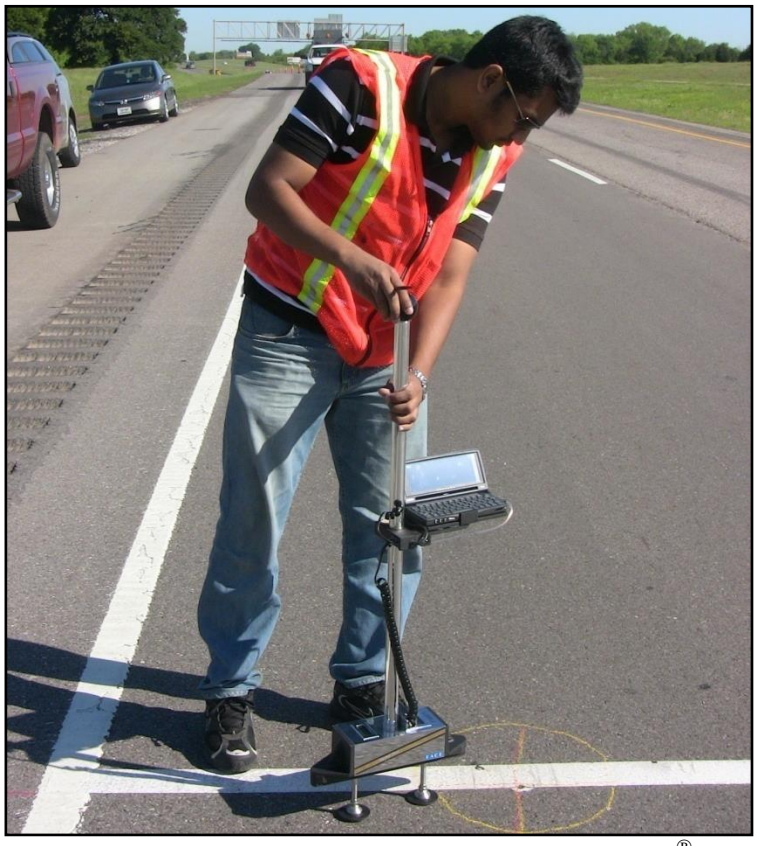

Figure 4-19 Data Collection with Face Dipstick®

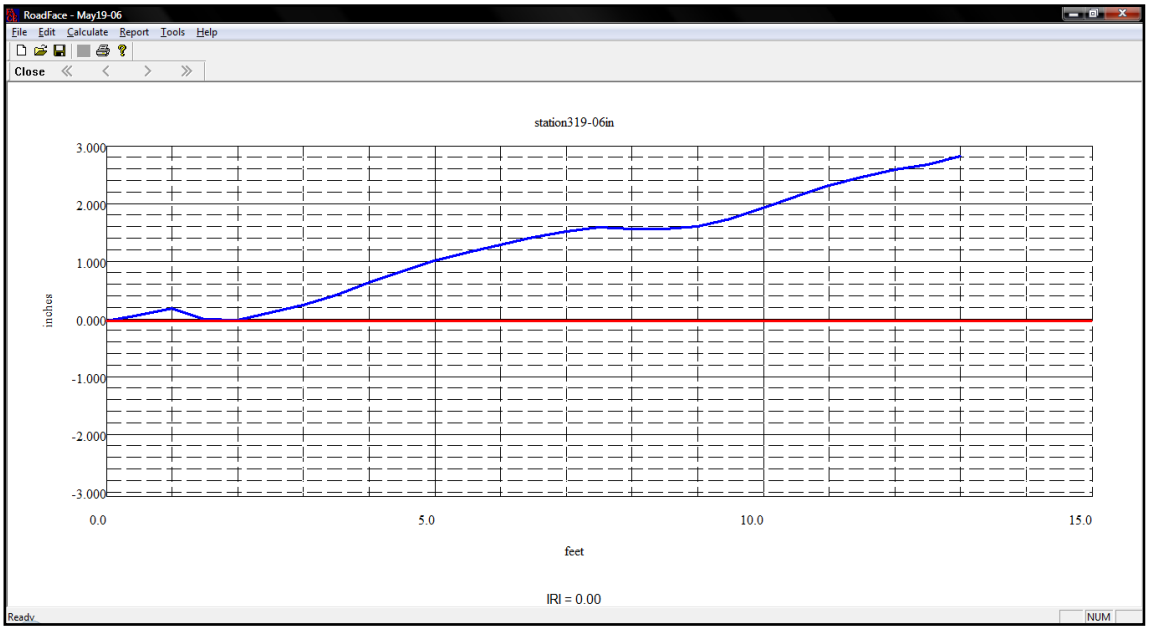

Figure 4-20 Graphical View of the Test Section at Station 319 (Obtained from RoadFace 6.0 Software)

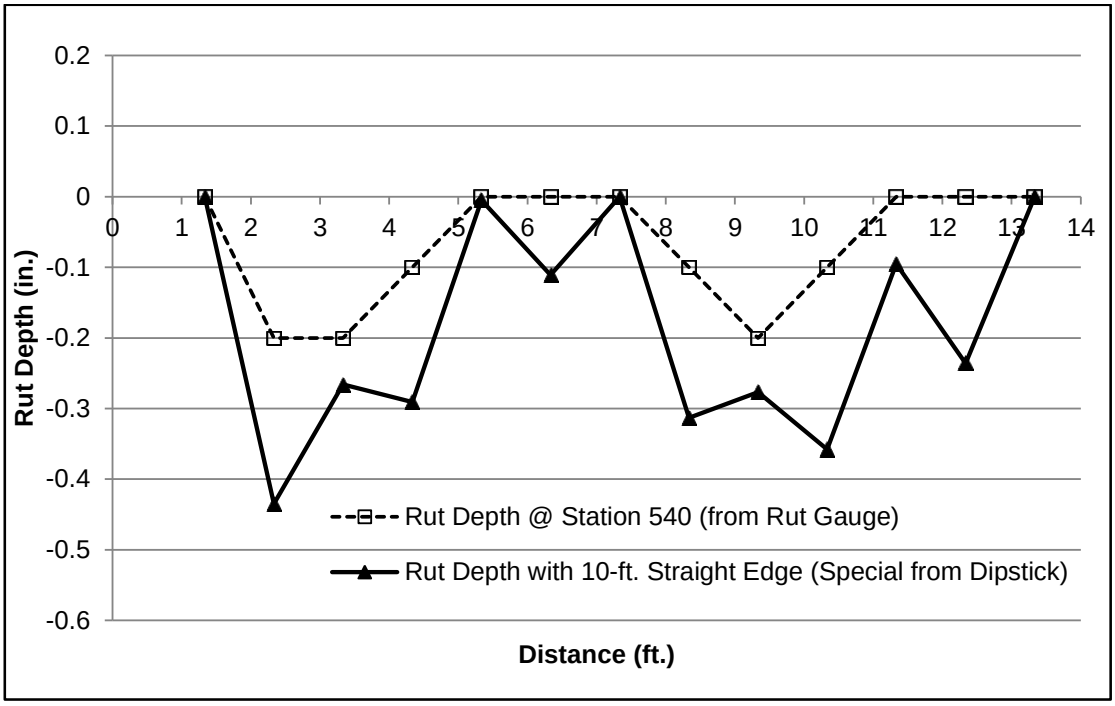

Figure 4-21 Comparison of Rut Depth between Face Dipstick® and Rut Gauge at Station 540

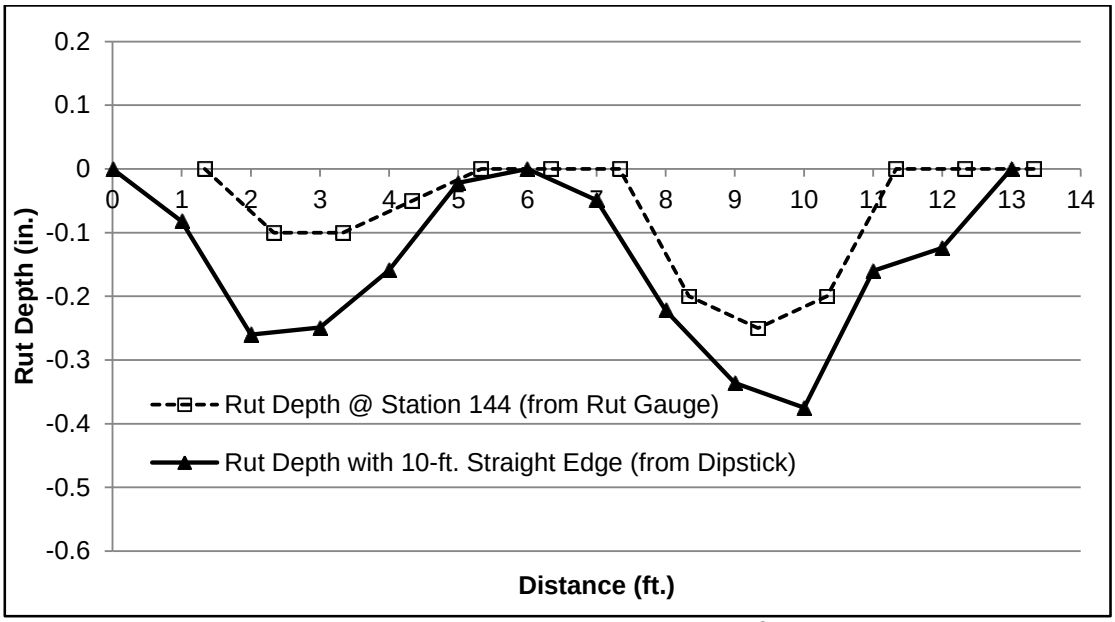

Figure 4-22 Comparison of Rut Depth between Face Dipstick® and Rut Gauge at Station 144

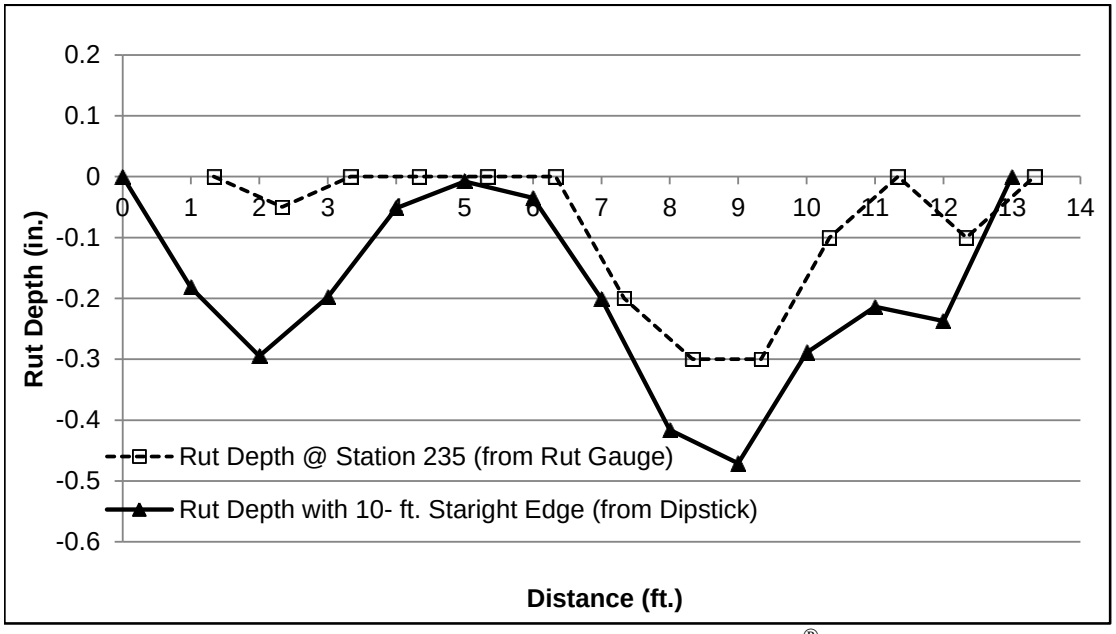

Figure 4-23 Comparison of Rut Depth between Face Dipstick® and Rut Gauge at Station 235

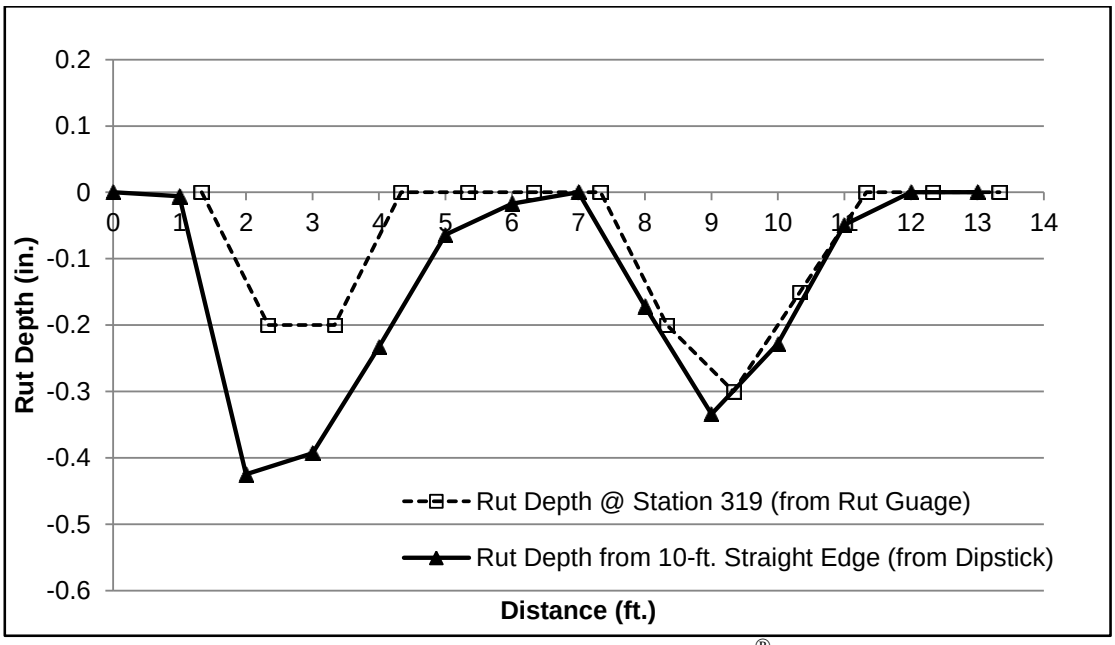

Figure 4-24 Comparison of Rut Depth between Face Dipstick® and Rut Gauge at Station 319

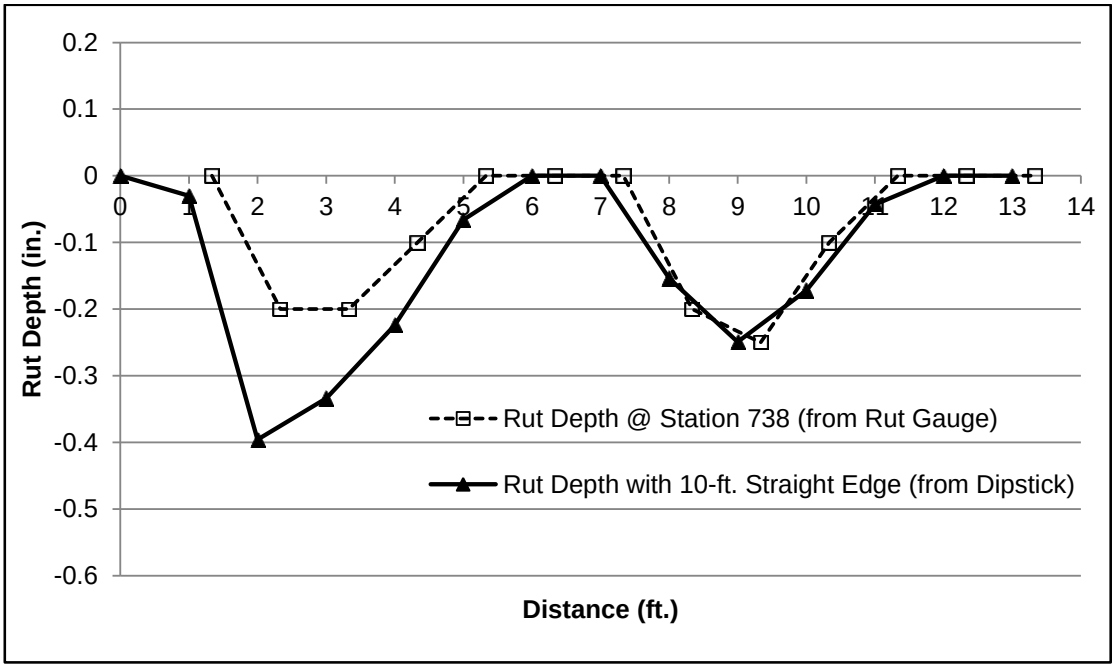

Figure 4-25 Comparison of Rut depth between Face Dipstick® and Rut Gauge at Station 738

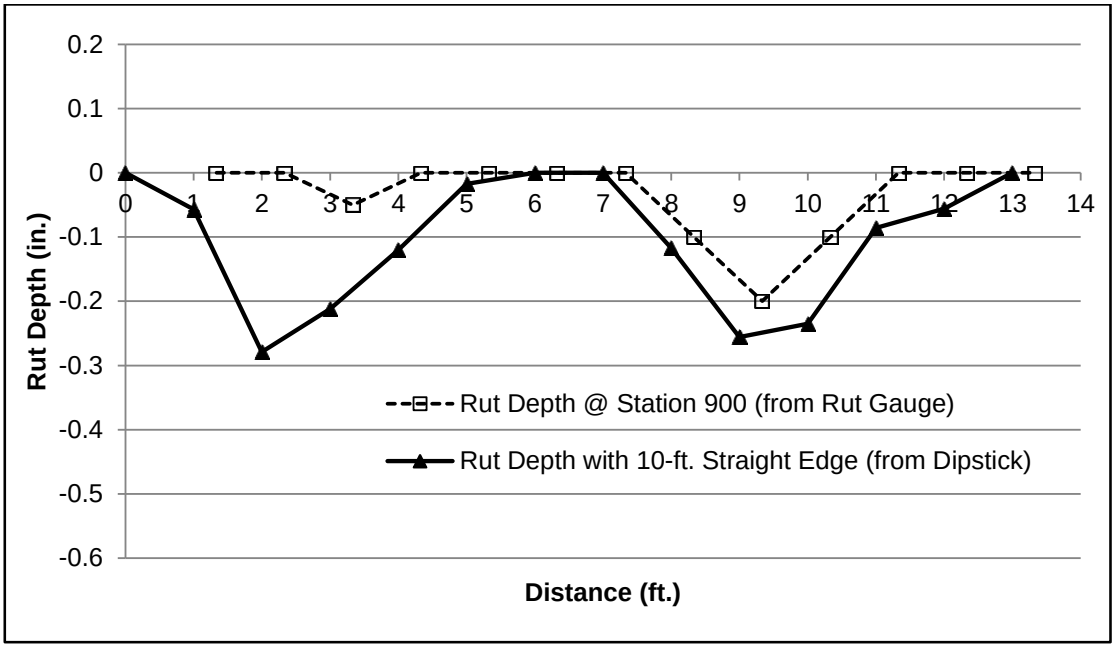

Figure 4-26 Comparison of Rut Depth between Face Dipstick® and Rut Gauge at Station 900

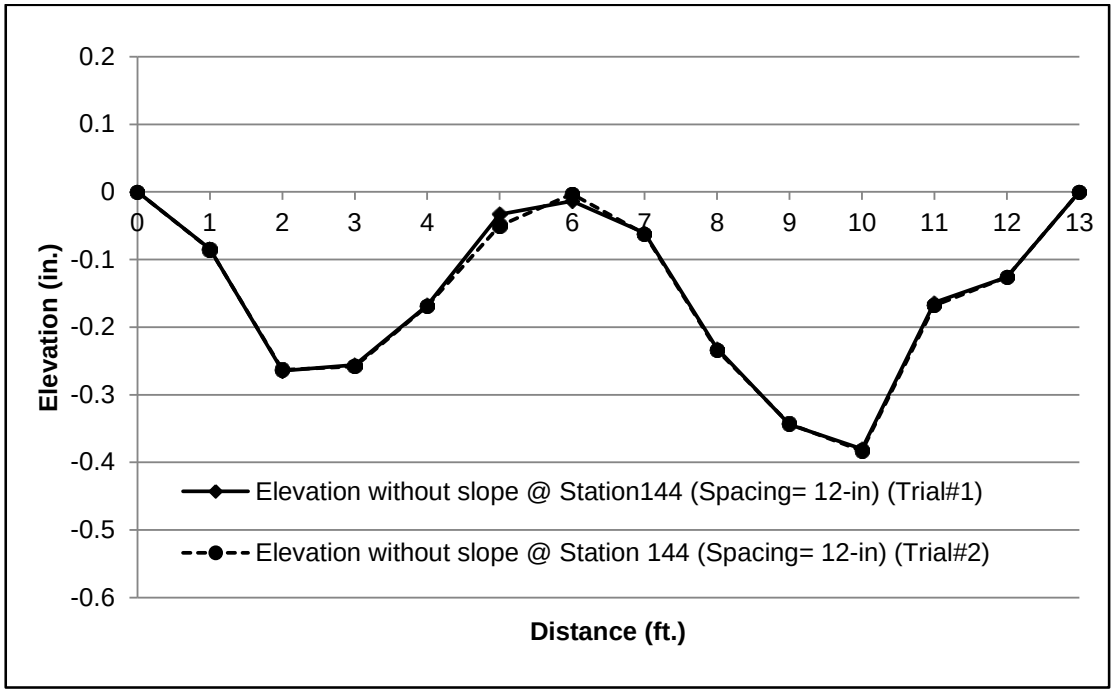

Figure 4-27 Pavement Profile without Slope at Station 144 (Moonfoot Spacing = 12-in.)

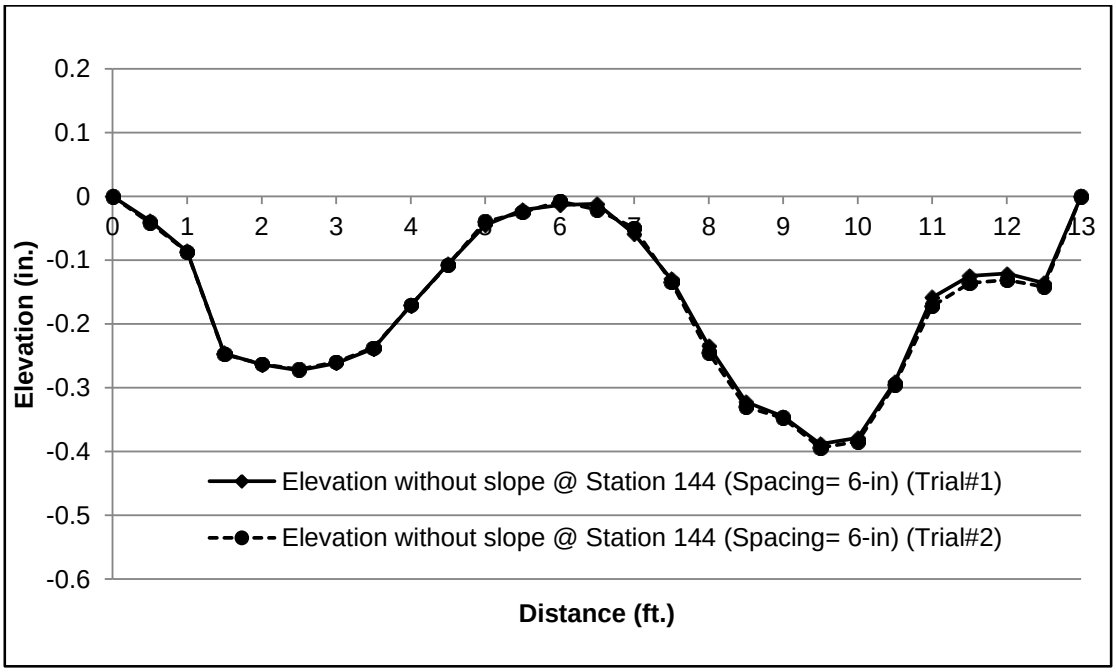

Figure 4-28 Pavement Profile without Slope at Station 144 (Moonfoot Spacing = 6-in.)

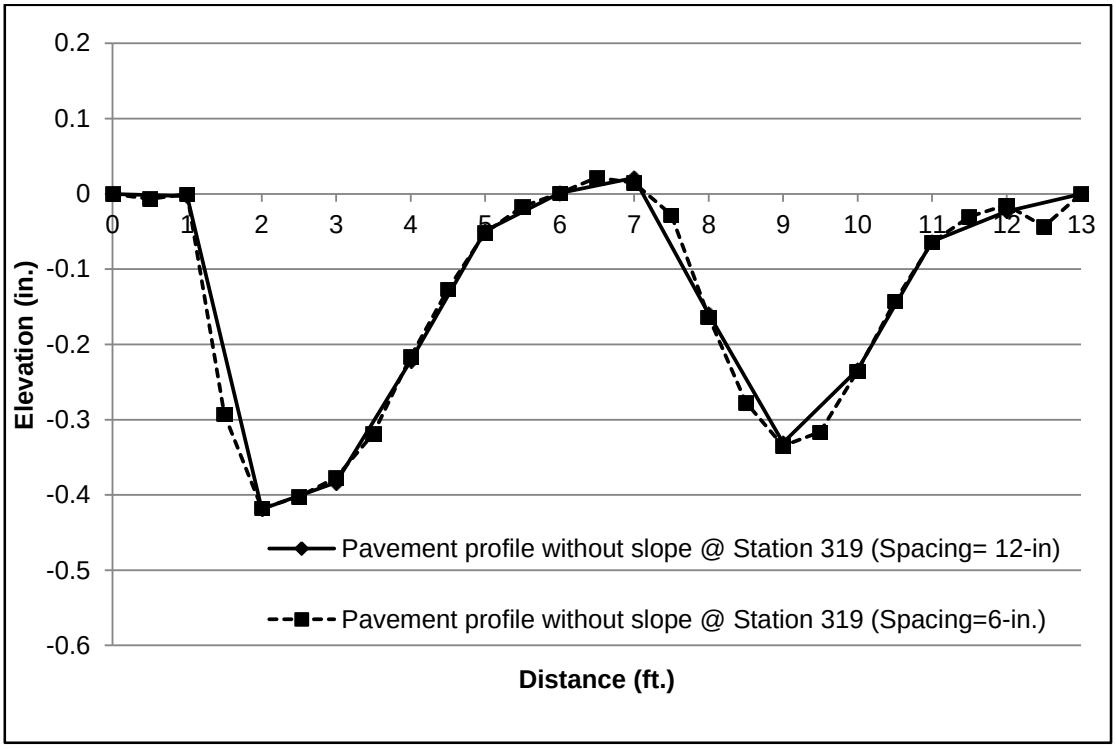

Figure 4-29 Superimposed Pavement Profile at Station 144 with Moonfoot Spacing 6-in. and 12-in.

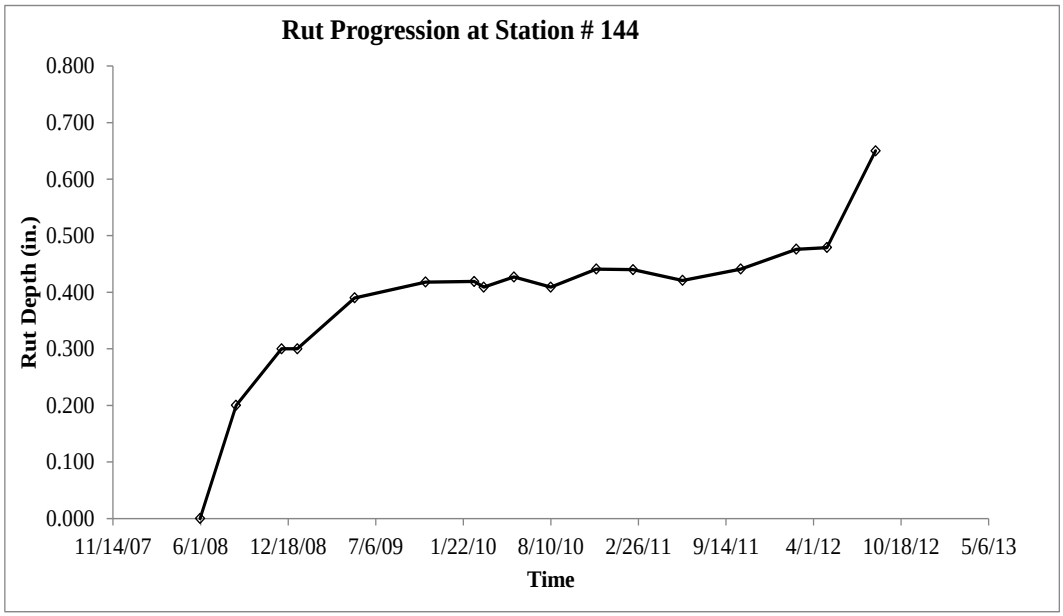

Figure 4-30 Rut Progression at Station No. 144

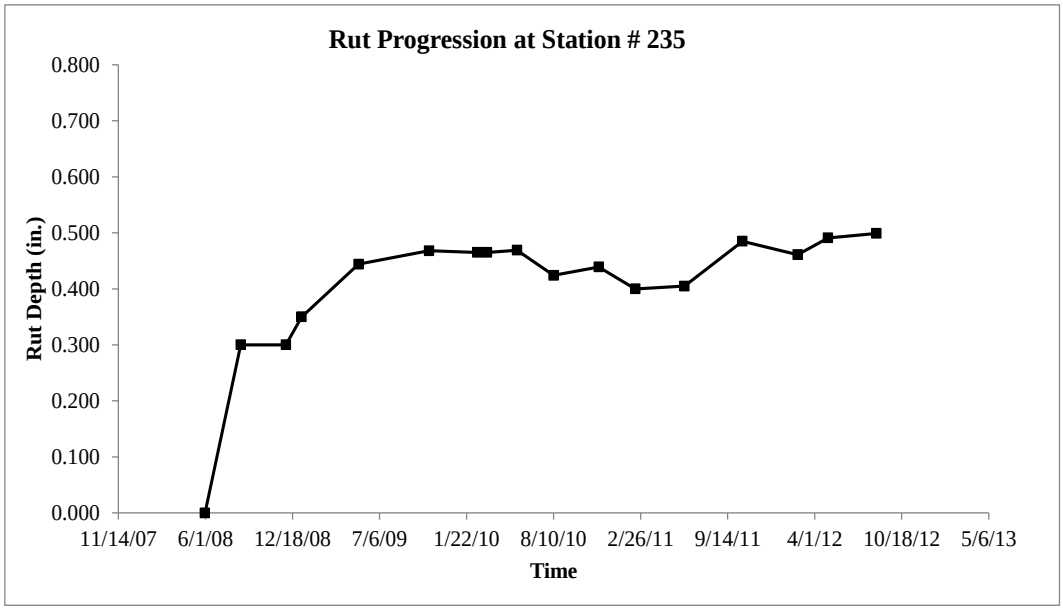

Figure 4-31 Rut Progression at Station No. 235

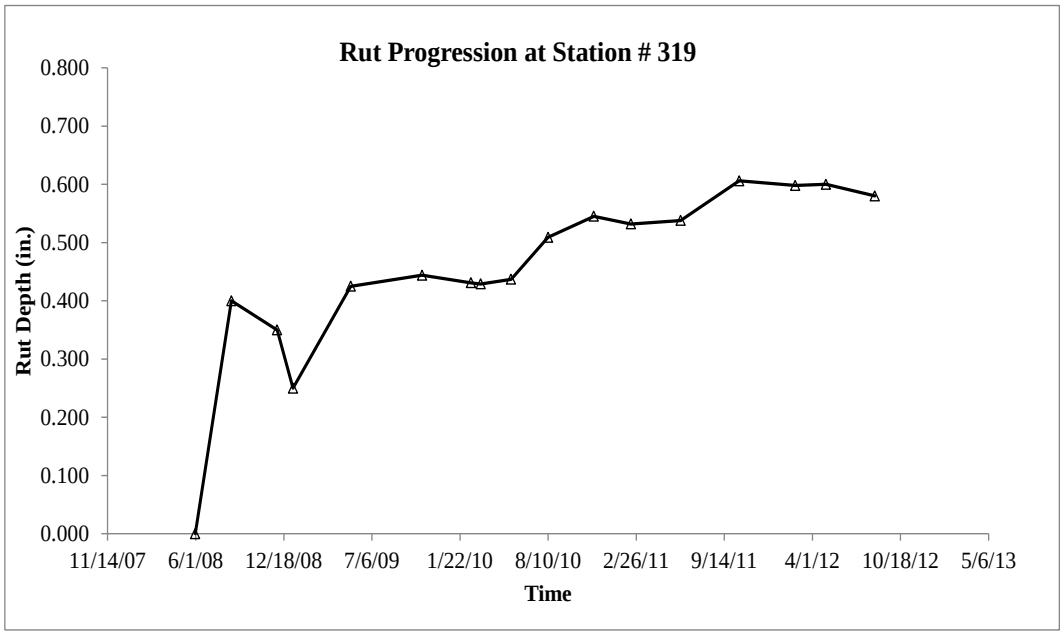

Figure 4-32 Rut Progression at Station No. 319

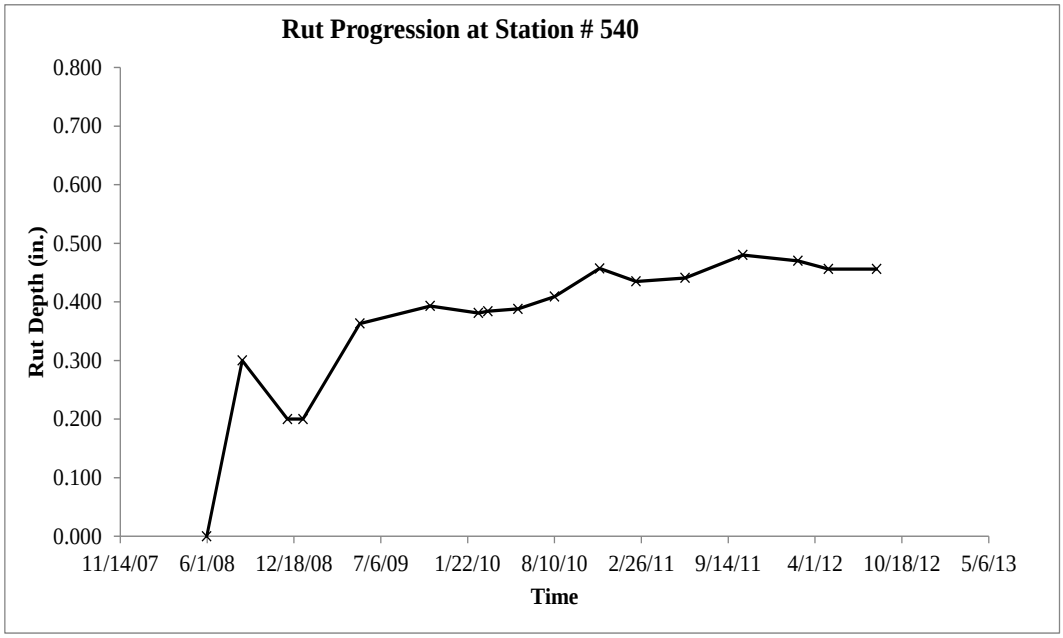

Figure 4-33 Rut Progression at Station No. 540

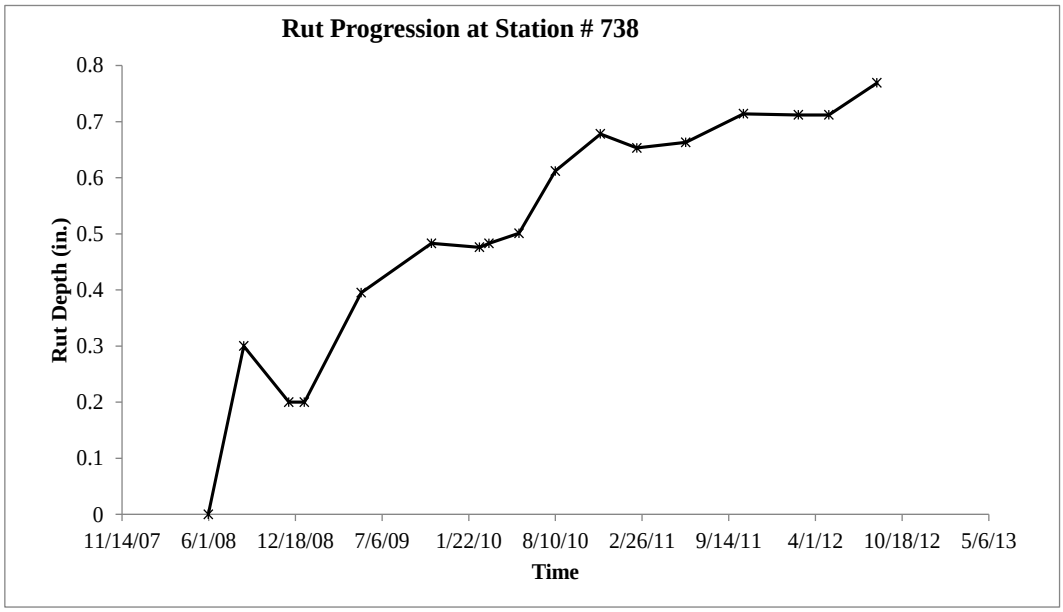

Figure 4-34 Rut Progression at Station No. 738

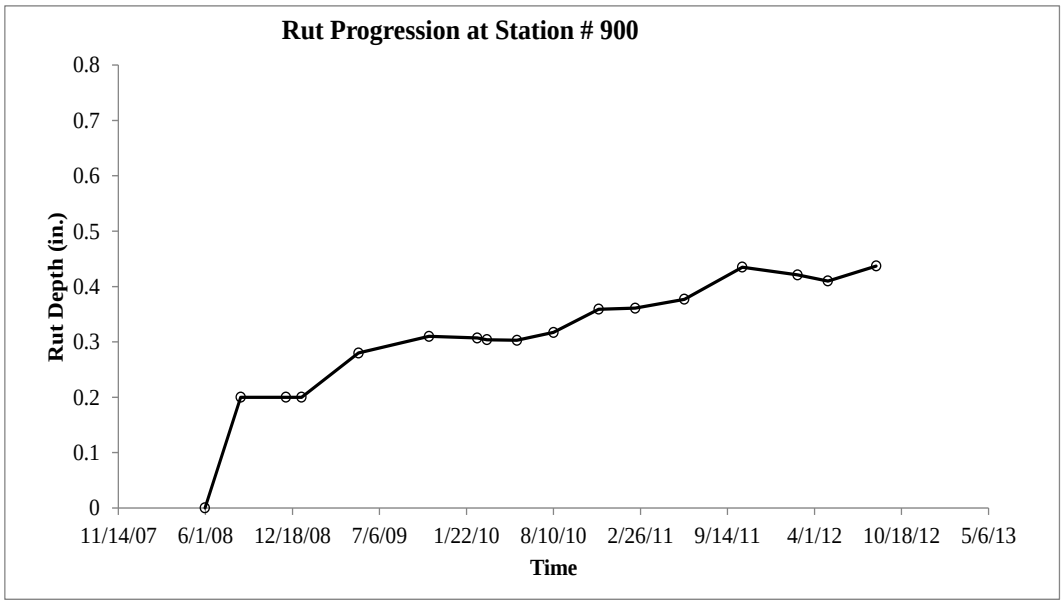

Figure 4-35 Rut Progression at Station No. 900

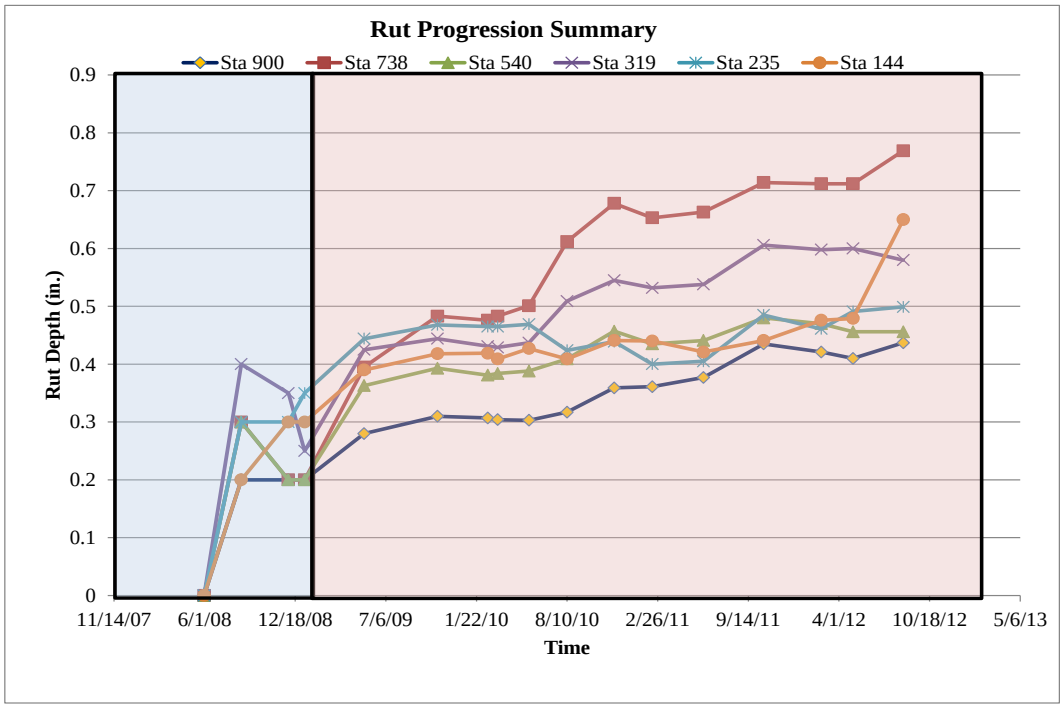

Figure 4-36 A Summary of Rut Progression on the Test Section

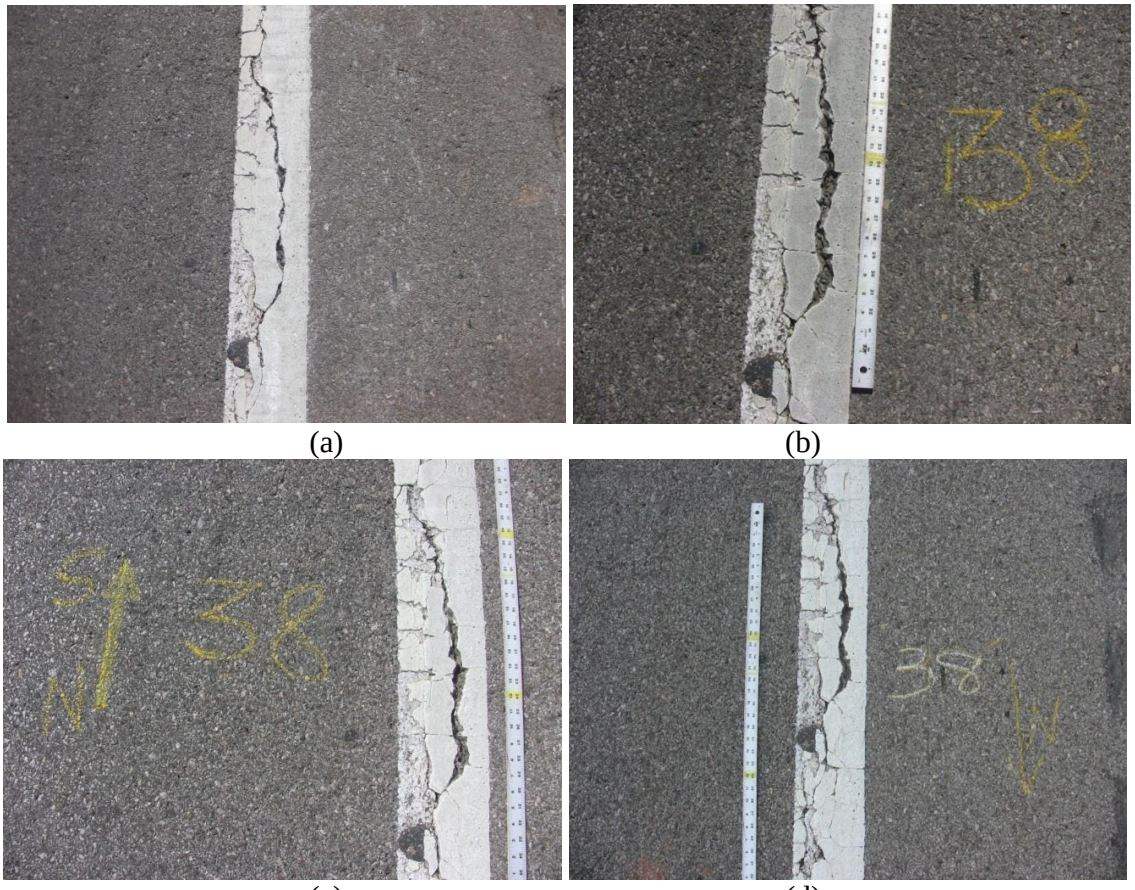

(a) (b)

(c) (d)

Figure 4-37 Photographic View of Construction Joint at a Distance of 38-ft from North End of the Test Section on (a) February 14, 2011, (b) February 22, 2012, (c) May 02, 2012, and (d) August 21, 2012

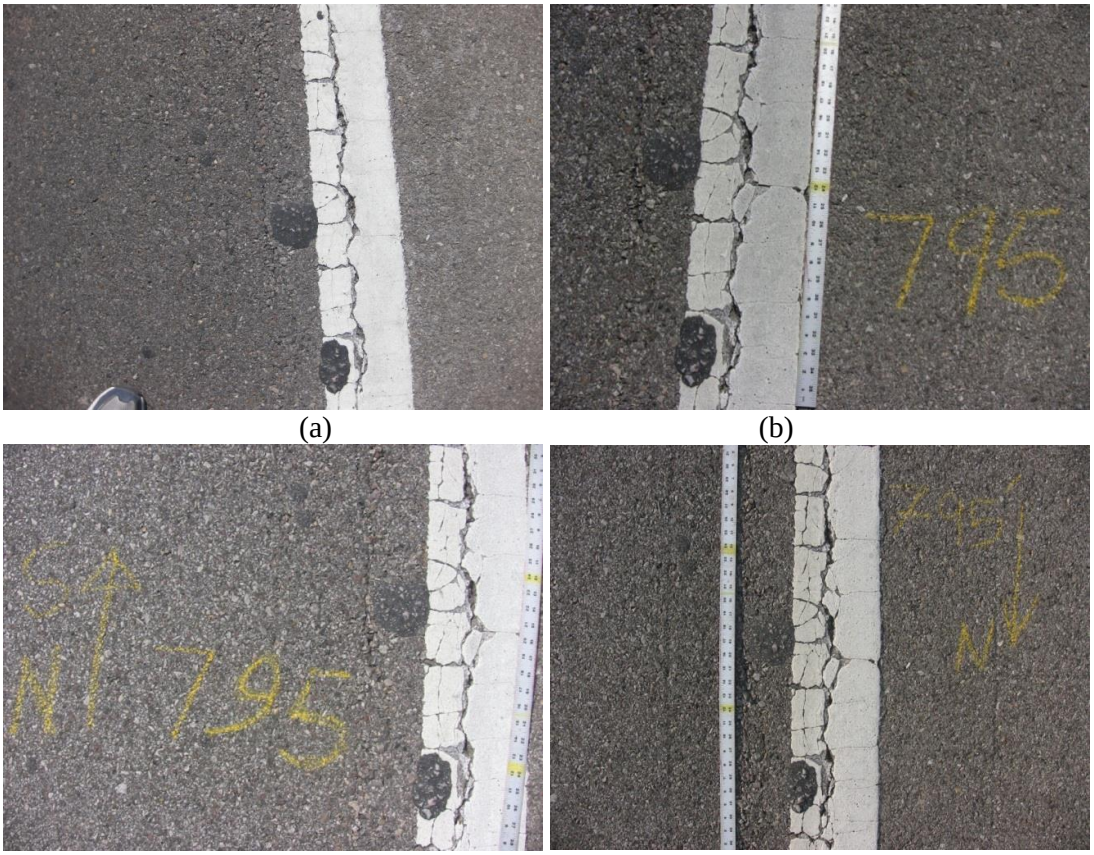

(a) (b)

(c)

Figure 4-38 Photographic View of Construction Joint at a Distance of 795-ft from North End of the Test Section on (a) February 14, 2011, (b) February 22, 2012, (c) May 02, 2012, and (d) August 21, 2012

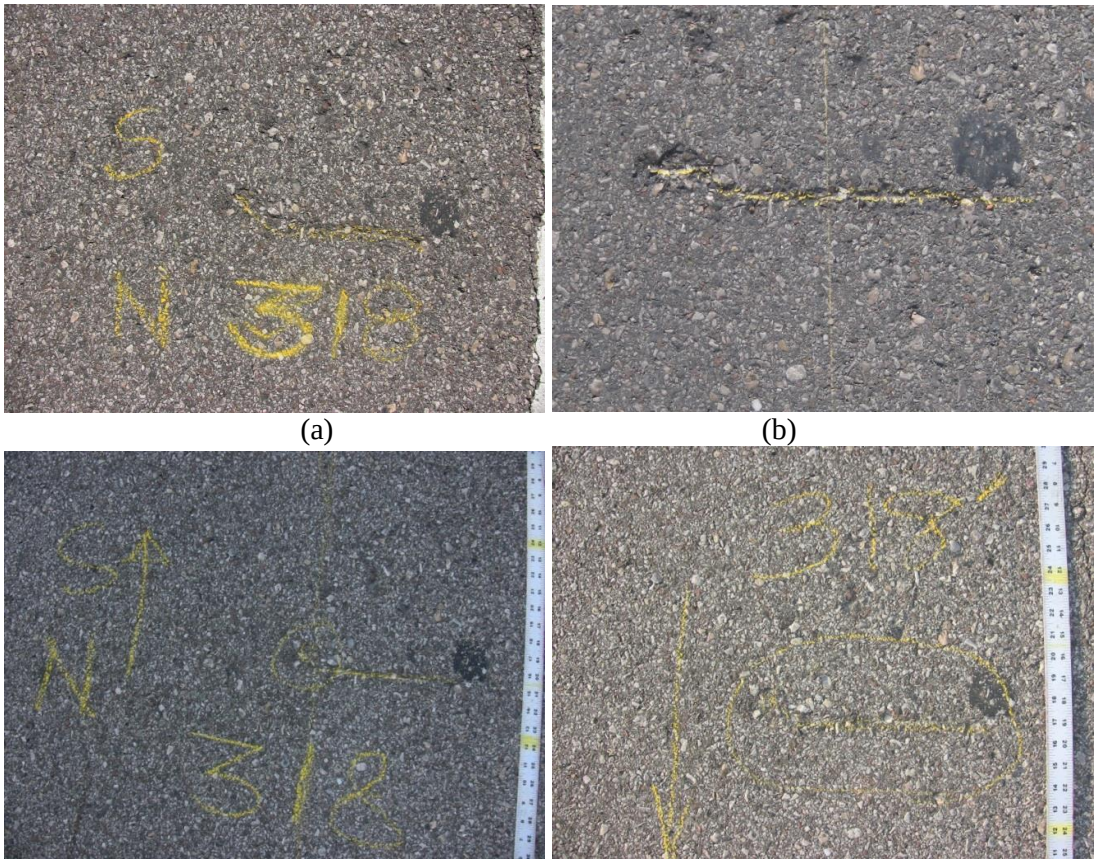

(a) (b)

(c)

Figure 4-39 Photographic View of Loss of Aggregates from Pavement at a Distance of 318-ft and from North End of the Test Section on (a) February 14, 2011, (b) February 22, 2012, (c) May 02, 2012, and (d) August 21, 2012

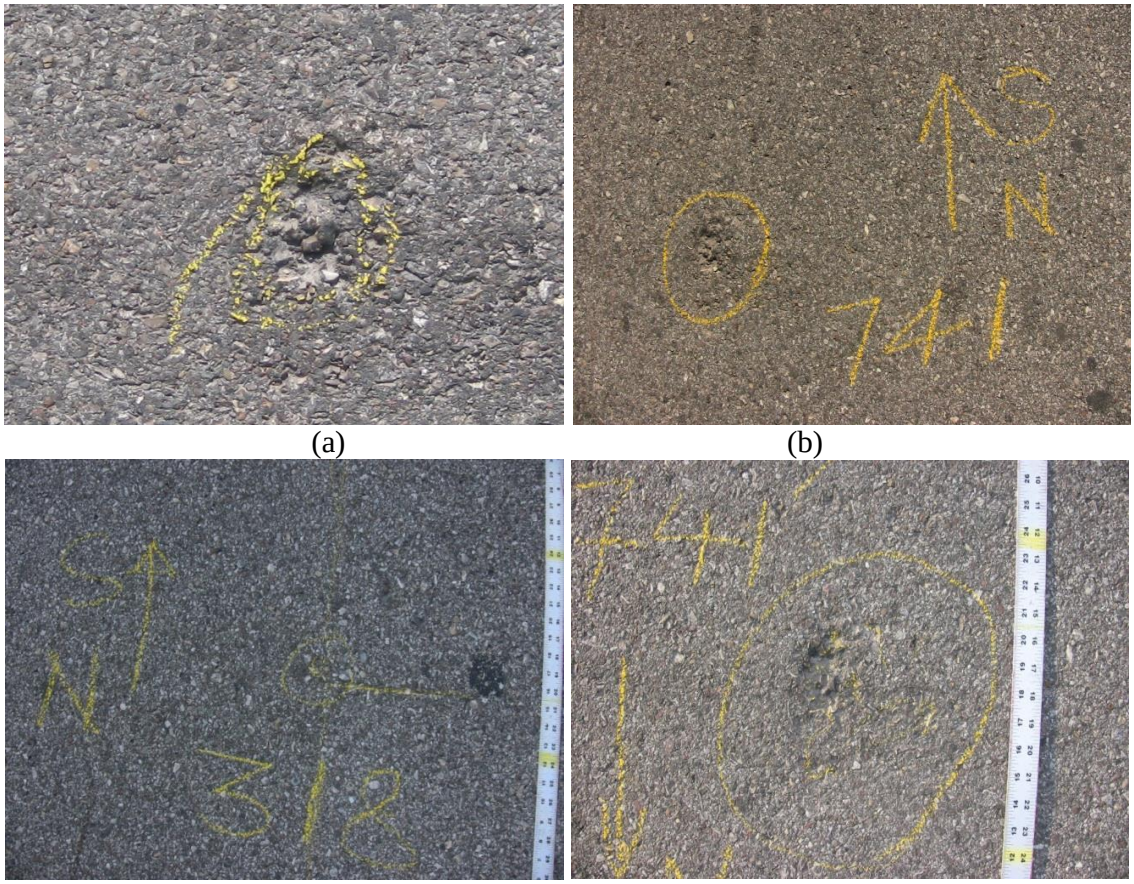

(a) (b)

(c)

Figure 4-40 Photographic View of Loss of Aggregates from Pavement at a Distance of 741-ft and from North End of the Test Section on (a) February 14, 2011, (b) February 22, 2012, (c) May 02, 2012, and (d) August 21, 2012

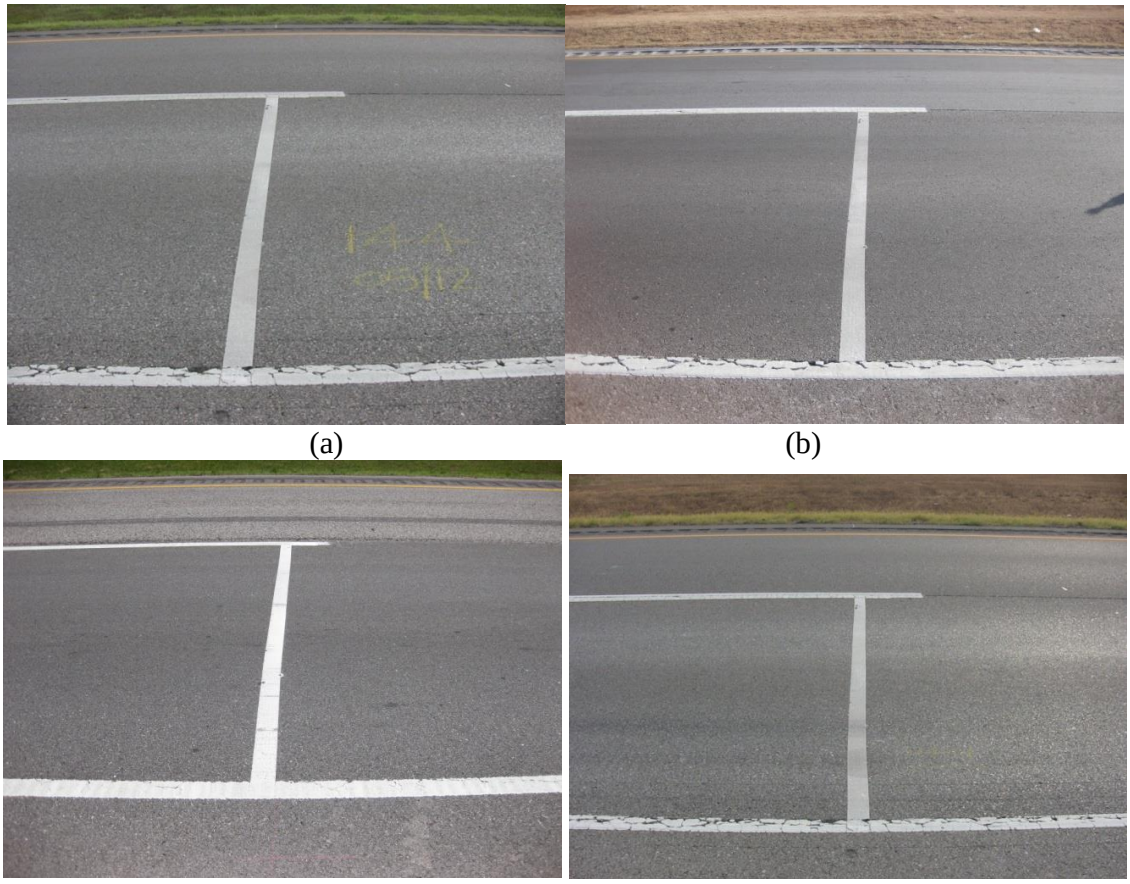

(a) (b)

(c) (d)

Figure 4-41 Photographic View of Pavement Surface at Station No. 144 taken on (a) June 05, 2009, (b) February 14, 2011, (c) May 02, 2012, and (d) August 21, 2012

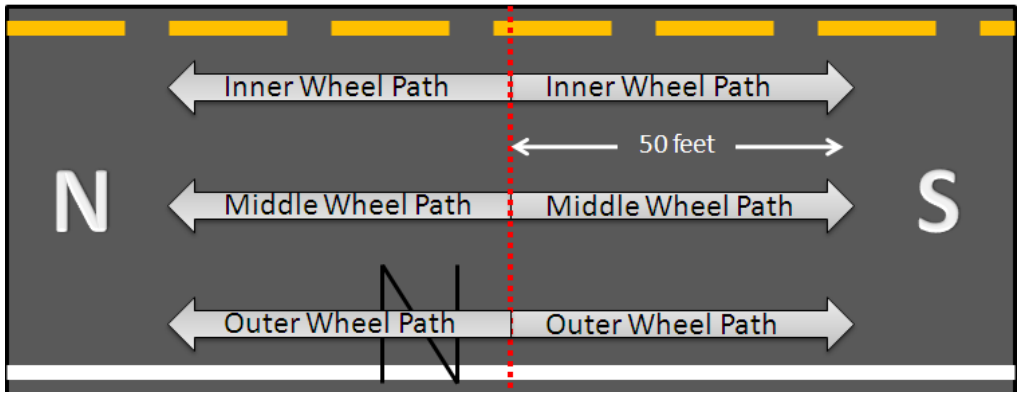

Figure 4-42 Sketch of IRI Locations on the Test Section

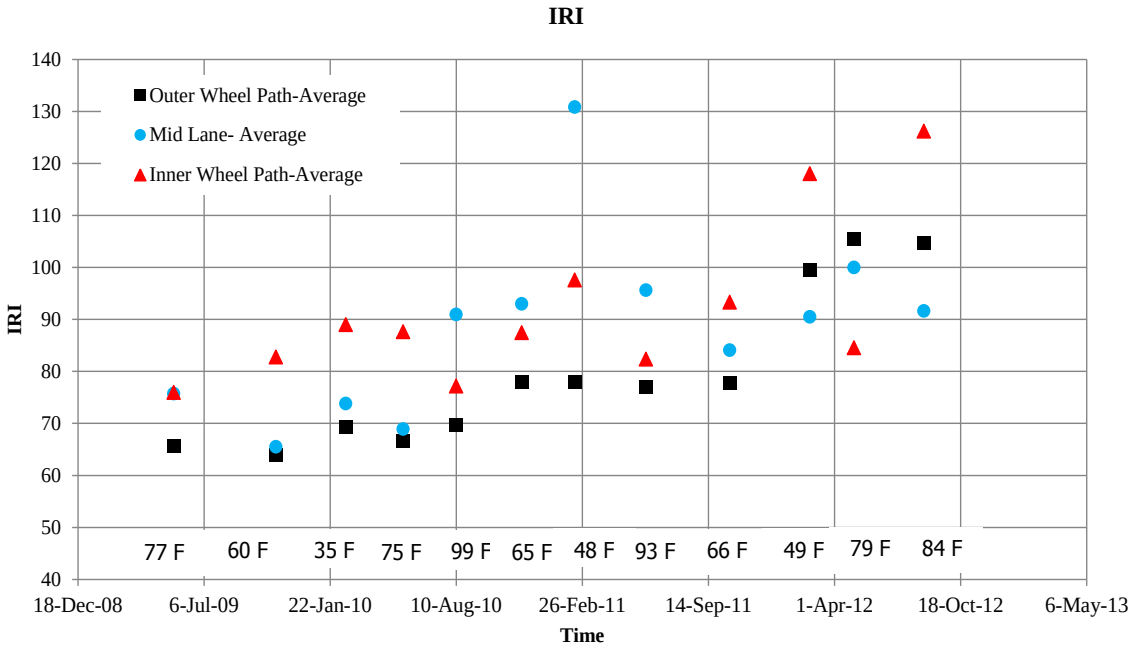

Figure 4-43 Progression of IRI Values with Time and Temperature

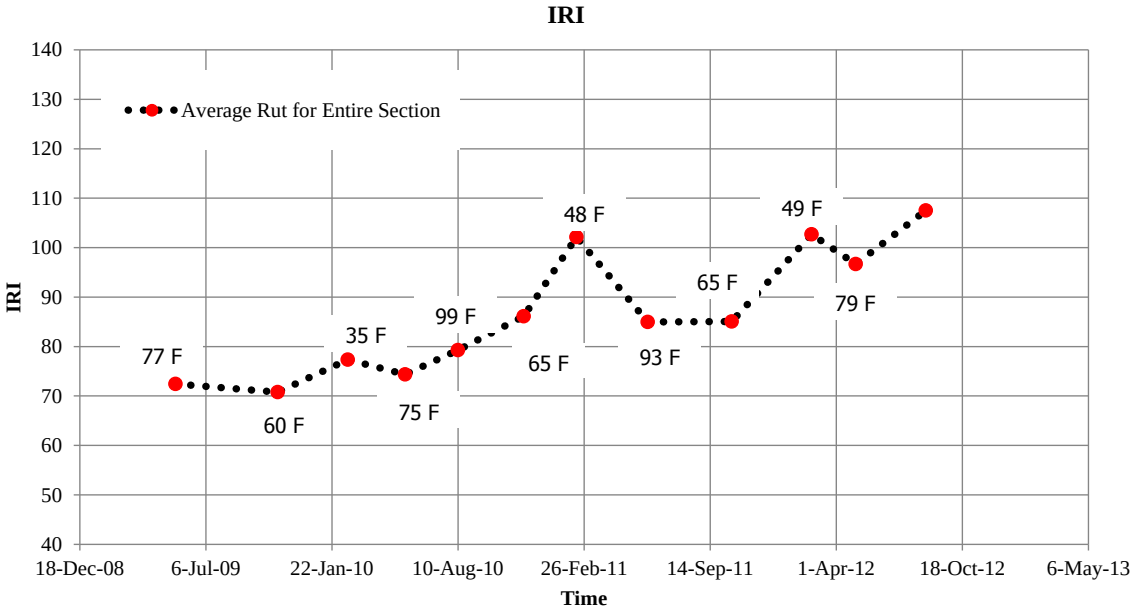

Figure 4-44 Progression of Average IRI Values with Time and Temperature

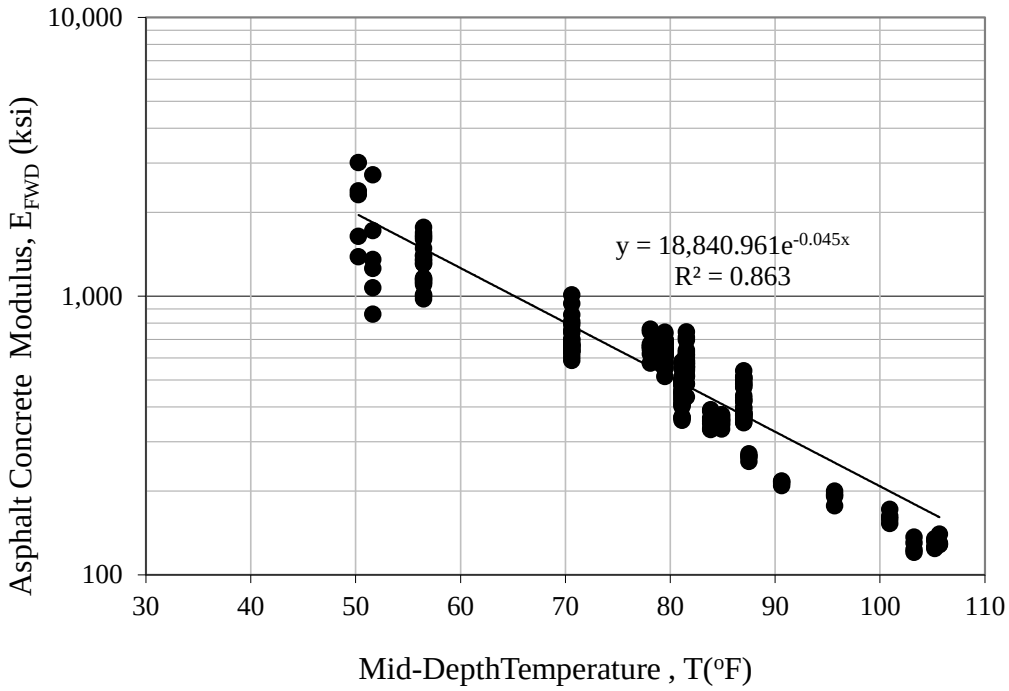

Figure 4-45 Variation of Asphalt Concrete Modulus with Mid-Depth Temperature (May 16, 2008 through October 28, 2009)

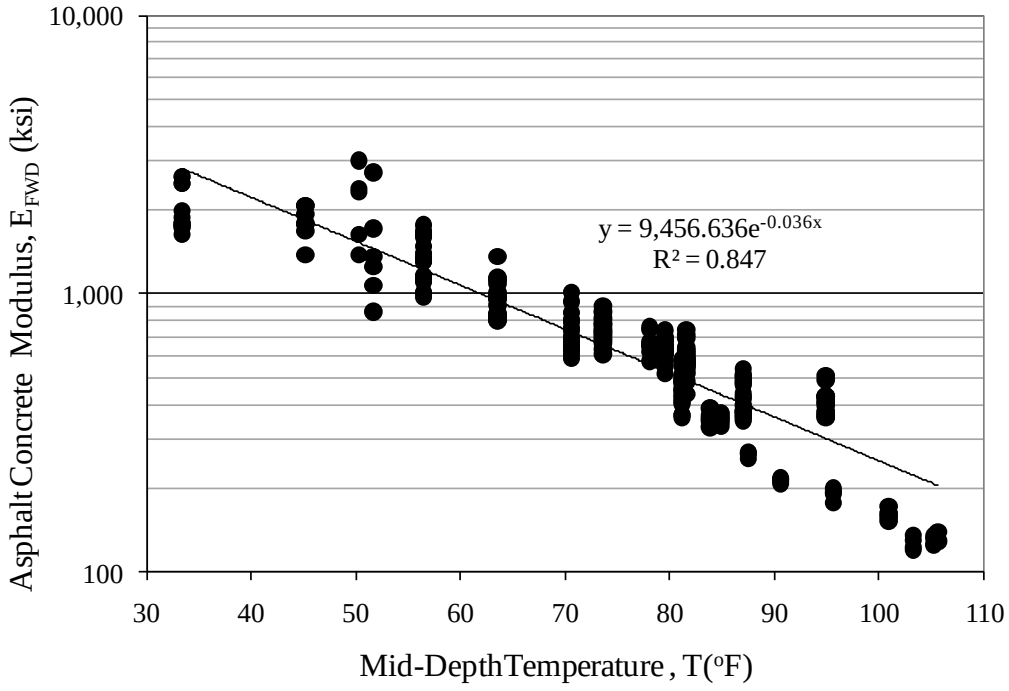

Figure 4-46 Variation of Asphalt Concrete Modulus with Mid-Depth Temperature (May 16, 2008 through February 14, 2011)

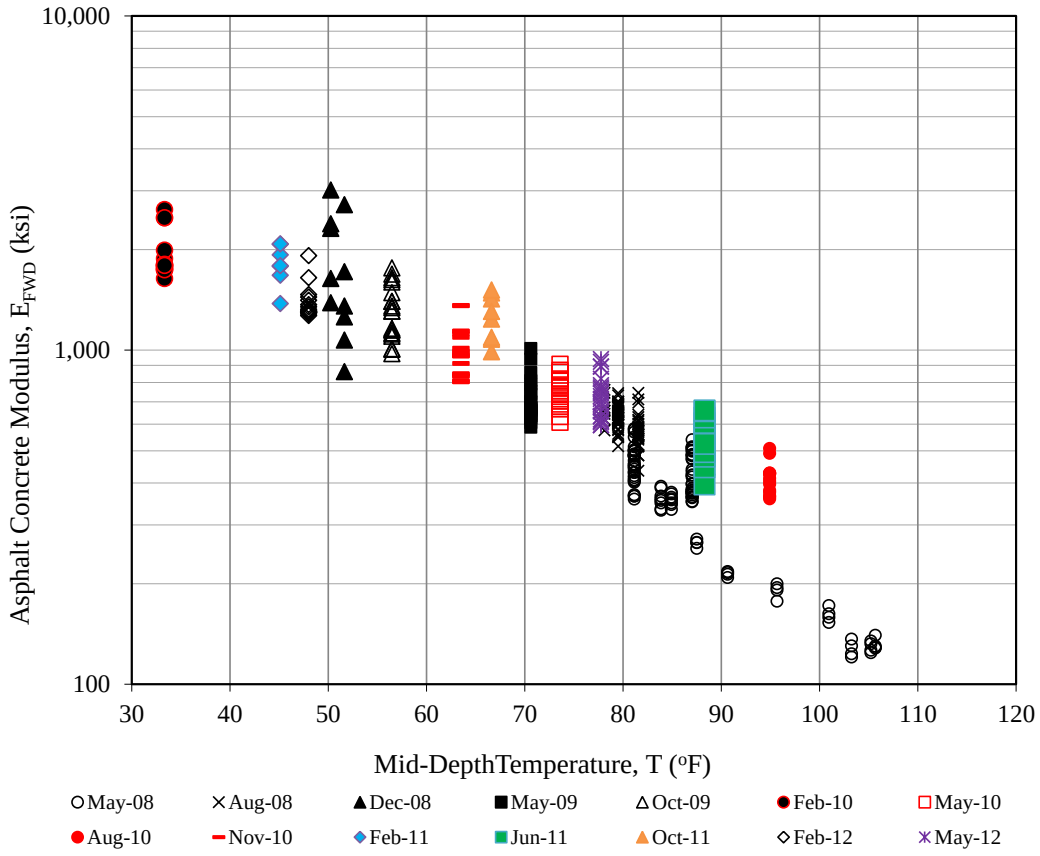

Figure 4-47 Variation of Asphalt Concrete Modulus with Mid-Depth Temperature (May 16, 2008 through February 14, 2011)

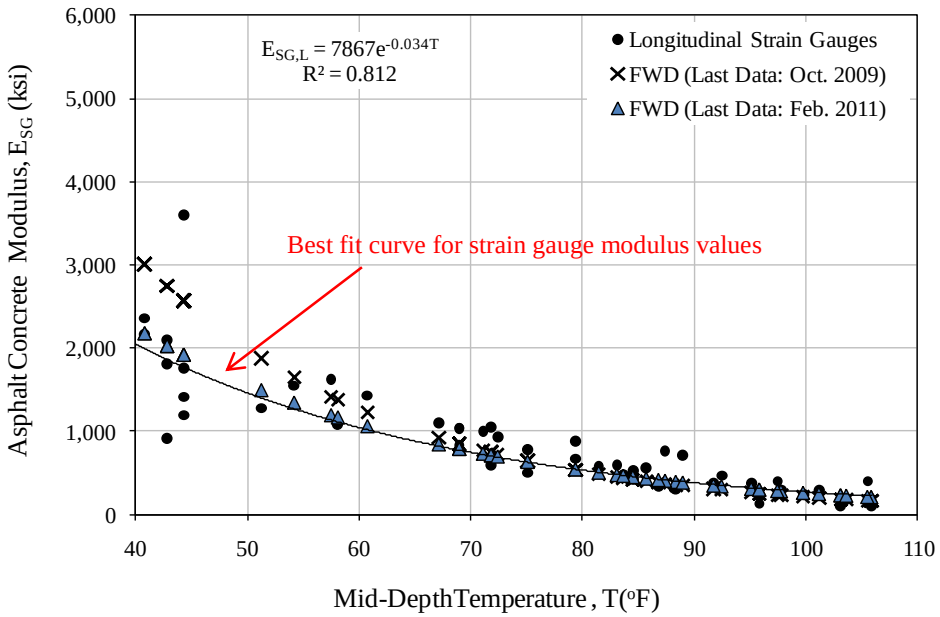

Figure 4-48 Back-calculated Modulus Values from Longitudinal Strain Gauges Versus Mid-Depth Temperature (on Linear Scale)

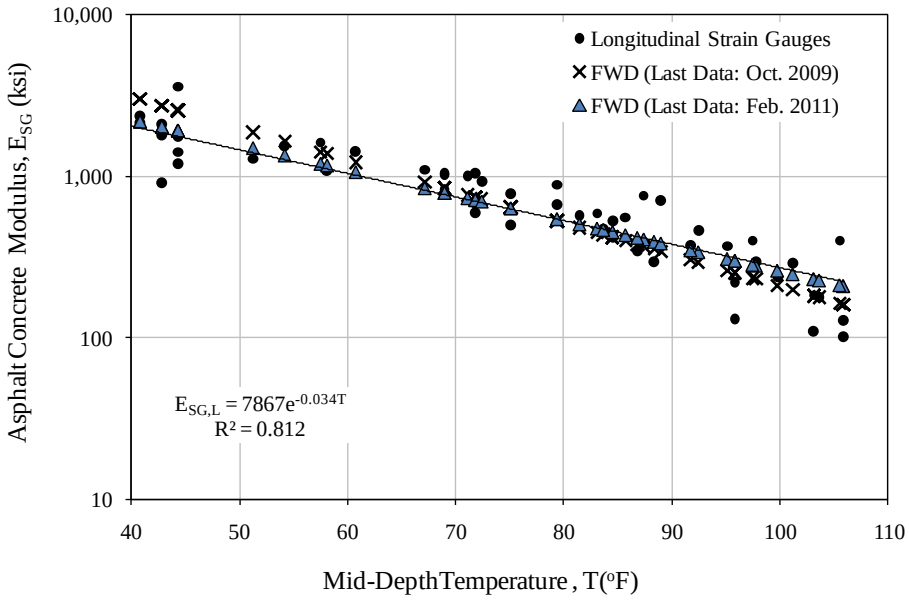

Figure 4-49 Back-calculated Modulus Values from Longitudinal Strain Gauges Versus Mid-Depth Temperature (On Semi-Logarithmic Scale)

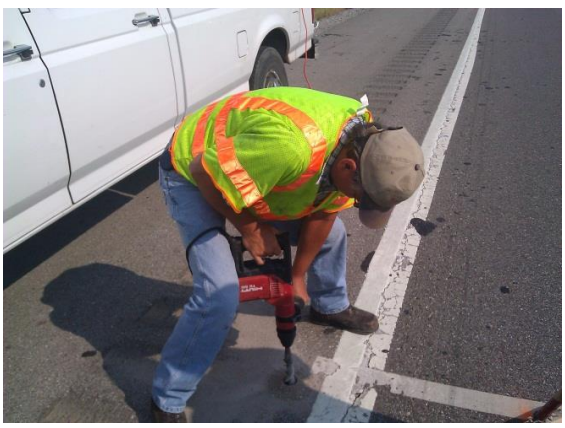

(a)

(b)

(c)

Figure 4-50 (a) Drilling of Hole for DCP Test, (b) DCP Test in Progress, and (c) Collection of Soil Sample for Moisture Content Test

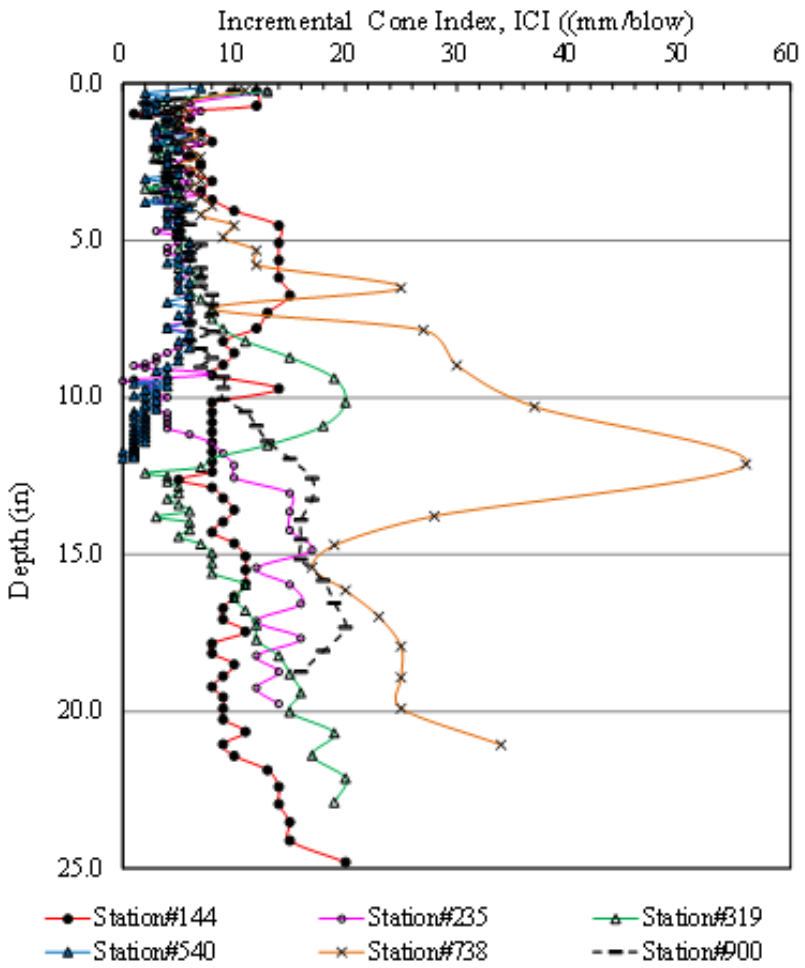

Figure 4-51 Summary of Dynamic Cone Penetrometer Test Results Conducted on June 07, 2011

Chapter 5 LABORATORY TESTING AND RUT MODEL DEVELOPMENT

5.1 Introduction

This chapter presents the details of the development of rut prediction model based on laboratory rut test data. It consists of two sections. The first section presents the sources of materials, sample preparation, and laboratory test procedures. The second section presents the test results and rut prediction model development.

5.2 Laboratory Rut Tests

In this study, a total of 100 specimens were compacted at different air void levels using a Superpave Gyratory Compactor (SGC). The air voids of the compacted specimens ranged from 1% to 11%. The rut tests were conducted at different temperatures using an Asphalt Pavement Analyzer (APA) (see Table 5.1 for specifics). A total of 30, 26, and 44 specimens were tested in the APA at 40^{o}C (104°F), 50^{o}C (122°F), and 64^{o}C (147°F), respectively.

5.2.1 Sources of Materials

One of the objectives of this study was to examine the laboratory rut characteristics of HMA mixes used in the construction of the instrumented Test Section on I-35. In order to achieve this objective, 1000-lb (453-kg) of bulk HMA mix (Type S4) was collected from the site during the construction of the Test Section. The collected bulk mix was used to prepare specimens in the laboratory. A summary of the mix properties for the collected loose HMA mix is given in Table 5.2. Additional information on the HMA mix is presented in the mix-design sheet in Appendix A. It is evident from Table 5.2 that the Type S4 mix used in the

construction has a nominal maximum aggregate size (NMAS) of ½-in. (12.7-mm). A PG 64-22 binder, having a binder content of 4.6%, was used in producing the mix.

5.2.2 Sample Preparation and APA Rut Test

As noted earlier, 100 specimens were compacted in the laboratory. The following steps were followed to prepare these specimens, as described in the Oklahoma Highway Department (OHD) test specifications OHD L-43 (OHD, 2001). First, the theoretical maximum specific gravity (G_{mm}) test was performed on reference samples in accordance with the AASHTO T209 test specifications (AASHTO T 209, 1999). Then, the loose HMA mix was heated in an oven for approximately two hours at a temperature of 149^{o}C (300°F). The heated loose mix was then compacted in a SGC using a 6-in. (150-mm) diameter cylindrical mold to achieve a 3-in. (75-mm) height (Figure 5.1). The weight of the loose mix was predetermined to obtain the desired air voids. The number of gyrations needed to compact the specimens was dictated by the target air voids. The compacted specimens were kept overnight at room temperature and then bulk specific gravity tests were performed in accordance with the AASHTO T 166 test specifications (AASHTO T 166, 1999). The APA machine was calibrated for pressure and horizontal and vertical displacement measurements in accordance with the instructions given in the APA manual (PTI, 1999). Two specimens were placed in each of the three molds, used for conducting the rut testing. The specimens having similar air voids (±0.5%) were placed in the same mold, for consistency in results (Figure 5.2). Then, specimens along with the molds were preconditioned at the required temperatures [40^{o}C (104°F), 50^{o}C (122°F), or 64^{o}C (147°F), depending upon the test temperature selected] for a minimum of 6 hours inside the APA test chamber. Switching on the APA chamber and setting the duration of preconditioning time accomplished this. Following preconditioning, the

desired vertical wheel load of 100-lbf was applied and the hose pressure was set at 100-psi (689-kPa). The APA was allowed to run for 8,000 loading cycles in accordance with the OHD L-43 test specifications (OHD, 2001). The rut depth was measured as a function of loading cycles by the automated rut depth measuring system. Also, manual measurements were taken by a digital measuring gauge to compare with the rut depths measured automatically. The average rut depths of two specimens were reported as the rut depth at an average air void of two specimens. A photographic view of specimens after APA rut test is presented in Figure 5.3.

5.3 APA Rut Test Results

The APA rut test results for laboratory prepared specimens are shown in Tables 5.3, 5.4, and 5.5 for test temperatures of 40^{o}C (104°F), 50^{o}C (122°F), and 64^{o}C (147°F), respectively. The reported rut values correspond to 8,000 loading cycles. An outlier approach was employed to discard test results for a given sample if the results deviated from the average of rut values of specimens compacted within an air void range of ±1%. This method is explained in the ODOT specification, OHD L-43 (OHD, 2001). According to this method, the critical value for student test (*t*-statistic) is taken to be 1.155 as the *m*-value. If the calculated t-statistic (or *t*-calculated) value (or *m*-value) is greater than or equal to this value (1.155) then there is one chance in one hundred that the value is from the same population as the other values. According to this procedure, 6 data sets (12 specimens) were rejected as outliers. Further, the APA rut values were measured at selected loading cycles, namely 500, 1000, 1500, 2000, 3000, 4000, 5000, 6000, 7000, and 8000. These rut values are presented in Appendix F.

5.3.1 Effect of Air Voids

As noted previously, air voids of laboratory-compacted specimens varied between 1% and 11%. For comparison, the final rut values (at 8000 cycles) were plotted as a function of air voids of the specimens (Figure 5.4). It is evident from Figure 5.4 that rut depth increases with an increase in air void content, as expected. For example, at a temperature of 40°C (104°F), an increase in air voids by 6.45% (2.17% to 8.62%) increased the rut depth by approximately 120% [0.037-in. (0.94-mm) to 0.081-in. (2.06-mm)]. Similarly, at 40°C (104°F) and 7.77% air voids, the measured rut depth was 0.075-in. (1.90-mm). However, at 64°C (147°F) and 7.65% air voids, which are similar in air voids at 40°C (104°F), the measured rut depth was 0.183-in. (4.65-mm). This means for similar air voids, as the temperature increased by 60% [from 40°C (104°F) to 64°C (147°F)] the rut depth increased by 144% [from 0.075-in. (1.91-mm) to 0.183-in. (4.65-mm)]. Tarefder (2003) and Navaratnarajah (2006) reported similar observations. According to Tarefder (2003), for specimens having air voids more than 5%, the rut depth generally increases with an increase in air voids.

5.3.2 Effect of Temperature

From Figure 5.4, it is evident that rut depth is sensitive to changes in temperature. For example, an increase in temperature from 40°C (104°F) to 50°C (122°F) increased the rut depth by almost 50% [0.081-in. (2.06-mm) to 0.118-in. (2.99-mm)] at an air void content of 8.5% (±0.5%). Similarly, an increase in temperature from 40°C (104°F) to 64°C (147°F) increased the rut depth by approximately 125% [0.081-in. (2.06-mm) to 0.183-in. (4.65-mm)] at an air void content of 8.5% (±0.5%). This behavior is consistent with the observations reported in other studies (e.g., Tarefder, 2003; Navaratnarajah, 2006). Tarefder (2003)

observed that a small increase in temperature [from 60°C (140°F) to 64°C (147°F)] could increase rut depth by almost two times. Therefore, temperature is a very significant influencing factor so far as ruttting is concerned.

5.3.3 Development of Laboratory Rut Model

Based on the aforementioned results from laboratory testing, regression models were developed correlating rut depths with three independent variables, namely initial air voids, test temperature, and number of loading cycles. The basic form of this laboratory rut prediction model is presented in Equation (4.1).

$$\frac{\mathrm{R}}{\mathrm{R}_0} = k_1 \left(\frac{N}{N_0}\right)^{k_2} e^{k_3\left(\frac{A}{A_0}\right)} e^{k_4\left(\frac{T}{T_0}\right)} \quad (5.1)$$

where

R = Predicted rut depth,

A = Air voids of the specimen,

T = Temperature at which the rut depth is measured,

N = Number of loading cycles at which the rut depth is measured,

R_o = Reference rut depth (0.179-in.) obtained from the APA rut test at the reference temperature ($T_0 = 64^oC$), reference air void (A_0 = 7%) and reference number of cycles (N_0 = 8000 cycles),

k_1, k_2, k_3, k_4 = Model constants.

A stepwise method of multiple linear regression (α = 0.05 option in SAS 9.1) was used for determining the model constants (k_1, k_2, k_3 and k_4). The F test for the multiple regressions was conducted using the same software to examine the significance of the relationship between rut depth and independent variables included in the model. The associated probability is

designated as Pr > F or p-value. A small p-value implies that the model is significant in explaining the variation in the dependent variables. It was found that the rut depth values were significantly influenced by the air voids content, test temperature, and number of loading cycles. The following laboratory rut prediction model was developed:

$$\frac{\mathrm{R}}{\mathrm{R}_0} = 0.0478\left(\frac{N}{N_0}\right)^{0.3795} e^{0.74303\left(\frac{A}{A_0}\right)} e^{2.27295\left(\frac{T}{T_0}\right)} \quad (5.2)$$

The Analysis of Variance (ANOVA) test on the developed model yield an F value of 1180 with a Pr of less than 0.0001 and an R^2 values of 0.91, which indicates that the model may be considered statistically significant in predicting the variation of rut depths with the selected parameters, namely air voids content, test temperature and number of loading cycles (Table 5.6). From the positive values of all model parameters, it is evident that the increasing air voids content, temperature, and number of loading cycle would increase the rut depth. A comparison between the predicted rut depths and actual rut depth is shown in Figure 5.5. From Figure 5.5, it is observed that the predicted rut values are closer to the equality line when the rut values are less than 0.10-in. (2.54-mm). This observation may be justified by the distribution of rut values in the dataset. Out of 750 rut values in the graph, 513 data points (about 68%) had rut values less than 0.10-in. (2.54-mm), whereas there are 237 (about 32%) data points having rut values less than 0.10-in. (2.54-mm). The correlation could be further improved by including more data points with rut values higher than 0.10-in. (2.54-mm).

5.4 Sensitivity Analysis of the Rut Prediction Model

To evaluate the effect of each independent variable, a sensitivity analysis was performed on the developed rut model. During the sensitivity analysis, only one independent variable was changed at a time. First, the average, minimum, and maximum of each

independent variable were determined from the laboratory dataset. The corresponding average values of each independent variable used in developing the regression model are shown in Table 5.7. Then, rut values were calculated by inputting the average value of each independent variable into the laboratory rut model. This calculated value was called the "Primary Rut Value." A series of rut values were then calculated by changing (within ±10% of average value) one independent variable at a time, while the other independent variables were kept at their average values. The series of the rut values thus obtained were compared with the "Primary Rut Value."

The results of this sensitivity analysis of the rut model are presented as percent difference in Table 5.7. It is evident from Table 5.7 that the temperature is the most critical variable in the model, followed by air voids and number of loading cycles. An increase of 24%, 21%, and 7% in rut values were obtained for temperature, air voids, and number of loading cycles, respectively. From these results, it can be concluded that the laboratory rut prediction model is more sensitive to temperature, followed by air voids and number of loading cycles.

5.5 Summary

In this study, a total of 100 cylindrical specimens were tested in the APA at three different temperatures [40^{o}C (104°F), 50^{o}C (122°F), or 64^{o}C (147°F)]. The specimens were prepared covering a wide range of air voids (1% - 11%). A rut prediction model was developed from the laboratory rut data. Based on the results presented in this chapter, the following conclusions can be drawn:

1) The test results suggest that the rut values are influenced by the air voids content of compacted specimen, test temperature, and number of loading cycles. Based on the

test results, the rut value increased with increased air voids content, temperature, and number of loading cycles.

2) The model developed in this chapter was found to be statistically significant (R^2 = 0.91).

3) Based on the sensitivity study of the independent variables, test temperature was found to be most influential, followed by air voids and number of loading cycles.

4) All model parameters (k_1, k_2, k_3, and k_4) were found to be positive, which indicates that rut depths will increase with the increase in temperature, air voids, and number of loading cycles.

Table 5-1 Test matrix for the APA Rut Test

Temperature (°C)	Air Voids (%)	No. of Specimens Tested	Total No. of Specimens Tested
40	2± 1 %	6	30
	4± 1 %	4	
	6± 1 %	4	
	8± 1 %	10	
	10± 1 %	6	
50	2± 1 %	6	26
	4± 1 %	4	
	6± 1 %	4	
	8± 1 %	7	
	10± 1 %	5	
64	2± 1 %	10	44
	4± 1 %	5	
	6± 1 %	12	
	8± 1 %	12	
	10± 1 %	5	

Table 5-2 Summary of Mix Properties for the Collected Loose HMA Mix

Blended Materials		**Binder Information**	
1.0-in. Rock	0 (%)	Binder Type	PG 64-22
5/8- in. Chips	25 (%)	Binder Content	4.6
Manufactured Sand	38 (%)	Binder Source	Valero, OK
Asphalt Sand	0 (%)	Binder Specific Gravity	1.02
Sand	15 (%)		
Screenings	22 (%)		
Recycled Asphalt Pavement (RAP)	0 (%)		
Aggregate Property		**Mixture Property**	
Maximum Aggregate Size (MAS)	¾ in.	Voids in the Mineral Aggregate (VMA)	14.1
Nominal Maximum Aggregate Size (NMAS)	½ in.	Indirect Tensile Strength (psi)	110.5
Sand Equivalent	70		
L.A. Abrasion % Wear	11		
Durability	63		
Ignition Oven Correction Factor	0.26		
Fractured Faces	100/100		
Effective Specific Gravity (G_{se})	2.678		

Table 5-3 Automated APA Rut Test Results at 40^{o}C*

Specimen No.	**Air Voids Range (%)**	**Air Voids of the Specimens (%)**	**Automated Rut Measurement at 8000 Cycles (in.)**	**Average Rut (in.)**	**Standard Deviation**	***m*-value**
L4CR-44,45	(2±1)%	0.817	0.031	0.036	0.004	1.121
L4CR-5,7		1.985	0.039			0.801
L4CR-42,43		2.170	0.037			0.320
T-9,10	(4±1)%	3.836	0.040	0.045	0.007	0.707
L4CR-89,90		4.320	0.050			0.707
L4CR-16,21	(6±1)%	5.282	0.072	0.068	0.006	0.707
T-3,7		6.078	0.063			0.707
L4CR-9,10	(8±1)%	7.059	0.087	0.081	0.005	0.968
L4CR-23,25		7.657	0.056			1.664
L4CR-26,27		7.770	0.075			0.051
L4CR-22,24		8.034	0.079			0.289
L4CR-40,41		8.616	0.081			0.458
L4CR-34,35	(10±1)%	9.769	0.104	0.111	0.011	0.623
L4CR-36,37		9.985	0.105			0.530
L4CR-38,39		10.102	0.123			1.153

* Specimens having *m*-value greater than 1.155 were discarded

Table 5-4 Automated APA Rut Test Results at 50°C*

Specimen No.	Air Voids Range (%)	Air Voids of the Specimens	Automated Rut Measurement	Average Rut (in.)	Standard Deviation	*m*-value
L4CR-50,52	(2±1)%	0.74	0.039	0.046	0.007	1.009
L4CR-91,92		1.87	0.046			0.017
L4CR-47,49		2.16	0.052			0.991
L4CR-69,70	(4±1)%	4.26	0.068	0.069	0.002	0.707
L4CR-66,73		4.7	0.071			0.707
L4CR-65,72	(6±1)%	5.23	0.090	0.094	0.005	0.707
L4CR-53,54		6.44	0.097			0.707
L4CR-64,75	(8±1)%	7.45	0.121	0.116	0.006	0.288
L4CR-63,74		8.17	0.109			0.772
L4CR-46,48		8.51	0.165			1.468
L4CR-76,77		8.98	0.118			0.408
L4CR-55,56	(10±1)%	9.45	0.141	0.171	0.043	0.707
L4CR-57,58		10.46	0.202			0.707

* Specimens having *m*-value greater than 1.155 were discarded

Table 5-5 Automated APA Rut Test Results at 64°C*

Specimen No.	Air Voids Range (%)	Air Voids of the Specimens (%)	Automated Rut Measurement at 8000 Cycles (in.)	Average Rut (in.)	Standard Deviation	*m*-value
L4CR-71,83	(2±1)%	1.54	0.062	0.131	0.030	1.372
L4CR-6,12		2.1	0.148			0.761
L4CR-81,82		2.13	0.090			0.668
L4CR-11,13		2.52	0.158			1.009
L4CR-79,80		2.9	0.128			0.270
L4CR-87,88	(4±1)%	4.23	0.165	0.170	0.006	0.707
L4CR-14,15		4.52	0.174			0.707
L4CR-2,3	(6±1)%	5.56	0.159	0.167	0.021	0.221
L4CR-85,86		5.66	0.190			0.705
T-4,5		6.47	0.151			0.458
T-6,8		6.49	0.123			1.287
T-1,2		6.63	0.209			1.261
T-13,15	(8±1)%	7.12	0.198	0.181	0.018	0.971
T-18,19		7.345	0.190			0.657
L4CR-18,19		7.37	0.150			0.830
T-16,17		7.53	0.129			1.614
L4CR-17,20		7.65	0.183			0.408
T-11,12		7.94	0.183			0.408
L4CR-30,31	(10±1)%	9.21	0.208	0.212	0.017	0.231
L4CR-28,29		9.86	0.197			0.865
L4CR-32,33		10.63	0.231			1.095

Table 5-6 Analyses of Variance on Automated APA Rut Test Results using Laboratory Rut Prediction Model

Independent Variables	Parameter Estimate	Standard Error	Type II Sum of Squares	F-Value	Pr > F	Significant
Intercept	-1.32029	0.02470	17.61260	2858.24	<0.0001	Yes
Log (A/A_0)	0.74303	0.02403	5.89211	956.19	<0.0001	Yes
Log (T/T_0)	2.27295	0.05832	9.36067	1519.08	<0.0001	Yes
(N/N_o)	0.37950	0.01076	7.66045	1243.17	<0.0001	Yes

Table 5-7 Sensitivity Analysis of Laboratory Rut Prediction Model

Independent Variables	**Average[a]**	**Average -10% of Average**	**Average +10% of Average**	**Percent Difference[b] (-)**	**Rank[b] (-)**	**Percent Difference[c] (+)**	**Rank[c] (+)**
Primary Rut (in.)	0.083	---	---	---	---	---	---
Temperature (°C)	52.84	47.558	58.127	-17.1	1	20.6	1
Air Voids (%)	6.380	5.742	7.018	-6.5	2	7.0	2
No. of APA Cycles	3772	3395	4149	-3.9	3	3.7	3

a = reference value; b = independent variable minus 10%; c = independent variable plus 10%

Figure 5-1 Setup for Specimen Preparation in the Superpave Gyratory Compactor

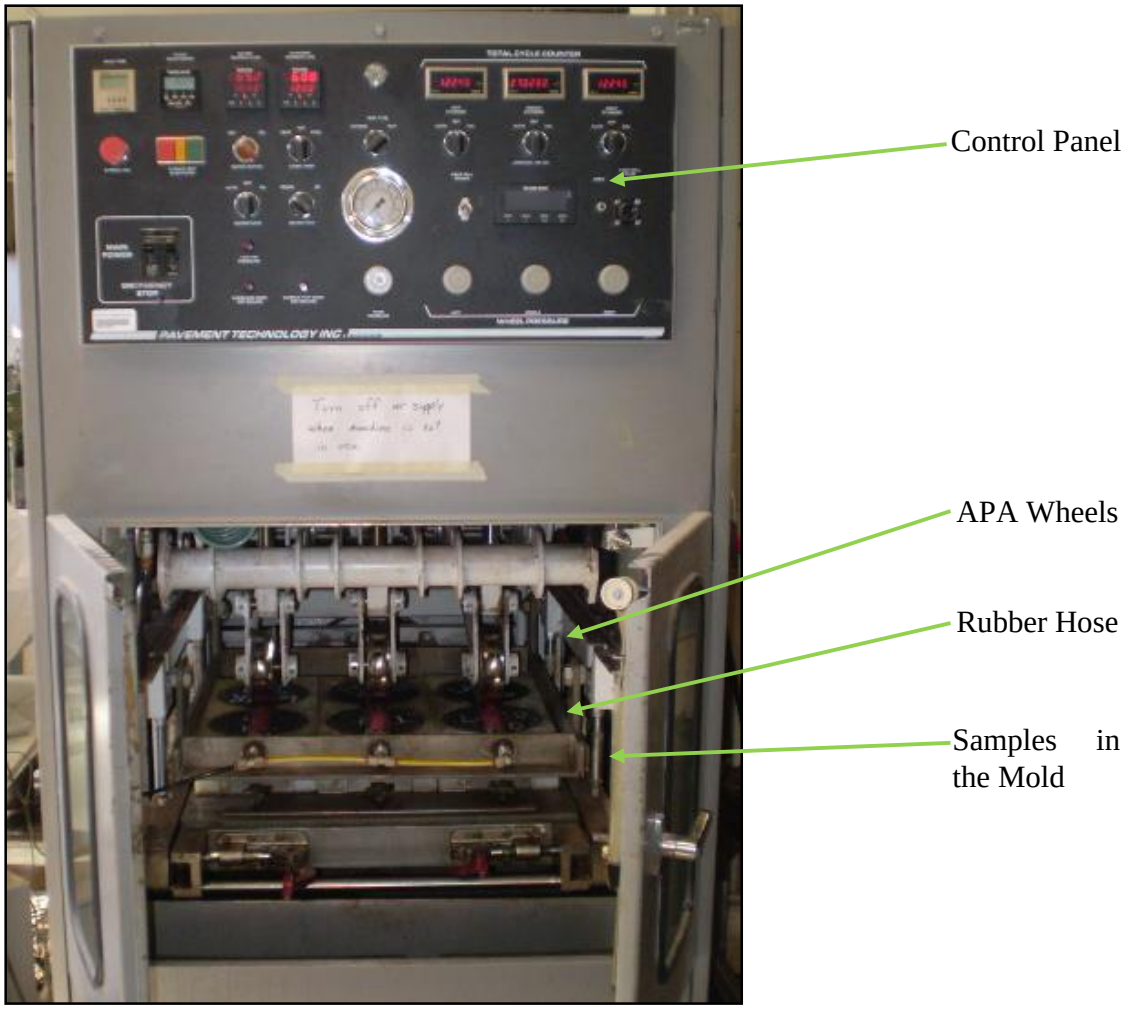

Figure 5-2 Setup for the APA Rut Test

Figure 5-3 Photograph of Selected Specimens after the APA Rut Test

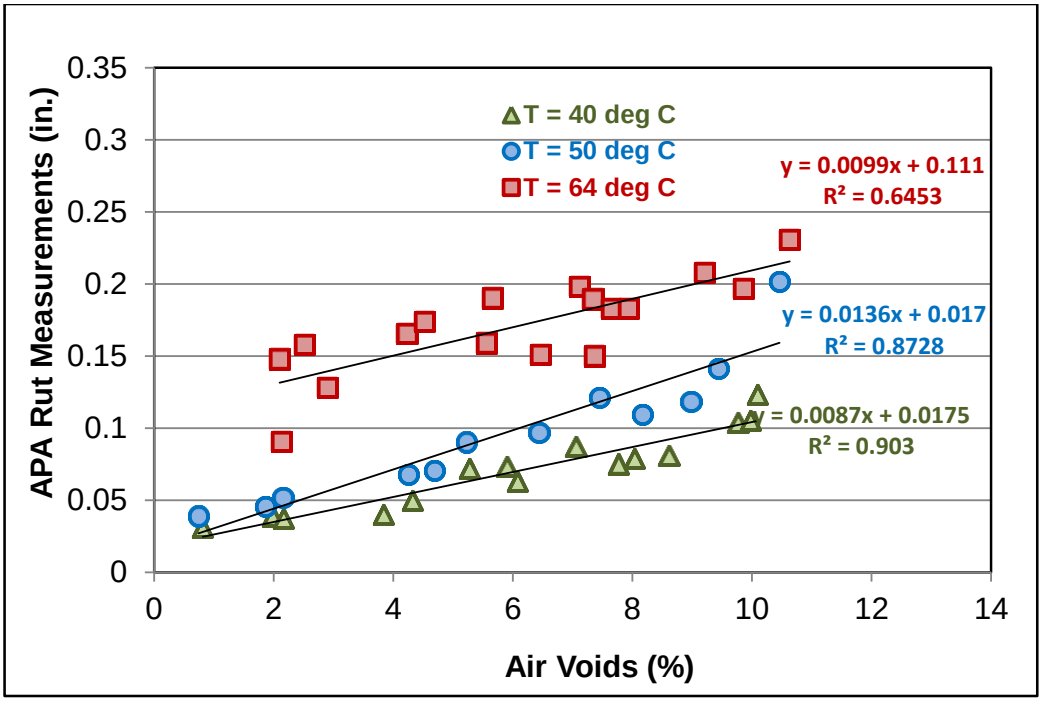

Figure 5-4 APA Rut Measurements after 8000 Loading Cycles (Temperature = 40°C, 50°C and 64°C)

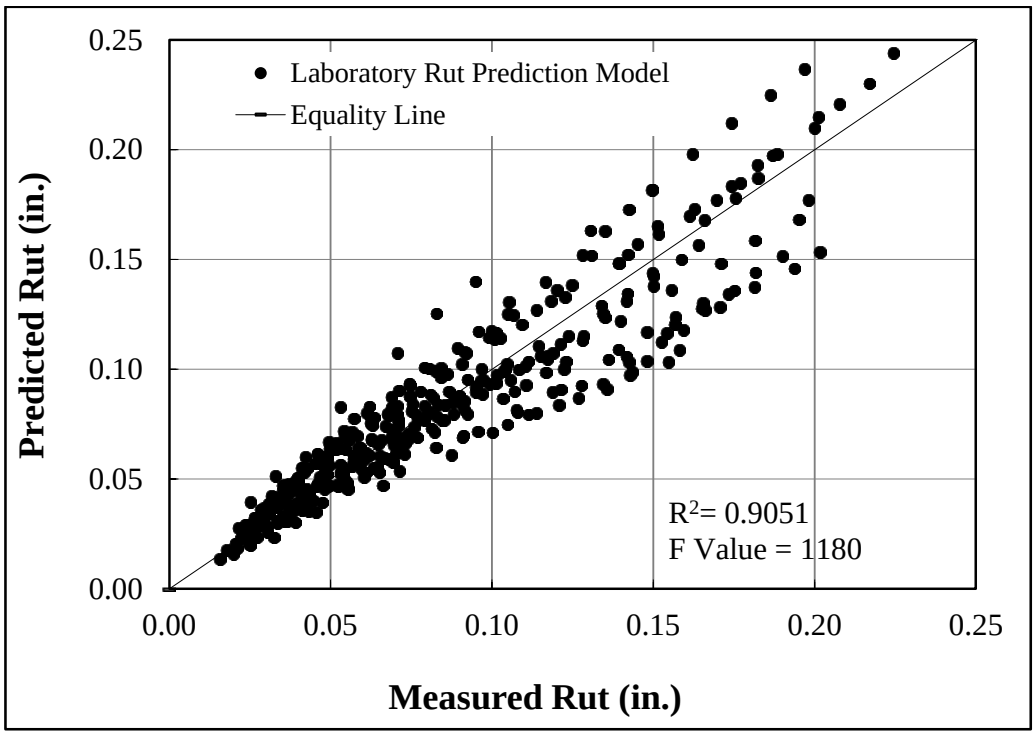

Figure 5-5 Rut Prediction from Developed Rut Prediction Model

Chapter 6 FIELD RUT PREDICTION MODEL DEVELOPMENT

6.1 Introduction

Accurate prediction of rutting for an in-service pavement under actual vehicular traffic loading and environmental conditions is critical for effective pavement design. Historically, two different approaches have been used to predict pavement rutting (Selvaraj, 2007). One approach involves predicting pavement rutting by calculating vertical strain on the top of the aggregate base or subgrade. Another approach is based on the consideration of shear strain calculation in the HMA layer. Although it is widely accepted that vertical strain on the top of aggregate base layer or subgrade layer is a major contributor to pavement rutting (Finn et al., 1977; Allen and Dean, 1980), recent studies have shown better correlations of shear strain along the tire edge to HMA layer with rutting. For example, a recent study by Selvaraj (2007) indicates that the magnitude of shear strain is strongly correlated to pavement rutting. Other researchers (Kim et al., 2000; Theyse et al., 2006) have also shown that it is difficult to control the pavement rutting only by controlling the vertical compressive strain on the top of the roadbed soil. Therefore, both vertical strain-based approach and shear strain-based approach were explored in the present study to develop rut prediction models. A comparison between the two models is also included in this chapter.

6.2 Methodology for Vertical Strain-based Rut Prediction Model

One of the primary objectives of this study was to develop a rut prediction model from real-life vehicular traffic data and environmental conditions that a typical secondary state highway in Oklahoma would experience during its lifetime. To achieve this objective, a

vertical strain-based approach was undertaken to develop a rut prediction model. The proposed methodology is summarized in the form of a flow chart in Figure 6.1.

In the flow chart, the time stamp (i) is used to link variables, namely measured mid-depth pavement temperature (T_i) and traffic axle count (N_i) for a particular period. The calculated vertical strain on the top of the pavement layers at a particular time (ε_i) and number of axle passes at that time (N_i) were selected as the independent variables in the rut prediction model. The total measured rut depth (Rut_i) at a particular time was calculated as a sum of the previous period's total rut (Rut_{i-1}) plus incremental rutting caused by additional traffic (N_i) at the calculated strain level (ε_i) for the current time increment (Selvaraj, 2007).

6.3 Vertical Strain-based Rut Prediction Model Development

The following data were used for developing the vertical strain-based rut model:

a. Material properties: HMA Modulus (backcalculated from FWD data).
b. Environmental data: Mid-depth pavement temperature (measured every minute, hourly averages stored).
c. Traffic data: Axle type and weight, irrespective of vehicle class.
d. Pavement performance: Rut measurements using straight edge/rut gauge combination and Face Dipstick®.
e. Tire inflation pressure: 120-psi (827-kPa) (recommended by AASHTO, 2004)

In this study, the modulus-temperature correlation established in Equation (4.5) was used to predict modulus at a particular temperature (*see Section 4.5.4.1 for details*). The average moduli of aggregate base layer, stabilized subgrade layer, and natural subgrade layer (backcalculated from the FWD data) were used for developing the rut prediction model. The

average modulus of aggregate base layer, stabilized subgrade layer, and natural subgrade layer, obtained from the FWD test data, were 28.2-ksi (194.4-MPa), 69.7-ksi (480.6-MPa), and 20.1-ksi (138.6-MPa), respectively.

6.3.1 Vertical Strain Calculation on Top of Aggregate Base

As described in the methodology, measured vertical strain response on the top of pavement layers is an important element of the rut model. Although there was no strain gauge installed to measure the vertical strain on the top of base or subgrade layers, WinJULEA, a commonly used multilayered linear elastic analysis software, was used here to predict vertical strains on the top of the base and the natural subgrade layers due to vehicular traffic. WinJULEA is recommended in the MEPDG (AASHTO, 2004) for calculating pavement response. Also, previous studies (see e.g., Monismith, 1992) have shown that linear elastic analysis is a reasonable tool for rut evaluation, when the pavement temperature does not exceed 40^{o}C (104^{o}F). Since the maximum pavement temperature (mid-depth) measured in the test section was below 47°C (112°F), it was considered reasonable to use the linear elastic model to predict vertical strains for developing the rut prediction model. WinJULEA analyses showed that, for a particular vehicular load, the maximum vertical strain is experienced on the top of the aggregate base layer (Figure 6.2). So, vertical strain on the top of the aggregate base layer was used to develop the vertical strain-based rut prediction model.

6.3.2 Separate Strain Calculation for Steering and Tandem Axles

In the WinJULEA calculations, steering axles and tandem axles were analyzed separately because of differences in vertical strain distribution. A steering axle has single wheels at axle ends, while a tandem axle has dual wheels at axle ends. In a tandem axle

configuration, two axles are joined together. Each axle of the tandem axle configuration was analyzed separately. Typical load distributions of a steering axle and tandem axle are shown in Figure 6.3.

As illustrated in Figure 6.3 (a), since there are two wheels on axle ends of a steering axle, each wheel was assumed to carry half of the steering axle load. Since the typical axle width of a truck is 8.5-ft. (2.6-meter) (AASHTO, 2004), the single wheels of a steering axle are 8.5-ft. (2.6-meter) apart. Primary strain calculation through WinJULEA showed that strain coming from one wheel does not contribute to (or interfere with) the strain coming from the other wheel, in the case of steering axles. However, the scenario is different in the case of tandem wheels. As illustrated in Figure 6.3 (b), there are four wheels (two dual wheels on each end of the tandem axle) for each axle of a tandem axle. So, each wheel would carry approximately one-fourth of the tandem axle load. As typical distance between the centers of dual wheel is only 12-in. (300-mm) (AASHTO, 2004), WinJULEA calculations showed that strain induced by one wheel (of the dual wheel) overlaps with the strain contributed by the other wheel.

Difference in strain distribution between a steering and tandem axle wheel is further clarified here using an example calculation. In this particular example, the load on each wheel (for both steering and tandem axle wheels) was assumed to be 2.36 kip (10.5 kN). As presented in Figure 6.4, the vertical strain due to a steering axle wheel (on the top of the aggregate base layer) under the center of the wheel is 0.000153 (in./in.). Whereas, in the case of a tandem axle, the vertical strain (on the top of the aggregate base layer) under the center of a wheel is 0.000184 (in./in.) (Figure 6.5). This means both the magnitude and distributions of

vertical strains for steering and tandem axles are different. These differences in strains necessitated separate calculations for steering axles and tandem axles.

6.3.3 Vertical Strain-Temperature Correlations

As described in the preceding sections, vertical strain from vehicular traffic on the top of the aggregate base layer was used to develop the vertical strain-based rut prediction model. An important step in developing the vertical strain-based rut prediction model was to develop correlations between vertical strain and mid-depth pavement temperature. The following steps were followed to develop the vertical strain-temperature correlations:

Step - 1:

A mid-depth pavement temperature for a particular hour was selected. Then, the HMA modulus for that particular temperature was calculated using Equation (6.1), as mentioned earlier in this chapter (Section 6.3).

Step - 2:

Then, for that particular hour, vehicular traffic data was obtained from the WIM station. Several vehicles including the lowest and the highest steering axle weights were selected and half steering axle weights noted (irrespective of class). Vertical strains were calculated for each axle weight using WinJULEA, which was used to obtain a correlation between vertical strain and half steering axle weights at that particular temperature. A general form of the correlation between vertical strain and half steering axle weights can be expressed by Equation (6.1):

$$\varepsilon_s = C_1 * (half\ steering\ axle\ weight) + C_2 \quad (6.1)$$

where

ε_s = Vertical strain from steering axle,

C_1, C_2 = Regression constants.

Similarly, a linear correlation was developed for vertical strain and 1/4th tandem axle weights for that particular temperature, as given by Equation (6.2):

$$\varepsilon_s = C_3 * \left(\frac{1}{4}th\ tandem\ axle\ weight\right) + C_4 \qquad (6.2)$$

where

ε_t = Vertical strain from tandem axle,

C_3, C_4 = Regression constants.

Step - 3:

In this step, vertical strains/kips for steering axles and tandem axles were calculated for that particular temperature. The vertical strain/kip from all the vehicle's steering and tandem axles at that particular hour and temperature were calculated using Equations (6.3) and (6.4) as noted below:

$$\varepsilon_s = \frac{\varepsilon_{s1}+\varepsilon_{s2}+\varepsilon_{s3}+\ \ldots\ldots\ldots\ldots+\varepsilon_{sn}}{W_{s1}+W_{s2}+W_{s3}+\ \ldots\ldots\ldots\ldots+W_{sn}} \qquad (6.3)$$

where

ε_s = Vertical strain of steering axles (per kip),

ε_{s1}, ε_{s2}, ε_{s3}, ε_{sn} = Vertical strains due to steering axles of Vehicle 1, Vehicle 2, Vehicle 3, and Vehicle n, respectively,

W_{s1}, W_{s2}, W_{s3}, W_{sn} = Weight of steering axles of Vehicle 1, Vehicle 2, Vehicle 3, and Vehicle n, respectively.

$$\varepsilon_t = \frac{\varepsilon_{t11}+\varepsilon_{t12}+\varepsilon_{t13}+\varepsilon_{t14}+\varepsilon_{t21}+\ \ldots\ldots\ldots\ldots+\varepsilon_{tnn}}{W_{t11}+W_{t12}+W_{t13}+W_{t14}+W_{t21}\ \ldots\ldots\ldots\ldots+W_{tnn}} \qquad (6.4)$$

where

ε_t = Vertical strain of tandem axles (per kip),

ε_{t11}, ε_{t12}, ε_{t13}, ε_{t14} = Vertical strains due to tandem axles of Vehicle 1,

ε_{t21} = Vertical strains due to tandem axle 1 of Vehicle 2,

ε_{tnn} = Vertical strains due to tandem axle n of Vehicle n,

W_{t11}, W_{t12}, W_{t13}, W_{t14} = Weight of tandem axles of Vehicle 1,

W_{t21} = Weight of tandem axle 1 of Vehicle 2,

W_{tnn} = Weight of tandem axle n of Vehicle n.

Step - 4:

WinJULEA simulations were conducted (following Step - 1 through Step - 3 several times) for a wide range of temperatures [from 10°C (50°F) to 45°C (113°F)] that are representative of pavement temperatures in the Test Section to get the vertical strain-temperature correlations. Two separate vertical strain-temperature correlations were obtained to predict vertical strain on the top of the aggregate base layer as a function of pavement temperature: one for steering axle and the other for tandem axle. The general form of the vertical strain-temperature correlation is presented in Equation (6.5) and in Equation (6.6).

$$\varepsilon_s = \beta_1 T^{\beta_2} \tag{6.5}$$

$$\varepsilon_t = \beta_1^{'} T^{\beta_2^{'}} \tag{6.6}$$

where

ε_s = Vertical strain per kip per steering axle for a particular temperature,

ε_t = Vertical strain per kip per tandem axle for a particular temperature,

T = Mid-depth pavement temperature (°F),

β_1, β_2, β'_1, β'_2 = Regression constants.

Figures 6.6 and 6.7 show the relationship between vertical strain on the top of the aggregate base layer and the mid-depth pavement temperature for single and tandem axles, respectively. The final vertical strain-temperature correlation for single axle and tandem axles is presented in Equation (6.7) and in Equation (6.8).

$$\varepsilon_s = 4 * 10^{-09} T^{2.1827} \quad (6.7)$$

$$\varepsilon_t = 2 * 10^{-08} T^{1.9228} \quad (6.8)$$

6.3.4 Traffic Data

As mentioned in Chapter 3, the vehicle category, axle weight, and loading configuration of each vehicle the Test Section was recorded at the WIM station. From May 30, 2008 to May 18, 2010, approximately a total of 2.2-million single axles and 6.9-million tandem axles have passed over the test section. Approximately, a total of 16,500 hours of vehicle data was collected with the WIM station within that timeframe. As temperature was recorded every hour, vertical strains/kips from steering and tandem axles were calculated using Equations (4.2) and (4.3) for each hour. Then, average hourly vertical strains for both steering and tandem axles were calculated using Equations (6.9) and (6.10).

$$\varepsilon_{si} = \varepsilon_s * \frac{W_{s1} + W_{s2} + W_{s3} + \ldots\ldots\ldots\ldots + W_{sn}}{N_{si}} \quad (6.9)$$

$$\varepsilon_{ti} = \varepsilon_t * \frac{W_{t11} + W_{t12} + W_{t13} + W_{t14} + W_{t21} \ldots\ldots\ldots\ldots + W_{tnn}}{N_{ti}} \quad (6.10)$$

where

ε_{si} = Average hourly vertical strain from steering axles,

ε_{ti} = Average hourly vertical strain from tandem axles,

N_{si} = Total number of steering axle passes at that particular hour,

N_{ti} = Total number of tandem axle passes at that particular hour.

The traffic data were linked with the environmental database (temperature) with the help of the time stamp (i), and thereby, at any given time, the vertical strain produced by a certain number of axle passes was available for model development.

6.4 Final Vertical Strain-based Rut Prediction Model

Rut measurements, made approximately every three months, were linearly interpolated to have a rut value for each hour of each day. As rut was measured at six stations, each trip's rut value was averaged to obtain one rut value for that particular field trip's rut measurement. By relating the measured hourly rutting to the vertical strain on the top of the aggregate base layer and the total number of steering and tandem axle passes, the rut prediction model was developed by performing a non-linear regression analysis using the least–square method available in the Excel spreadsheet. The general form of the vertical strain-based rut prediction model is given in Equation (6.11).

$$Rut_i = Rut_{i-1} + \lambda_1(N_{si}^{\lambda_2 * \varepsilon_{si}} + N_{ti}^{\lambda_3 * \varepsilon_{ti}}) \quad (6.11)$$

where

Rut_i = Rut at time "i" from field measurements,

Rut_{i-1} = Rut at time "i-1" from field measurements,

N_{si} = Total number of steering axle passes at time "i",

N_{ti} = Total number of tandem axle passes at time "i",

λ_1 = Regression constant for traffic (both steering and tandem axles),

λ_2, λ_3 = Regression constant for vertical strain.

The final form of the vertical strain-based rut prediction model is given in Equation (6.12).

$$Rut_i = Rut_{i-1} + 3.26 * 10^{-06}(N_{si}^{1.54*10^2*\varepsilon_{si}} + N_{ti}^{3.48*10^2*\varepsilon_{ti}}) \quad (6.12)$$

When rutting was predicted using the developed vertical strain-based model [Equation (6.12)], the R^2 value, based on the predicted and measured rut values, was found to be 0.86. Further, the positive coefficients for both traffic and vertical strains indicate that an increase in number of axle passes and strain levels will increase the rutting, as expected. Figure 6.8 shows the predicted rutting from the vertical strain-based model and the measured rutting from the Test Section as a function of increasing number of axles. Overall, the vertical strain-based rut prediction model satisfactorily predicted the field rutting.

6.5 Methodology for Shear Strain-based Rut Prediction Model

As mentioned earlier, rutting is thought to be a combination of two mechanisms: at the beginning of rutting, rutting is governed by the accumulation of vertical strain in the form of additional compaction, and afterwards rut is governed by the shear flow in the HMA layer. Therefore, a separate rut prediction model based on the shear strain in the HMA layer was needed. The methodology followed to develop the shear strain-based rut prediction model was very similar to the methodology followed for developing the vertical strain-based model. The only difference was that the vertical strain was substituted by the maximum shear strain. The proposed methodology is summarized in the form of a flow chart in Figure 6.9.

6.6 Shear Strain-based Rut Prediction Model Development

6.6.1 Maximum Shear Strain Computation

The approach to compute shear strain was similar to the approach to compute vertical strain. However, the shear strain was computed at different depths in the HMA layer using WinJULEA. Depending upon the vehicle weight, the maximum shear strain was observed at

the tire's edge and at a depth of about 0.5-in. (12.7-mm) to 2-in. (51-mm) below the pavement surface. A typical shear strain profile at different depths and at different distances from the center of a tire load is presented in Figure 6.10. In this figure, it is observed that the maximum shear strain for a particular load is located at the tire's edge [4.213-in. (107-mm)]. The blue line in Figure 6.10 represents the maximum shear strain profile in the HMA layer. It is also observed from Figure 6.10 that at a depth of 1-in. (25.4-mm) from the surface, the shear strain value reaches its maximum and beyond 1-in. (25.4-mm) the value starts decreasing. A recent study by Yoo and Al-Qadi (2007) also showed that the maximum shear strain was found at a depth of about 1-in. (25.4-mm) from the pavement surface.

6.6.2 Shear Strain-Temperature Correlations

A similar approach to develop vertical strain-temperature correlations was followed for developing shear strain-temperature correlations. The only difference is that the vertical strain was replaced by shear strain from Step - 2 to Step - 4 in Section 6.3.3 of this chapter. Also in this case, steering and tandem axles were analyzed separately. Equations (6.13) and (6.14) were used to calculate the maximum shear strains/kips for steering and tandem axles for a particular temperature.

$$\gamma_s = \frac{\gamma_{s1}+\gamma_{s2}+\gamma_{s3}+ \ldots\ldots\ldots\ldots+\gamma_{sn}}{W_{s1}+W_{s2}+W_{s3}+ \ldots\ldots\ldots\ldots+W_{sn}} \quad (6.13)$$

where

γ_s = Maximum shear strain of steering axles (per kip),

γ_{s1}, γ_{s2}, γ_{s3}, γ_{sn} = Maximum shear strains due to steering axles of Vehicle 1, Vehicle 2, Vehicle 3, and Vehicle n, respectively,

W_{s1}, W_{s2}, W_{s3}, W_{sn} = Weight of steering axles of Vehicle 1, Vehicle 2, Vehicle 3, and Vehicle n, respectively.

$$\gamma_t = \frac{\gamma_{t11}+\gamma_{t12}+\gamma_{t13}+\gamma_{t14}+\gamma_{t21}+ \ldots\ldots\ldots\ldots+\gamma_{tnn}}{W_{t11}+W_{t12}+W_{t13}+W_{t14}+W_{t21} \ldots\ldots\ldots\ldots+W_{tnn}} \quad (6.14)$$

where

γ_t = Maximum shear strain of tandem axles (per kip),

γ_{t11}, γ_{t12}, γ_{t13}, γ_{t14} = Maximum shear strains due to tandem axles of Vehicle 1,

γ_{t21} = Maximum shear strains due to tandem axle 1 of Vehicle 2,

γ_{tnn} = Maximum shear strains due to tandem axle n of Vehicle n,

W_{t11}, W_{t12}, W_{t13}, W_{t14} = Weight of tandem axles of Vehicle 1,

W_{t21} = Weight of tandem axle 1 of Vehicle 2,

W_{tnn} = Weight of tandem axle n of Vehicle n.

WinJULEA simulations were run for a wide range of temperatures [from 10°C (50°F) to 45°C (113°F)] to get the shear strain-temperature correlations. Two separate shear strain-temperature correlations were obtained to predict maximum shear strain in the HMA layer as a function of pavement temperature: one for steering axle and the other for tandem axle. Figures 6.11 and 6.12 show the relationship between maximum shear strain in the HMA layer and mid-depth pavement temperature for single axles and tandem axles, respectively. The final shear strain-temperature correlation for single axle and tandem axles are presented in Equations (6.15) and (6.16).

$$\gamma_s = 1 * 10^{-11}\, T^{3.4507} \quad (6.15)$$

$$\gamma_t = 7 * 10^{-12}\, T^{3.7057} \quad (6.16)$$

where

γ_s = Maximum shear strain per kip per steering axle for a particular temperature,

γ_t = Maximum shear strain per kip per tandem axle for a particular temperature,

T = Mid-depth pavement temperature (°F).

6.6.3 Traffic Data for Shear Strain Calculation

The procedure to collect traffic data for shear strain calculation was similar as described in the vertical strain portion. A general form of average hourly shear strain for steering and tandem axles is presented in Equations (6.17) and (6.18).

$$\gamma_{si} = \gamma_s * \frac{W_{s1} + W_{s2} + W_{s3} + \ldots\ldots\ldots\ldots + W_{sn}}{N_{si}} \quad (6.17)$$

$$\gamma_{ti} = \gamma_t * \frac{W_{t11} + W_{t12} + W_{t13} + W_{t14} + W_{t21} \ldots\ldots\ldots\ldots + W_{tnn}}{N_{ti}} \quad (6.18)$$

where

γ_{si} = Average hourly shear strain from steering axles,

γ_{ti} = Average hourly shear strain from tandem axles,

N_{si} = Total number of steering axle passes at that particular hour,

N_{ti} = Total number of tandem axle passes at that particular hour.

The traffic data were linked with the environmental database (temperature) with the help of the time stamp (i) and thereby, at any given time, the shear strain produced by a certain number of axle passes was available for model development.

6.7 Final Shear Strain-based Rut Prediction Model

The same approach described for vertical strain-based model building was used to develop the shear strain-based rut prediction model. A general form of shear strain-based rut prediction model is presented in Equation (6.19):

$$Rut_i = Rut_{i-1} + \lambda_1^{'}(N_{si}^{\lambda_2^{'}*\gamma_{si}} + N_{ti}^{\lambda_3^{'}*\gamma_{ti}}) \quad (6.19)$$

where

Rut_i = Rut at time "i" from field measurements,

Rut_{i-1} = Rut at time "i-1" from field measurements,

N_{si} = Total number of steering axle passes at time "i",

N_{ti} = Total number of tandem axle passes at time "i",

λ'_1 = Regression constant for traffic (both steering and tandem axles) ,

λ'_2 and λ'_3 = Regression constants for shear strain.

The final form of shear strain-based rut prediction model is presented in Equation (6.20).

$$Rut_i = Rut_{i-1} + 1.38 * 10^{-06}(N_{si}^{1.58*10^2*\gamma_{si}} + N_{ti}^{3.37*10^2*\gamma_{ti}}) \quad (6.20)$$

When rut was predicted using the developed shear strain-based model [Equation (6.20)], the R^2 value, based on the predicted and measured rut values, was obtained as 0.80. Further, the positive coefficients for both traffic and shear strains indicate that an increase in number of axle passes and strain levels will increase the rutting, as expected. Figure 6.13 shows the predicted rutting from the shear strain-based model and the measured rutting from the Test Section as a function of increasing number of axles. Overall, the shear strain-based rut prediction model satisfactorily predicted the field rutting.

6.8 Comparison between Vertical and Shear Strain-based Model

As both models predicted field rut satisfactorily, an attempt was made to compare the two models. Table 6.1 shows a comparison between the two models. Rut measurements from the field were taken as a reference to compare rut prediction efficiency of the two models.

From Table 6.1, it can be observed that in 15 occasions out of 16, the shear strain-based model has higher percentage difference from field rut measurements than the vertical strain-based model. For example, on December 3, 2008, the difference in rut prediction using the vertical strain-based model was 43%, whereas the difference using the shear strain-based model was 45%. On January 8, 2009, the difference between the vertical strain-based model's predicted rut and measured rut was 40%, whereas the difference between the shear strain-based model's predicted rut and measured rut was 42%. The percentage difference in rut prediction using the vertical strain-based model was higher than the shear strain-based model in only one occasion. On August 21, 2008, for the vertical strain-based rut prediction model, the difference between predicted and measured ruts was 62%. Comparatively, for the shear strain-based model, the corresponding difference was 59%. In general, it can be stated that rut prediction using the vertical strain-based model produced less error than the shear strain-based model.

6.9 Summary

In this chapter, the development of vertical and shear strain-based rut prediction models was explained. Both the models were developed using a least square regression analysis. Since the test section was located on I-35, with extremely high traffic volume, it was not practical to close the lanes frequently to measure field rutting. The developed models could have been significantly improved with the inclusion of additional rut measurement data.

Although both models predicted field rut reasonably well, the shear strain-based model performed slightly better than the vertical strain-based model. Therefore, both models are recommended for future rut prediction of similar in-service pavements.

Table 6-1 Comparison between Vertical and Shear Strain-based Model

Date	Measured Average Rut Depth (mm)	Vertical Strain Based Model Predicted Rut Depth (mm)	Percent Difference* (Vertical Strain Based Model)	Shear Strain Based Model Predicted Rut Depth (mm)	Percent Difference* (Shear Strain Based Mode)
August 21, 2008	7.20	2.71	62	2.99	59
December 3, 2008	6.56	3.75	43	3.62	45
January 8, 2009	6.35	3.84	40	3.67	42
May 19, 2009	9.72	4.41	55	3.97	59
October 28, 2009	10.65	7.98	25	7.41	30
February 16, 2010	10.49	8.20	22	7.53	28
March 10, 2010	10.47	8.26	21	7.56	28
May 18, 2010	10.69	8.67	19	7.78	27
August 11, 2010	11.35	10.17	10	9.58	16
November 22, 2010	12.36	11.47	7	10.82	12
February 14, 2011	11.94	11.66	2	10.93	8
June 7, 2011	12.04	12.40	3	11.41	5
October 18, 2011	13.38	16.59	24	17.67	32
February 22, 1012	13.28	16.97	28	17.88	35
May 2, 2012	13.33	17.37	30	18.10	36
August 21, 2012	14.35	19.32	35	21.01	46

*“Measured Rut” from field was taken as the reference value

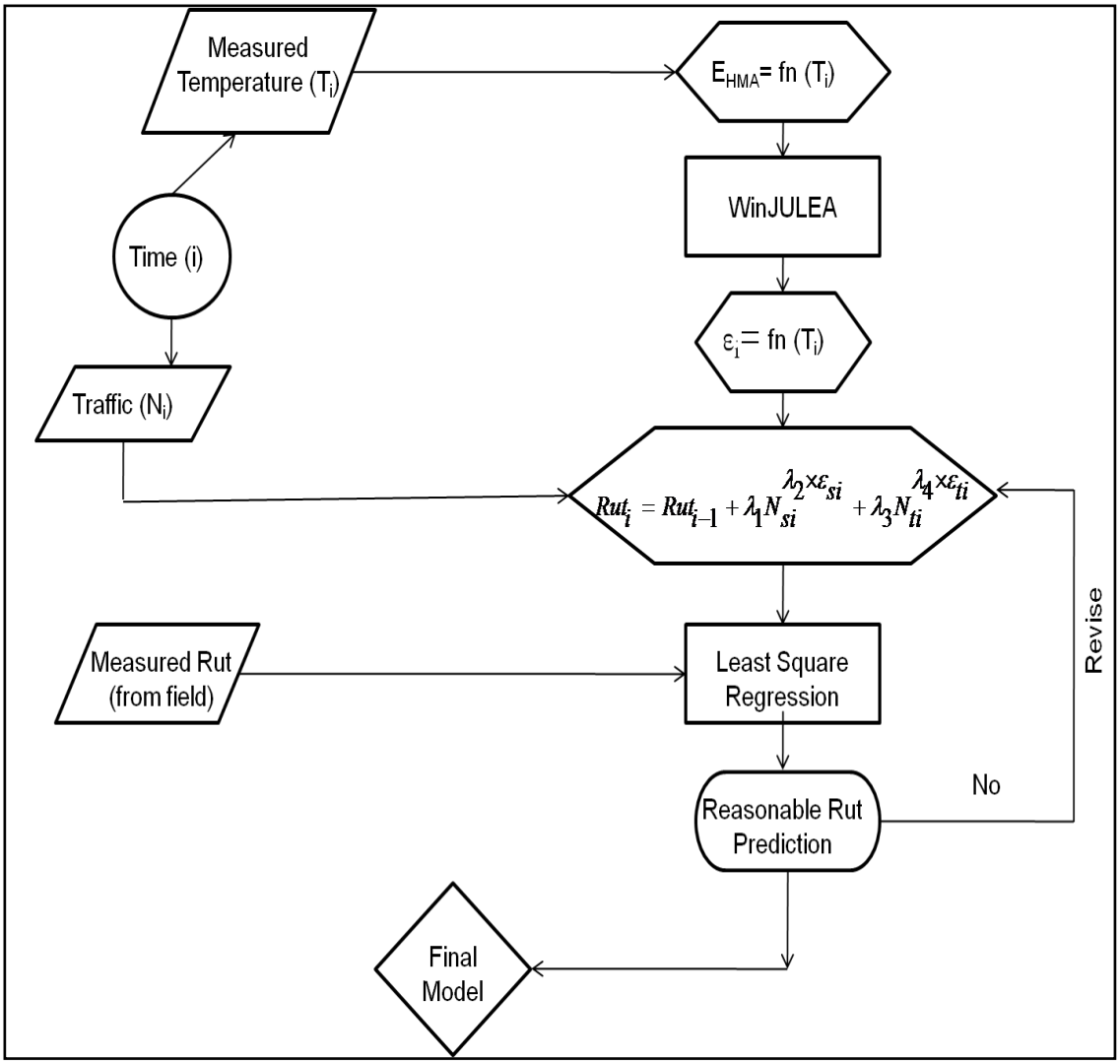

Figure 6-1 Vertical Strain-based Rut Prediction Model Methodology Flow Chart (Selvaraj, 2007)

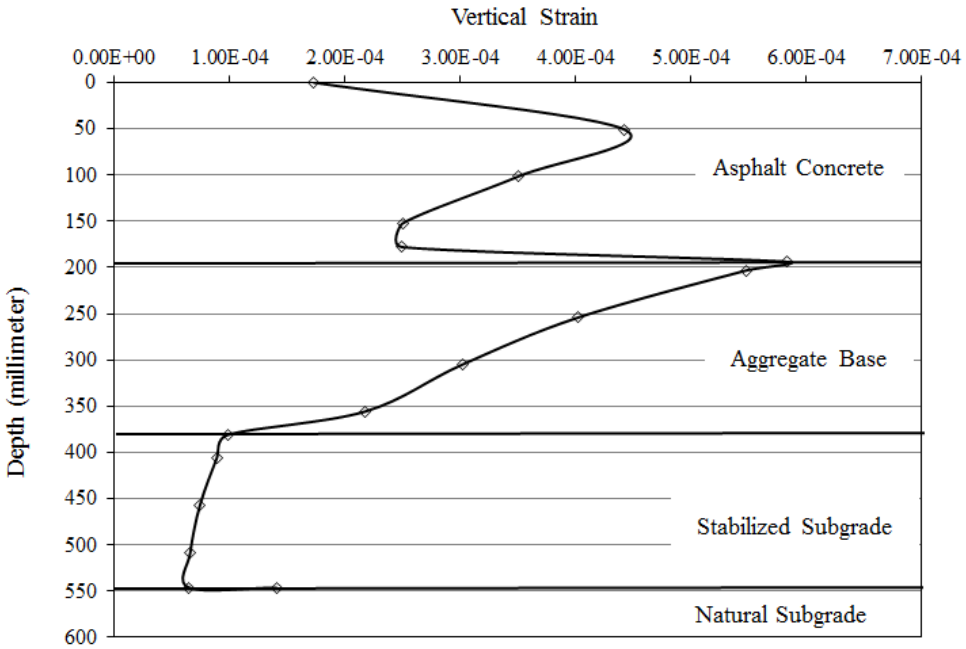

Figure 6-2 Typical Vertical Strain Distribution in the Test Section (at the Center of a Wheel) Load)

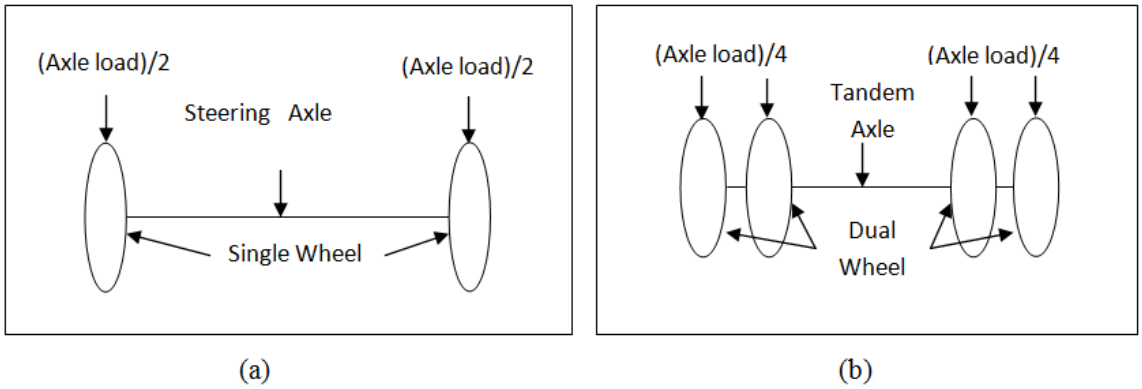

Figure 6-3 Loading Configuration of (a) Steering Axle and (b) Tandem Axle

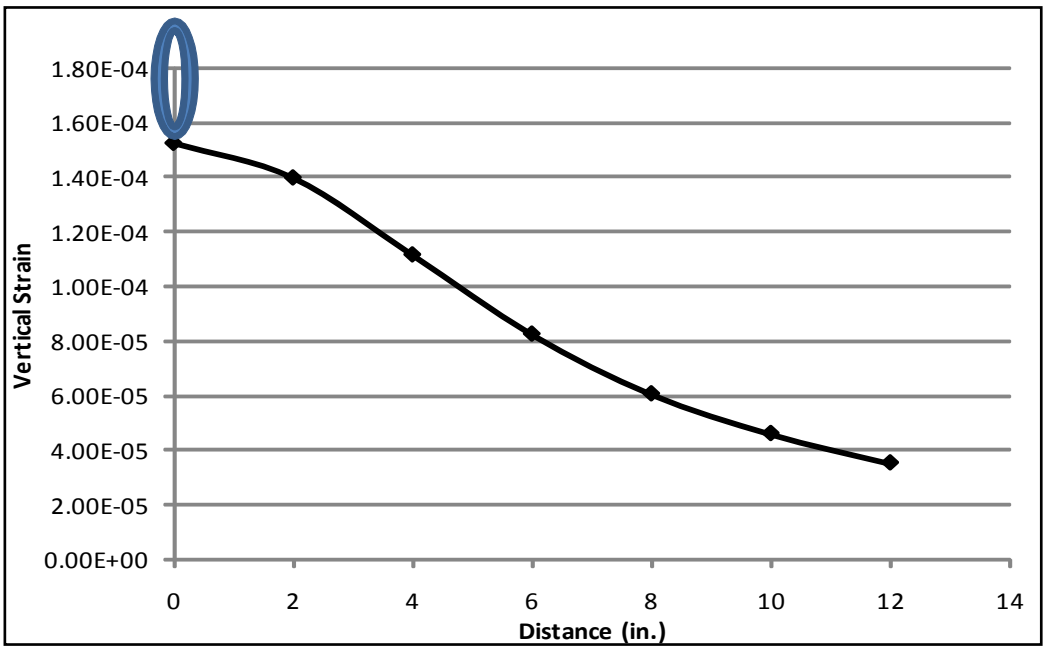

Figure 6-4 Vertical Strain Distribution for Single Wheel of Steering Axles

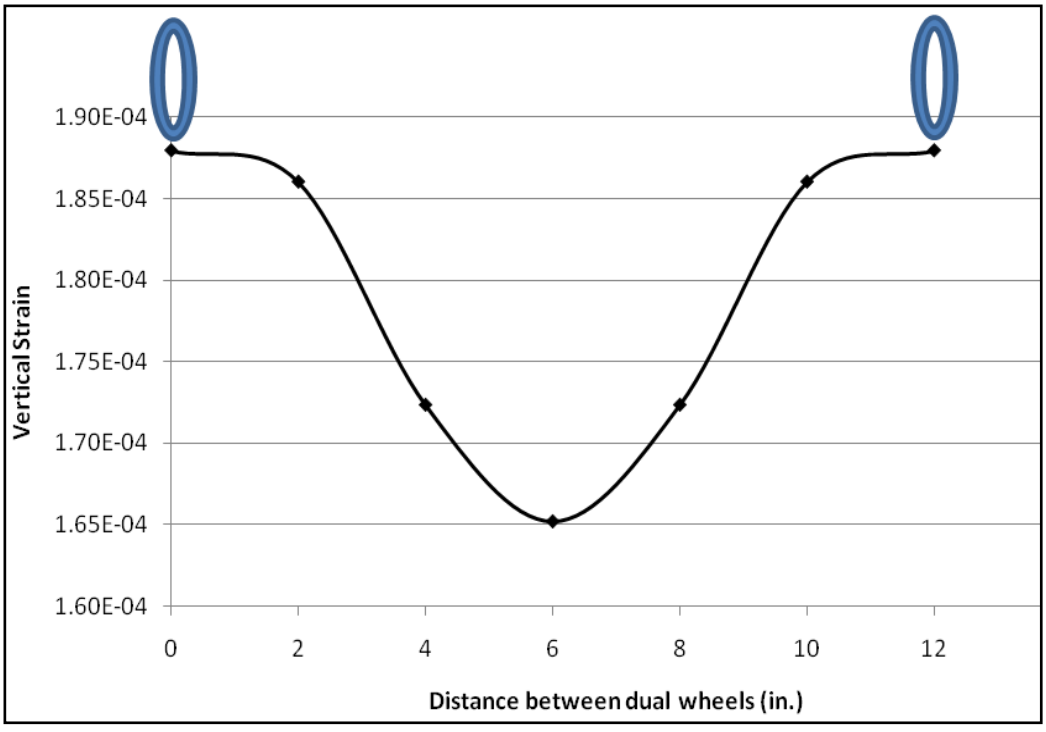

Figure 6-5 Vertical Strain Distribution for Dual Wheels of Tandem Axles

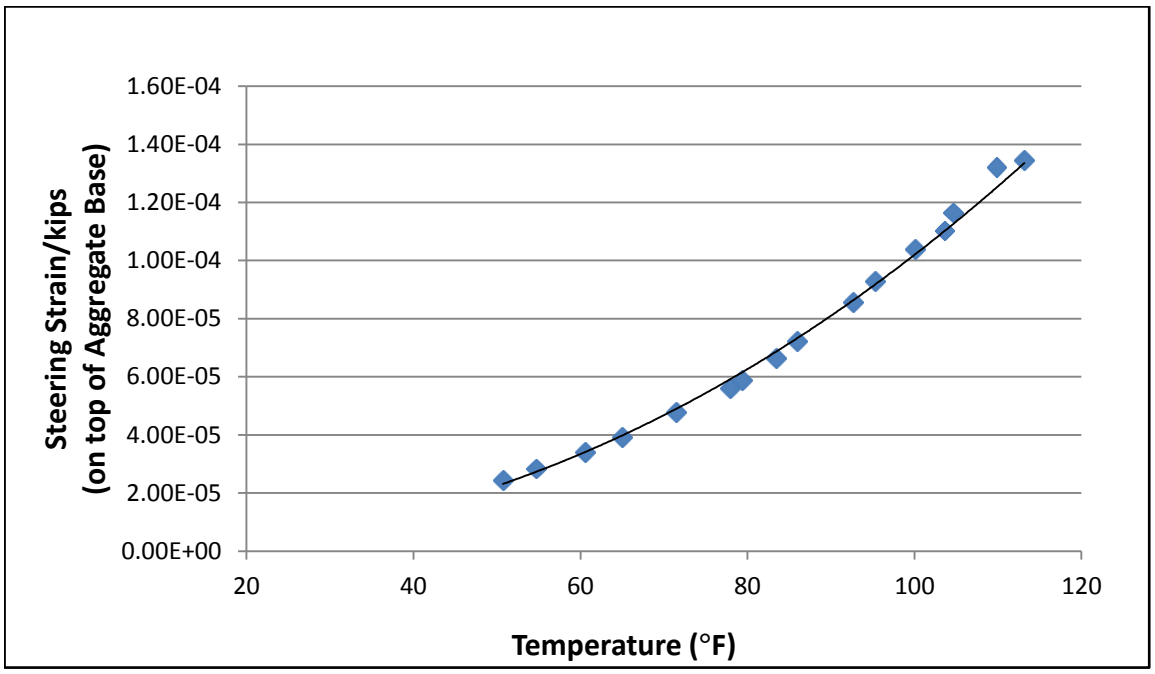

Figure 6-6 Vertical Strain-Temperature Correlation for Steering Axle

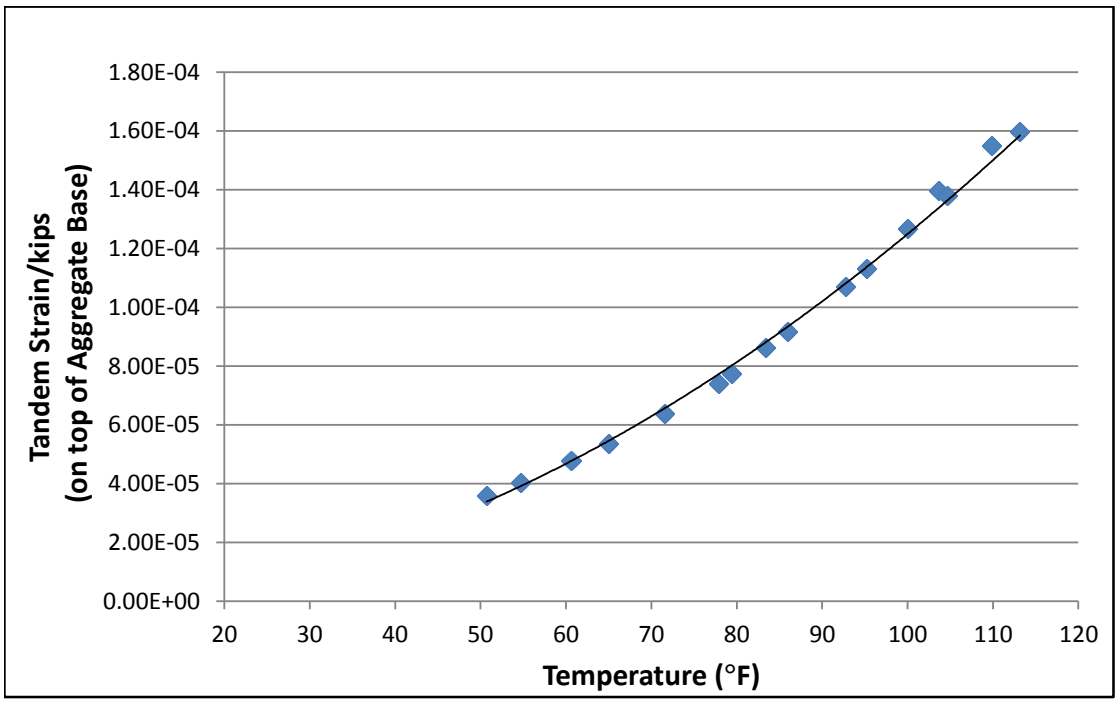

Figure 6-7 Vertical Strain-Temperature Correlation for Tandem Axle

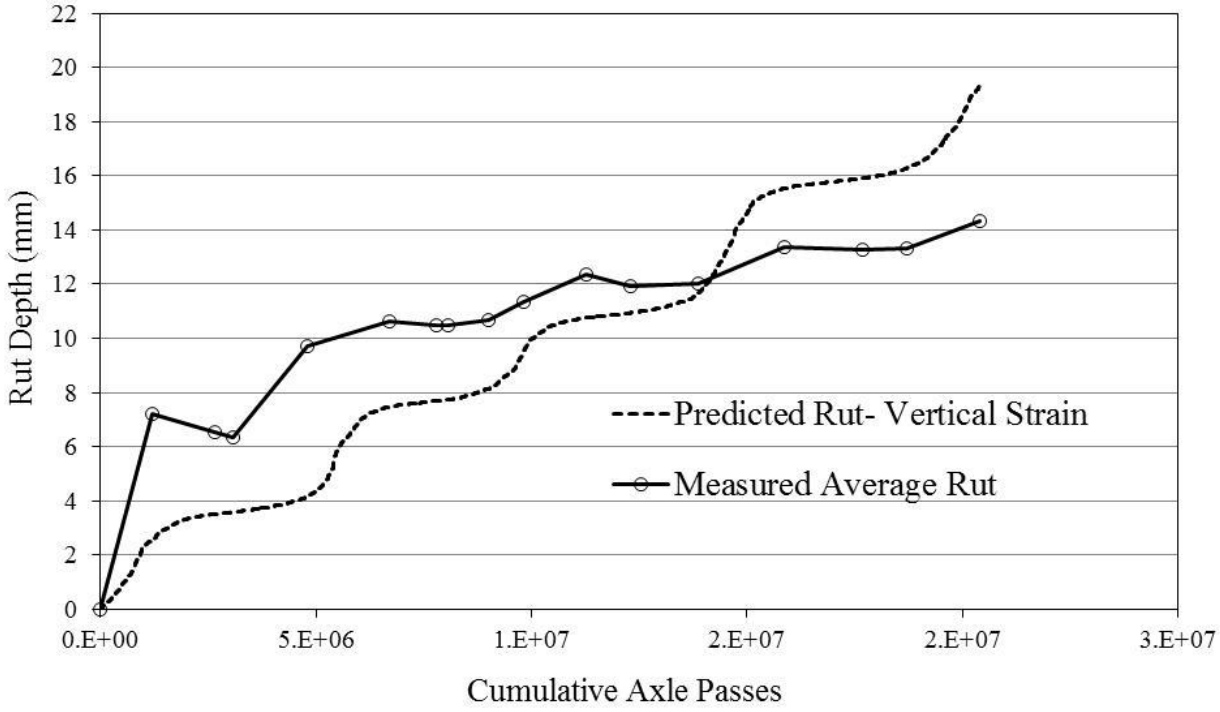

Figure 6-8 Vertical Strain Model: Predicted and Measured Rut in the Test Section

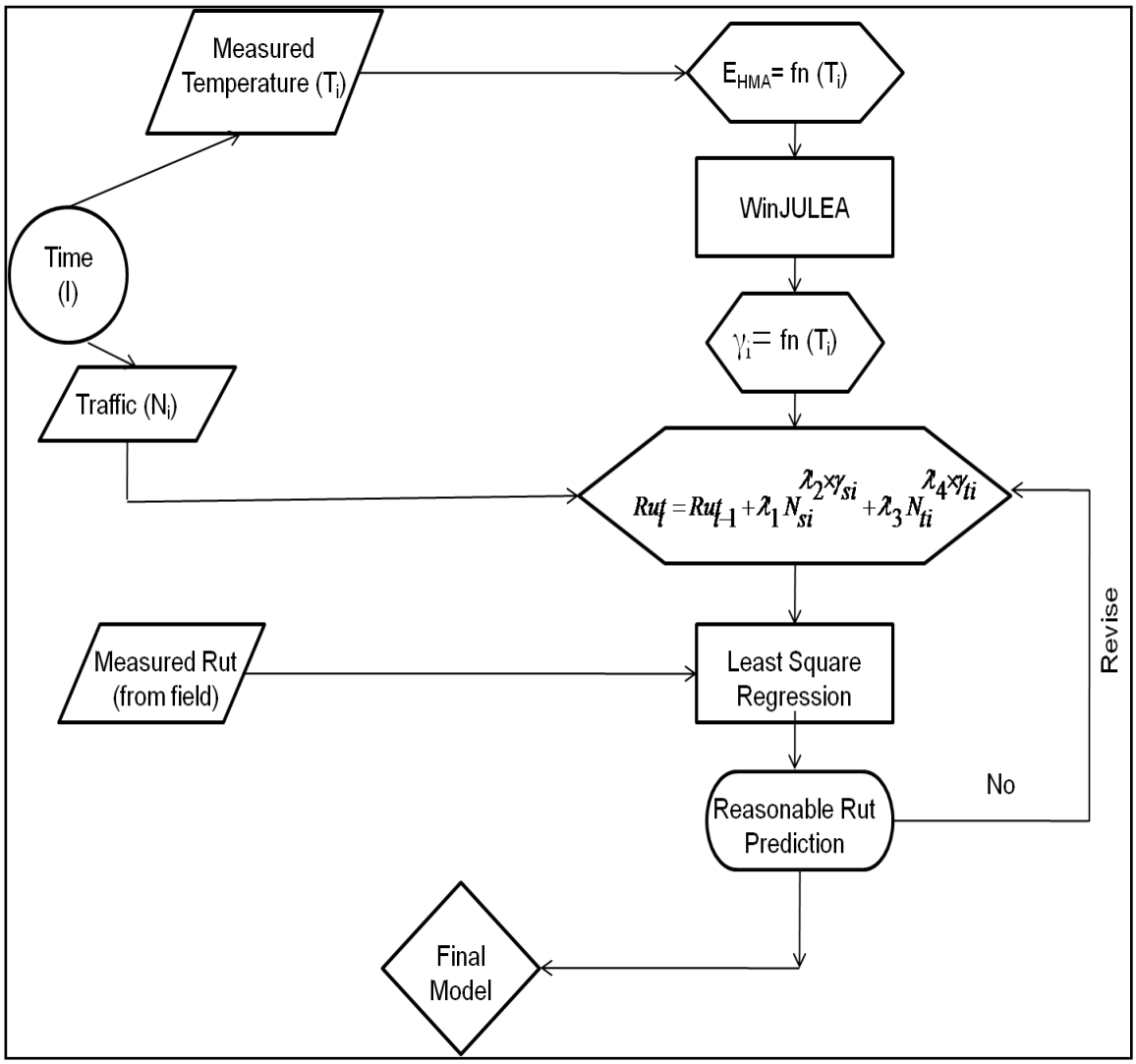

Figure 6-9 Shear Strain-based Rut Prediction Model Methodology Flow Chart (Selvaraj, 2007)

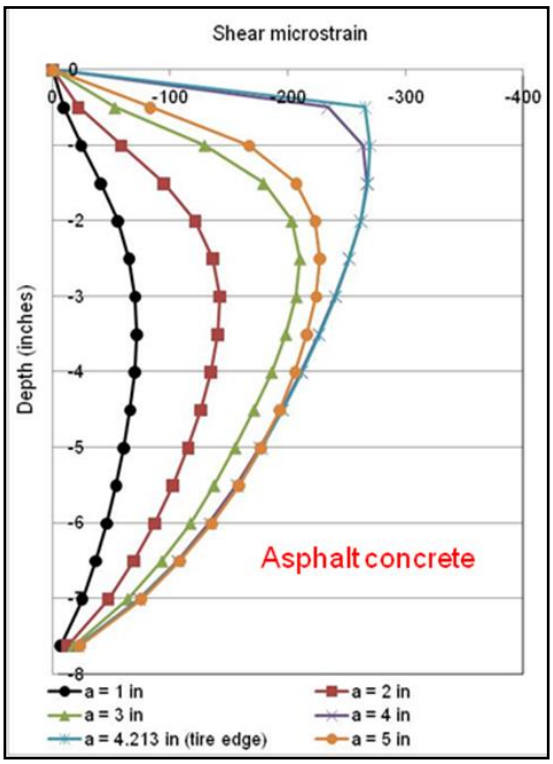

Figure 6-10 Typical Shear Strain Distribution in the HMA layer of the Test Section (a = Distance from the Center of a Wheel Load)

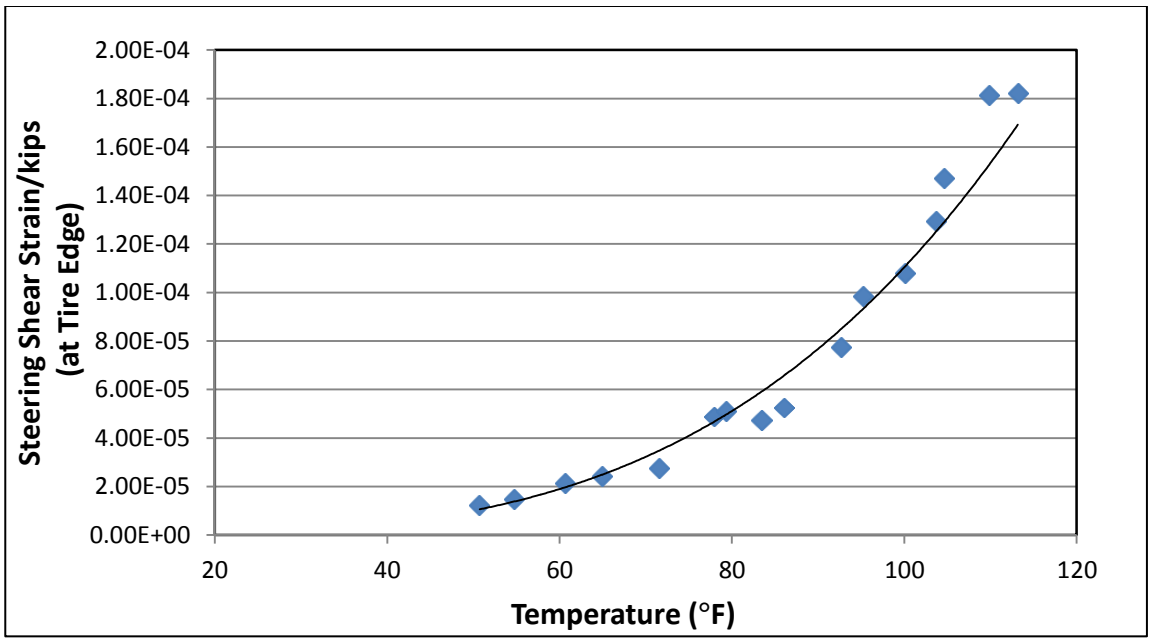

Figure 6-11 Shear Strain-Temperature Correlation for Steering Axle

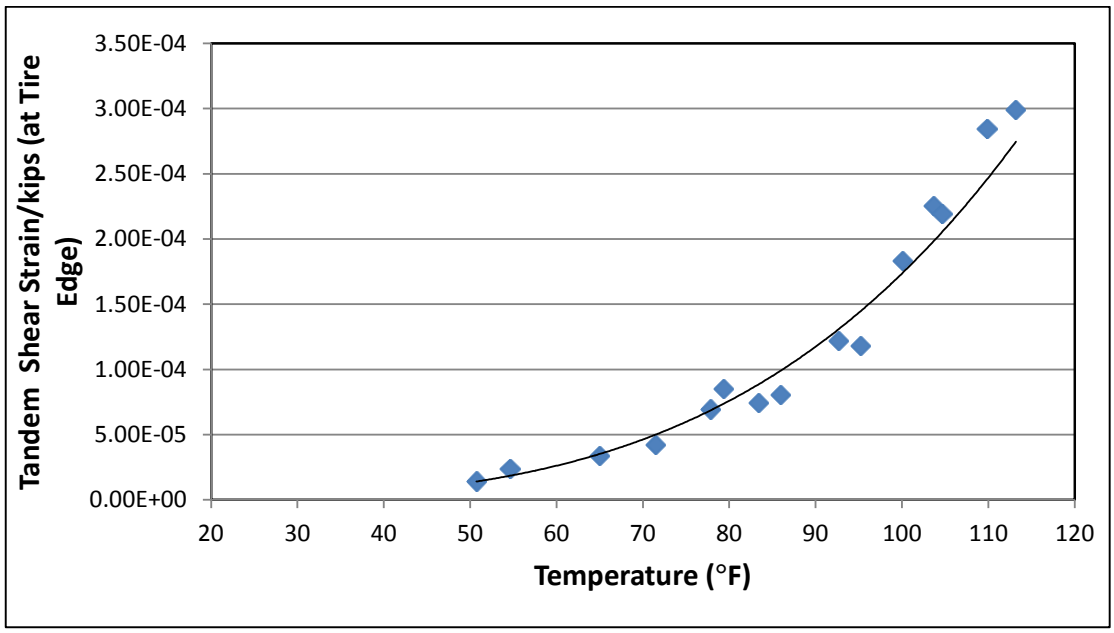

Figure 6-12 Shear Strain-Temperature Correlation for Tandem Axle

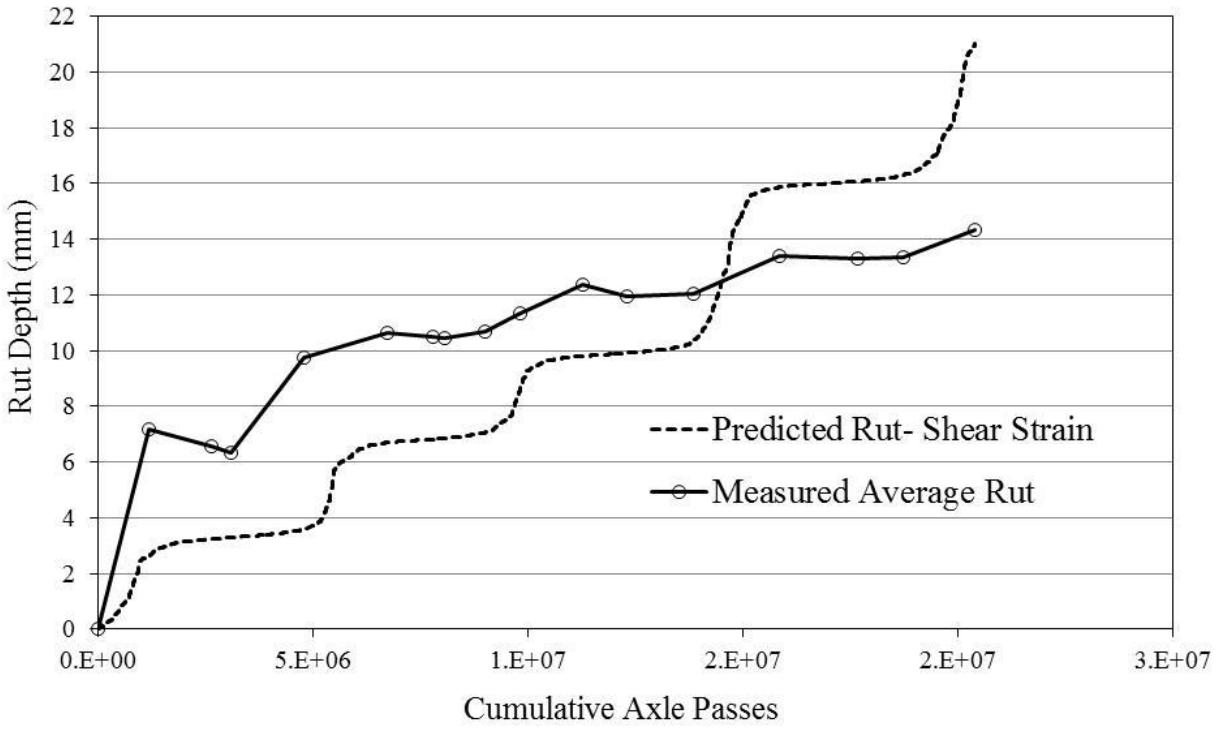

Figure 6-13 Shear Strain Model: Predicted and Measured Rut in the Test Section

Chapter 7 FATIGUE PREDICTION MODEL DEVELOPMENT

7.1 Introduction

As noted earlier, fatigue damage of HMA caused by cyclic stresses and strains due to vehicular traffic and environmental factors (temperature) is one of the primary distresses in flexible pavements. A widely accepted mechanism uses maximum tensile strains at the bottom of HMA layers to determine fatigue damage, which is generally caused by repeated heavy axle loads. A cumulative localized damage results from a build-up of irrecoverable strains. Fatigue cracking potential is generally thought to be the greatest at the bottom of the HMA layers, where critical tensile strain exists. Several existing models can be used to predict the fatigue life of flexible pavements from the tensile strain at the bottom of the HMA layers (Yoo and Al-Qadi, 2010). This chapter describes the development of fatigue transfer functions using field material and performance data collected from the I-35 Test Section over a three-year period. Additionally, the results of four-point fatigue tests conducted in the laboratory are discussed in this chapter.

7.2 Methodology

The model developed in this study is based on the hourly temperature data, which was collected continuously throughout the three-year period. Temperature was the critical link between HMA strain and stiffness data. For each hourly temperature, the *in-situ* HMA strain (for steering, and tandem axles) and stiffness values were calculated.

The HMA strain amplitude, ε_t, for steering and tandem axles was calculated using Equations (4.2) and (4.3), respectively, then multiplied with the average axle weights (steering and tandem) obtained from the WIM data. This was necessary to account for

different truckload magnitudes, since live vehicular traffic was involved. The HMA modulus value, *E*, was calculated using Equation (4.6), and was the same for both steering and tandem axles.

The number of load cycles, n_i, equaled the number of steering and tandem axles for each hour. With the applied loads, stiffness and strain values, cycles to failure, N_{fi}, was calculated assuming a fatigue transfer function. Following this, the incremental damage, D_i, was computed for each hour using the Miner's hypothesis shown in Equation (7.1):

$$D_i = \frac{n_i}{N_{fi}} \tag{7.1}$$

where

D_i = Incremental damage

n_i = Number of load applications at hour, *i*

N_{fi} = Number of load applications at failure for conditions at hour, *i*

The total damage at any time was taken as the sum of the incremental damages for steering and tandem axles, as shown here in Equations (7.2) and (7.3), respectively:

$$D_{steering} = \sum_{i=1} \frac{n_i}{N_{fi}} \tag{7.2}$$

$$D_{tandem} = \sum_{i=1} \frac{n_i}{N_{fi}} \tag{7.3}$$

Using the generated data above, the fatigue model was then calibrated to fit the observed performance. Since fatigue cracking had not yet been observed in the pavement at the test section prior to May 31, 2011, the regression coefficients were determined such that the total damage ratio, *D*, is assumed to be equal to 0.2. A similar assumption was considered in the NCAT fatigue model for Sections N3 and N4, where no cracking was observed (Timm and Priest, 2006). Recall that a damage ratio of 1.0 means that the pavement has failed in

terms of fatigue cracking, where 45-50 percent of the wheelpath or 20 percent of the total lane area shows fatigue cracks.

7.3 Fatigue Model

The current state of practice for fatigue transfer functions, including AI MS-1, Shell Oil Design Guide and the MEPDG, is in the form of (Timm and Priest, 2006):

$$N_f = k_1 \left(\frac{1}{\varepsilon_t}\right)^{k_2} \left(\frac{1}{E}\right)^{k_3} \quad (7.4)$$

where

N_f = Number of load cycles until fatigue failure

ε_t = Applied horizontal tensile strain (from strain-temperature relationship Equation (4.2) or (4.3))

E = HMA mixture stiffness (from stiffness-temperature relationship Equation (4.6))

k_1, k_2, k_3 = Regression constants

It may also contain a volumetric correction term including the voids filled with bitumen of the mix. These functions are often developed in the laboratory and then shifted or calibrated to field performance with correction factors. In the development of the MS-1 design guide by the Asphalt Institute (AI), just the constant k_1 was adjusted to match field observations (Finn et al., 1977). In the development of the MEPDG, however, all three regression constants were adjusted (El-Basyouny and Witczak, 2005).

For the fatigue model presented here, all three regression constants were calibrated to fit the data collected at the I-35 Test Section. Following the MEPDG, the AI MS-1 equation (Thickness Design, 1982) was used as the base model and developed to the calibration functions as shown below:

$$N_f = 18.4 * C * (0.00432 * (\frac{1}{\varepsilon_t})^{3.29} * (\frac{1}{E})^{0.854}) \quad (7.5)$$

where

$C = 10^M$

$M = 4.84 * (\frac{V_B}{V_B + V_V} - 0.69)$

V_B = Binder Volume

V_V = Air Voids

Based on the proportion of the asphalt materials used in the construction of the Test Section (Table 3.6), the volumetric correction, *C*, is calculated as 0.023, and Equation (7.5) was simplified as follows:

$$N_f = 0.00183(\frac{1}{\varepsilon_t})^{3.29} (\frac{1}{E})^{0.854} \quad (7.6)$$

The above equation served as the base model which was then recalibrated using field collected and analyzed data to create the final transfer functions. Recall that for the strain-temperature relationship, two equations were developed, one for steering axle and one for tandem axle; consequently, two transfer functions were needed, one for each:

For steering axles: $N_f = 0.8 * \left(\frac{1}{\varepsilon_{t_{steering}}}\right)^{4.0} * \left(\frac{1}{E}\right)^{1.0}$ (7.7)

For tandem axles: $N_f = 0.8 * \left(\frac{1}{\varepsilon_{t_{tandem}}}\right)^{4.0} * \left(\frac{1}{E}\right)^{1.0}$ (7.8)

Both equations correspond to an assumed damage ratio of 0.2, since the pavement didn't fail and no fatigue cracks had been observed. Note that the regression constants (k_1, k_2, k_3) used in Equations (7.7) and (7.8) are the same. Figure 7.1 shows the accumulation of fatigue damage over time, from May 30, 2008 to May 31, 2011, for the I-35 Test Section. It is

clear that the damage at the terminal date is equal to 0.2, as assumed. The red line represents a damage ratio of 1, where the curve will reach when the pavement fails due to fatigue cracking. Once the pavement starts showing cracks and begins to deteriorate, the transfer functions will have to be recalibrated. As for further comparison, the daily average temperature is plotted (grey dots; right y-axis) with the damage accumulation (black curve; left y-axis), presented in Figure 7.2. The damage accumulation matches well with the temperature data. The seasonal trend and the increase of fatigue damage in warmer temperatures are evident from Figure 7.2.

In order to verify the need for local calibration of fatigue transfer functions, the base model in Equation (7.5) is used in conjunction with the data collected from the Test Section to calculate the damage magnitude. The results are shown in Figure 7.3. A pattern similar to that in Figure 7.2 is observed, but the damage accumulated at the terminal date exceeds 3,000, which doesn't agree with the observed performance (i.e. no fatigue cracking). Furthermore, the NCAT model for 5-in. or thicker HMA Pavements, presented in Equation (2.38), was used to predict the damage accumulation at the I-35 Test Section. Based on the plot in Figure 7.4, the damage accumulated over the three-year period is 2.5, which is also different from the observed performance (i.e. no fatigue cracking). From these results, it is evident that local calibration of the M-E design procedures based on field data is essential for predicting the pavement fatigue life with reasonable confidence.

As mentioned earlier, the fatigue model developed and presented here is based on the assumption that the current state of pavement distress at the Test Section is 20% of the fatigue life. A different assumed value of fatigue distress level would predict a different fatigue life. Therefore, further calibration is needed as the pavement starts showing fatigue cracks.

7.4 Laboratory Four-Point Fatigue Tests

Laboratory four-point fatigue tests were conducted at a facility located in SemMaterials, L.P., (Now RoadScience, LLC), located in Tulsa, OK (Figure 7.5). Additional testing and sample preparation details are provided in subsequent sections.

7.4.1 Testing Methodology and Sample Preparation

In the present study, beams were tested for fatigue life under four-point loading inside a beam fatigue apparatus, in accordance with the AASHTO T 321 test method (Figure 7.6). The advantage of using a four-point fatigue apparatus is that it produces a constant bending moment over the center third span between the H-frame contact points on the beam specimen (ASTM D 7460). This apparatus also allows free rotation and translation at all load and reaction points, as shown in Figure 7.6.

The fatigue life tests consist of applying a repeated constant vertical strain to a beam specimen in flexural tension mode until failure or up to a specified number of load cycles. In this test, the input strain was sinusoidal shaped, applied at a frequency of 10 Hz in accordance with the AASHTO T 321 test method. The test was conducted at a strain level of approximately 400 microstrain, consistent with the AASHTO T 321 test method recommendations for conventional asphalt concrete. Failure is assumed to occur when the stiffness reached half of its initial value, which is determined from the load at 50^{th} cycle. The fatigue life (N_f) is the total number of load repetitions that cause a 50 percent decrease in initial stiffness (AASHTO T 321). The test is terminated manually when the initial stiffness has diminished by 50 percent or when a preset number of load cycles (2,000,000) is reached. The flexural stress, strain and stiffness of beams were determined by using the following expressions (AASHTO T 321):

$$\sigma_f = \frac{3aP}{bh^2} \tag{7.9}$$

$$\varepsilon_f = \frac{12\delta h}{\left(3L^2 - 4a^2\right)} \tag{7.10}$$

$$M_{rf} = \frac{\sigma_f}{\varepsilon_t} = \frac{aP\left(3L^2 - 4a^2\right)}{4b\delta h^3} \tag{7.11}$$

where σ_f = tensile stress at the bottom of beam, ε_t = tensile strain at the bottom of beam, M_{rt} = flexural stiffness, P = applied peak load, a = spacing between inside clamps (119 mm, i.e., 4.69 in), b = average beam width, h = average beam height, δ = beam deflection in neutral axis, L = length of beam between outside clamps or supports (35.56 mm, i.e., 14 in).

In this study, a total of 10 beam specimens were tested at three different temperatures, i.e., 5^{o}C, 20^{o}C, and 40^{o}C. Figures 7.7 (a) and (b) show a photographic view of beam specimens tested at a typical beam specimen after failure. The beam specimens (length = 15 in; width = 2.5 in; height = 2 in) were prepared by saw cutting block samples extracted from the field (*see Section 3.7.4.4 for details*). The air voids of the tested sample ranged from 8.04% to 9.71%. Table 7.1 shows the test matrix and air void content of each specific beam. It is evident from Table 7.1 that three beams were tested at 20^{o}C and 40^{o}C, and four beams were tested at 5^{o}C. The beams tested at 40^{o}C were stopped before completion of test as targets were pulled off the beam due to high temperature (Figure 7.7c).

7.4.2 Test Results

Test data were analyzed using Equations (7.9) through (7.11) to compute the stress, strain, and flexural stiffness per cycle as a function of the number of load cycles. In this study, fatigue life was defined as the number of repeated cycles corresponding to a 50 percent

reduction in initial stiffness, which was measured at the 50^{th} load cycle. Figures 7.8 and 7.9 show variation of flexural stiffness with number of cycles for beams tested at 5^{o}C and 20^{o}C, respectively. It is evident from Figures 7.8 and 7.9 that fatigue results are repeatable. It can also be seen that the flexural stiffness decreased as the number of cycles increases. That is, at the same strain level, a greater stress was needed to reach the desired strain values at the beginning of fatigue test than at the end of the test.

The initial stiffness values and number of cycles to fatigue failure of beams determined by initial tensile stress and strain are presented in Table 7.1. It is evident from Table 7.1 that due to an increase in temperature, the initial flexural stiffness of beams decreases and the number of cycles to failure increases. For example, an increase in temperature by 15^{o}C (5^{o}C to 20^{o}C) decreased the average initial stiffness by 62% (from 1,583 ksi to 595 ksi) and increased the average failure cycles from approximately 66,250 to 200,000 (202% increase).

Table 7-1 Summary of Four-Point Fatigue Tests

Temperature (^{o}C)	Specimen#*	Air Voids (%)	Initial Stiffness (ksi)	Final Stiffness (ksi)	Number of Cycles to Failure
5	540 R2	8.50	1,554	678	69,998
5	738-4	8.57	1,644	680	59,998
5	540 L1	9.19	1,579	578	34,998
5	540 R1	9.71	1,552	757	100,000
20	738-2	8.04	511	253	179,998
20	738-3	8.37	689	325	179,999
20	738-1	8.50	584	287	239,998
40	900-1	8.50	72	36	Target pulled out
40	900-2	9.19	83	42	
40	540 L2	9.71	95	48	of beam

*Indicates station number from which sample was extracted

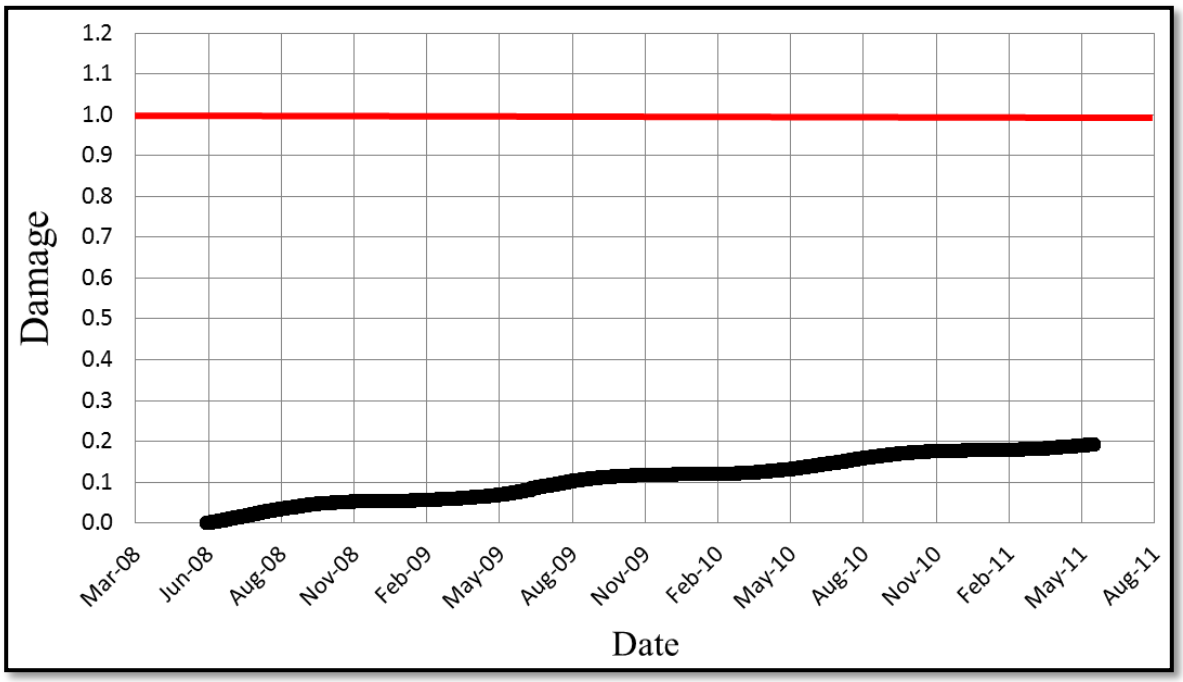

Figure 7-1 Damage Accumulation for the I-35 Test Section

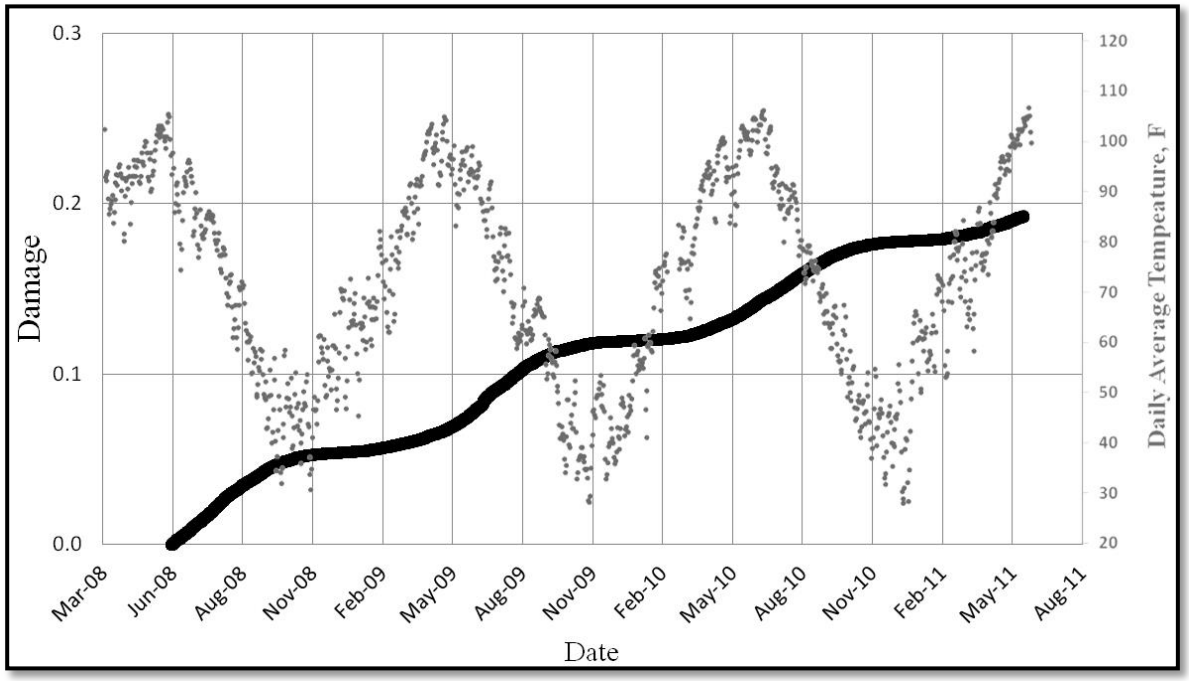

Figure 7-2 Damage Accumulation and Temperature Variation for the I-35 Test Section

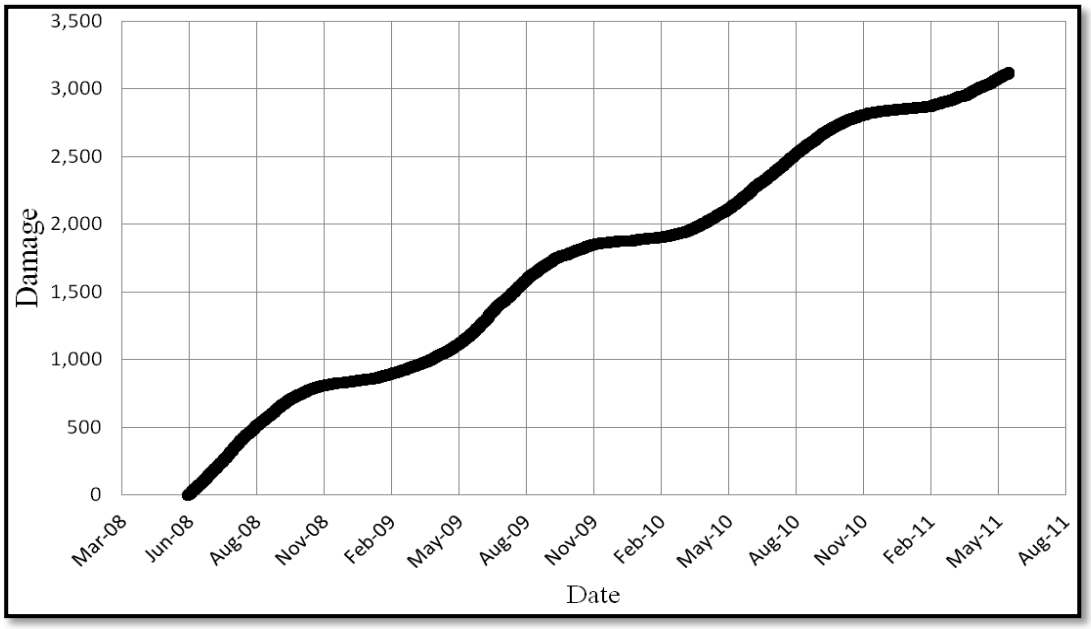

Figure 7-3 Base Model Damage Predictions

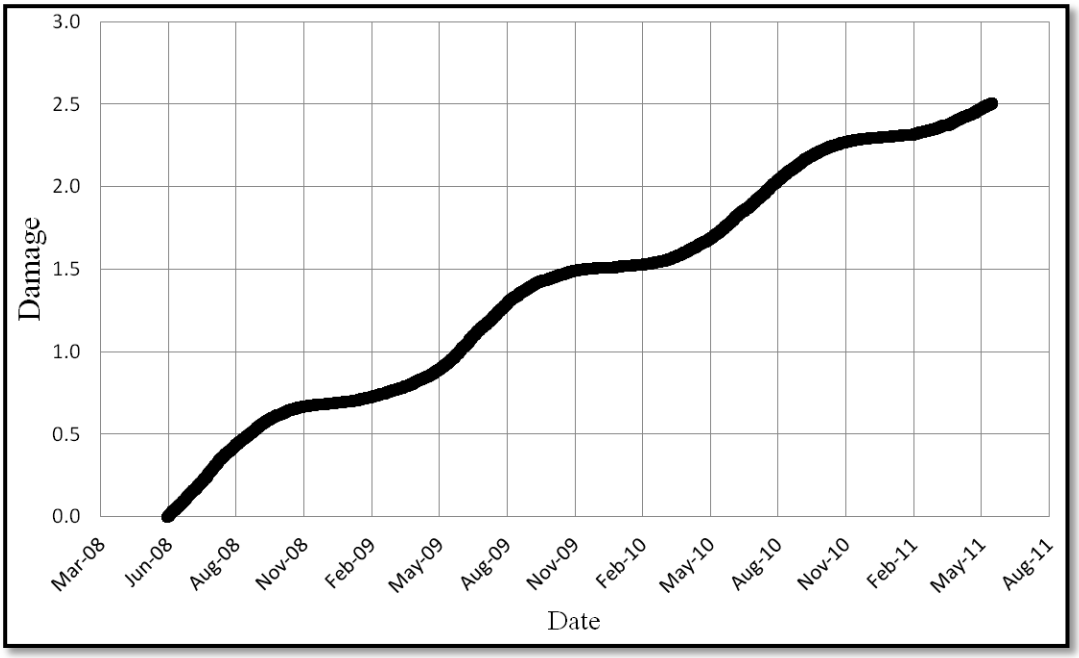

Figure 7-4 NCAT Thick Model Damage Predictions

Figure 7-5 MTS Environmental Chamber for Fatigue Test and Associated Computer/Software

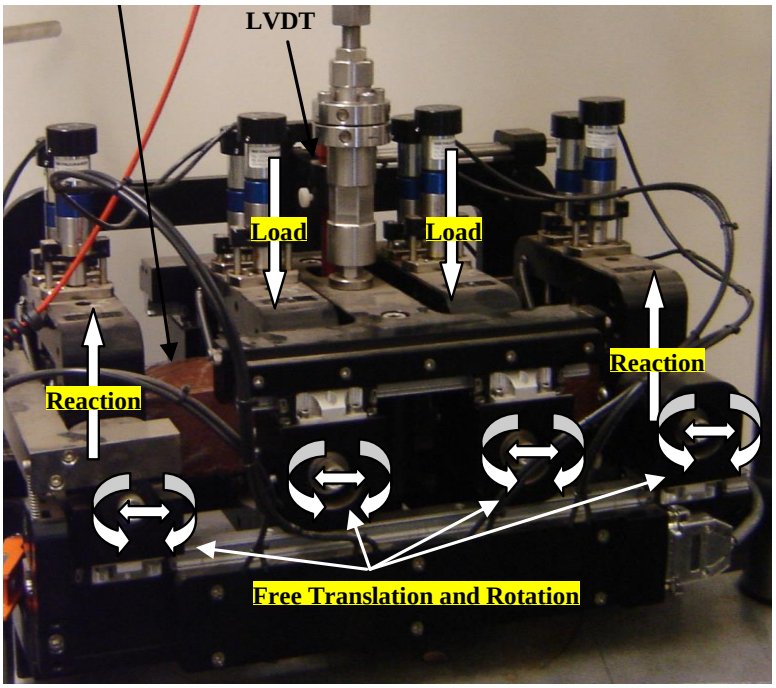

Figure 7-6 7.6 Setup for Four-Point Fatigue Test

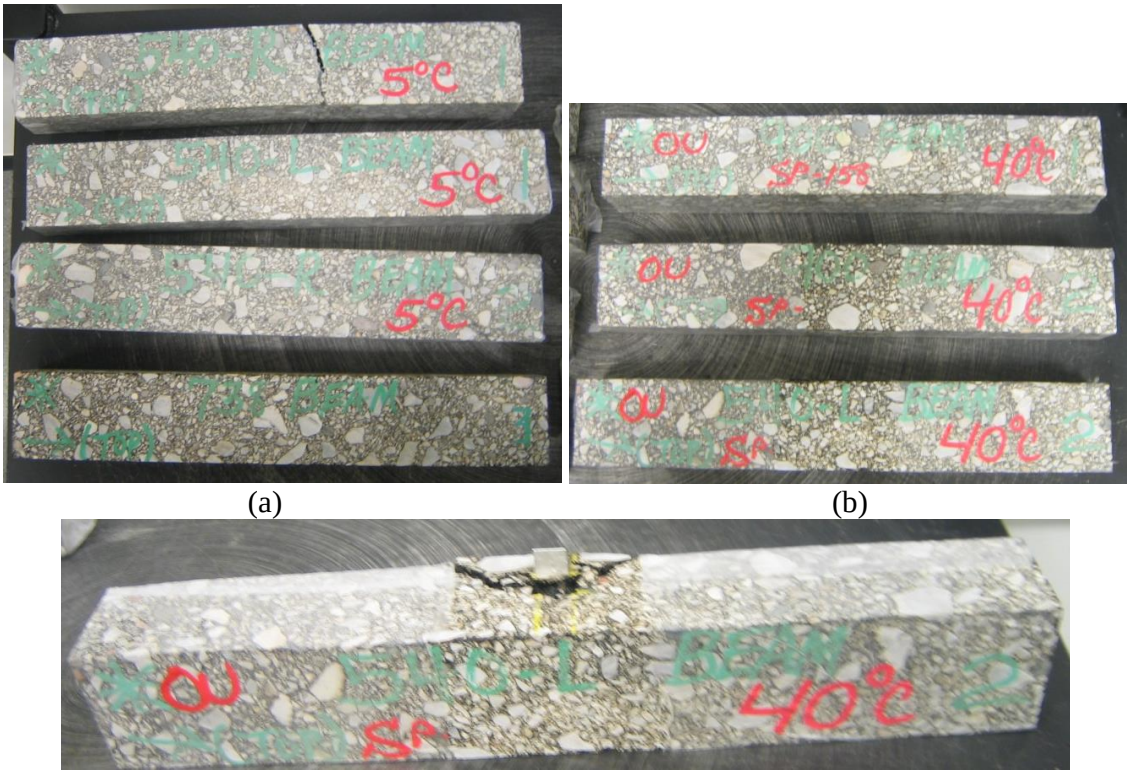

(a) (b)

(c)

Figure 7-7 Four-Point Fatigue Beams (a) Tested at 5°C, (b) Tested at 40°C, and (c) Target Pulled Out of Beam at 40°C

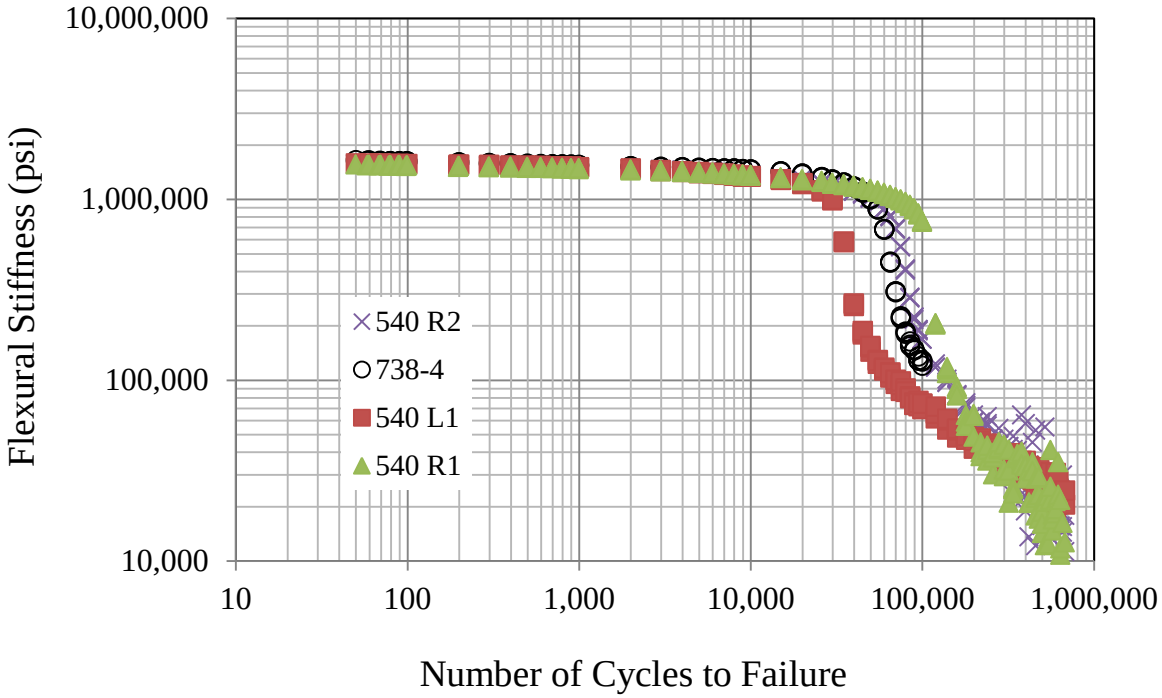

Figure 7-8 Flexural Stiffness Versus Number of Fatigue Cycles at 5°C

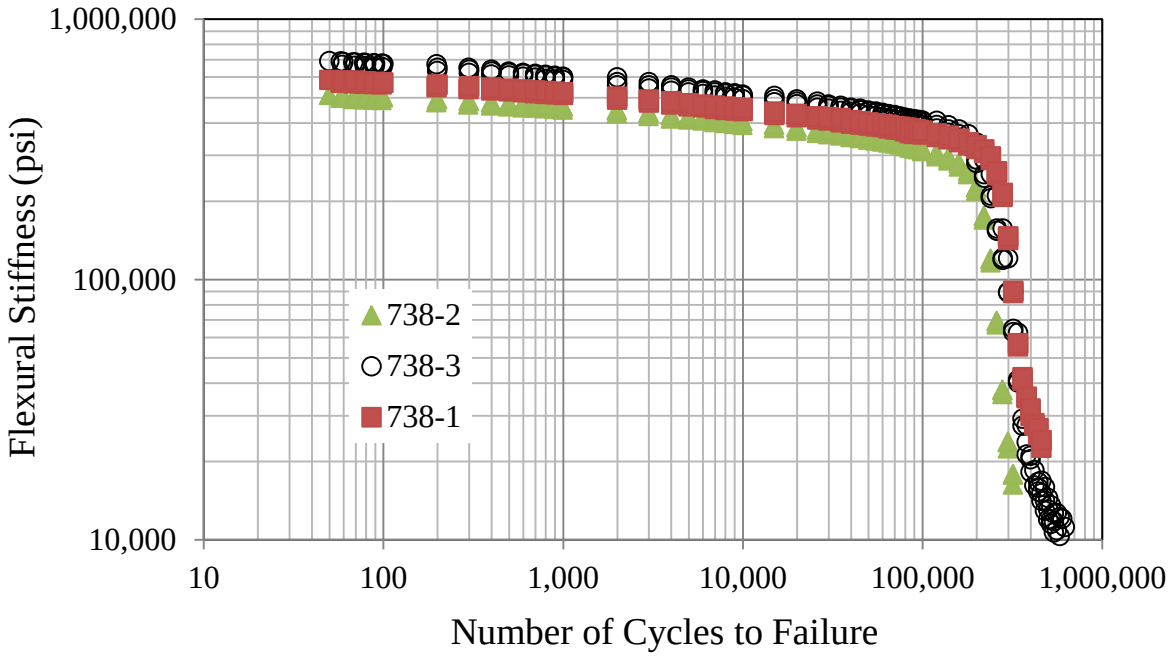

Figure 7-9 Flexural Stiffness Versus Number of Fatigue Cycles at 20°C

Chapter 8 SUMMARY, CONCLUSIONS AND RECOMMENDATIONS

8.1 Summary

To gain an insight into flexible pavement behavior under actual vehicular traffic and environmental conditions, a 1000-ft (305-m) long Test Section was constructed and instrumented on I-35 in McClain County, Oklahoma. In addition, a WIM station was installed approximately three-quarters of a mile downstream from the Test Section and was used for traffic data collection. The pavement design in the Test Section was selected to be thinner than a typical interstate pavement so that it would fail in a relatively short amount of time under heavy interstate traffic.

The construction and instrumentation of the section took approximately one month, and the Test Section was opened to traffic on May 30, 2008. Overall, four different materials, namely subgrade soil, stabilized subgrade, aggregate base, and asphalt concrete, were used in the construction. Additionally, during construction the section was instrumented with moisture, temperature, pressure, strain, and axle sensors to measure pavement response under actual traffic loading and environmental conditions.

The field data collection focused on pavement response data (longitudinal and transverse strains at the bottom of the asphalt layer, FWD testing), environmental data (temperature within the pavement), performance data (rutting, visual crack mapping, IRI values), and actual traffic data (number of trucks, axles, and axle load). DCP and moisture content data along the pavement cross-section was also collected as an additional performance indicator of the Test Section.

Field rut measurements were conducted periodically to monitor performance of the Test Section using a straight edge/rut gauge combination and a Face Dipstick®. WinJULEA, a

commonly used multilayered linear elastic analysis software, was used to model the Test Section and determine rut values due to axle (single and tandem) loading. Data obtained from the Test Section were used to develop two separate field calibrated rut prediction models. One model incorporated the traffic-induced vertical strain on the top of the aggregate base layer (i.e., bottom of the asphalt layers). The other model was based on the maximum shear strain in the HMA layer.

A separate statistical rut prediction model was developed from the laboratory rut tests using the Asphalt Pavement Analyzer (APA). A total of 100 specimens were compacted at different air voids, ranging between 1% and 11%, using a Superpave Gyratory Compactor (SGC). Out of these 100 specimens, a total of 30, 26, and 44 specimens were tested in the APA rut machine at 40^{o}C (104°F), 50^{o}C (122°F), and 64^{o}C (147°F), respectively. Based on the test results, a statistical model was developed correlating rut depths with three independent variables, namely air voids of the compacted sample, test temperature, and number of loading cycles.

Using the collected field data, a fatigue transfer function was developed to predict the failure of the pavement in fatigue. The fatigue model used in this study was based on the hourly temperature data, which was collected continuously throughout the three-year period. The fatigue model was then calibrated to fit the observed performance. Since the Test Section has not experienced any fatigue cracking in the pavement prior to May 31, 2011, the regression coefficients were determined for an assumed damaged ratio of 0.2. The results of four-point fatigue tests conducted on field compacted beams are also presented and discussed. Based on a recent meeting between ODOT and the OU research team, field data collection and analysis and quarterly field testing will continue as part of Phase II of this project for a

period of up to two years. A forensic investigation through trenching at selected sections is planned toward the end of Phase II.

8.2 Conclusions

From the laboratory results, field test results, and the rut and fatigue prediction models presented in the preceding chapters, the following conclusions can be drawn:

(1) The lateral positioning system successfully captured the wheel wander of passing trucks. The average distance from the right wheel to the edge stripe was found to be equal to 15.5 in. This distance is closer to strain gages 3, 6, 9, and 12 compared to other gauges.

(2) The strain gauge array was sufficient to capture the pavement strain response due to vehicular loading. Using two different orientations (longitudinal and transverse) was necessary to capture the maximum strain. It was found that longitudinal strain gauges recorded about 20 percent higher strain values than gauges oriented in the transverse direction.

(3) Strain quantification used in this research was very similar to that used by NCAT on their Test Track; however, the present study was unique in terms of factoring in live traffic load with varying axle weights.

(4) It is not necessary to collect and process continuous dynamic response data. This would be very time consuming, especially for a long duration project. Strain-temperature and stiffness-temperature relationships can be developed using data collected over a limited duration of time and used to predict the pavement response, as done in this project. To characterize the effect of temperature on strain, two relationships were established, one for the steering axle and one for the tandem axle. These relationships were found to remain relatively stable after certain time period.

(5) For the I-35 Test Section, Class-9 vehicles constitute the highest percentage (59.5**%)**. The second largest vehicle group is Class-5, with 14.8%.

(6) In this study, field rutting was measured using two different methods: a straight edge/rut gauge combination and a Face Dipstick®. From the field rut data, it can be concluded that the accuracy and repeatability of the Face Dipstick® is far superior to the straight edge/rut gauge combination. Therefore, Face Dipstick® is recommended for collecting field rut data.

(7) Field rut measurements showed that all stations in the I-35 Test Section have undergone both primary rutting and secondary rutting. No tertiary rut was observed in any station. After roughly four years of service, the maximum rut of 0.71-in. and the minimum rut of 0.28-in. were observed at Station 738 and Station 900, respectively. The corresponding cumulative axles traversing the test section were about 18.7-million.

(8) Although the rutting values increased with time, most of the rutting was accumulated during the summer months. Also, the rate of rutting during the first summer month was much higher than in the second, third, and fourth summer months, although the cumulative axles during each summer months were similar (approximately 1.2-million).

(9) The shape of the observed rut profile in the I-35 Test Section was similar to the profile reported in the NCHRP 468 study, where HMA layers and/or aggregate base layers were primary contributors to rutting. So, it is likely that the rutting of the I-35 Test Section has been contributed primarily by the HMA layers and by the aggregate base layer. This conclusion will be verified through the forensic investigation by trenching as part of Phase II of this study.

(10) Although both vertical strain-based and shear strain-based models predicted rutting with similar levels of accuracy, as evident from the high R^2 values (0.86 for vertical strain-based and 0.80 for shear strain-based model), the vertical strain-based model was found to slightly outperform the shear strain-based model when predicting rut. In this study the rut prediction models were developed by regression analyses. The models underestimated rut in the initial stages and overestimated in the later stages. Since the test section was located on I-35, with extremely high traffic volume, it was not practical to close the lanes frequently to measure field rut. The developed models could have been significantly improved with the inclusion of additional rut measurement data.

(11) The laboratory test results suggest that the rutting values are influenced by the air voids content, test temperature, and number of loading cycles. Based on the test results, the rut value increased with increased air voids content, temperature and number of loading cycles.

(12) The regression model developed from the APA rut data with three independent variables, namely air voids content, test temperature, and number of cycles, was found statistically significant (R^2 = 0.91). Based on the sensitivity analyses, among the independent variables, test temperature was found to be most influential, followed by air voids content and number of loading cycles.

(13) In the rut prediction model based on APA rut data, all of the model parameters were positive indicating that rut depths will increase with the increase in air voids content, test temperature, and number of loading cycles.

(14) The results from this study are expected to be useful in predicting rutting of state highway pavements under similar traffic and environmental conditions. Moreover, the

field rut prediction models developed in this study will be a helpful tool for implementing the Mechanistic-Empirical Pavement Design Guide (MEPDG) by the state agencies.

(15) During the four-year period the Test Section did not show any sign of fatigue cracking. No fatigue cracking was observed at any stations during the duration of this study; consequently, it was assumed that the pavement has endured 20% of fatigue for developing the fatigue prediction model.

(16) The following preliminary fatigue transfer functions were developed for the I-35 Test Section:

For steering axles: $N_f = 0.8 * \left(\frac{1}{\varepsilon_{t_{steering}}}\right)^{4.0} * \left(\frac{1}{E}\right)^{1.0}$

For tandem axles: $N_f = 0.8 * \left(\frac{1}{\varepsilon_{t_{tandem}}}\right)^{4.0} * \left(\frac{1}{E}\right)^{1.0}$

(17) These transfer functions should be recalibrated when the pavement shows fatigue cracking and eventually fails.

8.3 Recommendations

Based on this study, the following recommendations are made for future studies:

(1) In this study, multilayered linear elastic analysis software was used to simulate the pavement response (under vehicular traffic loading) to develop the field rut prediction models. However, in reality, pavement materials may not behave in a linear elastic manner under specific conditions (for example, at high temperatures). Therefore, use of different software which account for non-linear behavior of pavement materials is recommended for developing improved rut prediction models in future studies.

(2) The shear strain-based rut prediction model is more applicable when the HMA layer rutting is the predominant source of rutting. In some cases, where rutting is also contributed by other underlying layers, a more robust model (e.g., finite element-based) would be needed. Such models may be considered in future studies.

(3) The laboratory rut prediction model was developed on the basis of rut tests at 40°C (104°F), 50°C (122°F), and 64°C (147°F) on only one HMA mix (Type S4, PG 64-22). Calibration of the model is recommended by using an enriched database containing laboratory rut values for additional HMA mixes.

(4) During the construction phase, extra care should be given to instrumentation, specifically to pavement dynamic response devices, such as earth pressure cells and strain gauges, in addition to moisture probes, to avoid any malfunction. No moisture probe in this study provided any meaningful data.

(5) Installing two-temperature probe arrays instead of one is advised in future projects. Also, it would be preferable to have the WIM station right after the strain gauges array; that will save a lot of processing time and eliminate the possibility of trucks changing lanes. Furthermore, strain gauges can be installed under both wheel paths (right and left) and only in the longitudinal direction. Lastly, regarding the lateral positioning system, it is highly recommended to use a different type of system that can withstand heavy truck traffic.

(6) The field rut and fatigue prediction models developed in this study were based upon moderate climatic conditions in Central Oklahoma. The field rutting and fatigue prediction models are only applicable for similar pavement cross-sections and environmental conditions. Therefore, validation of the models is recommended for

regions where pavement temperatures often go below -7°C (20°F) and at high temperature regions where pavement temperatures often go above 47°C (117°F) and also for different pavement cross sections.

(7) Contribution of the different layers to rutting should be investigated through trenching, as planned for Phase II of this study.

(8) Local calibrations of the MEPDG relative to rutting and fatigue of the I-35 Test Section are recommended.

LIST OF REFERENCES

AASHTO (1993), "AASHTO Guide for Mechanistic-Empirical Design of New and Rehabilitated Pavement Structures." Final Report prepared for National Cooperative Highway Research Program (NCHRP), Transportation Research Board, National Research Council, Washington, D. C.

AASHTO (2004), "Guide for Mechanistic-Empirical Design of New and Rehabilitated Pavement Structures," Final Report prepared for National Cooperative Highway Research Program (NCHRP), Transportation Research Board, National Research Council, Washington, D.C.

AASHTO (2009), "Rough Road Ahead: Fix Them Now or Pay For It Later," Transportation Research Board, National Research Council, Washington, D.C.

AASHTO T 166 (1999), "Bulk Specific Gravity of Compacted Bituminous Mixtures Using Saturated Surface-Dry Specimens," AASHTO Standard Specification for Transportation Materials, Part II, Washington, D.C.

AASHTO T 209 (1999), "Maximum Specific Gravity of Bituminous Paving Mixtures," AASHTO Standard Specification for Transportation Materials, Part II, Washington, D.C.

AASHTO T 269 (1999), "Standard Method of Test for Percent Air Voids in Compacted Dense and Open Bituminous Mixtures," AASHTO Standard Specification for Transportation Materials, Part II, Washington, D.C.

AI (1982), "Research and Development of The Asphalt Institute's Thickness Design Manual (MS-1)." Ninth Edition, Research Report No. 82-2, College Park, MD: The Asphalt Institute.

Ali, H.A. and Tayabji, S.D. "Evaluation of Mechanistic-Empirical Performance Prediction Models for Flexible Pavements." Transportation Research Record No. 1629, Washington, D.C.: Transportation Research Board, 1998, pp.169-80.

Ali, Hesham A. and Shiraz D. Tayabji. "Evaluation of Mechanistic-Empirical Performance Prediction Models for Flexible Pavements." Transportation Research Record No. 1629, Washington, D.C.: Transportation Research Board, 1998, pp.169-80.

Allen, D., Deen, R. C. (1980), "Rutting Models for Asphaltic Concrete and Dense Graded Aggregate from Repeated Load Tests," Proceedings of the Association of Asphalt Paving Technologists, Louisville, Kentucky, pp. 653-667.

Al-Qadi, I. L., A. Loulizi, M. Elseifi and S. Lahouar. "The Virginia Smart Road: The Impact of Pavement Instrumentation on Understanding Pavement Performance." The Journal of Association of Asphalt Paving Technologists Vol. 83, 2004, pp. 427-66

Alvarez, C. and M.R. Thompson. "Mechanistic-Empirical Evaluation of the Mn/Road Mainline Flexible Pavement Sections," Project IHR-535, Illinois Cooperative Highway and Transportation Research Program, University of Illinois, Urbana, IL, 1998.

American Association of State Highway and Transportation Officials (AASHTO), 1986. AASHTO Guide for Design of Pavement Structures. Washington, DC: American Association of State Highway and Transportation Officials (AASHTO).

American Society of Testing and Materials. Designation: E 1318-02, Standard Specifications for Highway Weigh-in-Motion (WIM) Systems with User Requirements and Test Methods. West Conshohocken, PA., 2002.

Barksdale, R.D. (1972), "Laboratory Evaluation of Rutting in Base Course Materials," Proceedings, Third International Conference on the Structural Design of Asphalt Pavements, Vol.1, London, United Kingdom, pp. 161-174.

Beer, Michael G., Greg Johnson and Dave Van Deusen. "Performance of Mn/Road Load Response and Subsurface Instrumentation," Staff Paper, Office of Minnesota Road Research, Maplewood, MN: Minnesota Department of Transportation, 1996.

Breidy, M., Muraleetharan, K.K., and Zaman, M. (2011). "Data analysis report – Field performance monitoring and modeling of instrumented pavement on I-35 in McClain county," Technical Report, The University of Oklahoma.

Breidy, M., Muraleetharan, K.K. and Zaman, M. (2009), "Traffic Report – Field Performance Monitoring and Modeling of Instrumented Pavement on I-35 in McClain County," Technical Report, University of Oklahoma, Norman, Oklahoma.

Brown, C., E. R., Cooley, L. A., Hanson, D., Lynn, C., Powell, B., Prowell, B., and Watson, D. (2002), "NCAT Test Track Design, Construction, and Performance" , Report 2002-12, National Center for Asphalt Technology, Auburn University, Alabama.

Dean, J. (2008), Verbal Communication, Pavement Design Engineering at Oklahoma Department of Transportation, October, 2008.

Drumm, E. C., Reeves, J. S., Madgett, M. R., and Trolinger, W. D. (1997), "Subgrade Resilient Modulus Correction for Saturation Effects," Journal of Geotechnical and Geo-environmental Engineering, 23(7).

El-Basyouny, M. and Witczak, M. (2005), "Calibration of the Alligator Fatigue Cracking Model for the 2002 Design Guide." Transportation Research Board 84th Annual Meeting Compendium of Papers. CDROM. Washington, D.C., 2005.

El-Basyouny, M. and Witczak, M. (2005), "Development of the Fatigue Cracking Models for the 2002 Design Guide," Transportation Research Record 1919, Transportation Research Board, 2005, pp. 77-86.

El-Basyouny, M., and Matthew W. (2005). "Calibration of the Alligator Fatigue Cracking Model for the 2002 Design Guide." Transportation Research Board 84th Annual Meeting Compendium of Papers. CDROM. Washington, D.C.

Elseifi, M. A., Mohammad, L. N., King, W. B., and Zhang, Z. (2012), "Assessment of Stress and Strain Instrumentation in Accelerated-Pavement Testing," International Journal of Pavement Research and Technology, Vol. 5, No. 2, pp. 121 – 127.

Epps, J, Monismith, C. L., Seeds, S. B., Alavi, S. H., Ashmore, S. C., Leahy, R, and Mitchell, T. M. (1998), "Performance of HMA Test Sections at WESTRACK," Journal of the Association of Asphalt Paving Technologists, 67, 738-782.

Eres Consultants Division (2004), "Guide For Mechanistic-Empirical Pavement Design of New and Rehabilitated Pavement Structures," Final Report, NCHRP 1-37A.

Federal Highway Administration. Guide to LTPP Traffic Data Collection and Processing. U.S. Department of Transportation, Washington, D.C., 2001.

Finn, F., Saraf, C., Kulkarni, R., Nair, K., Smith, W., and Abdullah, A. (1977), "The Use of Distress Prediction Subsystems for the Design of Pavement Structures," Proceedings of the Fourth International Conference on the Structural Design of Asphalt Pavements, Ann Arbor, Michigan, pp. 3-37.

Guide for Mechanistic-Empirical Design of New and Rehabilitated Pavement Structures (2004). "Final Report". Part 2. Design Inputs. Chapter 4. Traffic.

Haddock, J., Pan, C., Feng, A., and Galal, K., and White, T. D. (1998), "Validation of SHRP Asphalt Mixture Specifications Using Accelerated Testing," Draft Interim report, National Pooled Fund Study No. 176.

Hallin, J., McGhee, K., and Schwartz, C. W. (2011). NCHRP Project 1-37A:Development of the 2002 Guide for the Design of New and Rehabilitated Pavement Structures, Accessed, Jun. 2011, http://www.eng.umd.edu/~schwartz/abstracts/nchrp_1_37a.html

Hallin, John. "Implementation of the 2002 Design Guide." 11 Jan 2004. Report, ERES Consultants. 13 Oct 2005 < http://www.webs1.uidaho.edu/bayomy/trb/afd60/TRB2004/Design%20Guide%20workshop/Hallin_Research%20Team%20Implementation%20Ideas.pdf >.

Hand, A.J., Epps, J.A., and Sebaaly, P.E. (1999), "Development of APT Based Permanent Deformation Prediction Models Translatable to Other Environments." Accelerated Pavement Testing International Conference, Reno, Nevada.

Harvey, J. T., Hoover, T., Coetzee, N. F., Nokes, W. A., and Rust, F. C. (1998), Caltrans Accelerated Pavement Test (CAL/APT) Program—Test Results: 1994–1997. AAPT Symposium on Accelerated Pavement Testing, Boston, MA, March 16-18, 1998

Harvey, John T., John A. Deacon, Bor-Wen Tsai and Carl L. Monismith. "Fatigue Performance of Asphalt Concrete Mixes and Its Relationship to Asphalt Concrete Performance in California," Report No. RTA-65W485-2, Berkeley: California Department of Transportation, 1995.

Highway Research Board (HRB) (1962), "The AASHO Road Test," Report 5, (http://www.highways.gov.sk.ca/docs/reports_manuals/manuals/STP_DOC/stp240-20.pdf).

Huang, Y. H. Pavement Analysis and Design New Jersey: Prentice Hall, 1993.

Huang, Y.H. (2004), "Pavement Analysis and Design", 2nd Edition, Prentice Hall, Inc. Englewood Cliffs, New Jersey.

International Road Dynamic (2003), "Installation Manual, General Reference, Part No. 69027701," Revision D.

Ioannides, A. M. (1992), "Full Mechanistic performance modeling: a contradiction of terms?" Proceedings of the Seventh International Conference on the Structural Design of Asphalt Pavements, Nottingham, U. K.

Kamon, M., and Nontananandh, S. (1991), "Combining Industrial Waste with Lime for Soil Stabilization," Journal of Geotechnical Engineering, 117(1), 1-17.

Kim, H.B., Buch, N., Park, D.Y. (2000), "Mechanistic-Empirical Rut Prediction Model for In-Service Pavements." Transportation Research Record, 1730, Paper No. 00-0165, pp. 99-109.

Leahy, R. B. (1989), "Permanent Deformation Characteristics of Asphalt Concrete," Ph.D. Dissertation, University of Maryland, College Park, Maryland.

Li, Q. (2009), "Database Support and Modeling for the Mechanistic Empirical Pavement Design Guide (M-EPDG)." Ph.D. Thesis, University of Arkansas, AR.

Loulizi, A. Al-Qadi, I. L., Lahouar, S. and Freeman, T. E. (2001), "Data Collection and Management of the Instrumented Smart Road Flexible Pavement Sections," Transportation Research Record, Transportation Research Board, 1769, 142-151.

Miller, G. A. and Zaman, M. M. (2000), "Field and Laboratory Evaluation of Cement Kiln Dust as a Soil Stabilizer," Transportation Research Record, Transportation Research Board, 1714. 25-32

Miller, John S. and William Y. Bellinger. Distress Identification Manual for the Long-Term Pavement Performance Project. FHWA-RD-03-031, Washington D.C.: FHWA, 2003.

Miner, M.A. (1959), "Estimation of Fatigue Life with Particular Emphasis on Cumulative Damage." Metal Fatigue, Edited by Sines and Waisman, McGraw Hill, pp. 278-289.

Minnesota Department of Transportation (1990), "Minnesota Road Research Project, Work Plan for Research Objectives," Report No. 90-03.

Minnesota Department of Transportation (MnDOT). About Minnesota Road Research. (http://www.mrr.dot.state.mn.us/research/MnROAD_Project/mnroadproject.asp), accessed October 3 2005.

Monismith Carl L. "Analytically Based Asphalt Pavement Design and Rehabilitation: Theory to Practice, 1962-1992." Transportation Research Record No. 1354, Washington, D.C.: transportation Research Board, 1992, pp. 5-26.

Monismith, C.L. and J.A. Epps. "Asphalt Mixture Behavior in Repeated Flexure," Transportation and Traffic Engineering, Berkeley, CA: University of California, 1969.

Monismith, C.L., J.A. Epps and F.N. Finn. "Improved Asphalt Mix Design," Proceedings, Association of Asphalt Paving Technologists Technical Sessions, San Antonio, Texas, 1985, pp. 347-406.

National Center for Asphalt Technology (NCAT, 2006), "Instrumented Pavement Maintenance Plan on I-35 in McClain," Research proposal submitted by NCAT to ODOT.

Navaratnarajah, S.K., (2006), "Performance Characteristics of Selected Asphalt Mixes: A Laboratory and Field Study," Master's Thesis, The University of Oklahoma, Norman, Oklahoma.

NCHRP Report 468 (2002), "Contributions of Pavement Structural Layers to Rutting of Hot Mix Asphalt Pavements," Transportation Research Board- National Research Council, Washington, D.C.

Oklahoma Department of Transportation (ODOT) (1999), "Standard Specifications for Highway Construction."

Oklahoma Department of Transportation Website (2010), "Planning and Research Division," (http://www.okladot.state.ok.us/hqdiv/p-r-div/spr-rip/project-list.htm).

Oklahoma Highway Department (2001), "Method of Test for Determining Rutting Susceptibility Using the Asphalt Pavement Analyzer," Oklahoma Highway Department Laboratory Test No. 43 (OHD L-43), Oklahoma City, Oklahoma.

Papagiannakis A. T., and Masad E. A. (2009). "Pavement Design and Materials", chapter 2, pp. 13.

Papagiannakis, A.T. and Masad, E.A. (2007). Pavement Design and Materials, John Wiley and Sons, Inc., NJ.

Pavement Interactive Website (2010), (http://pavementinteractive.org/index.php?title=Rutting).

PEEK ADR-3000 (2010), Automatic Data Recorder Product Datasheet. http://www.ustraffic.net/datasheets/adr3000datasheet.pdf

Pell, P. S. and K. E. Cooper. "The Effect of Testing and Mix Variables on the Fatigue Performance of Bituminous Materials." Proceedings, Association of Asphalt Paving Technologists Vol. 44, 1975, pp. 1-37.

Priest, A. and Timm, D., "Methodology and Calibration of Fatigue Transfer Functions for Mechanistic-Empirical Flexible Pavement" Report No. 06-03, Auburn University: National Center for Asphalt Technology, 2006.

Priest, A. L. (2005), "Calibration of Fatigue Transfer Functions for Mechanistic-Empirical Flexible Pavement Design," M.S thesis, Auburn University, Auburn, Alabama.

Priest, A.L., and Timm, D.H. (2006), "Methodology and Calibration of Fatigue Transfer Functions for Mechanistic-Empirical Flexible Pavement Design." Publication NCAT Report 06-03, National Center for Asphalt Technology, Auburn University, AL.

Research and Development of The Asphalt Institute's Thickness Design Manual (MS-1) Ninth Edition, Research Report No. 82-2, College Park, MD: The Asphalt Institute, 1982.

Saskatchewan Highways and Transportation (SHT) (1992), "Evaluation of Bearing Capacities of Subbase and Subgrade Using Dynamic Cone Penetration Test," Standard Test Procedure Manual, STP 240-20.

Schwartz, C.W., and Carvalho, R.L. (2007), "Implementation of the NCHRP 1-37A Design Guide," Volume 2: Implementation of Mechanistic-Empirical Design Procedure, Final Report UMD FRS No. 430572, University of Maryland, College Park, MD.

Selvaraj, S.I. (2007), "Development of Flexible Pavement Rut Prediction Models from the NCAT Test Track Structural Study Sections Data," Ph.D. Dissertation, Auburn University, Auburn, Alabama.

Shah, K. (2007), "Effects of Gradation and Compaction Energy on the Hydraulic Conductivity of an Aggregate Base Commonly used in Oklahoma," M. S. Thesis, University of Oklahoma, Norman, OK.

Shook, J.F., Finn, F.N., Witczak, M.W., and Monismith, C.L. (1982), "Thickness Design of Asphalt Pavements – The Asphalt Institute Method," Proceedings, 5th International Conference on the Structural Design of Asphalt Pavements, Vol.1, The Netherlands, pp. 17-44.

Smart Road (2003), Smart Road Pavement Research Team, http://www.cee.vt.edu/program_areas/tise/smart/, accessed December 1, 2003.

Solanki, P. (2010). "Characterization of Cementitiously Stabilized Subgrades for Mechanistic-Empirical Pavement Design," Ph.D. Dissertation, University of Oklahoma, Norman, OK.

Solanki, P., Khoury, N. and Zaman, M. M. (2007), "Engineering Behavior and Microstructure of Soil Stabilized with Cement Kiln Dust," Geotechnical Special Publication, 172, 1-10.

Solanki, P., Zaman, M. and Muraleetharan, K.K. (2009), "Field performance Monitoring and Modeling of Instrumented Pavement on I-35 in McClain County", Construction and Instrumentation Report, University of Oklahoma, Norman, Oklahoma.

Solanki, P., Zaman, M. M. and Muraleetharan, K.K. (2010), "Field performance Monitoring and Modeling of Instrumented Pavement on I-35 in McClain County," Construction and Instrumentation Report, University of Oklahoma, Norman, Oklahoma.

Solanki, P., Zaman, M. M., Muraleetharan, K.K. and Timm, D. (2009), "Evaluation of Resilient Moduli of Pavement Layers at an Instrumented Section on I-35 in Oklahoma," Road Materials and Pavement Design, 10, Special Issue (ICAM), pp. 167-188.

Solanki, P., Zaman, M.M., and Muraleetharan, K.K. (2011), "Validation of Back-Calculated Modulus Values from Falling Weight Deflectometer Through Instrumentation on I-35," Transportation Research Record: Journal of the Transportation Research Board, No. 2227, pp. 79–86.

Tangella, R., J. Craus, J. A. Deacon, and C. L. Monismith. Summary Report on Fatigue Response of Asphalt Mixtures. TM-UCB-A-003A-89-3, SHRP Project A-003-A. University of California, Berkeley: Institute of Transportation Studies, 1990.

Tarefder, R.A. and Zaman, M.M. (2001), "Evaluating Rut Potential of Selected Asphalt Mixes for Improved Pavement Performance," 2nd International Symposium on Maintenance and Rehabilitation of Pavements and Technological Control, Auburn, Alabama, pp. 1-14.

Tarefder, R.A., (2003), "Laboratory and Model Prediction of Rutting in Asphalt Concrete," Ph.D. Dissertation, The University of Oklahoma, Norman, Oklahoma.

Theyse, H L., De Beer, M. and Rust, F. C. (1996), "Overview of South African Mechanistic Pavement Design Method," Transportation Research Record, No. 1539, Transportation Research Board, pp. 6-17.

Timm, D. H. and Priest, A. L. (2005), "Wheel Wander at the NCAT Test Track," Report 05-02, National Center for Asphalt Technology, Auburn University, Alabama.

Timm, D. H., Priest, A. L. and McEwen, T. V. (2004), "Design and Instrumentation of the Structural Pavement Experiment at the NCAT Test Track," Report 04-01, National Center for Asphalt Technology, Auburn University, Alabama.

Timm, D.H., and Priest, A.L. (2005), "Wheel Wander at the NCAT Test Track," Report 05-02, National Center for Asphalt Technology, Auburn University, Alabama.

Timm, D.H., and Priest, A.L. (2006). "Methodology and calibration of fatigue transfer functions for mechanistic-empirical flexible pavement design," Technical Report, National Center for Asphalt Technology (NCAT), Auburn University.

Timm, D.H., Bjorn Birgisson and David E. Newcomb. "Development of Mechanistic-Empirical Design for Minnesota." Transportation Research Record No. 1629, Washington, D.C.: Transportation Research Board, 1998, pp. 181-88.

Timm, D.H., D.E. Newcomb and B. Birgisson. "Mechanistic-Empirical Flexible Pavement Thickness Design: The Minnesota Method," Staff Paper, MN/RC-P99-10, St. Paul: Minnesota Department of Transportation, 1999.

Timm, D.H., Priest, A.L., McEwen T.V. (2004), "Design and Instrumentation of the Structural Pavement Experiment at the NCAT Test Track," Report 04-01, National Center for Asphalt Technology, Auburn University, Alabama.

University of Washington – Design Parameters - Loads: http://training.ce.washington.edu/wsdot/Modules/04_design_parameters/04-3_body.htm

Virginia's Smart Road Project. Virginia Department of Transportation (VDOT), (http://www.virginiadot.org/projects/constsal-smartrd.asp), accessed October 23 2011.

Von Quintus, H.L., and Moulthrop, J.S. (2007), "Mechanistic-Empirical Pavement Design Guide Flexible Pavement Performance Prediction Models for Montana." Vol. III, Calibration and User's Guide for the Mechanistic-Empirical Pavement Design Guide, Montana Department of Transportation, Helena, MT.

Williams, R.C., Hill, D.W., and Rottermond, M.P. (2005), "Utilization of an Asphalt Pavement Analyzer for Hot Mix Asphalt Laboratory Mix Design." Journal of ASTM International, Volume 2, No. 4, pp. 16-40.

Willis, J. R., "Field-Based Strain Thresholds for Flexible Perpetual Pavement" PhD Dissertation Auburn University 2009, pp. 53

WSDOT (2003). "Washington State Pavement Design Guide", Available online, http://training.ce.washington.edu/WSDOT/, Accessed on May 30, 2006.

Yoder, E. J. and Witczak, M. W. (1975), "Principles of Pavement Design," Wiley, New York.

Yoo, P. J., and Al-Qadi, I. L. (2010). "Development of A Realistic Hot-Mix Asphalt Fatigue Model Considering Low and High Cycles", Transportation Research Record, Transportation Research Board.

Zhou, F., Scullion, T., and Sun, L. (2004), "Verification and Modeling of Three-Stage Permanent Deformation Behavior of Asphalt Mixes." Journal of Transportation Engineering, ASCE, Vol. 130, No. 4, pp. 486-494.

Appendix A: Mix Design Sheets

Table A-1 Mix Design Sheet for S3-type mix (Courtesy: Haskell Lemon Construction Co., Norman)

A.D. No. 006-005-006 S3 Recycle **Design No.** s3qc0130600101
Project No. IMY-0035-2(302)095 20998(04) **Hwy.** I-35 **ESAL** 30M+
Contractor Haskell Lemon Const. Co. **Producer** Haskell Lemon Const. Co.

MATERIAL	SOURCE	%USED
1" #67 Rock	Martin Marietta @ Davis, OK(5005)	20
Manufactured Sand	Martin Marietta @ Davis, OK(5005)	44
Asphalt Sand	GMI(MacArthur Pit) @ Oklahoma City, OK(1402)	11
R.A.P.	Stockpile @ Plantsite	25
Asphalt Cement (PG64-22OK)	Valero @ Ardmore, OK(m00352)	

Aggregate Percent Passing	1" #67 Rock	Man. Sand	Asph. Sand	R.A.P.	Combined Aggregate	Job Formula	JMF Tolerance
1"	100			100	100	100	± 0
3/4"	90			99	98	98	± 7
1/2"	43	100		95	87	87	± 7
3/8"	22	99	100	84	80	80	± 7
No. 4	4	85	98	38	58	58	± 7
No. 8	1	47	96	23	37	37	± 5
No. 16	1	24	93	18	25	25	± 4
No. 30	1	12	85	15	19	19	± 4
No. 50	1	6	54	11	12	12	± 4
No. 100	0	4	11	6	4	4	± 3
No. 200	0.4	3.8	1.5	4.0	2.9	2.9	± 2
%AC (PG64-22OK)				3.5		4.1	± 0.4
Mix Temperature @ discharge from Mixer, °F						305	± 20
Optimum Roadway Compaction Temperature, °F						290	

Tests on Asphalt Cement:

	Found	Required
Spec. Grav. @ 77 °F	1.01 Est.	

Tests on Compressed Mixtures (at Design AC Content):

	SGC	Dens. % o Gmm	Dens. % of Gmm Req'd
Nini	9	88.1	85.5 - 89
Ndes	125	96	96
Nmax	205	96.8	< 98

Tests on Aggregates:

	Found	Required
F.A.A. %U	45.1	45 Min.
Sand Equivalent	94	50 Min.
L.A. Abrasion	28.0	40 Max.
Durability (DC)	71	40 Min.
IOC	0.14	
Insoluble Residue	N/A	N/A
Fractured Faces	100/100	100/100 Min.
Gse	2.671	
Gsb	2.645	
Specimen Wt.	4870	

Tests on Compressed Mixtures:

Percent Asphalt	Gmb	Gmm	Dens. % of Gmm	Dens. % of Req'd of Gmm	V.M.A. (%)	V.M.A. (Min.%)	%VFA	%VFA Req'd	%DP	%DP Req'd
4.1	2.384	2.502	95.3		13.6		65.2		0.77	
4.6	2.405	2.483	96.9	95-97	13.3	13	76.3	65-76	0.68	0.6-1.6
5.1	2.427	2.464	98.5		12.9		88.2		0.61	

Mix Layer Depth: < 4 in.
TSR: 0.89 0.80 Min. (0.75 Min. Field) Required
Compacted Wt. 109.7 lbs/sq.yd/1" thickness
Lab Permeability Test(cm/sec) - $7x10^{-5}$ (Required: $12.5x10^{-5}$ Max.)
APA Rut Test Depth(mm) - 3.000 (Required: 3 mm Max.)
ITS(psi) - 158.8 (Required: 75 psi Min.)
Micro-Deval(% Wear) - 23.1 (Required: 25% Max.)
Recommended 3.4% New Asphalt Cement

Table A-2 Mix Design Sheet for S4-type mix (Courtesy: Haskell Lemon Construction Co., Norman)

A.D. No. 008-024-007 S4 **Design No.** s4qc0130702110
Project No. IMY-0035-2(302)095 20998(04) **Hwy.** I-35 **ESAL** 30M+
Contractor Haskell Lemon Const. Co. **Producer** Haskell Lemon Const. Co.

MATERIAL	SOURCE	%USED
5/8" Chips	Martin Marietta @ Davis, OK(5005)	25
Manufactured Sand	Martin Marietta @ Davis, OK(5005)	38
Screenings	Hanson Aggregates @ Davis, OK(5008)	22
Sand	GMI @ Oklahoma City, OK(1402)	15
Asphalt Cement (PG64-22OK)	Valero @ Ardmore, OK(m00352)	

Laboratory No.

Aggregate Percent Passing	5/8" Chips	Man. Sand	Scrns	Sand	Combined Aggregate	Job Formula	JMF Tolerance
3/4"	100				100	100	± 0
1/2"	91				98	98	± 7
3/8"	57	100	100	100	89	89	± 7
No. 4	12	82	65	98	63	63	± 7
No. 8	5	44	34	96	40	40	± 5
No. 16	5	22	20	95	28	28	± 4
No. 30	4	12	14	88	22	22	± 4
No. 50	4	6	11	55	14	14	± 4
No. 100	4	3	8	12	6	6	± 3
No. 200	3.8	2.6	6.1	2.6	3.7	3.7	± 2
%AC (PG64-22OK)						4.6	± 0.4
Mix Temperature @ discharge from Mixer, °F						305	± 20
Optimum Roadway Compaction Temperature, °F						290	

Tests on Asphalt Cement:

	Found
Spec. Grav. @ 77 °F	1.0173

Tests on Aggregates:

	Found	Required
F.A.A. %U	45.1	45 Min.
Sand Equivalent	70	50 Min.
L.A. Abrasion	11	40 Max.
Durability (DC)	63	40 Min.
IOC	0.26	
Insoluble Residue		N/A
Fractured Faces	100/100	100/100 Min.
Gse	2.678	
Gsb	2.658	
Specimen Wt..	4860	

Tests on Compressed Mixtures (at Design AC Content):

	SGC	Dens. % o Gmm	Dens. % of Gmm Req'd
Nini	9	87.5	85.5 - 89
Ndes	125	96	96
Nmax	205	97.0	< 98

Tests on Compressed Mixtures:

Percent Asphalt	Gmb	Gmm	Dens. % of Gmm	Dens. % of Req'd of Gmm	V.M.A. (%)	V.M.A. (Min.%)	%VFA	%VFA Req'd	%DP	%DP Req'd
4.6	2.394	2.490	96.1		14.1		72.5		0.84	
5.1	2.413	2.472	97.6	95-97	13.8	14	82.8	65-76	0.75	0.6-1.6
5.5	2.430	2.454	99.0		13.7		93.0		0.68	

Mix Layer Depth: < 4 in.
TSR: 0.92 0.80 Min. (0.75 Min. Field) Required
Compacted Wt. 109.6 lbs/sq.yd/1" thickness
Lab Permeability Test(cm/sec) - 0 $x10^{-5}$ (Required: 12.5$x10^{-5}$ Max.)
APA Rut Test Depth(mm) - 0.973 (Required: 3 mm Max.)
MicroDeval(% Wear) - 20.3 (Required 25% Max.)
Indirect Tensile Strength(psi) - 110.5 (Required 75 psi Min.)
QC/QA Project: Tolerances shall be governed by SP 411-3QA(a-g)99 rev. 4/12/07
CORRECTED (AC Grade)

Appendix B: Instrumentation Data Sheets

Asphalt
Strain Gage ASG-152

CTLGROUP
Building Knowledge. Delivering Results.

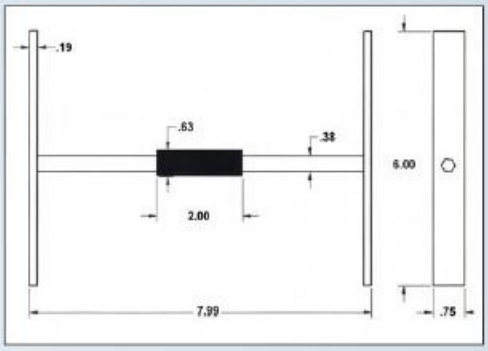

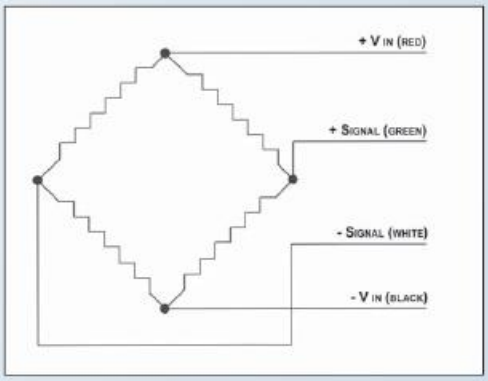

General Specifications

Bridge Completion ..... Full bridge, no completion required
Gage Resistance ..... 350 Ohm
Excitation ..... up to 10 Volts
Output ..... ≈ 2 mV/V @ 1500 µstrain
Calibration Factor ..... Individually provided
Grid Area ..... 0.133 cm²
Gage Area ..... 1.22 cm² overall
Fatigue Life ..... <10⁵ repetitions @ +/- 1500 µstrain
Modulus ..... ≈ 340,000 psi
Cell Material ..... Black 6/6 nylon
Coating ..... Two-part polysulfide liquid polymer, encapsulated in silicone with butyl rubber outer core

Quality Assurance

Water Submersion ..... 1 ft for 24 hours at 24°C (75°F)
Temperature ..... -34°C (-30°F) to 204°C (400°F)
Lead Wire .....30 ft of 22 AWG braided shield four wire

Background Information

CTLGroup's Asphalt Strain Gages are designed to withstand the high temperatures and compaction loads associated with asphalt pavement construction. The ASG-152 is a field-proven design that uses durable materials to ensure accurate long-term data collection. Its full-bridge configuration reduces costs by eliminating the need for expensive data-acquisition and signal-conditioning systems to provide bridge completion. Braided shielding protects the lead wire from electrical noise, while an abrasion-resistant, Teflon polymer coating withstands temperatures up to 205°C (400°F). This all leads to longer sensor life and long-term savings, by reducing redundancy in your instrumentation plan.

Price

Call for pricing.

Contact

Tom Weinmann
Sensors & Structural Diagnostics
847-972-3280 or TWeinmann@CTLGroup.com

Main Office 5400 Old Orchard Road, Skokie, Illinois 60077-1030 Phone 847-965-7500 Fax 847-965-6541 www.CTLGroup.com
Mid-Atlantic Office Phone 410-997-0400 Fax 410-997-8480
Northeast Office Phone 603-516-1500 Fax 603-516-1510

DI-785 Specifications

Analog Inputs

Number of Channels:	32 configured for DI-5B modules
Channel Configuration:	Defined by DI-5B module
Measurement Range:	Defined by DI-5B module
Measurement Accuracy:	±0.25% of full scale range, ±100 µV
Resolution:	1 part in 16,384 (14-bit)
Input Impedance:	Defined by signal conditioning module
Input offset voltage:	Defined by DI-5B module
Channel-to-channel crosstalk:	-75db @ 100 kHz sample throughput rate
Offset temperature coefficient:	±10 PPM/°C, plus DI-5B module
Analog Frequency Response:	Defined by DI-5B module
Digital filtering:	Peak, Valley, Average
CJC Error:	±1.5°C plus signal conditioning module (10-min. warm-up; still air; 2-amp max current draw for backplane; average IOS mode).
Gain:	1, 2, 4, 8 (software selectable per channel)

Isolation (via Signal Conditioning Modules)

Input-to-Output:	1000V
Channel-to-Channel:	500V

A/D Characteristics

Type:	Successive approximation
Resolution:	14-bit
Sample Rate Timing Accuracy:	50 PPM
Sample Rate Timing Resolution:	62.5 ns
Integral Linearity Error:	±1LSB
Minimum Conversion Time:	4 microseconds

Calibration

Calibration cycle:	One year

Digital I/O

Bits:	8 inputs and 8 outputs
Input voltage levels:	Min. required "1" 2V; Max allowed "0" 0.8V
Connections:	Two 37-pin D-sub male

Scanning Characteristics

Max. throughput sample rate:	Single Unit: 180,000 Hz Multiple Units (daisy-chained): 150,000 Hz per unit
Min. throughput sample rate:	0.01526 Hz
Max. scan list size:	34 entries
Sample buffer size:	2kb

Ethernet Interface (optional Ethernet to USB converter available)

Type:	10/100Base-T
Connectors:	RJ-45 (Two: Primary and Expansion)
Protocol:	TCP/IP
Server Type:	DHCP or Fixed IP
Cross-unit synchronization:	Via secondary Ethernet port (RJ-45)

Rear Panel I/O Connections

Power Cable:	Standard receptacle
Digital I/O and Monitor Out:	37 pin D sub (2)
Signal I/O:	Removable Phoenix-type screw terminals (8)

General

Front Panel Indicators:	Power LED and Active LED
Rear Panel Controls:	AC Power Switch
Internal I/O Connections:	DI-5B module inputs (32)
Operating Temperature:	0°C to 50°C
Storage Temperature:	-55°C to 125°C
Dimensions:	16.5W × 18.5D × 3.5H in. 41.9W × 47.0D × 8.9H cm.
Weight with no modules:	11 lbs. (5Kg)
Weight with 32 DI-5B modules:	15.44 lbs. (7Kg)

Power Characteristics

Type:	AC Line
Voltage Range:	88 to 264 VAC rms
Current Range:	1.3A @ 115VAC; 0.8A @ 230 VAC
Frequency Range:	47 to 63 Hz

Ordering Guide

Description	Order No.	Description	Order No.
DI-785 32-channel DI-5B module industrial data acquisition system.	DI-785	**USB to Ethernet Converter** Converter that allows you to connect your DI-785 to a USB port. Manufacturer varies. Adds an external network card to your PC through the USB port.	101014-EA
Rack Mounting Kit Optional 19-inch rack mounting kit.	RMK-500		

DATAQ® INSTRUMENTS

DATAQ Instruments, Inc.
241 Springside Drive
Akron, Ohio 44333
Phone: 330-668-1444
Fax: 330-666-5434

Data Acquisition Product Links
(click on text to jump to page)
Data Acquisition | Data Logger | Chart Recorder | Thermocouple | Oscilloscope

Appendix C: GPS Coordinates of Instruments and Identified Stations

Table C-1 GPS Coordinates of Instruments

Location	**GPS Coordination**			**Remarks**
	Northing	**Easting**	**Elevation**	
Control Slab	623620.302’	2154521.852’	1160.860’	
Station 144	623809.324’	2154533.375’	1161.909’	
Station 235	623723.825’	2154564.745’	1160.521’	
Station 540	623436.865’	2154665.786’	1155.307’	
Station 738	623249.904’	2154727.021’	1152.169’	
Station 900	623097.067’	2154775.223’	1148.873’	
Array Center (EPC1)	623645.052’	2154593.310’	1158.533’	On natural soil
Installed EPC2	623638.22’	2154595.82’	1159.08’	On stabilized soil
Installed EPC3	623649.81’	2154591.72’	1159.69’	On aggregate base
Installed MP2	623636.557’	2154596.306’	1158.190’	On natural soil
Installed MP3	623636.40’	2154596.27’	1159.06’	On stabilized soil
Installed MP4	623636.59’	2154596.21’	1159.55’	On aggregate base
EPC-1	623645.052’	2154593.310’	1158.533’	On natural soil
EPC-2	623638.22’	2154595.82’	1159.08’	On stabilized soil
EPC-3	623649.81’	2154591.72’	1159.69’	On aggregate base
Strain gauge 1	623647.19’	2154590.45’	1159.70’	Longitudinal
Strain gauge 2	623647.89’	2154592.35’	1159.73’	Longitudinal

Strain gauge 3	623648.60’	2154594.24’	1159.77’	Longitudinal
Strain gauge 4	623645.34’	2154591.05’	1159.67’	Transversal
Strain gauge 5	623645.91’	2154592.93’	1159.67’	Transversal
Strain gauge 6	623646.68’	2154594.85’	1159.73’	Transversal
Strain gauge 7	623643.30’	2154591.78’	1159.63’	Transversal
Strain gauge 8	623643.98’	2154593.64’	1159.68’	Transversal
Strain gauge 9	623644.78’	2154595.47’	1159.69’	Transversal
Strain gauge 10	623641.48’	2154592.42’	1159.58’	Longitudinal
Strain gauge 11	623642.17’	2154594.31	1159.64’	Longitudinal
Strain gauge 12	623642.90’	2154596.20’	1159.67’	Longitudinal
Moisture probe 2	623636.557’	2154596.306’	1158.190’	On natural soil
Moisture probe 3	623636.40’	2154596.27’	1159.06’	On stabilized soil
Moisture probe 4	623636.59’	2154596.21’	1159.55’	On aggregate base

Appendix D: Strain Calculations

Each data point on the strain-temperature graph (Figures 4.6 and 4.7) is obtained by using the following steps:

Step 1: Collect strain responses for 20 Class-9 vehicles.

Step 2: Clean (remove noise) and process (select the highest strain value for each strain gauge, for every passing axle) the recorded strain-time histories.

Step 3: Select the strain readings determined in Step 2 for strain gauges 3 and 12.

Step 4: Prepare a summary table for each site visit (Table D-1).

Table D-1 Field Visit Data Summary for Single Axles (May 07, 2010)

Half Axle Weight (kips)	Wheel Wander (in.)	Offset (in.)	Strain Gage 3 (με)	SG3/ Weight (με/kip)	Strain Gage 12 (με)	SG12/ Weight (με/kip)
4.71	29.90	9.07	45.74	9.72	33.90	7.21
5.25	25.99	5.16	68.58	13.07	65.48	12.48
4.92	31.20	10.37	34.05	6.92	28.86	5.87
5.73	22.91	2.08	95.82	16.74	95.13	16.62
5.59	39.81	18.98	16.30	2.92	11.67	2.09
5.09	32.40	11.57	33.04	6.50	28.93	5.69
4.80	32.91	12.08	27.30	5.69	19.98	4.17
5.85	19.31	1.52	95.33	16.31	88.04	15.06
5.15	23.90	3.07	82.86	16.11	77.64	15.09
5.35	29.78	8.95	44.85	8.38	39.90	7.46
5.04	24.92	4.09	72.52	14.39	60.93	12.09
5.45	20.01	0.82	99.44	18.25	90.18	16.55
5.02	33.78	12.95	28.61	5.70	25.25	5.04
4.89	30.11	9.28	40.30	8.24	42.43	8.68
5.04	25.97	5.14	67.81	13.47	61.15	12.14
5.32	24.82	3.99	59.07	11.10	50.76	9.54
4.67	26.41	5.58	52.42	11.24	45.19	9.69

Note: Offset is the distance between a strain gauge and the wheel. For strain gauges 3 and 12, Offset = $|$Wheel Wander – 20.83 in.$|$

Step 5: Plot gauge 3 and gauge 12 normalized strain values (strain/weight) versus offset (Figure D-1).

Step 6: Fit an exponential trend line through each of the strain gauge group points, and display the resulting equation with the R^2 value.

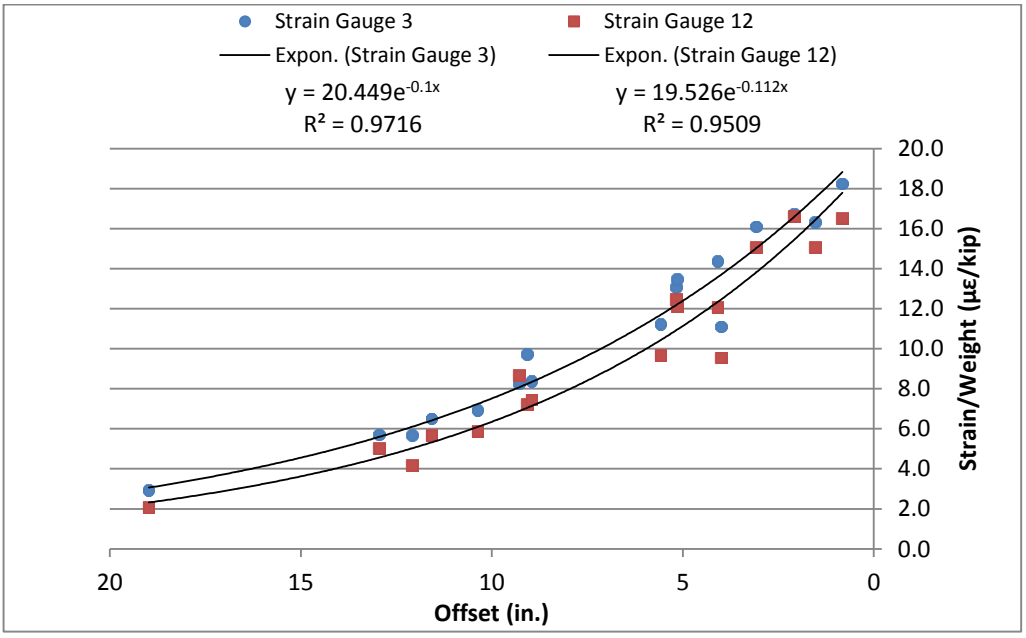

Figure D-1 Normalized Strain vs. Offset of Steering Axles (May 07, 2010)

Step 7: Calculate the resulting value of the equation (y) when x = 0 inches, y = 20.5 με/kip for strain gauge 3 and y = 19.5 με/kip for strain gauge 12. This represents the maximum strain value of one field trip when wheel is located directly over the strain gauge.

Step 8: Average maximum strain values of gauges 3 and 12.

Step 9: Plot the average strain value with its corresponding HMA mid-depth temperature (Figures 4.6 and 4.7).

Appendix E: FHWA Vehicle Classification

```
    Class 5:
      Axle Spacing: 13 Feet to 20 Feet
    Class 4:
      Axle Spacing: 20 Feet to 40 Feet
    Class 3:
      Axle Spacing: 10.2 Feet to 13 Feet
    Class 2:
      Axle Spacing: 6 Feet to 10.2 Feet
    Class 1:
      Axle Spacing: 0 Feet to 6 Feet
3 axle vehicles. Default class = 2
    Class 8:
      Axle Spacing: 6 Feet to 17 Feet, 14 Feet to 40 Feet
    Class 6:
      Axle Spacing: 6 Feet to 23 Feet, 0 Feet to 6 Feet
    Class 4:
      Axle Spacing: 20 Feet to 40 Feet, 0 Feet to 6 Feet
    Class 3:
      Axle Spacing: 10.2 Feet to 13 Feet, 6 Feet to 18 Feet
    Class 2:
      Axle Spacing: 6 Feet to 10.2 Feet, 6 Feet to 18 Feet
4 axle vehicles. Default class = 2
    Class 8:
      Axle Spacing: 6 Feet to 20 Feet, 0 Feet to 6 Feet, 6 Feet to 40 Feet
    Class 8:
      Axle Spacing: 6 Feet to 17 Feet, 14 Feet to 40 Feet, 0 Feet to 6 Feet
    Class 7:
      Axle Spacing: 6 Feet to 23 Feet, 0 Feet to 9 Feet, 0 Feet to 9 Feet
    Class 3:
      Axle Spacing: 10.2 Feet to 13 Feet, 6 Feet to 18 Feet, 0 Feet to 6 Feet
    Class 2:
      Axle Spacing: 6 Feet to 10.2 Feet, 6 Feet to 18 Feet, 0 Feet to 6 Feet
5 axle vehicles. Default class = 9
    Class 11:
      Axle Spacing: 6 Feet to 17 Feet, 11 Feet to 25 Feet, 6 Feet to 18 Feet, 11 Feet to 25 Feet
    Class 9:
      Axle Spacing: 6 Feet to 22 Feet, 0 Feet to 6 Feet, 6 Feet to 23 Feet, 0 Feet to 23 Feet
    Class 9:
      Axle Spacing: 6 Feet to 22 Feet, 0 Feet to 6 Feet, 6 Feet to 40 Feet, 0 Feet to 14 Feet
6 axle vehicles. Default class = 10
    Class 12:
      Axle Spacing: 6 Feet to 22 Feet, 0 Feet to 6 Feet, 0 Feet to 25 Feet, 6 Feet to 18 Feet, 11 Feet to 25 Feet
    Class 10:
      Axle Spacing: 6 Feet to 22 Feet, 0 Feet to 6 Feet, 0 Feet to 40 Feet, 0 Feet to 11 Feet, 0 Feet to 11 Feet
7 axle vehicles. Default class = 13
    Class 10:
      Axle Spacing: 6 Feet to 22 Feet, 0 Feet to 6 Feet, 0 Feet to 40 Feet,
0 Feet to 13 Feet, 0 Feet to 12 Feet, 0 Feet to 12 Feet
```

Appendix F: Automated Rut Test Results from the APA

Table F-1 Automated Rut Test Results from the APA

Specimen No.	Average Air Voids (%)	Temperature (°C)	Number of Cycles	Measured Rut (in.)
L4CR-44,45	0.82	40	500	0.016
L4CR-44,45	0.82	40	1000	0.018
L4CR-44,45	0.82	40	1500	0.021
L4CR-44,45	0.82	40	2000	0.022
L4CR-44,45	0.82	40	3000	0.023
L4CR-44,45	0.82	40	4000	0.026
L4CR-44,45	0.82	40	5000	0.027
L4CR-44,45	0.82	40	7000	0.029
L4CR-44,45	0.82	40	8000	0.031
L4CR-42,43	2.17	40	500	0.020
L4CR-42,43	2.17	40	1000	0.025
L4CR-42,43	2.17	40	2000	0.026
L4CR-42,43	2.17	40	3000	0.029
L4CR-42,43	2.17	40	4000	0.031
L4CR-42,43	2.17	40	5000	0.033
L4CR-42,43	2.17	40	6000	0.036
L4CR-42,43	2.17	40	7000	0.036
L4CR-42,43	2.17	40	8000	0.037
T-9,10	3.84	40	500	0.021
T-9,10	3.84	40	1000	0.024
T-9,10	3.84	40	1500	0.027
T-9,10	3.84	40	2000	0.028
T-9,10	3.84	40	3000	0.031
T-9,10	3.84	40	4000	0.034
T-9,10	3.84	40	5000	0.035
T-9,10	3.84	40	6000	0.037
T-9,10	3.84	40	7000	0.040

Table F-1 Automated Rut Test Results from the APA (Cont'd)

Specimen No.	Average Air Voids (%)	Temperature (°C)	Number of Cycles	Measured Rut (in.)
L4CR-89,90	4.32	40	500	0.025
L4CR-89,90	4.32	40	1000	0.031
L4CR-89,90	4.32	40	1500	0.034
L4CR-89,90	4.32	40	2000	0.035
L4CR-89,90	4.32	40	3000	0.039
L4CR-89,90	4.32	40	4000	0.043
L4CR-89,90	4.32	40	5000	0.046
L4CR-89,90	4.32	40	7000	0.048
L4CR-89,90	4.32	40	8000	0.050
T-3,7	6.08	40	500	0.027
T-3,7	6.08	40	1000	0.033
T-3,7	6.08	40	1500	0.038
T-3,7	6.08	40	2000	0.041
T-3,7	6.08	40	3000	0.046
T-3,7	6.08	40	4000	0.049
T-3,7	6.08	40	5000	0.053
T-3,7	6.08	40	6000	0.057
T-3,7	6.08	40	7000	0.059
T-3,7	6.08	40	8000	0.063
L4CR-26,27	7.77	40	500	0.030
L4CR-26,27	7.77	40	1000	0.038
L4CR-26,27	7.77	40	1500	0.043
L4CR-26,27	7.77	40	2000	0.046
L4CR-26,27	7.77	40	3000	0.057
L4CR-26,27	7.77	40	4000	0.060
L4CR-26,27	7.77	40	5000	0.066
L4CR-26,27	7.77	40	6000	0.069
L4CR-26,27	7.77	40	7000	0.071
L4CR-26,27	7.77	40	8000	0.075

Table F-1 Automated Rut Test Results from the APA (Cont'd)

Specimen No.	Average Air Voids (%)	Temperature (°C)	Number of Cycles	Measured Rut (in.)
L4CR-22,24	8.03	40	500	0.028
L4CR-22,24	8.03	40	1000	0.037
L4CR-22,24	8.03	40	1500	0.041
L4CR-22,24	8.03	40	2000	0.047
L4CR-22,24	8.03	40	3000	0.058
L4CR-22,24	8.03	40	4000	0.059
L4CR-22,24	8.03	40	5000	0.070
L4CR-22,24	8.03	40	6000	0.071
L4CR-22,24	8.03	40	7000	0.077
L4CR-22,24	8.03	40	8000	0.079
L4CR-40,41	8.62	40	500	0.037
L4CR-40,41	8.62	40	1000	0.045
L4CR-40,41	8.62	40	1500	0.050
L4CR-40,41	8.62	40	2000	0.053
L4CR-40,41	8.62	40	3000	0.059
L4CR-40,41	8.62	40	4000	0.063
L4CR-40,41	8.62	40	5000	0.067
L4CR-40,41	8.62	40	6000	0.071
L4CR-40,41	8.62	40	7000	0.075
L4CR-40,41	8.62	40	8000	0.081
L4CR-34,35	9.77	40	500	0.046
L4CR-34,35	9.77	40	1000	0.055
L4CR-34,35	9.77	40	1500	0.061
L4CR-34,35	9.77	40	2000	0.068
L4CR-34,35	9.77	40	3000	0.077
L4CR-34,35	9.77	40	4000	0.085
L4CR-34,35	9.77	40	5000	0.091
L4CR-34,35	9.77	40	6000	0.095
L4CR-34,35	9.77	40	7000	0.098
L4CR-34,35	9.77	40	8000	0.104

Table F-1 Automated Rut Test Results from the APA (Cont'd)

Specimen No.	Average Air Voids (%)	Temperature (°C)	Number of Cycles	Measured Rut (in.)
L4CR-36,37	9.98	40	500	0.041
L4CR-36,37	9.98	40	1000	0.052
L4CR-36,37	9.98	40	1500	0.060
L4CR-36,37	9.98	40	2000	0.066
L4CR-36,37	9.98	40	3000	0.074
L4CR-36,37	9.98	40	4000	0.083
L4CR-36,37	9.98	40	5000	0.092
L4CR-36,37	9.98	40	6000	0.095
L4CR-36,37	9.98	40	7000	0.102
L4CR-36,37	9.98	40	8000	0.105
L4CR-38,39	10.10	40	500	0.043
L4CR-38,39	10.10	40	1000	0.055
L4CR-38,39	10.10	40	1500	0.064
L4CR-38,39	10.10	40	2000	0.070
L4CR-38,39	10.10	40	3000	0.082
L4CR-38,39	10.10	40	4000	0.093
L4CR-38,39	10.10	40	5000	0.104
L4CR-38,39	10.10	40	6000	0.111
L4CR-38,39	10.10	40	7000	0.117
L4CR-38,39	10.10	40	8000	0.123
L4CR-47,49	2.16	50	500	0.025
L4CR-47,49	2.16	50	1000	0.027
L4CR-47,49	2.16	50	1500	0.028
L4CR-47,49	2.16	50	2000	0.032
L4CR-47,49	2.16	50	3000	0.036
L4CR-47,49	2.16	50	4000	0.040
L4CR-47,49	2.16	50	5000	0.042
L4CR-47,49	2.16	50	6000	0.045
L4CR-47,49	2.16	50	7000	0.049
L4CR-47,49	2.16	50	8000	0.052

Table F-1 Automated Rut Test Results from the APA (Cont'd)

Specimen No.	Average Air Voids (%)	Temperature (°C)	Number of Cycles	Measured Rut (in.)
L4CR-69,70	4.26	50	500	0.022
L4CR-69,70	4.26	50	1000	0.029
L4CR-69,70	4.26	50	1500	0.032
L4CR-69,70	4.26	50	2000	0.035
L4CR-69,70	4.26	50	3000	0.041
L4CR-69,70	4.26	50	4000	0.046
L4CR-69,70	4.26	50	5000	0.052
L4CR-69,70	4.26	50	6000	0.057
L4CR-69,70	4.26	50	7000	0.062
L4CR-69,70	4.26	50	8000	0.068
L4CR-66,73	4.70	50	500	0.024
L4CR-66,73	4.70	50	1000	0.034
L4CR-66,73	4.70	50	1500	0.037
L4CR-66,73	4.70	50	2000	0.039
L4CR-66,73	4.70	50	3000	0.047
L4CR-66,73	4.70	50	4000	0.053
L4CR-66,73	4.70	50	5000	0.058
L4CR-66,73	4.70	50	6000	0.063
L4CR-66,73	4.70	50	7000	0.068
L4CR-66,73	4.70	50	8000	0.071
L4CR-65,72	5.23	50	500	0.036
L4CR-65,72	5.23	50	1000	0.044
L4CR-65,72	5.23	50	1500	0.049
L4CR-65,72	5.23	50	2000	0.054
L4CR-65,72	5.23	50	3000	0.062
L4CR-65,72	5.23	50	4000	0.070
L4CR-65,72	5.23	50	5000	0.076
L4CR-65,72	5.23	50	6000	0.080
L4CR-65,72	5.23	50	7000	0.086
L4CR-65,72	5.23	50	8000	0.090

Table F-1 Automated Rut Test Results from the APA (Cont'd)

Specimen No.	Average Air Voids (%)	Temperature (°C)	Number of Cycles	Measured Rut (in.)
L4CR-53,54	6.44	50	500	0.038
L4CR-53,54	6.44	50	1000	0.048
L4CR-53,54	6.44	50	1500	0.053
L4CR-53,54	6.44	50	2000	0.061
L4CR-53,54	6.44	50	3000	0.069
L4CR-53,54	6.44	50	4000	0.077
L4CR-53,54	6.44	50	5000	0.083
L4CR-53,54	6.44	50	6000	0.087
L4CR-53,54	6.44	50	7000	0.093
L4CR-53,54	6.44	50	8000	0.097
L4CR-64,75	7.45	50	500	0.036
L4CR-64,75	7.45	50	1000	0.047
L4CR-64,75	7.45	50	1500	0.057
L4CR-64,75	7.45	50	2000	0.065
L4CR-64,75	7.45	50	3000	0.079
L4CR-64,75	7.45	50	4000	0.089
L4CR-64,75	7.45	50	5000	0.099
L4CR-64,75	7.45	50	6000	0.109
L4CR-64,75	7.45	50	7000	0.115
L4CR-64,75	7.45	50	8000	0.121
L4CR-63,74	8.17	50	500	0.032
L4CR-63,74	8.17	50	1000	0.043
L4CR-63,74	8.17	50	1500	0.050
L4CR-63,74	8.17	50	2000	0.055
L4CR-63,74	8.17	50	3000	0.062
L4CR-63,74	8.17	50	4000	0.075
L4CR-63,74	8.17	50	5000	0.084
L4CR-63,74	8.17	50	6000	0.092
L4CR-63,74	8.17	50	7000	0.099
L4CR-63,74	8.17	50	8000	0.109

Table F-1 Automated Rut Test Results from the APA (Cont'd)

Specimen No.	Average Air Voids (%)	Temperature (°C)	Number of Cycles	Measured Rut (in.)
L4CR-76,77	8.98	50	500	0.040
L4CR-76,77	8.98	50	1000	0.049
L4CR-76,77	8.98	50	1500	0.055
L4CR-76,77	8.98	50	2000	0.057
L4CR-76,77	8.98	50	3000	0.071
L4CR-76,77	8.98	50	4000	0.079
L4CR-76,77	8.98	50	5000	0.089
L4CR-76,77	8.98	50	6000	0.100
L4CR-76,77	8.98	50	7000	0.107
L4CR-76,77	8.98	50	8000	0.118
L4CR-55,56	9.45	50	500	0.055
L4CR-55,56	9.45	50	1000	0.071
L4CR-55,56	9.45	50	1500	0.081
L4CR-55,56	9.45	50	2000	0.092
L4CR-55,56	9.45	50	3000	0.106
L4CR-55,56	9.45	50	4000	0.117
L4CR-55,56	9.45	50	5000	0.128
L4CR-55,56	9.45	50	6000	0.135
L4CR-55,56	9.45	50	7000	0.142
L4CR-55,56	9.45	50	8000	0.150
L4CR-57,58	10.46	50	500	0.072
L4CR-57,58	10.46	50	1000	0.091
L4CR-57,58	10.46	50	1500	0.108
L4CR-57,58	10.46	50	2000	0.121
L4CR-57,58	10.46	50	3000	0.142
L4CR-57,58	10.46	50	4000	0.159
L4CR-57,58	10.46	50	5000	0.171
L4CR-57,58	10.46	50	6000	0.181
L4CR-57,58	10.46	50	7000	0.194
L4CR-57,58	10.46	50	8000	0.202

Table F-1 Automated Rut Test Results from the APA (Cont'd)

Specimen No.	Average Air Voids (%)	Temperature (°C)	Number of Cycles	Measured Rut (in.)
L4CR-6,12	2.10	64	500	0.039
L4CR-6,12	2.10	64	1000	0.052
L4CR-6,12	2.10	64	1500	0.063
L4CR-6,12	2.10	64	2000	0.073
L4CR-6,12	2.10	64	3000	0.096
L4CR-6,12	2.10	64	4000	0.114
L4CR-6,12	2.10	64	5000	0.127
L4CR-6,12	2.10	64	6000	0.135
L4CR-6,12	2.10	64	7000	0.144
L4CR-6,12	2.10	64	8000	0.148
L4CR-81,82	2.13	64	500	0.030
L4CR-81,82	2.13	64	1000	0.036
L4CR-81,82	2.13	64	1500	0.041
L4CR-81,82	2.13	64	2000	0.046
L4CR-81,82	2.13	64	3000	0.054
L4CR-81,82	2.13	64	4000	0.061
L4CR-81,82	2.13	64	5000	0.069
L4CR-81,82	2.13	64	6000	0.074
L4CR-81,82	2.13	64	7000	0.083
L4CR-11,13	2.52	64	500	0.038
L4CR-11,13	2.52	64	1000	0.055
L4CR-11,13	2.52	64	1500	0.070
L4CR-11,13	2.52	64	2000	0.083
L4CR-11,13	2.52	64	3000	0.105
L4CR-11,13	2.52	64	4000	0.121
L4CR-11,13	2.52	64	5000	0.136
L4CR-11,13	2.52	64	6000	0.143
L4CR-11,13	2.52	64	7000	0.155
L4CR-11,13	2.52	64	8000	0.158

Table F-1 Automated Rut Test Results from the APA (Cont'd)

Specimen No.	Average Air Voids (%)	Temperature (°C)	Number of Cycles	Measured Rut (in.)
L4CR-79,80	2.90	64	500	0.025
L4CR-79,80	2.90	64	1000	0.033
L4CR-79,80	2.90	64	1500	0.042
L4CR-79,80	2.90	64	2000	0.050
L4CR-79,80	2.90	64	3000	0.064
L4CR-79,80	2.90	64	4000	0.082
L4CR-79,80	2.90	64	5000	0.097
L4CR-79,80	2.90	64	6000	0.111
L4CR-79,80	2.90	64	7000	0.119
L4CR-79,80	2.90	64	8000	0.128
L4CR-87,88	4.23	64	500	0.043
L4CR-87,88	4.23	64	1000	0.059
L4CR-87,88	4.23	64	1500	0.071
L4CR-87,88	4.23	64	2000	0.085
L4CR-87,88	4.23	64	3000	0.107
L4CR-87,88	4.23	64	4000	0.123
L4CR-87,88	4.23	64	5000	0.139
L4CR-87,88	4.23	64	6000	0.148
L4CR-87,88	4.23	64	7000	0.157
L4CR-87,88	4.23	64	8000	0.165
L4CR-14,15	4.52	64	500	0.066
L4CR-14,15	4.52	64	1000	0.088
L4CR-14,15	4.52	64	1500	0.100
L4CR-14,15	4.52	64	2000	0.112
L4CR-14,15	4.52	64	3000	0.128
L4CR-14,15	4.52	64	4000	0.143
L4CR-14,15	4.52	64	5000	0.153
L4CR-14,15	4.52	64	6000	0.157
L4CR-14,15	4.52	64	7000	0.165
L4CR-14,15	4.52	64	8000	0.174

Table F-1 Automated Rut Test Results from the APA (Cont'd)

Specimen No.	Average Air Voids (%)	Temperature (°C)	Number of Cycles	Measured Rut (in.)
L4CR-2,3	5.56	64	500	0.054
L4CR-2,3	5.56	64	1000	0.074
L4CR-2,3	5.56	64	1500	0.088
L4CR-2,3	5.56	64	2000	0.097
L4CR-2,3	5.56	64	3000	0.111
L4CR-2,3	5.56	64	4000	0.124
L4CR-2,3	5.56	64	5000	0.134
L4CR-2,3	5.56	64	6000	0.142
L4CR-2,3	5.56	64	7000	0.150
L4CR-2,3	5.56	64	8000	0.159
L4CR-85,86	5.66	64	500	0.065
L4CR-85,86	5.66	64	1000	0.091
L4CR-85,86	5.66	64	1500	0.108
L4CR-85,86	5.66	64	2000	0.119
L4CR-85,86	5.66	64	3000	0.136
L4CR-85,86	5.66	64	4000	0.154
L4CR-85,86	5.66	64	5000	0.166
L4CR-85,86	5.66	64	6000	0.175
L4CR-85,86	5.66	64	7000	0.182
L4CR-85,86	5.66	64	8000	0.190
T-4,5	6.47	64	500	0.047
T-4,5	6.47	64	1000	0.063
T-4,5	6.47	64	1500	0.074
T-4,5	6.47	64	2000	0.086
T-4,5	6.47	64	3000	0.101
T-4,5	6.47	64	4000	0.114
T-4,5	6.47	64	5000	0.125
T-4,5	6.47	64	6000	0.139
T-4,5	6.47	64	7000	0.145
T-4,5	6.47	64	8000	0.151

Table F-1 Automated Rut Test Results from the APA (Cont'd)

Specimen No.	Average Air Voids (%)	Temperature (°C)	Number of Cycles	Measured Rut (in.)
T-13,15	7.12	64	500	0.061
T-13,15	7.12	64	1000	0.081
T-13,15	7.12	64	1500	0.101
T-13,15	7.12	64	2000	0.117
T-13,15	7.12	64	3000	0.140
T-13,15	7.12	64	4000	0.156
T-13,15	7.12	64	5000	0.171
T-13,15	7.12	64	6000	0.182
T-13,15	7.12	64	7000	0.195
T-13,15	7.12	64	8000	0.198
L4CR-18,19	7.37	64	500	0.055
L4CR-18,19	7.37	64	1000	0.069
L4CR-18,19	7.37	64	1500	0.084
L4CR-18,19	7.37	64	2000	0.092
L4CR-18,19	7.37	64	3000	0.105
L4CR-18,19	7.37	64	4000	0.117
L4CR-18,19	7.37	64	5000	0.128
L4CR-18,19	7.37	64	6000	0.135
L4CR-18,19	7.37	64	7000	0.143
L4CR-18,19	7.37	64	8000	0.150
L4CR-17,20	7.65	64	500	0.070
L4CR-17,20	7.65	64	1000	0.088
L4CR-17,20	7.65	64	1500	0.104
L4CR-17,20	7.65	64	2000	0.115
L4CR-17,20	7.65	64	3000	0.134
L4CR-17,20	7.65	64	4000	0.150
L4CR-17,20	7.65	64	5000	0.164
L4CR-17,20	7.65	64	6000	0.166
L4CR-17,20	7.65	64	7000	0.176
L4CR-17,20	7.65	64	8000	0.183

Table F-1 Automated Rut Test Results from the APA (Cont'd)

Specimen No.	Average Air Voids (%)	Temperature (°C)	Number of Cycles	Measured Rut (in.)
T-11,12	7.94	64	500	0.056
T-11,12	7.94	64	1000	0.075
T-11,12	7.94	64	1500	0.091
T-11,12	7.94	64	2000	0.103
T-11,12	7.94	64	3000	0.123
T-11,12	7.94	64	4000	0.140
T-11,12	7.94	64	5000	0.152
T-11,12	7.94	64	6000	0.163
T-11,12	7.94	64	7000	0.174
T-11,12	7.94	64	8000	0.183
L4CR-30,31	9.21	64	500	0.063
L4CR-30,31	9.21	64	1000	0.081
L4CR-30,31	9.21	64	1500	0.096
L4CR-30,31	9.21	64	2000	0.105
L4CR-30,31	9.21	64	3000	0.142
L4CR-30,31	9.21	64	4000	0.161
L4CR-30,31	9.21	64	5000	0.177
L4CR-30,31	9.21	64	6000	0.188
L4CR-30,31	9.21	64	7000	0.200
L4CR-30,31	9.21	64	8000	0.208
L4CR-28,29	9.86	64	500	0.053
L4CR-28,29	9.86	64	1000	0.071
L4CR-28,29	9.86	64	1500	0.083
L4CR-28,29	9.86	64	2000	0.095
L4CR-28,29	9.86	64	3000	0.131
L4CR-28,29	9.86	64	4000	0.150
L4CR-28,29	9.86	64	5000	0.162
L4CR-28,29	9.86	64	6000	0.174
L4CR-28,29	9.86	64	7000	0.187
L4CR-28,29	9.86	64	8000	0.197

Table F-1 Automated Rut Test Results from the APA (Cont'd)

Specimen No.	Average Air Voids (%)	Temperature (°C)	Number of Cycles	Measured Rut (in.)
L4CR-32,33	10.63	64	500	0.078
L4CR-32,33	10.63	64	1000	0.101
L4CR-32,33	10.63	64	1500	0.120
L4CR-32,33	10.63	64	2000	0.131
L4CR-32,33	10.63	64	3000	0.170
L4CR-32,33	10.63	64	4000	0.187
L4CR-32,33	10.63	64	5000	0.201
L4CR-32,33	10.63	64	6000	0.217
L4CR-32,33	10.63	64	7000	0.225
L4CR-32,33	10.63	64	8000	0.231

Appendix G: Difficulties Encountered During Instrumentation and Field Measurement

A large portion of this study is comprised of a comprehensive field study including instrumentation of a Test Section and field performance measurements on the Test Section. Several difficulties were encountered regarding instrumentation and field measurements. Difficulties relevant to field measurements and instrumentations are listed below:

1) There were three moisture probes installed in the Test Section on top of the aggregate base layer, stabilized subgrade layer, and natural subgrade layer. The purpose of installing moisture probes was to measure volumetric moisture content in the respective layers. Unfortunately, none of the moisture probes was able to collect any volumetric water content data from the Test Section.
2) Rut data measured with straight edge/rut gauge combination showed inconsistencies in some of the stations. These inconsistencies were discussed in Section 3.8. Based on the observations that straight edge/rut gauge combination could not capture the rut data from the field precisely, a more sophisticated equipment, called Face Dipstick®, was purchased for measuring changes in rut values more accurately. Rut data measured with the Face Dipstick® were consistent with the rut values reported in other Test Road studies (e.g., Finn. et al., 1977; Selvaraj, 2007). Therefore, rut measurement with a Face Dipstick® is recommended for future studies.
3) Three Dynax® axle sensors supplied by International Road Dynamics, Inc. were installed at the instrumentation site to measure the wheel wander of the vehicles traversing the Test Section. These axle sensors were prone to rupture. For example, these sensors had to be replaced on August 21, 2008, just approximately three months after the Test Section was opened to traffic. These sensors were again replaced on October 28, 2009. From these

observations, one could conclude that this type of axle sensors may not be suitable for a very high volume road.

4) There were five temperature probes installed in the Test Section to measure the temperature at different depths. During November, 2008, three temperature probes were reporting unrealistic data. Consequently, all the five temperature probes were replaced on December 3, 2008.